JOINT INSTITUTE FOR AERONAUTICS AND ACOUSTICS

STANFORD UNIVERSITY

AMES RESEARCH CENTER

MODAL CONTENT OF NOISE GENERATED BY A COAXIAL JET IN A PIPE

E. J. Kerschen and J. P. Johnston

STANFORD UNIVERSITY
Department of Aeronautics and Astronautics
Stanford, California 94305

May 1978

JIAA TR-11

MODAL CONTENT OF NOISE GENERATED BY A COAXIAL JET IN A PIPE

E.J. KERSCHEN AND J.P. JOHNSTON

THERMAL SCIENCES DIVISION
DEPARTMENT OF MECHANICAL ENGINEERING
STANFORD UNIVERSITY
STANFORD, CALIFORNIA

MAY 1978

The work here presented has been supported by the National Science Foundation under Grants NSF-GK-37294 and NSF-ENG-76-00819

And Partially By

The National Aeronautics and Space Administration under Grant NASA 2007

Acknowledgments

The authors gratefully acknowledge the support of the Engineering Division and the Fluid Mechanics Program of the National Science Foundation under grants GK-37294 and ENG-76-00819. In addition, the Stanford/NASA-Ames Research Center Joint Institute for Aeronautics and Acoustics provided incidental support, plus a Research Assistantship for the first author, during one year of the program. Additional support was provided by the Thermosciences Affiliates Program of the Stanford Mechanical Engineering Department.

Professors W. C. Reynolds and K. Karamcheti both provided valuable advice and ideas. J. Pope, E. E. Bouchard, P. M. Ligrani, and many other people in the Mechanical Engineering Department contributed suggestions and assisted in the research. We thank all of these people for their generous help.

Table of Contents

		Page
Acknowledgments		iii
List of Tables		vii
List of Figures		viii
Abstract		x
Nomenclature		xii
Chapter		
1	INTRODUCTION AND OBJECTIVES	1
2	DEVELOPMENT OF MODAL SEPARATION TECHNIQUES	6
	2.1 Previous Work	6
	2.2 Acoustic Propagation Inside a Pipe Containing a Nonuniform Mean Flow	7
	2.3 The Instantaneous Mode Separation Technique	10
	2.4 The Time-Averaged Mode Separation Technique	12
	2.5 Instrumentation for the Instantaneous Mode Separation Technique	14
	2.6 Instrumentation for the Time-Averaged Mode-Separation Technique	14
	2.7 Comparison of Spectra Measured with the Instantaneous and Time-Averaged Techniques	15
	2.8 Summary	18
3	EXPERIMENTAL MEASUREMENTS OF NOISE GENERATED BY FLOW THROUGH COAXIAL RESTRICTIONS IN PIPES	20
	3.1 Previous Research	20
	3.2 Experimental Apparatus and Instrumentation	22
	3.3 Definition of Parameters	23
	3.4 Parameter Ranges Covered in the Experiments	24
	3.5 Experimental Results	25
	3.5.1 Characteristics of the Modal Pressure Spectra	26
	3.5.2 Modal Power—Spectra and Overall Efficiency Levels	30
	3.6 Magnitudes of the Hydrodynamic Pressure Fluctuations at the Measurement Station	35
	3.7 Background Noise	37
	3.8 Pipewall Excitation by Acoustic Duct Modes	38
	3.9 Effect of the Outlet Plenum on Acoustic Waves	40
	3.10 Summary	42

Table of Contents (cont.)

Chapter | Page

4 ACOUSTIC ENERGY PROPAGATION IN A CIRCULAR DUCT CONTAINING AN AXISYMMETRIC, SUBSONIC MEAN FLOW 45

4.1 Previous Work 45
4.2 Derivation of the Physical Energy Equation 51
4.3 Application of the Physical Energy Equation to Acoustic Propagation Inside Ducts 54
4.3.1 Evaluation of $\int_s < J^p_{s_z} > ds$ 55
4.3.2 Evaluation of $\mathbb{P}^p_a$ 57
4.3.3 Evaluation of $\mathbb{P}^p_b$ 58
4.3.4 Evaluation of $\int_{z_1}^{z_2} \int_s < - \rho_o u_r' u_z' \frac{dU_o}{dr} > ds\, dz$. 60
4.3.5 Substitution into the Integrated Form of the Time-Averaged Physical Energy Equation 61
4.4 Acoustic Energy Flow Expressions Based on the Conservation Equations of Blockhintsev and Möhring . . . 62
4.5 Numerical Results 66
4.5.1 Numerical Techniques 66
4.5.2 Comparison of Blockhintsev and Möhring Energy Weighting Functions 67
4.5.3 General Characteristics of the Möhring Energy Weighting Functions and Comparison to Slug Flow Approximations 69
4.5.4 Comparison of the Möhring and Physical Energy Weighting Functions 71
4.5.5 Importance of the Terms Containing dM/dr in the Möhring and Physical Energy Weighting Functions 72
4.5.6 Orthogonality of the Mode Shape Function 73
4.6 Summary 74

5 CONCLUSIONS AND RECOMMENDATIONS 77

5.1 Conclusions 77
5.2 Recommendations 80

Tables 82

Figures 85

References 111

Table of Contents (cont.)

Appendix		Page
A1	COMPUTER PROGRAMS FOR THE MODE SEPARATION TECHNIQUES . .	115
	A1.1 Program PIPE	115
	A1.2 Program PIPE4	124
	A1.3 Program PIPE2	133
A2	COMPUTER PROGRAM FOR ACOUSTIC POWER ANALYSIS	139
A3	MODAL PRESSURE AND POWER SPECTRA	146
A4	TABULATED EXPERIMENTAL RESULTS	181
A5	UNCERTAINTY ANALYSIS	189
A6	WALL STATIC PRESSURE PROFILES FOR THE 16.2 mm NOZZLES .	195
A7	CROSS-CORRELATION MEASUREMENTS OF THE HYDRODYNAMIC PRESSURE FLUCTUATIONS	199
A8	DERIVATION OF THE PHYSICAL ENERGY EQUATION AND ACOUSTIC ENERGY FLOW EXPRESSIONS	201
	A8.1 Introduction	201
	A8.2 A Detailed Derivation of the Physical Energy Equation	201
	A8.3 Evaluation of $\int_s \langle J^p_{s_z} \rangle ds$	207
	A8.4 Evaluation of $\mathcal{I}^p_b$	210
A9	DERIVATION OF ACOUSTIC ENERGY EXPRESSIONS BASED ON THE WORK OF BLOCKHINTSEV AND MÖHRING	213
	A9.1 Results Based on the Work of Blockhintsev	213
	A9.2 Results Based on the Work of Möhring	218
A10	COMPUTER PROGRAMS FOR THE ENERGY-WEIGHTING FUNCTION ANALYSIS	222
	A10.1 Program MODE	222
	A10.2 Program INTGRTE	237
A11	TABULATED ENERGY-WEIGHTING FUNCTION RESULTS	248

List of Tables

Table | | Page
1 Accuracy of Geometric Acoustics Limit for 1/7th Power Mean Profile 82

2 A Comparison of the Möhring and Physical Energy Weighting Functions for 1/7th Power Mean Flow Profiles 83

3 Percentage Contributions of the Terms Containing $(dM/d\bar{r})$ to the Total Values of EWF^P and EWF^M 84

List of Figures

Figure		Page
1	An illustration of the physical characteristics of flow-generated noise	85
2	Schematic of the experimental apparatus	86
3	Duct geometry and coordinate system	87
4a	Line diagram of instrumentation for the instantaneous mode separation technique	88
4b	Line diagram of instrumentation for the time-averaged mode separation technique	88
5	Modal pressure spectra measured with the instantaneous mode separation technique	89
6	Modal pressure spectra measured with the time-averaged mode separation technique using 64 ensembles. Output of the instantaneous technique shown for comparison	90
7	Modal pressure spectra measured with the time-averaged mode separation technique using 256 ensembles. Output of the instantaneous technique shown for comparison	91
8	Photograph of experimental apparatus	92
9	Photograph of microphone assembly	93
10	Photograph showing microphones mounted on the pipe	93
11	Typical modal pressure spectra for a low value of the frequency ratio, $f_r = 1.19$	94
12	Typical modal pressure spectra for a high value of the frequency ratio, $f_r = 7.42$	94
13	A comparison of two sets of modal pressure spectra with closely matching frequency ratio	95
14	A comparison of two sets of modal pressure spectra with closely matching frequency ratio	96
15	Typical modal pressure spectra for the 3.18 mm diameter nozzle	97
16	Modal power spectra calculated using the modal pressure spectra shown in Fig. 11	98

List of Figures (cont.)

Figure		Page
17	Overall noise generation efficiency plotted as a function of jet indicated Mach number	99
18	Overall noise generation efficiency divided by area ratio plotted as a function of jet indicated Mach number	100
19	Modal pressure spectra illustrating the relative levels of acoustic and hydrodynamic pressure fluctuations at the measurement station	101
20	Modal pressure spectra measured 2.2 meters downstream of the restriction. Note dip in the (1,0) mode at 2500 Hz and in the (2,0) mode at 5000 Hz	102
21.	Cross-sectional pressure patterns for the first three acoustic duct modes	103
22.	Modal pressure spectra measured 2.36 meters downstream of the restriction with stiffened pipe configuration. Experimental conditions (M_i and (d/D)) are identical to those for Fig. 20	104
23a.	Modal pressure spectra measured upstream of the outlet plenum (2.2 meters downstream of the restriction). M_i and d/D are identical to those for Fig. 23b	105
23b.	Modal pressure spectra measured in the downstream no-flow zone. M_i and d/D are identical to those for Fig. 23a .	105
24.	Proposed modification to outlet plenum section of experimental apparatus	106
25.	Schematic of possible surfaces for measurement for acoustic energy flow from duct end	106
26a.	(0,0) mode energy weighting functions for sheared mean flow profiles and comparison to slug flow approximations	107
26b.	(1,0) mode energy weighting functions for sheared mean flow profiles and comparison to slug flow approximations	108
26c.	(2,0) mode energy weighting functions for sheared mean flow profiles and comparison to slug flow approximations	109
26d.	(0,1) mode energy weighting functions for sheared mean flow profiles and comparison to slug flow approximations	110

Abstract

The basic problem investigated was that of noise generated by air flow through a coaxial obstruction in a long, straight pipe. This study concentrated on the modal characteristics of the noise field inside the pipe and downstream of the restriction.

Two measurement techniques were developed for separation of the noise into the acoustic duct modes. The instantaneous mode separation technique uses four microphones, equally spaced in the circumferential direction, at the same axial location. Instantaneous addition of various microphone outputs separates the (0,0), (1,0), and (2,0) modes. Higher modes can be separated approximately.

The time-averaged mode separation technique uses three microphones mounted at the same axial location. A matrix operation on time-averaged data produces the modal pressure levels. This technique requires the restrictive assumption that the acoustic modes are uncorrelated with each other. Comparison of the results of the two techniques shows that this is in fact the case, for the type of noise source examined in this study.

Downstream modal pressure spectra in the 200-6000 Hz frequency range were measured for orifices and nozzles ranging in diameter from 3.18 to 50.8 mm. The shape of the modal frequency spectrum was found to be determined by the frequency ratio, $f_r = \frac{\gamma}{\pi St} = U_1 D/a_o d$. This parameter is the ratio of two nondimensional frequencies, γ, which controls acoustic propagation inside circular ducts, and St, which scales the jet noise spectrum shape. At low f_r (< 3) the higher modes dominate the noise spectrum above their cutoff frequencies, while for higher f_r all modes are of approximately equal amplitude. The nature of large-scale turbulence structures in the region of the jet near the nozzle exit may be used to explain these phenomena.

The measured modal pressure spectra were converted to modal power spectra and integrated over the frequency range 200-6000 Hz. The acoustic efficiency levels (acoustic power normalized by jet kinetic energy flow), when plotted vs. jet Mach number, showed a strong dependence on the ratio of restriction diameter to pipe diameter. Dividing the efficiency levels by the area ratio produced the correlation $\eta/(d/D)^2 = 3.47 \times 10^{-5} M_1^{4.6}$,

valid over a reasonable range of (d/D). The acoustic efficiency levels of the nozzles and orifices agreed closely, when the comparison was made using nozzle exit plane and orifice vena contracta conditions.

In a separate part of the study, acoustic energy flow expressions were developed for the case of a hard-walled cylindrical duct containing a sheared mean flow. Formulations using three different approaches were examined: (i) the thermodynamic energy equation, (ii) the conservation equation of Blockhintsev, i.e., the geometric acoustics limit, and (iii) the conservation principle of Möhring.

The acoustic energy flux derived from the thermodynamic energy equation consists of the flow work $(< p'\overline{v}' >)$ of the acoustic wave plus the acoustic energy density convected by the mean flow. This flux is conserved in a constant-area duct containing a sheared mean flow, but is not conserved in a general, nonuniformly moving medium.

Comparison of the Möhring and Blockhintsev energy flux expressions defines the extent to which the geometric acoustics limit is valid. To assess this, these energy flux expressions were compared for 1/7th power mean flow profiles with centerline Mach numbers up to 0.9. For the (0,0) mode, the differences were uniformly small for low and high frequencies. For the higher modes, the differences were greatest at frequencies near cutoff and approached those seen for the (0,0) mode at higher frequencies. The general validity of the geometric acoustics limit was remarkable.

The values of the energy flux expressions calculated for sheared mean flow profiles were compared to approximate values obtained using a slug flow profile with the same overall flowrate. The agreement was very poor, except for the (0,0) mode at low frequencies and the higher modes close to their cutoff frequencies.

The acoustic energy flow analyses based on the thermodynamic energy equation and on the results of Möhring both resulted in orthogonality properties for the eigenfunctions of the radial mode shape equation. These orthogonality relationships involve the eigenvalues and derivatives of the radial mode shape functions.

Nomenclature

English Letter Symbols

a	Adiabatic speed of sound, $a = \sqrt{\left.\frac{\partial P}{\partial \rho}\right\|_s}$.
C	Modal amplitude coefficient.
d	Orifice or nozzle diameter.
D	Pipe inside diameter.
$\bar{e}$	Unit vector.
EWF	Energy weighting function (see Chapter 4).
f	Frequency
f_r	Frequency ratio, $f_r = U_i D/a_o d$.
f_{St}	Frequency based on Strouhal number, $f_{St} = 0.2(U_i/d)$.
h	Enthalpy
i	$\sqrt{-1}$.
$\bar{J}_s$	Acoustic intensity (see Chapter 4).
k	Wavenumber, $k = \omega/a_o$.
$\bar{k}$	Nondimensionalized axial wavenumber, $\bar{k} = k_z/k$.
K	$K = (1 - \bar{k}M)$.
L_t	Nozzle throat length.
m, n	Acoustic duct mode numbers (m - circumferential, n - radial)
$\dot{m}$	Mass flow rate.
M	Mach number, $M = U/a$.
p	Pressure.
p'	Acoustic pressure.
P_o	Mean flow pressure; stagnation pressure.
$P(r,\theta)$	Acoustic pressure mode shape function, see p. 8.
$P_w(\theta)$	Fluctuating pressure measured at inner pipe wall.

$\mathbb{P}$	Acoustic power.
r	Radius.
r_o	Duct radius.
$\bar{r}$	Nondimensionalized radius, $\bar{r} = r/r_o$.
$R(\bar{r})$	Radial mode shape function.
Re	Reynolds number, $Re = \rho_i U_i d/\mu_i$.
s	Entropy; duct cross section.
St	Strouhal number, $St = fd/U$.
t	Time.
T_o	Stagnation temperature.
u	Velocity (scaler).
u'	Acoustic velocity (scaler).
U	Mean flow velocity (scaler).
$\bar{v}$	Velocity (vector).
$\bar{v}'$	Acoustic velocity (vector).
$\bar{V}_o$	Mean flow velocity (vector).
$V(r,\theta)$	Acoustic velocity mode shape function, see p. 8.
z	Axial coordinate.
$\bar{z}$	Normalized axial coordinate, $\bar{z} = kz$.
$\bar{z}_o$	Axial location of measurements.

<u>Superscripts</u>

( )'	Acoustic fluctuation.
B	Blockhintsev.
M	Möhring.
P	Physical
*	Complex conjugate.

Subscripts

ac	Acoustic.
a	Portion of acoustic power that is independent of $\overline{z}$.
b	Portion of acoustic power that is not independent of $\overline{z}$.
cr	Value for mode cutoff.
℄	Duct centerline.
hydro	Hydrodynamic.
i	Indicated conditions of vena contracta of orifice jet or exit plane of nozzle jet.
mn	Refers to (m,n) acoustic duct mode.
o	Mean flow conditions; stagnation conditions.
r	Component in radial direction.
w	Duct inside wall.
z	Component in axial direction.
θ	Component in circumferential direction.

Greek Letter Symbols

γ	Reduced frequency, $\gamma = \omega r_o/a_o$; ratio of specific heats.
Γ	Represents quantity $= \frac{1}{a}\frac{\partial}{\partial\rho}(\rho a)$.
δ	Shear layer thickness; uncertainty in a measurand.
ε	Small parameter in perturbation expansion.
ε_m	$\varepsilon_m = 0$, $m = 0$; $\varepsilon_m = 1$, $m = 1, 2, 3, \ldots$.
η	Acoustic efficiency, $\eta = \mathbb{P}/(\frac{1}{2}\dot{m}U_1^2)$
θ	Circumferential coordinate.
μ	Zeros of $\frac{d}{dx}(J_m(x))$; absolute viscosity.
ξ_s	Acoustic energy density (see p. 45).
ρ	Density
ρ'	Acoustic density.

ρ_o Mean flow density.

ϕ Acoustic duct mode phase angle.

ω Circular frequency.

Special Symbols

$\overline{[\quad]^2}$ Mean square value.

$<\quad>$ Time-averaged value.

Chapter 1

INTRODUCTION AND OBJECTIVES

Noise generation by internal flows and propagation in ducts are subjects of concern in many technical areas. The noise levels generated by flow metering and throttling equipment in power plants and chemical plants are often very high, causing annoyance and in some cases hearing damage to workers in the vicinity of the equipment. In many applications, fans and compressors generate noise levels inside pipes and ducts comparable to those produced by flow throttling equipment, with the same undesirable results. A substantial quantity of fundamental research has been directed towards fan and compressor noise, principally because of the aircraft engine noise problem. The present research program is a fundamental study of the former, less well-known problem, that of noise generation by flow through obstructions in pipes.

The physical problem under investigation is illustrated in Fig. 1. Typically, a low to moderate speed flow approaches a restriction in a pipe. A high-speed turbulent jet, surrounded by a very low velocity recirculation zone, forms just downstream of the restriction. The jet width grows with distance downstream of the restriction, until the flow eventually reattaches to the pipe wall. In industrial applications, the geometry of the restrictions (valves, flow regulators, etc.) is often complex, and the pressure drop across the device may be large enough to produce regions of supersonic flow and strong shocks downstream of the restriction. Noise generation by restrictions causing very high pressure drops has been studied by Witczak (1976); the present research considered the subsonic flow regime. Restrictions of simple geometry (orifices and nozzles) were chosen for this fundamental study.

For discussion purposes, the flow field can be separated into two regions. The first region is the source region, in which the noise is actually generated. In the second region the noise only propagates; there is no significant noise generation. These regions are indicated in Fig. 1. The noise generation and flow characteristics of the source region are very similar to the case of a free jet. In a free jet, the kinetic energy of the jet is dissipated by turbulent mixing, as ambient fluid is entrained by the jet, causing the jet width to grow. The unsteady fluid dynamical processes associated with the turbulent mixing are the source of the noise in the free jet case. For a confined jet, the turbulent mixing is also a very important noise source. However, the characteristics of the turbulent mixing may be altered by the effect of the confining pipe wall on the entrainment process. Also, the jet flow reattaches to the pipe wall before its kinetic energy is fully dissipated. Unsteady behavior in the reattachment region may be an additional important noise source for a confined jet.

Compared to a free jet, the confined jet differs significantly in its noise-radiation condition. For a free jet, the noise radiates into an infinite medium, and at large distances from the jet the acoustic waves appear to be locally plane. The radiation condition for a confined jet is radically different. Noise propagation inside a duct is governed by the solution of an eigenvalue equation, and the noise propagates in particular acoustic duct modes. The lowest mode propagates at all frequencies, while each higher mode propagates only above its own cutoff frequency. At frequencies below cutoff a given mode is exponentially attenuated. In most situations, the noise generated by confined jets extends over a frequency range in which several acoustic duct modes are propagating. Thus, to accurately measure the noise produced by confined jets, measurement techniques which separate the noise field into the acoustic duct modes are necessary.

The noise generated by confined jets normally reaches the observer in one of two ways. First, the noise may propagate inside the pipe in the direction of the duct axis and leave through the duct inlet or outlet. In this situation it is important to be able to estimate the acoustic energy flow in the direction of the duct axis. The acoustic energy flow for a given pressure level is different for different acoustic duct modes, and also depends on the frequency of the acoustic wave. Thus an accurate determination of the acoustic energy flow requires modal separation of the pressure spectra. Also, the attenuation caused by pipe wall acoustic treatment, changes in pipe cross-sectional area, tees, and other pipe fittings and terminations is different for different acoustic duct modes.

Therefore, an accurate assessment of the effect of configuration changes on the noise that propagates out of a piping system inlet or outlet depends upon a knowledge of the modal characteristics of the sound field.

A second way in which the noise inside a pipe may reach the observer is for it to pass through the pipe wall. Acoustic pressure fluctuations inside a pipe may excite pipe wall vibrations, which in turn radiate noise to the surroundings. The pipe wall excitation seems to be fundamentally different for different acoustic duct modes. Thus, the efficiency with which acoustic pressure fluctuations inside the pipe are transmitted through the pipe wall may be strongly mode-dependent. This again emphasizes the importance of modal separation in experimental measurement techniques.

Most of the previous studies of noise generated by flow through restrictions in pipelines have ignored the modal characteristics of the sound field inside the pipe. These experiments can basically be grouped into two types. In type (i) a pipe containing a restriction is passed through a room, and the noise level outside the pipe is measured. Thus only the noise transmitted through the pipe wall is detected, and the characteristics of this noise are influenced strongly by the sound transmission and vibrational characteristics of the pipe and the supporting structure. In the experiments of type (ii) the flow exhausts into a reverberant chamber, with only a short section of pipe downstream of the restriction. In this situation there can be strong reflections at the end of the pipe, and again the measurements outside the pipe may not be very representative of the noise field inside the pipe.

The research presented in this report is a continuation of the program initiated by Roberts and Johnston (1974), who studied noise generation by flow through sharp-edged orifices. In order to overcome the problems associated with the previously discussed experimental approaches, they designed an experimental rig which allowed measurements of the acoustic pressure inside the pipe, but without signal contamination by the hydrodynamic pressure fluctuations present in turbulent pipe flow. The rig, a schematic of which is shown in Fig. 2, consists of a thick-walled plastic pipe (4 inch nominal diameter) terminated on both ends by anechoic terminations. Flow enters and exits radially through bronze porous elements of the same inner diameter as the pipe (97 mm). Roberts made wall sound pressure measurements with a single microphone in the no-flow zones upstream and downstream of the inlet and outlet plenums. In these no-flow zones the measurements were not affected by the hydrodynamic pressure fluctuations present in the regions of the pipe containing turbulent flow. However, the acoustic waves seemed to suffer some attenuation as they passed through the plenum sections. Also, a substantial portion of the noise was at frequencies above the first cutoff frequency of the duct, where more than one mode starts propagating. In calculating acoustic energy flow, Roberts assumed that the total signal measured by the wall microphone was that of a plane wave. He also added a correction factor for outlet plenum attenuation. The present research examined the accuracy of these assumptions during the course of a much deeper study.

The present work had the following specific objectives.

- To develop experimental measurement techniques which separate the noise field into the different acoustic duct modes.
- To measure modal pressure spectra for a variety of restriction shapes, sizes, and flowrate conditions.
- To relate the measured pressure spectra to acoustic energy flow in the direction of the pipe axis.
- To estimate the error bound for acoustic power measurements which use only one microphone, located flush with the inner pipe wall, and assume plane wave propagation.

The main body of this report is contained in Chapters 2, 3, and 4. Chapter 5 contains a summary of the results, conclusions, and recommendations for further study. The development of experimental modal separation techniques is covered in Chapter 2. The main experimental results of the research are presented in Chapter 3. These include modal spectra and overall efficiency levels for nozzles and orifices in the subsonic flow regime. In Chapter 4, an energy flux expression is developed from the thermodynamic energy equation. This "physical" energy flux is compared to energy flux expressions developed from two conservation equation approaches. The accuracy with which the actual mean flow profile in the pipe can be approximated by a slug flow profile for acoustic energy flow calculations is examined.

Because the subject matter of each chapter comes historically from only loosely related areas, detailed discussions of background references and state of the art are given in the individual chapters rather than in this brief introduction.

Chapter 2

DEVELOPMENT OF MODAL SEPARATION TECHNIQUES

2.1 Previous Work

Previous research on experimental techniques to separate noise inside ducts into the acoustic duct modes has largely been concerned with fan noise. Mugridge (1969) used a technique in which the outputs of two hot-wire anemometers were cross-correlated, after having been narrow bandpass filtered at a pure tone* frequency. The technique required that the probes be traversed around the circumference of the duct. Bolleter and Crocker (1972) and Harel and Perulli (1972) both used a similar technique employing microphones instead of hot-wire anemometers. In these techniques separation of the radial mode orders requires radial as well as circumferential traversing. Yardley (1975) developed a modified technique which separates the radial mode orders without radial traversing. This technique requires measurements at several axial stations and uses the solution of the wave equation in the data reduction. A complication of this technique is that the wave equation solution can be expressed in analytical form only for the simple case of a uniform mean flow. Another type of measurement technique, which uses the principles of eduction rather than cross-correlation, has been presented by Moore (1972). In this approach the pressure field in the duct is sampled and phase-averaged relative to the fan shaft rotation. In this way the part of the pressure field coherent with shaft rotation is educted. Cumpsty (1977) summarizes the current state of the art in modal measurements in a recent paper. He states that, "All of the in-duct methods are difficult to apply, and it is hard to obtain adequate accuracy, particularly when several modes are present, some of which may be cut-off, and where the modes are reflected back to the source from the intake or exhaust plane. Nevertheless, they represent an important area where work should be continued."

The techniques explained above are not particularly well suited to the measurement of broadband noise generated by a coaxial jet in a pipe.

---

*A frequency corresponding to a harmonic of the blade-passing frequency, for example.

The eduction approach used by Moore is of no use, because there is no applicable phase reference signal. Although the cross-correlation approaches are more suitable, they require phase-matched narrow bandpass filtering and microphone traversing. Any differences in filter phase or amplitude response will cause measurement inaccuracies, in addition to errors associated with finite filter bandwidth effects. A second type of error results if the source exhibits any unsteadiness or long-term drift during the microphone traverses. As well as the errors which may be introduced by the filtering process, measurement techniques which require narrow bandpass filtering are rather poorly suited for situations where the noise is essentially broadband in character, and measurements must be made at many frequencies. The need for microphone traversing adds complications to the measurement techniques and also introduces a potential source of error.

The mode separation techniques developed in this research avoid some of the complications of the previously discussed measurement techniques, such as phase-matched narrow bandpass filtering and microphone traversing. Only fixed-position microphones are used, and the signals are not narrow bandpass filtered. However, the assumption that the higher mode nodal diameters have no preferred angle in a time-averaged sense is necessary for both of the new techniques, the instantaneous and the time-averaged methods, which are developed in this chapter. The time-averaged mode separation technique requires the additional assumption that the modes be uncorrelated. The number of modes which can be separated is limited, but the results have high accuracy and the implementation of these new techniques is very simple compared to the previously discussed techniques.

2.2 Acoustic Propagation Inside a Pipe Containing a Nonuniform Mean Flow

In order to present the measurement techniques developed in this research, it is first necessary to briefly review the analysis of acoustic propagation inside circular ducts. The geometry being considered is shown in Fig. 3. The duct is of radius r_o, and the mean flow is in the axial direction and only a function of the radius. The equations are linearized about the mean flow, i.e., $p = P_o + p'$, etc. Furthermore, the flow is idealized to be inviscid and isentropic. Thus the equation of state reduces to $p' = a_o^2 \rho'$, where $a_o^2 = \left.\frac{dp}{d\rho}\right|_s$, the adiabatic speed of sound in the medium. The duct walls are assumed to be hard; thus $u_r = 0$ at $r = r_o$. The linearized continuity equation takes the form

$$\frac{\partial \rho'}{\partial t} + U_o \frac{\partial \rho'}{\partial z} + \rho_o \left(\frac{\partial u_r'}{\partial r} + \frac{u_r'}{r} + \frac{1}{r} \frac{\partial u_\theta'}{\partial \theta} + \frac{\partial u_z'}{\partial z} \right) = 0 \qquad (2\text{-}1)$$

The linearized Euler equations are given by

$$\frac{\partial u_r'}{\partial t} + U_o \frac{\partial u_r'}{\partial z} = -\frac{1}{\rho_o} \frac{\partial p'}{\partial r} \qquad (2\text{-}2a)$$

$$\frac{\partial u_\theta'}{\partial t} + U_o \frac{\partial u_\theta'}{\partial z} = -\frac{1}{\rho_o r} \frac{\partial p'}{\partial \theta} \qquad (2\text{-}2b)$$

$$\frac{\partial u_z'}{\partial t} + U_o \frac{\partial u_z'}{\partial z} + u_r' \frac{\partial U_o}{\partial r} = -\frac{1}{\rho_o} \frac{\partial p'}{\partial z} \qquad (2\text{-}2c)$$

The perturbation quantities are assumed to be of a propagating form, thus set

$$p'(r,\theta,z,t) = \mathrm{Re}\left\{ P(r,\theta)\, e^{i(\omega t - k_z z)} \right\}$$

$$u_r'(r,\theta,z,t) = \mathrm{Re}\left\{ V_r(r,\theta)\, e^{i(\omega t - k_z z)} \right\}, \quad \text{etc.}$$

Here $P(r,\theta)$, $V_r(r,\theta)$, etc., are mode shape functions which depend only on the transverse coordinates, ω is the circular frequency, and k_z is the axial wavenumber. With this substitution, $\left(\frac{\partial}{\partial t} + U_o \frac{\partial}{\partial z}\right) = i(\omega t - k_z U_o)$. Thus, after substitution of the propagating form, V_r, V_θ, and V_z in Eqns. (2-2a, -2b, and -2c) can be solved for in terms of derivatives of $P(r,\theta)$. Substitution into Eqn. (2-1) produces an equation for $P(r,\theta)$, when ρ' is replaced by p'/a_o^2. Furthermore, the equation is separable, $P(r,\theta) = R(r)\Theta(\theta)$ and $\Theta(\theta) = A \cos m\theta + B \sin m\theta$, $m = 0,1,\ldots$. Equivalently, this can be written as $\Theta(\theta) = C \cos(m\theta + \phi)$ where ϕ is an arbitrary phase angle. Nondimensionalizing in the following way,

$$\bar{r} = \frac{r}{r_o}, \quad \gamma = \frac{\omega r_o}{a_o}, \quad \bar{k} = \frac{k_z a_o}{\omega} = \frac{k_z}{k}, \quad \text{and} \quad M = \frac{U_o}{a_o},$$

the equation for $R(\bar{r})$ takes the form

$$\frac{d}{d\bar{r}}\left[\frac{\bar{r}}{(1-\bar{k}M)}\frac{dR}{d\bar{r}}\right]+\left[\left(\gamma^2\bar{r}-\frac{m^2}{\bar{r}(1-\bar{k}M)^2}\right)-\bar{k}^2\frac{\gamma^2\bar{r}}{(1-\bar{k}M)^2}\right]R = 0 \qquad (2\text{-}3)$$

Equation (2-3) was given in a slightly different form by Mungur and Plumblee (1969). The boundary condition can be obtained simply from Eqn. (2-2a) as $dR/d\bar{r} = 0$ at $\bar{r} = 1$. The solutions will be normalized such that $R(1) = 1$. This is an eigenvalue equation which has solutions only for certain values of $\bar{k}$. No closed-form solution exists for general $M(\bar{r})$.

The solution for $M = \text{const.}$ is

$$R_{mn}(\bar{r}) = \frac{J_m(\mu_{mn}\bar{r})}{J_m(\mu_{mn})}, \quad m = 0,1,2,\ldots, \quad n = 0,1,2,\ldots \qquad (2\text{-}4a)$$

and

$$\bar{k}_{mn} = \frac{-M \pm \sqrt{1-(1-M^2)(\mu_{mn}/\gamma)^2}}{(1-M^2)} \qquad (2\text{-}4b)$$

where J_m is the Bessel function of order m and μ_{mn} are the values of x for which $\frac{d}{dx}(J_m(x)) = 0$. The + sign is used in Eqn. (2-4b) for downstream propagation. If $\gamma > \mu_{mn}\sqrt{1-M^2}$, $\bar{k}_{mn}$ is real and the wave propagates down the duct with no attenuation. If $\gamma < \gamma_{cr_{m,n}} = \mu_{mn}\sqrt{1-M^2}$, the wave is exponentially attenuated with distance down the duct. Thus $\gamma_{cr_{m,n}}$ is called the cutoff frequency.

The behavior of the solution when Mach number depends on radius is similar to that for constant M. Above a certain frequency, $\bar{k}_{mn}$ is real and $R_{mn}(\bar{r})$ can also be shown to be real. However, $R_{mn}(\bar{r})$ and $\bar{k}_{mn}$ must be determined by numerical methods. In the experimental measurements, the noise level in all modes below their respective cutoff frequencies was negligible. Thus, only propagating modes with real $\bar{k}_{mn}$ will be considered.

Finally, the general solution can be written in the form

$$p'(\bar{r},\theta,\bar{z}) = \sum_m \sum_n C_{mn}R_{mn}(\bar{r})\cos(m\theta+\phi_{mn})\, e^{i(\omega t-\bar{k}_{mn}\bar{z})} \qquad (2\text{-}5)$$

where $\bar{z} = kz$.

2.3 The Instantaneous Mode Separation Technique

This technique uses four microphones located at the same axial station and mounted such that their diaphragms are flush with the inner pipe wall. The microphones are spaced 90° apart in the circumferential direction.

Consider a situation in which only the first three modes are propagating. Thus the pressure at the inner pipe wall is given by

$$p'(1,\theta,\bar{z}_o) = P_w(\theta) = C_{00}\cos(\omega t-\bar{k}_{00}\bar{z}_o) + C_{10}\cos(\theta+\phi_{10})\cos(\omega t-\bar{k}_{10}\bar{z}_o) + C_{20}\cos(2\theta+\phi_{20})\cos(\omega t-\bar{k}_{20}\bar{z}_o) \tag{2-6}$$

Adding and subtracting the instantaneous outputs of the four microphones, we obtain

$$P_w(0) + P_w\left(\frac{\pi}{2}\right) + P_w(\pi) + P_w\left(\frac{3\pi}{2}\right) = 4C_{00}\cos(\omega t-\bar{k}_{00}\bar{z}_o) \tag{2-7a}$$

$$P_w(0) - P_w(\pi) = 2C_{10}\cos\phi_{10}\cos(\omega t-\bar{k}_{10}\bar{z}_o) \tag{2-7b}$$

$$P_w(0) + P_w(\pi) - P_w\left(\frac{\pi}{2}\right) - P_w\left(\frac{3\pi}{2}\right) = 4C_{20}\cos\phi_{20}\cos(\omega t-\bar{k}_{20}\bar{z}_o) \tag{2-7c}$$

after simplification by trigonometric identities. These functions will now be squared and time-averaged. To perform this operation, the behavior of ϕ_{10} and ϕ_{20} must be examined. For fixed ϕ_{mn},

$$\overline{\cos^2\phi_{mn}\cos^2(\omega t-\bar{k}_{mn}\bar{z}_o)} = \frac{1}{2}\cos^2\phi_{mn} ,$$

where the bar denotes time-averaging. However, for a coaxial turbulent jet in a pipe there would be no preferred angle. Indeed, all angles would be equally probable. Under the assumption that ϕ_{mn} varies randomly, the $\cos^2\phi_{mn}$ term would produce an average value of 1/2. It is reasonable, then, to define the modal time-averaged mean square pressure $\overline{P^2_{mn}}$ by

$$\overline{P^2_{mn}} = \left(\frac{1}{2}\right)\frac{C^2_{mn}}{1+\varepsilon_m} , \quad \varepsilon_m = 0,\ m = 0 ;\quad \varepsilon_m = 1,\ m = 1,2,3,\ldots \tag{2-8}$$

The expressions for the (0,0), (1,0), and (2,0) mode time-averaged mean square pressures are then given by

$$\overline{P_{00}^2} = \frac{1}{16}\overline{\left[P_w(0) + P_w\left(\frac{\pi}{2}\right) + P_w(\pi) + P_w\left(\frac{3\pi}{2}\right)\right]^2} \qquad (2\text{-}9a)$$

$$\overline{P_{10}^2} = \frac{1}{4}\overline{\left[P_w(0) - P_w(\pi)\right]^2} \qquad (2\text{-}9b)$$

$$\overline{P_{20}^2} = \frac{1}{16}\overline{\left[P_w(0) + P_w(\pi) - P_w\left(\frac{\pi}{2}\right) - P_w\left(\frac{3\pi}{2}\right)\right]^2} \qquad (2\text{-}9c)$$

where $P_w(\theta)$ is the pressure measured at the duct wall, at $\overline{z} = \overline{z}_o$

If the fourth mode is also included in the analysis (i.e.. if $C_{01} \cdot \cos(\omega t - \overline{k}_{01}\overline{z}_o)$ is added to the right-hand side of Eqn. (2-6)) and a fifth microphone is mounted at $\overline{r} = 0$, $\overline{z} = \overline{z}_o$, a similar analysis leads to the following expressions for the (0,0), (1,0), (2,0), (3,0), and (0,1) modal pressures.

$$\overline{P_{00}^2} = \frac{1}{31.483}\overline{\left[P_w(0) + P_w\left(\frac{\pi}{2}\right) + P_w(\pi) + P_w\left(\frac{3\pi}{2}\right) + 1.611\ P_{\mathfrak{L}}\right]^2} \qquad (2\text{-}10a)$$

$$\overline{P_{10}^2} = \frac{1}{4}\overline{\left[P_w(0) - P_w(\pi)\right]^2} \qquad (2\text{-}10b)$$

$$\overline{P_{20}^2} = \frac{1}{16}\overline{\left[P_w(0) + P_w(\pi) - P_w\left(\frac{\pi}{2}\right) - P_w\left(\frac{3\pi}{2}\right)\right]^2} \qquad (2\text{-}10c)$$

and

$$\overline{P_{01}^2} = \frac{1}{194.1}\overline{\left[P_w(0) + P_w\left(\frac{\pi}{2}\right) + P_w(\pi) + P_w\left(\frac{3\pi}{2}\right) - 4P_{\mathfrak{L}}\right]^2} \qquad (2\text{-}10d)$$

In the above equations, $P_{\mathfrak{L}}$ is the pressure at $\overline{r} = 0$, $\overline{z} = \overline{z}_o$. The constants in Eqns. (2-10a) and (2-10d) are based on (0,0) and (0,1) mode shapes for a uniform mean flow profile. If these mode shapes were changed significantly by a nonuniform mean flow profile, the constants would have to be adjusted accordingly.

A turbulent jet by nature produces broadband noise which is steady only in a statistical sense. Although the technique has been presented using monochromatic waves, the technique is also valid for broadband noise as long as the noise can be resolved into acoustic duct modes. Thus the technique really measures the mean square value of the modal amplitudes.

In noise generated by turbomachinery the modes may be phase-locked to the rotor rotation, which would cause the nodal diameters to spin with constant angular velocity. Although the phase angle ϕ_{mn} would not vary randomly in this case, the nodal diameter would have no preferred direction in a time-averaged sense. Thus the mode separation technique would still be applicable, and the averaging would go through in a similar manner.

2.4 The Time-Averaged Mode Separation Technique

This technique uses three microphones mounted flush with the pipe wall at the same axial location. The microphones are spaced 90° apart in the circumferential direction, i.e., at $\theta = 0$, $\pi/2$, and π.

Again, consider the situation in which only the first three modes are propagating. Setting $\theta = 0$ in Eqn. (2-6), squaring, and time-averaging,

$$\begin{aligned}\overline{P_w^2(0)} = {} & \overline{P_{00}^2} + \overline{P_{10}^2} + \overline{P_{20}^2} + 2C_{00}C_{10}\,\overline{\cos\phi_{10}\cos(\omega t - \bar{k}_{00}\bar{z}_o)\cos(\omega t - \bar{k}_{10}\bar{z}_o)} \\ & + 2C_{00}C_{20}\,\overline{\cos\phi_{20}\cos(\omega t - \bar{k}_{00}\bar{z}_o)\cos(\omega t - \bar{k}_{20}\bar{z}_o)} \\ & + 2C_{10}C_{20}\,\overline{\cos\phi_{10}\cos\phi_{20}\cos(\omega t - \bar{k}_{10}\bar{z}_o)\cos(\omega t - \bar{k}_{20}\bar{z}_o)}\end{aligned} \tag{2-11a}$$

Similarly,

$$\begin{aligned}\overline{\left[P_w(0) - P_w\left(\frac{\pi}{2}\right)\right]^2} = {} & 4\overline{P_{20}^2} + C_{10}^2\,\overline{(\cos\phi_{10} + \sin\phi_{10})^2\cos^2(\omega t - \bar{k}_{10}\bar{z}_o)} \\ & + 4C_{10}C_{20}\,\overline{(\cos\phi_{10} + \sin\phi_{10})\cos\phi_{20}\cos(\omega t - \bar{k}_{10}\bar{z}_o)\cos(\omega t - \bar{k}_{20}\bar{z}_o)}\end{aligned} \tag{2-11b}$$

With the assumption that ϕ_{10} and ϕ_{20} vary randomly, the fourth and fifth terms on the right-hand side of Eqn. (2-11a) average to zero, and the second term on the right-hand side of Eqn. (2-11b) becomes $2\overline{P_{10}^2}$. To eliminate the terms involving products of functions of ϕ_{10} and ϕ_{20}, an additional assumption that the values of ϕ_{10} and ϕ_{20} are uncorrelated with each other is necessary. For example, if ϕ_{10} and ϕ_{20} were the same random function of time, these terms would have the same order of magnitude as $\overline{P_{10}^2}$ and $\overline{P_{20}^2}$. Making the assumption that the modes are uncorrelated with each other, these equations reduce to

$$\overline{P_w^2}(0) = \overline{P_{00}^2} + \overline{P_{10}^2} + \overline{P_{20}^2} \tag{2-12a}$$

and

$$\overline{\left[P_w(0) - P_w\left(\frac{\pi}{2}\right)\right]^2} = 4\overline{P_{20}^2} + 2\overline{P_{10}^2} \tag{2-12b}$$

If Eqn. (2-10b) is added to the system, the set of three simultaneous equations can be solved for $\overline{P_{00}^2}$, $\overline{P_{10}^2}$, and $\overline{P_{20}^2}$ in terms of the measured quantities. The results are

$$\overline{P_{00}^2} = \overline{P_w^2}(0) - \left(\frac{1}{8}\right)\overline{\left[P_w(0) - P_w(\pi)\right]^2} - \frac{1}{4}\overline{\left[P_w(0) - P_w\left(\frac{\pi}{2}\right)\right]^2} \tag{2-13a}$$

$$\overline{P_{10}^2} = \left(\frac{1}{4}\right)\overline{\left[P_w(0) - P_w(\pi)\right]^2} \tag{2-13b}$$

and

$$\overline{P_{20}^2} = \left(\frac{1}{4}\right)\overline{\left[P_w(0) - P_w\left(\frac{\pi}{2}\right)\right]^2} - \left(\frac{1}{8}\right)\overline{\left[P_w(0) - P_w(\pi)\right]^2} \tag{2-13c}$$

Thus the time-averaged mode separation technique uses three microphones to separate the (0,0), (1,0), and (2,0) duct modes. The assumption of uncorrelated modes is vital to the approach. The technique could be expanded easily to separate more modes. For example, to also separate the (0,1) and (3,0) modes would require only a total of five microphones, as opposed to nine for the instantaneous mode separation technique. Also, if the noise field is sufficiently steady, the measurements need not be taken simultaneously, and only two microphones would be necessary. There is no requirement for microphone traversing or narrow bandpass filtering. Modal spectra are easily calculated by obtaining spectra of the measurands

$$\overline{P_w^2(0)} \quad , \quad \overline{\left[P_w(0) - P_w(\pi)\right]^2} \quad , \quad \text{and} \quad \overline{\left[P_w(0) - P_w\left(\frac{\pi}{2}\right)\right]^2} \quad ,$$

and solving Eqns. (2-13) at each frequency.

2.5 Instrumentation for the Instantaneous Mode Separation Technique

A line diagram of the instrumentation used for the instantaneous technique is shown in Fig. 4a. Four B & K 1/4 in. condenser microphones were located at the same axial station and spaced 90° apart in the circumferential direction. The microphones were mounted such that their diaphragms were flush with the inner pipe wall. The four microphone outputs were fed into an analogue circuit which performed additions and subtractions according to Eqn. (2-9a, -b, or -c), depending on which mode was being analyzed. The output of the analogue circuit was then lowpassed to avoid aliasing in the digital sampling. The 3 dB rolloff point was set at 5 KHz to match the characteristics of the filters used with the time-averaged mode separation technique. The sampling rate of the digital sampling system was 20 KHz. The B & K analyzer was used to amplify the signal before digital sampling by the analogue to digital converter.

The spectra were obtained by the averaged periodogram method (see Rabiner and Gold, 1975). In this technique, successive data samples are discrete Fourier transformed, after being operated upon with a window function. The resulting Fourier transforms are then averaged. For the instantaneous technique, 64 discrete Fourier transforms were averaged. Since the data were analyzed real time on a H-P 2100 minicomputer, the samples were spaced out over a time period of approximately ten minutes. The spectra were averaged over 31.6 Hz bandwidths before being normalized to a bandwidth of 1 Hz. Final results were plotted in the frequency range 200-6000 Hz. The computer program PIPE was used to perform these operations. A listing can be found in Appendix A1.

2.6 Instrumentation for the Time-Averaged Mode Separation Technique

The instrumentation used for the time-averaged mode separation technique is shown in Fig. 4b. The three microphone signals were first lowpassed to avoid aliasing problems, then amplified to be compatible with the digital sampling system. The sampling system was used in the simultaneous sample and hold mode. The data acquisition rate was approximately 42 KHz, which is the maximum for the system. Thus aliasing would occur for frequencies above approximately 7 KHz. The 3 dB rolloff point of the filters was set at approximately 5 KHz to avoid this problem. The filters were adjusted so that their frequency response curves matched as closely as possible. The maximum deviation in amplitude response between the three filters was 0.2 dB. The deviations were largest in the 3-4 KHz frequency range. The instantaneous subtractions $(P_w(0) - P_w(\pi))$ and $(P_w(0) - P_w(\frac{\pi}{2}))$ required for the technique were performed digitally. Spectra of

$$\overline{P_w^2(0)} \ , \ \overline{(P_w(0) - P_w(\pi))^2} \ , \text{ and } \ \overline{(P_w(0) - P_w(\tfrac{\pi}{2}))^2}$$

were then obtained in a manner similar to the instantaneous technique. The computer program PIPE4 was used for this purpose. The time-averaged data were then separated into the three acoustic modes by use of Eqns. (2-13). The computer program PIPE2 solved this set of equations at each center frequency of the 31.6 Hz bandwidth data. The final spectra were normalized to 1 Hz bandwidth and plotted in the frequency range 200-6000 Hz. Computer programs PIPE2 and PIPE4 are listed in Appendix A1.

2.7 Comparison of Spectra Measured with the Instantaneous and Time-Averaged Techniques

To further assess the advantages and disadvantages of the two measurement techniques, their outputs were compared for the case of a coaxial jet in a pipe. As well as examining the relative merits of the two techniques, this comparison answers the question of whether or not the noise propagating in different acoustic duct modes is correlated, for this particular case. The spectra discussed here were measured 2.36 meters downstream of a 31.8 mm orifice located concentrically in a 97 mm I.D. pipe*. The Mach number of the flow through the orifice was 0.37.

The spectra measured with the instantaneous mode separation technique are shown in Fig. 5. The (0,0) mode is completely separated out up to

*For a detailed discussion of the experimental apparatus, see Chapter 3.

4400 Hz, the frequency corresponding to $\gamma_{cr_{0,1}}$, where the (0,1) mode starts propagating. Above this frequency the signal is a combination of the (0,0) and (0,1) modes. The (1,0) mode is completely separated out up to 4800 Hz, the frequency corresponding to $\gamma_{cr_{3,0}}$, beyond which it combines with the (3,0) mode. However, in the example shown there is a large increase (approximately 7 dB) in the signal above 4800 Hz. Thus the output at frequencies greater than 4800 Hz is dominated by the (3,0) mode. The level of the (1,0) mode is obscured in this region. The (2,0) mode is completely separated out to a frequency corresponding to $\gamma_{cr_{2,1}}$, where it combines with the (2,1) mode. This frequency is too high to be seen on Fig. 5.

To check the assumption made in developing the instantaneous mode separation technique, the assumption of no preferred angle for the nodal diameters, the microphone array was rotated and the measurements were repeated. The results were unchanged, confirming the validity of this assumption.

The first set of modal spectra measured with the time-averaged separation technique utilized spectra of

$$\overline{P_w^2(0)} \quad , \quad \overline{\left[P_w(0) - P_w(\pi)\right]^2} \quad , \text{ and } \quad \overline{\left[P_w(0) - P_w\left(\frac{\pi}{2}\right)\right]^2}$$

which were obtained by averaging 64 discrete Fourier transforms. The results are shown in Fig. 6. The spectra exhibit the same overall character as those obtained with the instantaneous technique. However, the (0,0) mode has much larger fluctuations, at frequencies above the cutoff frequency of the (1,0) mode, than those obtained with the instantaneous technique. The (1,0) mode agrees very well with the results of the instantaneous technique. This is to be expected, since no subtraction of time-averaged data is involved in Eqn. (2-13b). The (2,0) mode has a substantial amount of noise below its cutoff frequency and in the vicinity of 5 KHz. To explain the significance of the sharp spikes in the spectra, a note on the way the spectra are plotted may be helpful. The spectral points are first plotted and then connected with straight lines. Thus a single spectral point far off the curve can cause a spike of the type seen.

The similarity of the overall shape and levels of the spectra obtained by the instantaneous and time-averaged techniques leads to the conclusion that the modes are uncorrelated, or at least that they are not correlated over a broad frequency range. To strengthen this conclusion it is necessary to reduce the difference in the spectra obtained by the two techniques to the experimental uncertainties inherent in the methods.

The uncertainty in the measurement techniques can basically be thought of as consisting of two parts. The first part results from an insufficient averaging process during the measurement. It is normally characterized by a symmetric scattering of points about the true value. An increase in the number of samples obtained reduces this error. The second type of error is a fixed error related to the type of instrumentation used in the experiment.. The fluctuations seen in the time-averaged output in general seem to be of the first type. To check if this was the case, the time-averaged mode separation measurement was repeated, using a larger number of discrete Fourier transforms in the averaging process. The results obtained, using an average of 256 discrete Fourier transforms, are shown in Fig. 7. A marked improvement is seen in the (0,0) mode spectra and in the (2,0) mode spectra above its cutoff frequency. The improvement in the (2,0) mode spectra below its cutoff frequency is not as striking. However, this can be explained by fixed system error. The equation from which the (2,0) mode is calculated (Eqn. (2-13c)) contains

$$\overline{\left[P_w(0) - P_w\left(\frac{\pi}{2}\right)\right]^2} \quad \text{and} \quad \overline{\left[P_w(0) - P_w(\pi)\right]^2}$$

The filters used to lowpass $P_w(0)$ and $P_w(\pi)$ matched very closely in amplitude response. However, the filter used to lowpass $P_w\left(\frac{\pi}{2}\right)$ deviated approximately 0.2 dB in amplitude response form the other two filters, for frequencies above 2 KHz. This will cause approximately a 5% cancellation error in Eqn. (2-13c). The magnitudes of

$$\overline{\left[P_w(0) - P_w\left(\frac{\pi}{2}\right)\right]^2} \quad \text{and} \quad \overline{\left[P_w(0) - P_w(\pi)\right]^2}$$

in the 2-3.4 KHz range are such that the incomplete cancellation will result in an average signal level of approximately 56 dB, with a large amount of scatter. This is basically the behavior seen in the (2,0) mode spectra below its cutoff frequency, 3400 Hz.

In the region above the cutoff frequency the amplitude of the signals is such that this type of error is not significant. The (1,0) mode is much cleaner below its cutoff frequency, because the filters matched very well in this frequency range, and no time-averaged subtraction is involved. Thus the deviations between the output of the instantaneous and time-averaged techniques are relatively small and can be explained in terms of measurement error. This result leads to the conclusion that the noise generated by a coaxial jet in a pipe and propagating in different acoustic duct modes has in fact no inter-mode correlation.

2.8 Summary

Two new modal separation measurement techniques have been developed and applied to the case of noise generated by flow through a coaxial obstruction in a pipe. One technique requires the assumption that noise in the different acoustic duct modes is uncorrelated. The other does not. Comparison of the results of the two techniques shows that this is in fact the case, for the type of source considered here.

The instantaneous mode separation technique uses four wall-mounted microphones, spaced 90° apart in the circumferential direction, to separate the first three acoustic duct modes below the frequency at which the fourth mode starts propagating. The only assumption required is that the higher mode nodal diameters have no preferred angle in a time-averaged sense. The technique could also be extended to situations where this is not the case. All modes are completely separated below the cutoff frequency of the (0,1) mode. The (1,0) and (2,0) modes are actually separated out over a wider frequency range, and information about higher modes, such as the (3,0) mode, can often be obtained. The technique only requires instantaneous addition and subtraction of the microphone outputs in addition to common spectral measurement techniques. No microphone traversing or phase-matched narrow band filters are required by the method. The accuracy of the technique is high (unwanted mode rejectic on the order of 40 dB), even when several modes are present. The technique could be extended to separate the (0,1) mode with only the addition of one more microphone at the center of the pipe. However, a complete separation of the (3,0) mode in the presence of all the lower modes would require four additional microphones. This problem would not be so severe if all of the lower modes were not present.

The time-averaged mode separation technique uses three wall-mounted microphones to separate out the first three acoustic duct modes, but requires the additional assumption that the modes are uncorrelated. A matrix operation on three time-averaged spectra produces the modal pressure spectra. The technique requires only two microphones if the noise source is sufficiently steady. This technique is easily extended to measure a larger number of modes. Only one more microphone (or one additional measurement for a steady source) is required for each additional mode.

Chapter 3

EXPERIMENTAL MEASUREMENTS OF NOISE GENERATED BY FLOW THROUGH COAXIAL RESTRICTIONS IN PIPES

3.1 Previous Research

A majority of the research on noise generated by flow through restrictions in pipes has been concerned with the problem of control valve noise (Allen, 1969; Baumann, 1970; Heymann, 1973; Nakano, 1968; and Seebold, 1970). Much of this research is aimed at developing low noise values and/or predicting the overall noise level of specific types of valves. The noise level at a given distance away from the pipe is commonly the quantity predicted, and the results are strongly dependent on the actual design of the valve and on its installation. Thus these engineering prediction schemes lack universality and should be considered as schemes which interpolate specific sets of experimental data, rather than as scientific prediction methods. To produce more fundamental prediction techniques than those presently available, a deeper understanding of the noise generation process and the coupled process of noise transmission through the fluid inside the pipe and through the pipe wall itself is necessary.

Fundamental studies of noise generated by flow through restrictions have concentrated on measurement of the noise levels inside the pipe; these studies entail two complications. First, the noise is usually in the frequency range where more than one acoustic mode is propagating inside the duct. Second, hydrodynamic as well as acoustic pressure fluctuations exist inside the pipe. The experimental problem of separation of the acoustic pressure signal from hydrodynamic noise has received the most attention. Only a few techniques are available for this purpose. Karvelis (1975) used a cross-correlation technique to separate the acoustic pressure from the hydrodynamic pressure in the region downstream of an orifice. This method works well when only plane waves, the (0,0) mode, are present. His technique and our adaptation use two microphones mounted flush with the inner pipe wall. One microphone is displaced some distance in the axial direction with respect to the other. The outputs of the two microphones are time delay cross-correlated. A peak in the correllelogram occurs at a delay time equal to the time it takes for the acoustic wave to traverse the distance between the two microphones. The hydrodynamic pressures measured by the two microphones are generally uncorrelated at this delay time, and hence the peak value of the cross-correlation gives the amplitude of the acoustic wave. This technique does not work as well when higher acoustic duct modes are propagating, since the higher modes are dispersive (i.e., the phase speed of the wave is a function of frequency). The proper delay time then becomes a function of frequency, making the results difficult to interpret.

In a different study, Roberts and Johnston (1974) used a specially designed rig (see Fig. 2) to separate the acoustic pressure fluctuations from the hydrodynamic pressure fluctuations. The flow enters and exits the rig radially through sections of porous pipe. Acoustic waves generated by flow through a centrally located restriction propagate on past these porous sections into the no-flow regions of the pipe before being absorbed by the anechoic terminations. In the no-flow regions of the pipe only acoustic pressures are present. However, elimination of the hydrodynamic pressure fluctuations by this method causes some attenuation of the acoustic waves.

The present research is a continuation of the program initiated by Roberts. Cross-correlations of the type just discussed were obtained during an early phase of the research. These measurements showed that, for circular obstructions with a flow passage diameter less than one half of the pipe diameter, hydrodynamic pressure fluctuations were small compared to the acoustic pressure, at locations greater than 10 pipe diameters downstream of the restrictions. Therefore, the present study concentrated on measurement of the modal characteristics of the sound field downstream of the source region near the restriction, without the necessity to resort to cross-correlations or placement of microphones in a no-flow zone. To the author's knowledge, modal spectra of this type have never been presented in the open literature for the case studied here, that of noise generated by flow through coaxial restrictions (orifices and nozzles) in pipes.

3.2 Experimental Apparatus and Instrumentation

The experimental apparatus, a sketch of which is shown in Fig. 2, is basically a 4 in. nominal diameter P.V.C. schedule 80 pipe, approximately 11 meters long. The pipe is terminated on both ends by anechoic terminations, which have excellent absorption coefficients (above 98%) at frequencies greater than 250 Hz. Thus 250 Hz is the lower frequency limit for the measurements. The flow enters and exits radially through bronze porous elements of the same inner diameter as the pipe (97 mm). The air is supplied by a 300 SCFM compressor at a flowrate controlled by a pressure regulator upstream of the inlet plenum. Flow metering is by a Meriam laminar flow meter.

The maximum attainable mean velocity in the 97 mm. diameter sections of the pipe is approximately 15 m/sec. The pipe is equipped with static pressure taps and probe ports for flush mounting of 1/4 in. and 1/2 in. microphones. A picture of the rig is shown in Fig. 8.

Bruel and Kjaer 1/4 in. condensor microphones were used in the measurements. The microphones are not designed to be exposed to a higher level static pressure than the attached preamp. To permit measurements inside the pipe, at pressures up to 3 atmospheres, it was necessary to seal the adapter between the 1/4 in. microphone and the 1/2 in. preamplifier. The R.T.V.* sealant used for this purpose did not affect the output or frequency response of the microphone system. A picture of the microphone, adaptor and preamp is shown in Fig. 9. The four microphones are shown mounted in position for the measurements in Fig. 10.

The instantaneous mode separation technique of Chapter 2 was used for the measurements presented in this chapter. The instrumentation for the technique was identical to that discussed previously, except for the method of analogue filtering. The data presented in this chapter were

---

*General Electric R.T.V. Type 102.

taken using two analogue filters to bandpass the signal between 300 and 7000 Hz. The pressure spectra are presented in the frequency range 200-6000 Hz. The measurements were made 1.1 meters (11.5 pipe diameters) downstream of the front face of the restriction, unless otherwise indicated. Other pertinent dimensions are shown on Fig. 2. For more information on the experimental apparatus, consult Roberts and Johnston (1974).

3.3 Definition of Parameters

Several of the parameters used in presentation of the data require some explanation. The flow speed through the restriction is characterized by the indicated Mach number, M_i. This Mach number is calculated by assuming an isentropic expansion of the gas from upstream conditions (P_o, T_o) to the minimum wall static pressure (P_i) measured just downstream of the restriction. When the restriction is an orifice, the minimum wall pressure occurs at or near the vena contracta of the orifice jet. For a nozzle jet the indicated Mach number is calculated using the pipe wall static pressure measured very near the axial location of the nozzle exit. In the jet, at the vena contracta of an orifice or the exit plane of a nozzle, the mean velocity profile is nearly uniform and parallel and the total pressure and temperature are equal to the upstream conditions. The pipe wall static pressure equals jet static pressure in subsonic flow, in which case M_i is very nearly equal to the real jet Mach number. For choked flow cases, M_i exceeds 1.0 and is only a rough indication of the average jet speed. In this situation the jet will successively over-expand and shock down at a few axial stations until mixing reduces the mean Mach number to subsonic speed (at $x/d \geq 10$, see Thompson (1972), Fig. 9.18, p. 463). However, since the noise generation is predominantly in the shear layers immediately downstream of the orifice or nozzle exit, a Mach number representative of the velocities in the core of the jet before substantial mixing has occurred seems most appropriate for correlation of the noise data.

The frequency ratio, f_r, is a second parameter used in presentation of the experimental results. This parameter is the ratio of two nondimensional frequencies, both of which are important in the case of a confined jet. The frequency spectrum of free jet noise can be roughly scaled by the Strouhal number (see Banerian, 1974), $St = fd/U$, where f is the frequency, d is the jet diameter, and U is the jet velocity at the nozzle exit. This nondimensional frequency is also important in the confined jet case. However, for a confined jet the noise propagates in the acoustic duct modes. The behavior of the acoustic duct modes propagating inside a circular duct is governed by the nondimensional frequency $\gamma = \omega r_o/a_o$, where ω is the circular frequency, r_o is the duct radius, and a_o is the adiabatic speed of sound in the gas. The frequency ratio, defined by $f_r = \gamma/\pi St = U_i D/a_o d$, has been found to be useful for correlating the spectral measurements presented in this report. The physical reasons for this are discussed in detail in Section 3.5.1.

3.4 Parameter Ranges Covered in the Experiments

Modal pressure spectra were measured for four orifice sizes (12.7, 19.0, 31.8, and 50.8 mm diameters) and three nozzles (3.18 mm diameter and two 16.2 mm diameter nozzles with respective throat length-to-diameter ratios of 1 and 8). Thus the ratio of restriction diameter to pipe diameter, d/D, ranged from 0.03 to 0.52.

In order to compare noise generation by an orifice to that by a nozzle, the size of the 16.2 mm nozzle was chosen to match the cross-sectional area of the 19.0 mm orifice vena contracta, for a value of $M_i \approx 1$. The purpose of the extended throat nozzle was to produce a thicker boundary layer at the nozzle exit. The displacement thickness at the nozzle exit, estimated from mass flow measurements, was approximately 0.10 mm for the short nozzle and 0.25 mm for the long nozzle.

The values of the indicated Mach number, M_i, ranged from 0.15 to 1.23. The Reynolds numbers, based on orifice diameter and vena contracta conditions, or nozzle exit conditions, covered the range

4×10^4 to 6×10^5. The frequency ratio, f_r, varied from 0.18 to 28.0, although this large range of f_r values could not be attained with a single restriction.

3.5 Experimental Results

In this section the major experimental results are presented. To insure that the measured fluctuating pressure levels were actually due to noise generated at the restriction, the hydrodynamic and rig background noise levels were also measured. For convenience, these measurements are presented and discussed later in Sections 3.6 and 3.7. With few exceptions, the rms levels of the hydrodynamic and background pressure fluctuations were 15 to 20 dB below those of the noise generated at the restriction.

During the course of the preliminary measurements it was found that the experimental rig selectively absorbed noise in the higher modes at particular frequencies. This behavior is discussed in Section 3.8. The measurements presented in this section were taken sufficiently close to the noise source that they were not affected by the selective sound absorption process.

The effect of the outlet plenum on the sound waves was also examined during the preliminary experiments. The measurements of outlet plenum attenuation are given in Section 3.9. The data presented in the present section were not affected by outlet plenum attenuation, as the measurements were made upstream of the outlet plenum.

The modal pressure spectra were measured using the instantaneous mode separation technique discussed in Chapter 2. The spectral results were stored on digital magnetic tape for later analysis. The axial sound power spectra for the (0,0), (1,0), (2,0), and (3,0) modes were calculated using the measured pressure spectra. These power spectra were integrated to obtain downstream overall power levels, and the acoustic source efficiencies were then calculated. The acoustic efficiency was defined as overall downstream power level normalized by the total jet kinetic energy. The energy calculations were performed by the computer program PIPE5, listed in Appendix A2. The modal pressure and power spectra, as well as overall sound pressure, power, efficiency and flow rate data in tabular form, are presented in Appendices A3 and A4.

The experimental uncertainties in the results were calculated using the method of Kline and McClintock (1953), appropriate for single-sample experiments. The uncertainty in all the measurands was estimated at 20:1 odds; see Appendix A5 for details. The experimental uncertainty in the sound pressure level measurements was estimated to be ±0.2 dB. This results in an uncertainty in the efficiency level of less than ±6%. The uncertainty in the flow rate measurement was generally about ±1%, and that in M_i was less than ±1%.

No fluid dynamic data other than flow rate parameters were measured for the orifices. Wall static pressure profiles and mean velocity profiles for the orifices are presented by Roberts and Johnston (1974). The wall static pressure profiles for the two 16.2 mm nozzles were measured in the present investigation. These static pressure profiles are presented in Appendix A6. The agreement with the wall static pressure profiles for the 19.0 mm orifice which were presented by Roberts is excellent, for similar values of M_i. This indicates that there is little difference in the fluid dynamic behavior produced by a nozzle and by an orifice, if the nozzle cross-sectional area is chosen to match the orifice vena contracta.

3.5.1 Characteristics of the Modal Pressure Spectra

The shape of the modal pressure spectra was found to be strongly dependent on the frequency ratio, $f_r = U_i D/a_o d$. A typical set of modal pressure spectra for a low value of the frequency ratio, $f_r = 1.19$, is shown in Fig. 11. The spectra fall off rapidly with increasing frequency, and the (1,0), (2,0), and (3,0) modes dominate the (0,0) mode above their respective cutoff frequencies. The spectra of the higher modes rise to a sharp peak at their cutoff frequencies, where the mode is at a resonance condition. The cuton of a particular mode seems to have no influence on other modes already propagating.

Although the (0,1) mode* (seen as a spike on the (0,0) mode curve) has a sharp rise at the cutoff frequency, the amplitude of the (0,1) mode dies off very rapidly with increasing frequency, in contrast to the behavior of the other higher modes. Thus, compared to the other modes, it appears that the (0,1) mode transmits little acoustic power in the axial direction. This idea is further strengthened by the fact that at frequencies very near cutoff the ratio of acoustic power flow to acoustic pressure is much lower than at frequencies farther above cutoff.

A set of modal pressure spectra for a higher value of the frequency ratio, $f_r = 7.4$, is shown in Fig. 12. At high f_r the spectra are fairly flat over the frequency range measured, and the higher modes no longer dominate the spectrum above their cutoff frequencies. Except for the resonance peaks associated with the cuton of the higher modes, the (0,0) mode dominates the spectrum out to approximately 5000 Hz, where the (3,0) mode starts propagating. Also, the (3,0) mode no longer strongly dominates the (1,0) mode above the (3,0) mode cutoff frequency, as was the case at low f_r .

A comparis two sets of spectra with closely matching f_r is shown in Figs. 13 and 14. The results indicate that the shape of the frequency spectrum is primarily determined by f_r , with no significant dependence on the separate values of M_i and (d/D), for the (d/D) range $0.13 \leq (d/D) \leq 0.52$. The two sets of spectra with the same value of f_r are seen to collapse onto one curve, when plotted as a function of frequency, in Figs. 13 and 14. However, this happens only because (D/a_o) is nearly constant for these experiments. To obtain this same collapse onto one curve in the general case, it would be necessary to plot the spectra as a function of St or γ .

*A more complete examination of the (0,1) mode could be made if the instantaneous mode separation technique were extended to include this mode. Such an extension was discussed in Chapter 2.

Modal pressure spectra were also measured for a 3.18 mm diameter nozzle ($d/D = 0.03$, $15 \le f_{r} \le 28$) . A typical set of spectra for this restriction is shown in Fig. 15. These spectra exhibit the same general characteristics as seen for larger restrictions at high values of the frequency ratio, except for the behavior of the (0,1) mode. In the case of the 3.18 mm nozzle, the (0,1) mode did not die off rapidly above its cutoff frequency, as it did for cases with larger (d/D) . The stronger excitation of the (0,1) mode in this case is due to the noise source region for the 3.18 mm nozzle being concentrated closer to the pipe axis than the source regions for the larger restrictions. Since the (0,1) mode shape has its maximum value at the pipe center, a noise source concentrated near the pipe axis would be expected to excite this mode.

To understand why the spectrum shape varies in the manner discussed above, it is necessary to review briefly the dimensional arguments normally used in explaining a free jet spectrum shape (see, for example, Ribner, 1964). The free jet spectrum exhibits a broad peak in the vicinity of $St = 0.2$ and rolls off at high and low frequencies (Banerian, 1974). In the dimensional reasoning, the assumption is made that a given region of the jet emits only a single frequency. Thus different regions of the jet are responsible for different parts of the frequency spectrum. The high frequency noise is generated in the region close to the nozzle exit. In this region the characteristic velocity is given by the jet velocity, U , and the characteristic length is given by the shear layer thickness, δ . The characteristic frequency is then given by U/δ . Since δ grows rapidly with axial distance from the nozzle exit, the highest frequencies are generated very close to the nozzle exit plane. The spectrum peak, at $St \simeq 0.2$, is considered to be generated 5-10 diameters downstream of the nozzle exit, and the low frequency end of the noise spectrum is generated in the fully developed region of the jet far downstream ($x/d \geq 10$) of the nozzle exit.

For jets confined in a pipe of diameter D , where the (d/D) ratio is small, it is reasonable to assume that the mean flow and turbulence levels in the jet are not greatly affected by the presence of the confining pipe wall. In this situation the noise source itself is very similar to a free jet, and only the radiation conditions are different. Thus it might be reasonable to assume that the noise spectrum peak would occur in the vicinity of $St = 0.2$, i.e., near the frequency given by $f_{St} = 0.2 U_i/d$. The Strouhal frequencies calculated in this manner are noted on Figs. 11-14. In our experiments f_{St} is proportional to the frequency ratio, f_r , as (D/a_o) was nearly constant for all test cases. It can be seen that the lower the value of f_{St} the more rapidly the spectra fall off with increasing frequency. For high values of f_{St} the spectrum is basically constant. Thus, for low values of the frequency ratio, f_r , the spectrum in the 200-6000-Hz range is basically the high-frequency end of the jet noise spectrum. For high values of f_r the wide peak of the jet noise spectrum lies in the range 200-6000 Hz. No cases for which measurements were taken resulted in values of f_{St} high enough to show the extreme low end of the jet noise spectrum in the 200-6000 Hz range.

Although the overall shape of the noise spectrum can be explained easily from dimensional reasoning, an understanding of why the higher modes are dominant above 2000 Hz for low f_r and are almost equal to the (0,0) mode for high f_r requires a more detailed examination of the turbulence structure in the jet. Recent research (Mollo-Christensen, 1967; Fuchs, 1972; Lau et al., 1972; Moore, 1977) has indicated that large-scale structures exist in turbulent jets. The structures are strongly coherent in the initial regions of the jet, before the potential core disappears. The coherence of the structures seems to decrease gradually with distance downstream of the nozzle exit. These large coherent structures are often described as coalesced vortex rings generated by the instability and subsequent rollup of the vortex sheet (Yule, 1977). The vortex rings are thought to be subject to circumferential instabilities which, when experimentally observed, are called fluting. This fluting, regardless of its origin, can be described as a wave-like formation on the vortex rings, with various numbers of nodes and antinodes spaced about the circumference. Such a structure would generate pressure fluctuations with circumferential coherence, and thus be a very effective source mechanism for higher-mode noise generation. The fact that the vortices seem unstable to circumferential disturbances would emphasize production of higher circumferential modes ((1,0), (2,0), (3,0), etc.) over the circumferentially symmetric (0,0) and (0,1) modes.

At distances farther downstream in the jet, where the lower frequencies would be generated, the large-scale structures have lost much of their circumferential coherence. Thus the higher modes would not be expected to dominate over the (0,0) mode in cases where the noise in the frequency range 2000-6000 Hz is generated sufficiently far downstream. This is the case for high frequency ratio.

The description of the large-scale structures given above has generally been observed in low Reynolds number jets by means of flow visualization techniques. It is not clear that the above description is in all ways appropriate to the actual experimental conditions, which involve much higher Reynolds numbers. However, experimental measurements of a higher Reynolds number jet ($Re = 4 \times 10^5$) by Michalke and Fuchs (1975) have shown that circumferentially coherent structures exist in the initial region of the jet, and that higher circumferential modes are important at higher frequencies. This work supports the above explanation of higher mode dominance for low f_r.

3.5.2 Modal Power Spectra and Overall Efficiency Levels

The modal pressure spectral measurements were converted to modal power spectra by use of the energy weighting function. The energy weighting function relates a wall pressure fluctuation to acoustic power flow in the direction of the pipe axis. The energy weighting function is a function of frequency, and is different for different acoustic duct modes. Thus the total downstream acoustic energy flow is calculated by

$$\mathbb{P} = \sum_{m,n} \int_{\omega_{lower}}^{\omega_{upper}} \overline{P^2_{mn}}(\omega)\ EWF_{mn}(\omega)\ d\omega \qquad (3\text{-}1)$$

The theoretical development of the energy weighting functions is covered later in Chapter 4. In this chapter we chose to utilize the physical energy flux definition,* with the assumption of a uniform mean flow profile. The slug flow assumption gives accurate results (less than 2% error) in the flow rate and frequency ranges encountered in the experiments.

The modal power spectra were calculated by multiplying each spectral point (an average over a bandwidth of 31.6 Hz) by the energy weighting function associated with the bandwidth center frequency. Two modifications to the measured modal pressure spectra were performed prior to calculation of the power spectra. First, the (0,0) mode pressure spectrum has a sharp peak in the vicinity of 4500 Hz, where the (0,1) mode starts propagating. However, this peak dies off rapidly** and is not associated with power flow in the (0,0) mode. The (0,1) mode peak was removed by making a straight line approximation to the (0,0) mode pressure spectrum in this region. Secondly, above 4800 Hz the (1,0) mode is combined with the (3,0) mode. However, in many cases the (3,0) mode dominates the signal strongly. Thus the modal pressure spectrum in this region is assumed to be equal to the (3,0) mode only, and a straight line approximation to the (1,0) mode pressure spectrum was used above 4800 Hz. For illustration, the calculated modal power spectra associated with the pressure spectra in Fig. 11 are shown in Fig. 16.

The overall acoustic efficiency and the efficiency of each mode were calculated using the following definition of acoustic efficiency,

---

*Use of the Möhring or Blockhintsev energy flux definitions, also discussed in Chapter 4, would change the calculated acoustic energy flow by less than 3%.

**Except for the 3.18 mm nozzle data.

$$\eta = \frac{\mathcal{P}}{\frac{1}{2}\,\dot{m}\,U_i^2} \qquad (3\text{-}2)$$

where $\mathcal{P}$ is the calculated downstream energy flow, $\dot{m}$ is the mass flow rate through the restriction, and U_i is the indicated velocity calculated by an isentropic expansion to the minimum wall pressure measured just downstream of the restriction. The overall efficiency, which is the sum of the efficiencies of the (0,0), (1,0), (2,0), and (3,0) modes, is plotted as a function of M_i in Fig. 17.

The overall efficiencies for the 12.7 and 19.0 mm orifices vary approximately as $M_i^{4.6}$, very similar to the M^5 dependence predicted for a free jet by the Lighthill theory. The overall efficiency curve normally associated with free jets, $\eta = 2 \times 10^{-5} M_i^5$, is plotted on Fig. 17 for comparison. It can be seen that the order of magnitude of the present results is also similar to that of the free jet case.

The overall efficiencies for the two 16.2 mm nozzles agree very closely with each other and with the results for the 19.0 mm orifice. The cross-sectional area of the nozzles was chosen to match the vena contracta of the 19.0 mm orifice. Thus the close agreement in these experimental results indicates that the exact shape of the obstruction is not critically important in determining the sound power generated.

The efficiency curves in Fig. 17 show a strong dependence on the diameter ratio, (d/D). An increase in (d/D) produces a higher value of the efficiency, for constant M_i. There are two possible reasons why this might be the case. First, as (d/D) increases, the influence of the confining pipe wall on the jet structure increases. The entrainment and turbulence structure within the jet will be altered, and the noise generated by unsteadiness in the region where the jet reattaches to the pipewall may also become important. However, as (d/D) becomes sufficiently small, effects based on such hydrodynamic causes should become unimportant.

Mean flow and wall hydrodynamic pressure measurements indicate that the type of (d/D) effects discussed above are probably not important for the 12.7 and 19.0 mm orifices. However, large differences exist between the efficiencies for these cases. A second explanation of the (d/D) effect is thus required. It is based on acoustic considerations.

If a noise source spans a large part of the pipe cross-sectional area, it may be more effective in generating propagating acoustic duct modes than one which spans only a small portion of the cross section. To test this supposition for cases with small (d/D) ratio, the efficiency was divided by the area ratio, $(d/D)^2$, and plotted in Fig. 18. Good agreement is obtained for the 12.7 and 19.0 mm orifice data. However, the results for the 31.8 mm orifice and the 3.18 mm nozzle now fall slightly below those for the 12.7 and 19.0 mm orifices.

When interpreting the values of efficiency shown on Figs. 17 and 18, it must be kept in mind that only the frequency range 200-6000 Hz was measured. Thus, for low values of the frequency ratio (or Strouhal frequency), only the energy associated with the upper end of the jet noise spectrum is accounted for, and for high values of f_r only the low frequency end of the jet noise spectrum would be accounted for. For the 12.7 and 19.0 mm orifice cases, the Strouhal frequencies were between 1000 and 6000 Hz, and comparison of the results for these two orifices is probably affected little by differences in f_r.

Although the modal spectra for the 3.18 mm nozzle $(d/D = 0.02)$ appear to be fairly flat, the Strouhal frequencies for this restriction $(10{,}600 \text{ Hz} \leq f_{St} \leq 19{,}900 \text{ Hz})$ are substantially above the measured frequency range. Thus, in calculating the acoustic energy flow the high frequency end of the jet noise spectrum has been neglected, which may in part explain why the data for the 3.18 mm nozzle does not collapse on the same curve as that for the 12.7 and 19.0 mm orifices. As f_{St} increases, the 3.18 mm nozzle data points lie successively farther below the 12.7 and 19.0 mm orifice results, which supports this explanation.

The 31.8 mm orifice data have much lower values of the frequency ratio $(0.46 \leq f_r \leq 1.50$, $325 \text{ Hz} \leq f_{St} \leq 1060 \text{ Hz})$ than those associated with the 12.7 and 19.0 mm orifices. In calculating the acoustic power generated by the 31.8 mm orifice, a portion of the lower end of the jet noise spectrum has been neglected. This could explain why the data for the 31.8 mm orifice fall below the data for the 12.7 and 19.0 mm orifices in Fig. 18. However, if the lower values for the 31.8 mm orifice were exclusively due to the measured frequency range being off the peak of the jet noise spectrum, the data at lower values of M_i would appear proportionately farther below the 12.7 mm and 19.0 mm orifice data, since this effect increases for lower f_r. Comparison with the extrapolated curve on Fig. 18 shows that this is not the case, contradicting a simple explanation that the lower values for the 31.8 mm orifice are simply due to the measured frequency range being off the peak of the jet noise spectrum. This result leads us to believe that those (d/D) effects which are caused by the influence of the confining pipewall on jet turbulence and entrainment, or possibly the noise generation associated with flow reattachment, are of importance for the 31.8 mm orifice.

The results for the 50.8 mm orifice are also shown on Figs. 17 and 18. Although the two points show (d/D) trends similar to those observed for the 31.8 mm orifice, the actual values should be viewed with some skepticism, for the reasons discussed in Sections 3.6 and 3.7.

The result of a simple acoustic power measurement, using one wall-mounted microphone, was compared to the exact acoustic power in the frequency range 200-6000 Hz calculated by use of the modal pressure spectra. For the single microphone measurement it was assumed, in calculating the acoustic power flow, that the total signal measured by the microphone was that of a plane wave. The single microphone measurement typically gave a sound power level approximately 1.5 dB above the actual sound power. The greatest difference between the two measurements was less than 2 dB. An overestimation of the acoustic efficiency by approximately 40% would result from an error in sound power measurement of 1.5 dB. Although an overestimation of this amount is not extremely bad for such an easily obtained acoustic measurement, the lack of information about the modal characteristics of the sound field might result in a much more serious error in estimating the noise that would be transmitted through the pipewall or out the pipe inlet or outlet.

3.6 Magnitudes of the Hydrodynamic Pressure Fluctuations at the Measurement Station

The modal pressure measurements were made upstream of the outlet plenum in the region containing turbulent pipe flow. No effort was made to eliminate the influence of hydrodynamic pressure variations in the development of the modal measurement technique. Thus the acoustic measurements would be incorrect if the acoustic pressure fluctuations were not large compared to hydrodynamic pressure fluctuations. This potential source of error was easily checked by use of a cross-correlation technique (discussed on page 20), at least in the 200-2100 Hz frequency range, where only plane waves propagate. Cross-correlation measurements showed that the hydrodynamic pressure fluctuations were approximately 15 dB below the acoustic pressure fluctuations in the 200-2100 Hz frequency range, for all restrictions except the 50.8 mm orifice. In the case of the 50.8 mm orifice, with $M_1 = 0.225$ (the highest flowrate), the cross-correlation measurement showed that the hydrodynamic pressure fluctuations were approximately 9 dB below the acoustic pressure fluctuations in the 200-2100 Hz range. Details of these measurements are given in Appendix A7.

Above 2100 Hz, higher modes can propagate and the cross-correlation technique is not as useful. However, at sufficiently high frequencies, the turbulent pressure fluctuations will be essentially uncorrelated over distances of the order of the pipe radius. Then, separating the wall pressure fluctuations into the acoustic and hydrodynamic parts, i.e., $p_w(\theta) = p_{ac}(\theta) + p_{hydro}(\theta)$, and substituting into Eqns. (2-9), we obtain

$$\frac{1}{16}\overline{\left[P_w(0) + P_w\left(\frac{\pi}{2}\right) + P_w(\pi) + P_w\left(\frac{3\pi}{2}\right)\right]^2} = \overline{P_{00}^2} + \frac{1}{4}\overline{P_{hydro}^2} \tag{3-3a}$$

$$\frac{1}{4}\overline{\left[P_w(0) - P_w(\pi)\right]^2} = \overline{P_{10}^2} + \frac{1}{2}\overline{P_{hydro}^2} \tag{3-3b}$$

$$\frac{1}{16}\overline{\left[P_w(0) + P_w(\pi) - P_w\left(\frac{\pi}{2}\right) - P_w\left(\frac{3\pi}{2}\right)\right]^2} = \overline{P_{20}^2} + \frac{1}{4}\overline{P_{hydro}^2} \tag{3-3c}$$

Thus the error term associated with the (0,0) and (2,0) mode measurements is 3 dB below the corresponding term in the (1,0) mode measurement, for uncorrelated hydrodynamic pressure fluctuations. Now, below the cutoff frequency of a particular mode, acoustic pressure fluctuations die off exponentially from the source. Thus, at a reasonable distance downstream of the noise-generating region ($\geq$ 5D), for frequencies below the mode cutoff frequency, essentially only hydrodynamic pressure fluctuations will be detected by the measurement technique. Therefore, examination of the (1,0) and (2,0) mode spectra below their cutoff frequencies will give a good indication of the magnitude of the hydrodynamic pressure fluctuations at higher frequencies.

Typical modal spectra for the 50.8, 31.8, and 19.0 mm orifices are shown in Fig. 19. The 50.8 mm orifice has the largest hydrodynamic pressure fluctuations. However, even in this case the higher mode acoustic pressures are at least 20 dB higher than the contributions due to the hydrodynamic pressure fluctuations, as evidenced by the rise in the (1,0) mode spectra at its cutoff frequency. However, the (0,0) mode spectra may have been influenced by hydrodynamic pressure fluctuations, for the 50.8 mm orifice. Examination of the higher mode spectra below their cutoff frequencies for the 31.8 and 19.0 mm orifices shows that these measurements were uninfluenced by hydrodynamic pressure fluctuations. The hydrodynamic pressure fluctuations are smaller, compared to the acoustic pressures, for the 19.0 mm orifice than for the 31.8 mm orifice, as would be expected.

A final point of interest is that the difference between the error terms for the (1,0) and (2,0) mode spectra (i.e., the spectral curves below the (1,0) mode cutoff frequency, 2100 Hz) is approximately 3 dB. This was the result obtained in Eqns. (3-3), in which it was assumed that the hydrodynamic pressure fluctuations at each microphone were uncorrelated. Also, for the highest flowrate case with the 50.8 mm orifice, $M_i = 0.225$, the (1,0) mode error-term lies approximately 12 dB below the (0,0) mode spectra.* Since the (1,0) mode error term in Eqn. (3-3b) is equal to $\frac{1}{2}\overline{P^2_{hydro}}$, this shows good agreement with the cross-correlation measurement, which gave a value of $\overline{P^2_{hydro}}$ 9 dB below the acoustic pressure in this frequency range.

The results presented in this section show that the acoustic modal pressure measurements were not influenced by hydrodynamic pressure fluctuations, with the possible exception of the (0,0) mode for the case of the 50.8 mm orifice.

3.7 Background Noise

In the previous section, the possibility of noise measurement errors due to the presence of hydrodynamic pressure fluctuations was discussed. However, even though the hydrodynamic pressure fluctuations are small compared to the acoustic pressure fluctuations, the background noise generated by the rig itself may influence the measurements. To check these background noise levels, modal pressure spectra were measured with no restriction in the test section. The background noise levels were then compared to pressure spectra measured with a restriction in the pipe, at the same mass flow rate. For the 31.8 mm orifice the background noise levels were always at least 15 dB below the equivalent modal spectra measured with the restriction in place. The comparative background noise levels were even lower for the smaller diameter restrictions.

---

*See Fig. A3-15.

For the 50.8 mm orifice, the background noise levels were very close to the levels measured with the restriction in place, for all but the two highest flowrate cases, $M_i = 0.187$ and 0.225. For the $M_i = 0.187$ case, the background levels were approximately 5 dB below the levels measured with the restriction in place. In the highest flowrate case, $M_i = 0.225$, the comparative background noise levels should be somewhat lower. However, the 50.8 mm orifice data should be viewed with some skepticism, especially as to the exact magnitude of the noise levels generated by the orifice.

3.8 Pipewall Excitation by Acoustic Duct Modes

Modal pressure measurements taken 2.2 meters downstream of the restriction in an early phase of the research showed unexpected dips in the higher-mode spectra. An example of this behavior is shown in Fig. 20. The (1,0) mode spectra has a pronounced dip at approximately 2500 Hz, and the (2,0) mode has a similar dip at approximately 5000 Hz. The other modes are unaffected at the frequencies of the dips. When the measurement location was moved much closer to the restriction (0.7 meters downstream), the dips disappeared.

Many possible explanations for these dips were considered to be theoretically feasible. However, our conclusions on this matter are based on experiments using simple modifications to the apparatus. (i) To see if the dips were related to the particular restriction, several different restrictions were tested. (ii) The outlet plenum and associated downstream pipe were removed, to check if the dips were related to physical characteristics of the plenum. (iii) The distance between the restriction and the outlet plenum was substantially shortened to check finite length tube impedance effects. (iv) The pipe support spacing and locations, as well as total pipe length, were changed to see if the dips were related to overall vibrational characteristics of the rig. In all of these tests there was no substantial change in the frequency or magnitude of the dips. Thus, it was concluded that the dips were related to an interaction of the acoustic waves with the pipewall itself, rather than to the effect of a particular feature of the rig.

At this point it is helpful to examine the type of pipewall vibration caused by different acoustic duct modes. The cross-sectional pressure patterns for the first three modes are shown in Fig. 21. The (0,0) mode has a circumferentially symmetric pressure field and thus tends to expand the pipe in a breathing mode, where the pipe cross section simply expands and contracts. The pipe is very stiff with respect to this type of excitation. The (1,0) mode has an asymmetric pressure distribution, with one half of the cross section positive and the other half negative at any instant. This mode represents a fluctuating unbalanced force on the pipe and would tend to excite the bending or extensional vibrations of the pipe. The (2,0) mode has two quadrants positive and two negative at any instant in time. This mode will tend to excite the hoop vibrations of the pipe wall, in which the pipe wall is deformed as sketched in Fig. 21. The pipe is relatively flexible to vibration in an inextensional mode of the latter type.

There are two ways that the pipe wall vibration could selectively absorb noise in a given mode at a particular frequency. If the axial phase velocity of the acoustic mode matches the axial phase velocity for the pipe vibrational mode with the same circumferential mode shape, the acoustic and vibrational modes would be phase-locked as they propagated down the pipe. This would permit very effective energy transfer from the acoustic wave to the pipe wall. Such a situation would in general occur at only one frequency, since the phase velocities are functions of frequency. A second way for the pipe to selectively absorb one frequency of a particular mode is for the frequency to be a natural frequency of vibration for a compatible vibrational mode of the pipe. Such modes exist only for finite-length pipes. In the experimental apparatus the natural modes would most likely be related to the length between pipe flanges, as the flanges are much stiffer than the pipe wall and effectively serve as vibrational boundary conditions. To check this, the 1.5 meter length pipe section which was upstream of the measurement location for the spectra shown in Fig. 20 was replaced by several 0.6 meter length sections. The measurement station was 2.36 meters downstream of the orifice in the new configuration, as opposed to 2.2 meters downstream for the spectra in Fig. 20. The spectra taken at the new location are shown in Fig. 22. It can be seen that the dip in the (1,0) mode is very similar to that in Fig. 20, while the dip in the (2,0) mode has been substantially reduced. This result indicates that the mechanism that produced the dip at 2500 Hz is somewhat different from the one that produced the dip at 5000 Hz. Further research would be necessary to develop a complete explanation of this behavior, but this mode selective absorption is believed to be a result of pipe wall modal vibration.

It is clear from the above discussion that to adequately predict the noise field outside a pipe, research on the modal transmission characteristics of pipes is necessary. The importance of the higher modes should not be underestimated. Results presented by Kuhn (1974) indicate that the (1,0) mode can transmit a significant amount of sound through the pipe wall, even below its cutoff frequency. Because of greater pipe wall flexibility to higher modes, noise transmitted by higher modes may be of major importance, even when the plane wave ((0,0) mode) pressure is the dominant component inside the pipe.

3.9 Effect of the Outlet Plenum on Acoustic Waves

As discussed in the introductory section of this chapter, one of the design objectives of the experimental apparatus was to eliminate the influence of hydrodynamic pressure fluctuations on the acoustic measurements. This was accomplished by allowing the acoustic waves to propagate through the outlet plenum into the no-flow zone behind the plenum. However, acoustic measurements in the downstream no-flow zone must be corrected for any attenuation caused by the outlet plenum section. Roberts and Johnston (1974) used a correction factor of 1-2 dB to compensate for outlet plenum attenuation.

In an early phase of the present research, it was found that the hydrodynamic pressure fluctuations were small compared to the acoustic pressure fluctuations in the regi upstream of the outlet plenum, for sufficiently small (d/D) . This result allowed a direct comparison of modal pressure spectral measurements ahead of and behind the outlet plenum. A set of spectra measured in the flow zone upstream of the outlet plenum is shown in Fig. 23a. The pressure spectra in the no-flow zone for the same experimental conditions are shown in Fig. 23b. Comparision of the spectra shows an approximately constant 2-3 dB attenuation of the (0,0) mode across the outlet plenum, for frequencies below 4400 Hz. The higher modes were much more strongly attenuated. The (1,0) mode shows a typical reduction of approximately 7 dB, and the (2,0) mode shows a typical reduction of approximately 12 dB. The (3,0) mode was not even distinguishable from the (1,0) mode in the no-flow zone spectra, compared to a rise of approximately 9 dB over the (1,0) mode in the flow zone upstream of the outlet plenum. The attenuation of the higher-mode resonance peaks was more than 15 dB. Thus the outlet plenum had a strong effect on the acoustic waves, especially the higher modes, and measurements in the downstream no-flow zone are not very representative of the noise field generated by flow through the restriction (except possibly for the (0,0) mode, if an appropriate correction factor is used).

The attenuation produced by the outlet plenum is caused either by absorption of the acoustic waves or by reflection of the waves back upstream. The higher mode spectra taken upstream of the outlet plenum (Fig. 23a) have small, regularly spaced fluctuations of 1-2 dB. These samll fluctuations are characteristic of standing waves or strong reflections, in which the reflected wave either reinforces or partially cancels the downstream propagating wave at the measurement location. The spectra taken downstream of the outlet plenum for the same flow conditions (Fig. 23b) do not exhibit such strong standing wave behavior, indicating that the outlet plenum section causes stronger reflections of the higher modes than the anechoic termination.

There are two main changes in acoustic properties caused by the outlet plenum. One of these is the change in the wall impedance due to the porous element, and the other is the deceleration of the mean flow.

A rig modification, which might significantly decrease the reflections caused by the outlet plenum, would be to mount the anechoic termination cone so that it extended into the plenum in the same region as the porous pipe section. This modification is illustrated in Fig. 24. As well as possibly reducing reflections caused by the change in wall impedance, the change in cross-sectional area would decrease the rapid deceleration due to the flow exiting through the porous element. In this modification, it might also prove convenient to mount a fifth microphone in the cone tip, for use with an extension of the mode separation techniques.

3.10 Summary

Downstream modal pressure spectra have been measured for the case of noise generated by air flow through a number of different coaxial restrictions in a long, straight, 97 mm diameter pipe. The restrictions tested were A.S.M.E. flow-metering orifices with diameters of 12.7, 19.0, 31.8, and 50.8 mm, and three nozzles (3.18 mm diameter and two 16.2 mm diameter nozzles with respective throat length-to-diameter ratios of 1 and 8). The Mach numbers of the flow through the restrictions ranged from 0.15 to slightly supercritical flow.

The modal pressure spectra were measured in the 200-6000 Hz frequency range. The (0,0), (1,0), (2,0), (0,1), and (3,0) modes are propagating modes in this frequency range.

The shape of the modal pressure spectra was found to be determined chiefly by the frequency ratio, $f_r = \gamma/\pi St = U_i D/a_o d$. γ is the nondimensional frequency governing acoustic mode propagation inside the pipe, and St is the nondimensional frequency governing the jet noise spectrum shape. At low values of f_r the measured frequency range is in the upper end of the jet noise spectrum, and the spectra fall off rapidly with increasing frequency. At higher f_r the measured frequency range contains the broad peak of the jet noise spectrum, and the spectra are basically flat in the range 200-6000 Hz.

The relative amplitude of the (0,0) mode and the higher modes, at frequencies above the higher mode cutoff frequency, depends strongly on the frequency ratio. For low f_r the (1,0), (2,0), and (3,0) modes dominate the spectrum above their cutoff frequencies. At high values of f_r all modes have approximately equal amplitudes. This behavior can be understood by realizing that at low f_r the noise at frequencies where the higher modes propagate is generated in the initial region of the jet near the nozzle exit. Large-scale structures which exhibit circumferential coherence are found in this region. Higher mode dominance indicates that the higher-order-circumferential structures ("fluting") are more important than the zero-order symmetrical structures in the initial region of the jet. At higher values of f_r the noise in this same frequency band is generated much farther downstream in the jet. In this downstream region the large-scale structures have lost much of their circumferential coherence, and thus the higher modes do not dominate the noise spectrum.

All of the higher modes rise to a sharp peak at their cutoff frequencies, where the mode is at a resonance condition. However, with the exception of the 3.18 mm nozzle case, the amplitude of the (0,1) mode dies off rapidly at frequencies above its cutoff frequency, while the amplitudes of the (1,0), (2,0), and (3,0) modes do not exhibit this behavior. For the 3.18 mm nozzle, the amplitude of the (0,1) mode did not die off rapidly at frequencies above its cutoff frequency. This can be explained by the fact that, for this restriction, the noise source region spans only a very small portion of the duct cross-sectional area.

Modal acoustic power spectra were calculated using the measured pressure spectra and integrated over the frequency range 200-6000 Hz. The overall efficiencies were plotted vs. the indicated Mach number of the jet that issues from the orifice or nozzle. In general, the efficiencies were of the same order of magnitude as those for free jets.

The values of the efficiencies for the 16.2 mm nozzles and the 19.0 mm orifice agreed very closely. The nozzle size was chosen to match the vena contracta of the 19.0 mm orifice. Thus, this result indicates that the exact shape of the restriction is not very important in determining the sound power produced.

The ratio of the restriction diameter to pipe diameter, (d/D), had a considerable effect on the efficiency results. In general, the value of the efficiency increased as (d/D) increased, for constant M_i. The efficiencies for the 12.7 and 19.0 mm orifices varied approximately as $M_i^{4.6}$. The data for the 31.8 mm orifice extended to lower values of M_i and had a slightly lower slope than that of the smaller orifices. The data for the 3.18 mm nozzle also had a slightly lower slope than that for the 12.7 and 19.0 mm orifices. It was found that when the efficiency was divided by the area ratio, $(d/D)^2$, the data for the 12.7 and 19.0 mm orifices collapsed on a single curve. The 31.8 mm orifice data, when η was divided by $(d/D)^2$, fell slightly below the correlated data for the smaller orifices. This result is thought to be due to the increased effect of the confining pipe wall in determining the fluid dynamic noise generation characteristics of the jet, for larger (d/D). The data for the 3.18 mm nozzle, when divided by the area ratio, also fell somewhat below the correlated data for the small orifices. This may have been due to a failing of the area scaling law for small (d/D), or simply to the fact that only a limited frequency range, 200-6000 Hz, was measured. However, considering the simplicity of the scaling law, the success of this correlation over a large range of (d/D) values is quite striking.

Hydrodynamic pressure fluctuations due to the turbulent pipe flow were measured and found to be unimportant compared to the acoustic pressure levels downstream of the restriction, for values of $(d/D) \leq 1/3$. For the 50.8 mm orifice, the hydrodynamic pressure fluctuations were most important at low flowrates, but affected only the (0,0) mode. The rig background noise was much higher than the level of the hydrodynamic pressure fluctuations, and became significant for large (d/D).

Chapter 4

ACOUSTIC ENERGY PROPAGATION IN A CIRCULAR DUCT CONTAINING AN AXISYMMETRIC, SUBSONIC MEAN FLOW

4.1 Previous Work

The development of concepts of and expressions for acoustic energy propagation inside ducts have in general followed the development of similar expressions for acoustic propagation in an unbounded medium. The classical expressions for the acoustic energy flux and acoustic energy density in the case of an initially uniform and motionless medium are

$$\overline{J_s} = p'\overline{v}' \tag{4-1a}$$

and

$$\xi_s = \frac{1}{2}\frac{p'^2}{\rho_o a_o^2} + \frac{1}{2}\rho_o \overline{v}'^2 \tag{4-1b}$$

respectively. In Eqns. (4-1), p' is the perturbation pressure, $\overline{v}'$ is the perturbation velocity, ρ_o is the density of the undisturbed medium, and a_o is the adiabatic speed of sound in the medium. The instantaneous quantities ξ_s and $\overline{J}_s$ satisfy the special form of the thermodynamic energy equation,

$$\frac{\partial \xi_s}{\partial t} + \operatorname{div} \overline{J_s} = 0 \tag{4-1c}$$

when heat conduction and viscosity effects are ignored. Eqn. (4-1c) is satisfied up to second order in the perturbation quantities $(p',\overline{v}')$ and can be derived by a straightforward manipulation of the second-order acoustic equations (the derivation is a special case of the more general analysis given in Section 4.2).

The quantities in Eqn. (4-1c) have easily recognizable physical significances. The acoustic energy flux, $\overline{J_s}$, is the flow work term. The acoustic energy density, ξ_s , consists of two parts. In essence, the first part is the elastic energy of the acoustic wave, and the second part is the kinetic energy of the acoustic wave. The acoustic energy flux given by Eqn. (4-1a) is directly applicable to acoustic propagation inside ducts and has found widespread use for cases with no mean flow. Eqn. (4-1c) contains no source terms and thus time-averaging the equation gives $\mathrm{div} < \overline{J_s} > = 0$, which is a very useful property. For example, the total acoustic energy radiated from a duct end (i.e., the acoustic energy crossing surface S_2 in Fig. 25) can be determined by measuring the acoustic energy which crosses surface S_1 inside the duct. This considerably simplifies the measurement.

An acoustic energy equation for the case of a uniformly moving medium can be derived using the same approach as used for the case of a medium with no mean flow. The energy equation is the same as Eqn. (4-1c), except that $\overline{J_s}$ is modified to include the convection of the acoustic energy density by the mean flow; i.e.,

$$\overline{J}_s^P = \xi_s \overline{V}_o + p'\overline{v}' \tag{4-2}$$

This result is also a special case of the analysis in Section 4.2. Because of the simple physical interpretation of Eqn. (4-2), this energy flux will be called the <u>physical energy flux</u> (denoted by $\overline{J}_s^P$). Thus, for the case of a uniform mean flow the acoustic energy equation still contains no source terms. An analysis very similar to this, but restricted to acoustic propagation inside of constant area ducts, has been presented by Eversman (1971).

One of the first important steps in analyzing acoustic propagation in a nonuniformly moving medium was made by Blockhintsev (1946). He considered the case of high frequency waves where the acoustic wavelength is short compared to the length over which substantial changes in the mean flow occur, i.e., the geometric acoustics limit. The analysis of Blockhintsev is basically a perturbation expansion in terms of a wavelength parameter where only the lowest-order terms are retained. In this limit the acoustic waves appear locally as plane waves that propagate along acoustic rays. The geometry of the acoustic rays is given by the solution of the eikonal equation, and the variation of amplitude along the ray is given by an equation which Blockhintsev calls "the law of conservation of the average energy in geometrical acoustics." This equation has the form of an energy equation, and the energy density and energy flux agree with Eqns. (4-1) for the case of no mean flow. However, the energy density and energy flux defined by Blockhintsev do not reduce, in the limit of a uniform mean flow, to those quantities derived from the thermodynamic energy equation, ξ_s and $\overline{J}_s^P$. This leads to the conclusion that the "energy flux" defined by Blockhintsev is not the physical energy flux, but rather a particular flux that is conserved in the geometric acoustics limit.

This last point has been amplified by Bretherton and Garrett (1969), and by Hayes (1968). Bretherton and Garrett, utilizing a Lagrangian description of the fluid motion and Hamilton's principle (following the approach of Whitham (1965)), showed that a quantity they called "wave action density" is conserved in the geometric acoustics limit, whereas wave energy is not. Bretherton and Garrett define wave action density as $E = \xi_s/\omega'$, where ξ_s is the acoustic energy density (Eqn. (4-1b)) and ω' is the intrinsic frequency of the wave, i.e., the frequency as measured by an observer moving with the mean flow. This quantity satisfies a conservation equation, i.e.,

$$\frac{\partial E}{\partial t} + \mathrm{div}(\overline{C}E) = 0 . \qquad (4\text{-}3)$$

In Eqn. (4-3) $\overline{C} = a_o\overline{n} + \overline{V}_o$, where $\overline{n}$ is a unit vector in the direction of the acoustic velocity $\overline{v}'$. Multiplication of the wave action density by the circular frequency, ω (a constant), leaves Eqn. (4-3) unchanged. Blockhintsev's result is obtained simply by setting $E = \omega\xi_s/\omega'$ in Eqn. (4-3).

Hayes (1968) derived this result in an entirely different manner. He showed that for isentropic acoustic fluctuations in a nonuniformly moving medium, the perturbation equations can be manipulated to yield

$$\frac{\partial \xi_s}{\partial t} + \operatorname{div} \overline{J}_s^P = -\rho_o(\overline{v}' \cdot \overline{V_o}) \cdot \overline{v}' - (\Gamma-1) \frac{p'^2}{\rho_o a_o^2} \operatorname{div} \overline{V}_o \, . \tag{4-4}$$

$\Gamma = 1/a\,(\partial \rho a/\partial \rho)_s$, evaluated at the mean flow conditions. This equation, which is only stated in final form by Hayes, was derived independently during the course of the present investigation. It was later found that Hayes had presented this result in his 1968 paper. Eqn. (4-4) is accurate to $O(\varepsilon^2)$, and contains only the first-order perturbation quantities. The left-hand side of Eqn. (4-4) is identical to the result derived previously for a uniformly moving medium (Eqns. (4-2) and (4-1b)). However, for a nonuniformly moving medium, the right-hand side is no longer equal to zero. The terms on the right-hand side of Eqn. (4-4) are normally referred to as source terms, although this separation into right-hand and left-hand sides is somewhat arbitrary. Due to the physical interpretation of the terms on the left-hand side, as discussed earlier, and the fact that the right-hand side cannot be expressed as a simple divergence term, this view seems appropriate. For the cases of zero mean flow and uniform mean flow, the source terms in Eqn (4-4) are zero and the resulting equation agrees with Eqns. (4-1) and (4-2).

Hayes evaluates Eqn. (4-4) in the geometric acoustics limit. He then adds an expression to each side of Eqn. (4-4) in order to cancel the source terms. The resulting equation can then be written in the form of Eqn. (4-3), which is the result obtained by Blockhintsev and by Bretherton and Garrett. Various other investigators (Guiraud, 1964; Cantrell and Hart, 1964; Ryshov and Schefter, 1962; and Morfrey, 1971a) have also obtained results similar to those discussed above. However, these analyses will not be discussed in detail here. A convenient form of the Blockhintsev type energy flux is given by Cantrell and Hart (1964) as

$$\vec{J}_s^B = p'\vec{v}' + \rho_o(\vec{V}_o \cdot \vec{v}')\,\vec{v}' + \frac{p'^2}{\rho_o a_o^2}\vec{V}_o + \frac{p'}{a_o^2}(\vec{V}_o \cdot \vec{v}')\,\vec{V}_o \tag{4-5}$$

Equation (4-5) will be used in the remainder of this chapter when discussing Blockhintsev type energy fluxes, and is denoted by $\vec{J}_s^B$ for clarity.

A number of investigators have applied the Blockhintsev type energy analysis to acoustic propagation inside of ducts with flow. Morfey (1971b) considered the case of a uniform axial flow in a constant area duct. Candel (1975) considered propagation in acoustic ducts of slowly varying cross section. In his analysis, the mean flow was assumed to be uniform at each axial station. In principle, the Blockhintsev type energy flux can be applied inside a duct when the mean flow is sheared, at least in the high frequency limit. The validity of this approach for hard-walled cylindrical ducts is examined later in this chapter.

Möhring (1971) has developed acoustic energy quantities for the case of a parallel sheared mean flow in a constant area duct. He used a conservation equation derived from Seliger and Whitham's (1968) form of Hamilton's principle. There is no restriction to high frequencies or low values of mean shear. The energy flux derived by Möhring is a conserved quantity for all conditions and reduces to the Blockhintsev energy flux for high frequencies and low values of the mean shear.

To summarize, there have been basically two approaches followed in defining acoustic energy quantities. The first approach uses the thermodynamic energy equation and equations of motion to derive an acoustic energy equation. The acoustic energy density and acoustic energy flux defined by this approach are appealing, because of the direct physical interpretation of the expressions. However, the acoustic energy equation developed from the thermodynamic energy equation contains source terms in the general case of a nonuniformly moving medium, and thus the time-averaged energy flux is not divergence free.

In the second approach, expressions which fulfill a conservation equation, i.e., an energy equation without source terms, are sought. Normally such an equation applies only to certain classes of problems. For example, the Blockhintsev flux is a conserved quantity only in the geometric acoustics limit, and Möhring's result applies only to ducts with a parallel shear flow. Although the flux defined by such an equation is a conserved quantity, this flux is not always the thermodynamic energy flow associated with the acoustic perturbation. This distinction should be kept in mind when considering acoustic energy flux expressions developed from a conservation equation approach.

The research presented in this chapter examines two aspects of acoustic energy flow in ducts containing a mean flow with axisymmetric nonuniformity. The first of these concerns the applicability of energy flux expressions based on the thermodynamic energy equation (Eversman, 1971; Ryshov and Shefter, 1962; and Guiraud, 1964) to the case of a parallel sheared mean flow in a duct. This energy flux (Eqn. (4-2)) has been thought to be applicable only to cases with very low mean shear, because it does not reduce to Blockhintsev's energy flux in the geometric acoustics limit. However, in this chapter it is shown that the energy flux given by Eqn. (4-2), with minor modifications, is indeed a valid formulation for acoustic propagation in a circular, constant-area duct containing an axisymmetric sheared mean flow.

A second aspect of the energy flux inside ducts which was examined in the present investigation concerns the agreement between the flux term derived by Möhring and that derived for the geometric acoustics limit, Eqn. (4-5). The Blockhintsev type flux is conserved in the geometric acoustics limit, but for lower frequencies or high mean shear the Blockhintsev energy equation (4-3) would contain source terms and thus this flux would not be conserved. It would be useful to have a quantitative understanding of the conditions under which this flux is conserved. Since the Möhring flux is conserved under all conditions, and agrees with the Blockhintsev flux in the geometric acoustics limit, a direct comparison of these flux terms for specific cases will indicate the importance of the source term in the Blockhintsev energy equation.

The comparison of the Möhring and Blockhintsev energy flux terms will also serve a second purpose. The usefulness of the Möhring acoustic energy flux is somewhat limited in that the flux is not defined except for the case of a constant area duct containing a parallel sheared mean flow. Thus, although Möhring's energy flux is a conserved quantity in the duct, it is not clear how to relate this conserved quantity to the acoustic energy that propagates out the duct inlet or outlet into the surrounding region. Since the Blockhintsev flux is defined outside as well as inside the duct, a comparison of the two energy flux quantities serves to relate the Möhring flux to a flux quantity defined outside the duct.

4.2 Derivation of the Physical Energy Equation

In this section an acoustic energy equation (4-4) is derived from the thermodynamic energy equation. Viscous and heat conduction effects are ignored in the analysis. A nonuniform and, in general, rotational mean flow is considered, but the entropy of the mean flow is assumed to be constant. There is some question as to what extent the assumptions of constant entropy and rotational flow apply together, since vorticity is normally generated as a result of viscous effects, which increase the entropy locally*. However, this has been the approach

*In a long duct, where the pressure is constant across the duct at a given section and heat transfer is sufficiently rapid, thermal equilibrium across a section may be approached. Under these conditions, constant entropy may be a reasonable approximation. In a duct with adiabatic walls and high subsonic mean velocities, this approximation may be unrealistic.

generally followed in analyzing acoustic propagation in a duct containing a nonuniform mean flow (Pridmore-Brown, 1958; Mungur and Plumblee, 1969; Savkar, 1971; Shankar, 1972) and, with this in mind, will be used here. The mean flow is assumed to be steady, although the analysis could be extended to include the effects of a slow variation in the mean flow. A complete development of the following analysis is given in Appendix A8. For brevity, only the essential steps are outlined below.

The variables are first separated into mean and perturbation quantities, i.e., $p = P_o + p'$, etc. The perturbation is considered to be of order ε and for the present may be assumed to include all higher-order terms, i.e., $p' = \varepsilon P_1 + \varepsilon^2 P_2 + \ldots$. The continuity equation can be written as

$$\frac{\partial \rho'}{\partial t} + \mathrm{div}(\rho'\overline{V}_o + \rho_o\overline{v}' + \rho'\overline{v}') = 0 \qquad (4\text{-}6)$$

after noting that $\mathrm{div}(\rho_o\overline{V}_o) = 0$.

Similarly, the momentum equation can be written as (neglecting $O(\varepsilon^3)$ terms)

$$(\rho_o+\rho')\frac{\partial \overline{v}'}{\partial t} + (\rho_o+\rho')(\overline{V}_o\cdot\nabla\overline{v}' + \overline{v}'\cdot\nabla\overline{V}_o) + \rho_o\overline{v}'\cdot\nabla\overline{v}' + \rho'\overline{V}_o\cdot\nabla\overline{V}_o + \nabla p' = 0 \qquad (4\text{-}7)$$

after noting that $\rho_o\overline{V}_o \cdot \nabla\overline{V}_o + \nabla P_o = 0$. Multiplying Eqn. (4-6) by $\overline{v}'$ and adding to Eqn. (4-7), we obtain

$$\rho_o\frac{\partial \overline{v}'}{\partial t} + \frac{\partial(\rho'\overline{v}')}{\partial t} + \overline{v}'\,\mathrm{div}(\rho'\overline{V}_o+\rho_o\overline{v}') + (\rho_o+\rho')(\overline{V}_o\cdot\nabla\overline{v}' + \overline{v}'\cdot\nabla\overline{V}_o) + \rho_o\overline{v}'\cdot\nabla\overline{v}' + \rho'\overline{V}_o\cdot\nabla\overline{V}_o + \nabla p' = 0 \qquad (4\text{-}8)$$

The thermodynamic energy equation can be written as

$$\frac{\partial}{\partial t}\left\{\rho\left(e + \frac{\overline{v}^2}{2}\right)\right\} + \text{div}\left\{\rho\left(e + \frac{\overline{v}^2}{2} + \frac{p}{\rho}\right)\overline{v}\right\} = 0 \qquad (4\text{-}9)$$

when viscous, heat conduction and potential field effects are ignored. Substituting in the perturbation expressions, and noting that $\rho e = \rho_o e_o + h_o\rho' + (a_o^2/2\rho_o\ \rho'^2$,

$$\frac{\partial \xi_s}{\partial t} + \text{div}\ \overline{J}_s^P + \overline{V}_o \cdot \left[\rho_o \frac{\partial \overline{v}'}{\partial t} + \frac{\partial(\rho'\overline{v}')}{\partial t} + \overline{v}'\ \text{div}(\rho'\overline{V}_o + \rho_o\overline{v}') + \right.$$

$$\left.(\rho_o + \rho')\ \nabla(\overline{V}_o \cdot \overline{v}') + \nabla p'\right] + \overline{v}' \cdot \left[\rho_o \nabla(\overline{V}_o \cdot \overline{v}') + (\rho_o + \rho')\ \nabla\left(h_o + \frac{\overline{V}_o^2}{2}\right)\right] +$$

$$p'\ \text{div}\ \overline{V}_o = 0 \qquad (4\text{-}10)$$

accurate to $O(\varepsilon^2)$. ξ_s and $\overline{J}_s^P$ are given by Eqns. (4-1b) and (4-2), respectively. When the third team in Eqn. (4-10) is simplified by use of Eqn. (4-8), one obtains

$$\frac{\partial \xi_s}{\partial t} + \text{div}\ \overline{J}_s^P + \frac{\rho'}{\rho_o}\nabla p_o \cdot \overline{V}_o + p'\ \text{div}\ \overline{V}_o + \rho_o \overline{v}' \cdot (\overline{v}' \cdot \nabla\overline{V}_o) = 0 \qquad (4\text{-}11)$$

This equation is accurate to $O(\varepsilon^2)$, and thus ρ' and p' are needed to second-order accuracy. However, note that the mean flow continuity equation can be expressed as

$$\rho_o\ \text{div}\ \overline{V}_o + \frac{1}{a_o^2}\nabla p_o \cdot \overline{V}_o = 0 \qquad (4\text{-}12)$$

Using Eqn. (4-12) and the equation of state $p' = f(\rho')$ accurate to second order, the terms involving ρ' and p' can be combined, resulting in

$$\frac{\partial \xi_s}{\partial t} + \text{div}\ \overline{J}_s^P = -\rho_o \overline{v}' \cdot (\nabla \overline{V}_o) \cdot \overline{v}' - \frac{(\Gamma-1)}{\rho_o a_o^2} p'^2\ \text{div}\ \overline{V}_o \qquad (4\text{-}4)$$

accurate to $O(\varepsilon^2)$. The equation is instantaneously satisfied by the first-order perturbation quantities. Eqn. (4-4) is the equation presented by Hayes (1968), as discussed in Section 4.1. When this equation is specialized to the case of a uniform mean flow, the source terms (the right-hand side) become zero. For the case of no mean velocity, Eqns. (4-1) are recovered.

Time-averaging Eqn. (4-4) gives

$$\text{div} < \overline{J}_S^P > \ = \ < -\rho_o \overline{v}' \cdot (\nabla \overline{V}_o) \cdot \overline{v}' - \frac{(\Gamma-1)}{\rho_o a_o^2} p'^2\ \text{div}\ \overline{V}_o > \qquad (4\text{-}13)$$

This result will be applied to the case of acoustic propagation inside a duct containing a nonuniform mean flow in the following section.

4.3 Application of the Physical Energy Equation to Acoustic Propagation Inside Ducts

The time-averaged physical energy equation derived in the previous section will be applied to acoustic propagation inside a hard-walled circular duct. The geometry being considered is shown in Fig. 3. The mean flow is assumed to be an axisymmetric parallel shear flow, i.e., $\overline{V}_o = U_o(r)\overline{e}_z$. As a result, the source term in Eqn. (4-13) simplifies to $< -\rho_o u_r' u_z' (dU_o/dr) >$. Integrating Eqn. (4-13) over the duct volume between two different axial sections z_1 and z_2, we obtain

$$\int_s < J_{s_z}^P > ds \Big|_{z_1}^{z_2} = \int_{z_1}^{z_2} \int_s < -\rho_o u_r' u_z' \frac{dU_o}{dr} > dsdz \qquad (4\text{-}14)$$

where $J_{s_z}^P$ is the component of the physical energy flux vector in the axial direction and ds denotes the differential element of duct cross-sectional area.

The integrals on the right-hand and left-hand sides of Eqn. (4-14) will be evaluated separately.

4.3.1 Evaluation of $\int_s < J^P_{s_z} > ds$

The left-hand side of Eqn. (4-14) will now be evaluated. The details of this calculation are given in Appendix A8. We have

$$< J^P_{s_z} > \;=\; < \frac{p'^2}{2\rho_o a_o^2} + \frac{\rho_o}{2}\left(u_r'^2 + u_\theta'^2 + u_z'^2\right) > U_o + < p'u'_z > \tag{4-15}$$

The solution forms for p', u_r', etc., were given in Chapter 2 as

$$p' = \sum_{m,n} \mathrm{Re}\left[P_{mn}(r,\theta)\; e^{i(\omega t - k_{z_{mn}} z)} \right]$$

$$u_r' = \sum_{m,n} \mathrm{Re}\left[V_{r_{mn}}(r,\theta)\; e^{i(\omega t - k_{z_{mn}} z)} \right], \quad \text{etc.}$$

Substituting these expressicns in Eqn. (4-15) and time-averaging, we obtain

$$< J^P_{s_z} > = \frac{1}{2}\mathrm{Re}\left\{ \sum_{m,n}\sum_{b,c} \left[\left(\frac{P_{mn}P^*_{bc}}{2\rho_o a_o^2} + \frac{\rho_o}{2} V_{r_{mn}} V^*_{r_{bc}} + \frac{\rho_o}{2} V_{\theta_{mn}} V^*_{\theta_{bc}} + \frac{\rho_o}{2} V_{z_{mn}} V^*_{z_{bc}} \right) U_o + P_{mn} V^*_{z_{bc}} \right] e^{i(k_{z_{bc}} - k_{z_{mn}})} \right\} \tag{4-16}$$

We also have

$$V_{r_{mn}} = \frac{i\,\dfrac{\partial P_{mn}}{\partial r}}{\rho_o(\omega - k_{z_{mn}} U_o)} \tag{4-17a}$$

$$V_{\theta_{mn}} = \frac{i\,\dfrac{\partial P_{mn}}{r\partial\theta}}{\rho_o(\omega - k_{z_{mn}} U_o)} \tag{4-17b}$$

and

$$V_{z_{mn}} = \frac{k_{z_{mn}} P_{mn}}{\rho_o(\omega - k_{z_{mn}} U_o)} - \frac{\dfrac{\partial P_{mn}}{\partial r}\dfrac{dU_o}{dr}}{\rho_o\left(\omega - k_{z_{mn}} U_o\right)^2} \tag{4-17c}$$

where P_{mn} is given by

$$P_{mn} = C_{mn}\cos(m\theta + \phi_{mn})\, R_{mn}(r) \tag{4-18}$$

Substituting Eqn. (4-18) into Eqns. (4-17) and using these expressions in Eqn. (4-16), the following result is obtained, when $< J^P_{s_z} >$ is integrated across the duct cross section.

$$\int_s < J^P_{s_z} > ds = \frac{\pi r_o^2}{\rho_o a_o} \sum_{m,n} \sum_c \frac{C_{mn} C_{mc} \cos(\phi_{mc} - \phi_{mn})}{2(1+\epsilon_m)} \int_0^1 \left\{ \frac{M}{2} \left[R_{mn} R_{mc} \right. \right.$$

$$+ \frac{\frac{dR_{mn}}{d\bar{r}} \frac{dR_{mc}}{d\bar{r}}}{\gamma^2 K_{mn} K_{mc}} + \frac{m^2 R_{mn} R_{mc}}{\gamma^2 \bar{r}^2 K_{mn} K_{mc}} + \frac{\bar{k}_{mn} \bar{k}_{mc} R_{mn} R_{mc}}{K_{mn} K_{mc}} + \frac{\frac{dR_{mn}}{d\bar{r}} \frac{dR_{mc}}{d\bar{r}} \left(\frac{dM}{d\bar{r}}\right)^2}{\gamma^4 K_{mc}^2 K_{mn}^2}$$

$$\left. - \frac{\bar{k}_{mn} R_{mn} \frac{dR_{mc}}{d\bar{r}} \frac{dM}{d\bar{r}}}{\gamma^2 K_{mn} K_{mc}^2} - \frac{\bar{k}_{mc} R_{mc} \frac{dR_{mn}}{d\bar{r}} \frac{dM}{d\bar{r}}}{\gamma^2 K_{mc} K_{mn}^2} \right]$$

$$\left. + \frac{\bar{k}_{mc} R_{mn} R_{mc}}{K_{mc}} - \frac{R_{mn} \frac{dR_{mc}}{d\bar{r}} \frac{dM}{d\bar{r}}}{\gamma^2 K_{mc}^2} \right\} 2\bar{r} d\bar{r} \cos(\bar{k}_{mc} - \bar{k}_{mn}) \bar{z} \qquad (4\text{-}19)$$

The summation is assumed to extend over all cuton modes, and the expression has been nondimensionalized using

$$\bar{r} = \frac{r}{r_o}, \quad \bar{k}_{mn} = \frac{k_{z_{mn}} a_o}{\omega}, \quad M = \frac{U_o}{a_o}, \quad K_{mn} = (1 - \bar{k}_{mn} M),$$

$$\gamma = \frac{\omega r_o}{a_o} \quad \text{and} \quad \bar{z} = \frac{\omega z}{a_o}$$

The original summation over four indices in Eqn. (4-16) has been reduced to a summation over three indices by virtue of the orthogonality properties of the cosine functions. The terms multiplied by $M/2$ are the expansion of $< \xi_s > U_o$, and the last two terms in the integral are related to $< p' u_z' >$. The terms for which $c = n$ are independent of $\bar{z}$, while the terms for which $c \neq n$ have a cosine dependence on $\bar{z}$ and an amplitude which is related to the difference in phase angle between the (m,n) and (m,c) modes.

When the integrated flux $\int_s < J^P_{s_z} > ds$ is substituted into Eqn. (4-14), the terms for which $n = c$ will cancel out, as these terms are independent of $\bar{z}$. Thus it proves convenient to break the integrated acoustic energy flux into two parts. The part for which $n = c$ will be designated by $\mathcal{P}_a^P$, and that for which $n \neq c$ will be designated by $\mathcal{P}_b^P$. We thus have

$$\int_s < J^P_{s_z} > ds = \mathcal{P}_a^P + \mathcal{P}_b^P \tag{4-20}$$

Further manipulations of $\mathcal{P}_a^P$ and $\mathcal{P}_b^P$ will be performed separately.

4.3.2 Evaluation of $\mathcal{P}_a^P$

The part of the integrated acoustic energy flux which is independent of the axial coordinate, $\bar{z}$, will now be examined. Collecting the terms in Eqn. (4-19) for which $n = c$, we have

$$\begin{aligned}
\mathcal{P}_a^P = \frac{\pi r_o^2}{\rho_o a_o} \sum_{m,n} \overline{P_{mn}^2} \int_0^1 \Bigg\{ \frac{M}{2} \Bigg[& R_{mn}^2 + \frac{\left(\frac{dR_{mn}}{d\bar{r}}\right)^2}{\gamma^2 K_{mn}^2} + \frac{m^2 R_{mn}^2}{\gamma^2 \bar{r}^2 K_{mn}^2} + \frac{\bar{k}_{mn}^2 R_{mn}^2}{K_{mn}^2} \\
& + \frac{\left(\frac{dR_{mn}}{d\bar{r}}\right)^2 \left(\frac{dM}{d\bar{r}}\right)^2}{\gamma^4 K_{mn}^4} - \frac{2\bar{k}_{mn} R_{mn} \frac{dR_{mn}}{d\bar{r}} \frac{dM}{d\bar{r}}}{\gamma^2 K_{mn}^3} \Bigg] + \frac{\bar{k}_{mn} R_{mn}^2}{K_{mn}} \\
& - \frac{R_{mn} \frac{dR_{mn}}{d\bar{r}} \frac{dM}{d\bar{r}}}{\gamma^2 K_{mn}^2} \Bigg\} 2\bar{r} d\bar{r}
\end{aligned} \tag{4-21}$$

where $\overline{P_{mn}^2}$ is given by Eqn. (2-8). The portion of $\mathcal{P}_a^P$ associated with the convection of $< \xi_s >$ by the mean flow can be simplified by an integration by parts. We have

$$\int_0^1 \frac{M\left(\frac{dR_{mn}}{d\bar{r}}\right)^2}{K_{mn}^2} \bar{r} d\bar{r} = -\int_0^1 MR_{mn} \frac{d}{d\bar{r}} \left[\bar{r} \frac{\frac{dR_{mn}}{d\bar{r}}}{K_{mn}^2} \right] d\bar{r} - \int_0^1 \frac{R_{mn} \frac{dR_{mn}}{d\bar{r}} \frac{dM}{d\bar{r}}}{K_{mn}^2} \bar{r} d\bar{r} \tag{4-22}$$

as the contributions from the end points vanish by virtue of the boundary conditions on R_{mn}. The first integral on the right-hand side can be re-written by use of the differential equation for R_{mn} (Eqn. (2-3)). When this result is substituted back into Eqn. (4-21), the following result is obtained.

$$\mathcal{P}_a^P = \frac{\pi r_o^2}{\rho_o a_o} \sum_{m,n} \overline{p_{mn}^2} \int_0^1 \left\{ \left[M + \frac{\bar{k}_{mn}}{K_{mn}} \right] R_{mn}^2 - \left[\frac{1}{K_{mn}} + \frac{1}{2} \right] \frac{R_{mn} \frac{dR_{mn}}{d\bar{r}} \frac{dM}{d\bar{r}}}{\gamma^2 K_{mn}^2} \right.$$

$$\left. + \frac{M}{2} \frac{\left(\frac{dR_{mn}}{d\bar{r}}\right)^2 \left(\frac{dM}{d\bar{r}}\right)^2}{\gamma^4 K_{mn}^4} \right\} 2\bar{r}d\bar{r} \qquad (4\text{-}23)$$

The expression $\mathcal{P}_a^P$ is actually the total energy flow in the direction of the duct axis. The contribution of $\mathcal{P}_b^P$ to the total energy flow is cancelled by the source term in the physical energy equation, as will be shown in Section 4.3.5. When $dM/d\bar{r}$ is set to zero in Eqns. (4-23), $\mathcal{P}_a^P$ reduces to the time-averaged energy flow derived by Eversman (1971). For convenience in later work, the acoustic energy flow will be expressed as

$$\mathcal{P}_a^P = \frac{\pi r_o^2}{\rho_o a_o} \sum_{m,n} \overline{p_{mn}^2}\, EWF_{mn}^P \qquad (4\text{-}24a)$$

where the physical energy weighting function is given by

$$EWF_{mn}^P = \int_0^1 \left\{ \left[M + \frac{\bar{k}_{mn}}{K_{mn}} \right] R_{mn}^2 - \left[\frac{1}{K_{mn}} + \frac{1}{2} \right] \frac{R_{mn} \frac{dR_{mn}}{d\bar{r}} \frac{dM}{d\bar{r}}}{\gamma^2 K_{mn}^2} + \frac{M}{2} \frac{\left(\frac{dR_{mn}}{d\bar{r}}\right)^2 \left(\frac{dM}{d\bar{r}}\right)^2}{\gamma^4 K_{mn}^4} \right\} 2\bar{r}d\bar{r} \qquad (4\text{-}24b)$$

This expression is called an energy weighting function because it relates the wall acoustic pressure level to acoustic energy flow in the direction of the pipe axis.

4.3.3 Evaluation of $\mathcal{P}_b^P$

The part of the integrated acoustic energy flux which is a function of $\bar{z}$ will now be examined. Collecting the terms in Eqn. (4-19) for which $n \neq c$ and noting that the summations over n and c both have the same upper bound, $\mathcal{P}_b^P$ can be manipulated to yield

$$
\begin{aligned}
\mathcal{P}_b^P = {} & \frac{\pi r_o^2}{\rho_o a_o}\sum_{m,n}\sum_{c<n} \frac{C_{mn}C_{mc}\cos(\phi_{mc}-\phi_{mn})}{2(1+\varepsilon_m)}\cos(\bar{k}_{mc}-\bar{k}_{mn})\,\bar{z}\int_0^1 \Bigg\{ M\Bigg[R_{mc}R_{mn} \\
& + \frac{\frac{dR_{mc}}{d\bar{r}}\frac{dR_{mn}}{d\bar{r}}}{\gamma^2 K_{mc}K_{mn}} + \frac{m^2 R_{mn}R_{mc}}{\gamma^2\bar{r}^2 K_{mn}K_{mc}} + \frac{\bar{k}_{mn}\bar{k}_{mc}R_{mn}R_{mc}}{K_{mn}K_{mc}} + \frac{\frac{dR_{mn}}{d\bar{r}}\frac{dR_{mc}}{d\bar{r}}\left(\frac{dM}{d\bar{r}}\right)^2}{\gamma^4 K_{mn}^2K_{mc}^2} \\
& - \frac{\bar{k}_{mn}R_{mn}\frac{dR_{mc}}{d\bar{r}}\frac{dM}{d\bar{r}}}{\gamma^2 K_{mn}K_{mc}^2} - \frac{\bar{k}_{mc}R_{mc}\frac{dR_{mn}}{d\bar{r}}\frac{dM}{d\bar{r}}}{\gamma^2 K_{mc}K_{mn}^2}\Bigg] + \left[\frac{\bar{k}_{mc}}{K_{mc}}+\frac{\bar{k}_{mn}}{K_{mn}}\right]R_{mc}R_{mn} \\
& - \frac{R_{mn}\frac{dR_{mc}}{d\bar{r}}\frac{dM}{d\bar{r}}}{\gamma^2K_{mc}^2} - \frac{R_{mc}\frac{dR_{mn}}{d\bar{r}}\frac{dM}{d\bar{r}}}{\gamma^2K_{mn}^2}\Bigg\}\,2\bar{r}\,d\bar{r}
\end{aligned}
\qquad (4\text{-}25)
$$

The part of the integrand multiplied by M can again be simplified by an integration by parts and utilization of the differential equation for the mode-shape functions R_{mn} and R_{mc}. The final result is

$$
\begin{aligned}
\mathcal{P}_b^P = {} & \frac{\pi r_o^2}{\rho_o a_o}\sum_{m,n}\sum_{c<n} \frac{C_{mn}C_{mc}\cos(\phi_{mc}-\phi_{mn})}{2(1+\varepsilon_m)}\cos(\bar{k}_{mc}-\bar{k}_{mn})\,\bar{z}\ \times \\
& \int_0^1 \Bigg\{\left[\frac{M}{2}\left(\frac{(K_{mc}+K_{mn})^2-(\bar{k}_{mc}-\bar{k}_{mn})^2}{K_{mn}K_{mc}}\right) + \frac{\bar{k}_{mc}}{K_{mc}} + \frac{\bar{k}_{mn}}{K_{mn}}\right]R_{mn}R_{mc} \\
& - \left[\frac{1-2\bar{k}_{mc}M+\bar{k}_{mc}\bar{k}_{mn}M^2}{2K_{mn}^2} + \frac{1}{K_{mn}}\right]\frac{R_{mn}\frac{dR_{mc}}{d\bar{r}}\frac{dM}{d\bar{r}}}{\gamma^2K_{mc}^2} - \left[\frac{1-2\bar{k}_{mn}M+\bar{k}_{mn}\bar{k}_{mc}M^2}{2K_{mc}^2}\right. \\
& \left. + \frac{1}{K_{mc}}\right]\frac{R_{mc}\frac{dR_{mn}}{d\bar{r}}\frac{dM}{d\bar{r}}}{\gamma^2K_{mn}^2} + \frac{M\frac{dR_{mn}}{d\bar{r}}\frac{dR_{mc}}{d\bar{r}}\left(\frac{dM}{d\bar{r}}\right)^2}{\gamma^4K_{mn}^2K_{mc}^2}\Bigg\}\,2\bar{r}\,d\bar{r}
\end{aligned}
\qquad (4\text{-}26)
$$

For the case of $M = \text{const}$ we have $\int_0^1 R_{mn}R_{mc}\,\bar{r}\,d\bar{r} = 0$, and thus $\mathcal{P}_b^P = 0$ for this condition. However, for arbitrary $M(\bar{r})$, $\mathcal{P}_b^P$ is not equal to zero.

4.3.4 Evaluation of $\int_{z_1}^{z_2}\int_s <-\rho_o u_r' u_z' \frac{dU_o}{dr}> ds\, dz$

The integral on the right-hand side of Eqn. (4-14) will now be evaluated. Again, considering only cuton modes (for which $\bar{k}_{mn}$ is real), we have, using Eqns. (4-17),

$$< u_r' u_z' > = \frac{1}{2}\sum_{m,n}\sum_{b,c} \mathrm{Re}\left\{ \frac{i\,\frac{\partial P_{mn}}{\partial r}\, e^{i(k_{z_{bc}}-k_{z_{mn}})z}}{\rho_o(\omega - k_{z_{mn}} U_o)} \left[\frac{k_{z_{bc}} P_{bc}}{\rho_o(\omega - k_{z_{bc}} U_o)} - \frac{\frac{\partial P_{bc}}{\partial r}\frac{dU_o}{dr}}{\rho_o(\omega - k_{z_{bc}} U_o)^2} \right] \right\} \tag{4-27}$$

Applying Eqn. (4-18) and integrating over the duct cross section, we obtain

$$\int_s < u_r' u_z' > \left(-\rho_o \frac{dU_o}{dr}\right) ds = \frac{\pi r_o^2}{\rho_o a_o} \sum_{m,n}\sum_{c\neq n} \frac{C_{mn}C_{mc}\cos(\phi_{mc}-\phi_{mn})}{2(1+\varepsilon_m)} \times$$

$$\int_0^1 \left\{ \frac{\bar{k}_{mc}R_{mc}\frac{dR_{mn}}{d\bar{r}}\frac{dM}{d\bar{r}}}{r_o\gamma K_{mc}K_{mn}} - \frac{\frac{dR_{mn}}{d\bar{r}}\frac{dR_{mc}}{d\bar{r}}\left(\frac{dM}{d\bar{r}}\right)^2}{r_o\gamma^3 K_{mn}K_{mc}^2} \right\} 2\bar{r}d\bar{r}\, \sin(\bar{k}_{mc}-\bar{k}_{mn})\,\bar{z} \tag{4-28}$$

Note that the terms for which $n = c$ have disappeared in the time average. Integrating over $\bar{z}$ and noting that the summations over n and c have the same upper bound, we can combine terms to obtain

$$\int_{\bar{z}_1}^{\bar{z}_2}\int_s < u_r' u_z' > \left(-\rho_o\frac{dU_o}{dr}\right) ds\, \frac{a_o}{\omega}\, d\bar{z} = \frac{\pi r_o^2}{\rho_o a_o}\sum_{m,n}\sum_{c<n} - \frac{C_{mn}C_{mc}\cos(\phi_{mc}-\phi_{mn})}{2(1+\varepsilon_m)} \times$$

$$\cos(\bar{k}_{mc}-\bar{k}_{mn})\bar{z}\Big|_{\bar{z}_1}^{\bar{z}_2} \times \int_0^1 \left\{ \frac{\bar{k}_{mc}R_{mc}\frac{dR_{mn}}{d\bar{r}}\frac{dM}{d\bar{r}}}{(\bar{k}_{mc}-\bar{k}_{mn})\gamma^2 K_{mc}K_{mn}} + \frac{\bar{k}_{mn}R_{mn}\frac{dR_{mc}}{d\bar{r}}\frac{dM}{d\bar{r}}}{(\bar{k}_{mn}-\bar{k}_{mc})\gamma^2 K_{mn}K_{mc}} \right.$$

$$\left. - \frac{\frac{dR_{mn}}{d\bar{r}}\frac{dR_{mc}}{d\bar{r}}\left(\frac{dM}{d\bar{r}}\right)^2}{(\bar{k}_{mc}-\bar{k}_{mn})\gamma^4 K_{mn}K_{mc}^2} - \frac{\frac{dR_{mc}}{d\bar{r}}\frac{dR_{mn}}{d\bar{r}}\left(\frac{dM}{d\bar{r}}\right)^2}{(\bar{k}_{mn}-\bar{k}_{mc})\gamma^4 K_{mc}K_{mn}^2} \right\} 2\bar{r}d\bar{r} \tag{4-29}$$

4.3.5 Substitution into the Integrated Form of the Time-Averaged Physical Energy Equation

The expressions evaluated in the previous subsections will now be substituted into the integrated form of the physical energy equation (4-14). Noting that $\mathbb{P}_a^P$ is independent of $\bar{z}$, Eqn. (4-14) reduces to

$$\mathbb{P}_b \Big|_{\bar{z}_1}^{\bar{z}_2} = -\int_{\bar{z}_1}^{\bar{z}_2} \int_{s} \left(-\rho_o \frac{dU_o}{dr}\right) < u_r' u_z' > ds \frac{a_o}{\omega} dz$$

Using Eqns. (4-26) and (4-29), we obtain

$$0 = \frac{\pi r_o^2}{\rho_o a_o} \sum_{m,n} \sum_{c<n} \frac{C_{mn} C_{mc} \cos(\phi_{mc} - \phi_{mn})}{2(1+\varepsilon_m)} \cos(\bar{k}_{mc} - \bar{k}_{mn})\, \bar{z} \Big|_{\bar{z}_1}^{\bar{z}_2} \times$$

$$\int_0^1 \left\{ \left[\frac{M}{2} \left(\frac{(K_{mc} + K_{mn})^2 - (\bar{k}_{mc} - \bar{k}_{mn})^2}{K_{mc} K_{mn}} \right) + \frac{\bar{k}_{mc}}{K_{mc}} + \frac{\bar{k}_{mn}}{K_{mn}} \right] R_{mn} R_{mc} \right.$$

$$+ \left[\frac{\bar{k}_{mc}}{(\bar{k}_{mn} - \bar{k}_{mc})} - \frac{(1 - 2\bar{k}_{mc} M + \bar{k}_{mc} \bar{k}_{mn} M^2)}{2K_{mn}^2} \right] \frac{R_{mn} \frac{dR_{mc}}{d\bar{r}} \frac{dM}{d\bar{r}}}{\gamma^2 K_{mc}^2} + \left[\frac{\bar{k}_{mn}}{(\bar{k}_{mc} - \bar{k}_{mn})} \right.$$

$$\left. - \frac{(1 - 2\bar{k}_{mn} M + \bar{k}_{mn} \bar{k}_{mc} M^2)}{2K_{mc}^2} \right] \left. \frac{R_{mc} \frac{dR_{mn}}{d\bar{r}} \frac{dM}{d\bar{r}}}{\gamma^2 K_{mn}^2} \right\} 2\bar{r} d\bar{r} \qquad (4\text{-}30)$$

Now, in general, the terms in Eqn. (4-30) are not linearly dependent and thus each term must vanish independently. Therefore, the integral in Eqn. (4-30) must vanish for any set of propagating modes R_{mn} and R_{mc}, provided $c \neq n$. Thus the source term $< -\rho_o u_r' u_z' \frac{dU_o}{dr} >$ cancels with the cross-mode flux $\mathbb{P}_b^P$, and in so doing presents an orthogonality property for the eigenfunctions R_{mn} and R_{mc}. Although the orthogonality relationship is by no means simple and involves the eigenvalues $\bar{k}_{mn}$ and $\bar{k}_{mc}$ as well as derivatives of the eigenfunctions R_{mn} and R_{mc}, it could be of use in further developing the mathematical properties of the eigenvalue equation (2-3).

Thus the application of the physical energy equation to the case of acoustic propagation inside a circular duct has shown that a time-averaged energy flux of the type presented by Eversman, Ryshov and Shefter and by Guiraud, i.e., $\overline{J}_s^P = < p'\overline{v}' > + < \xi_s > \overline{V}_o$, can be extended to the case of a duct containing a sheared mean flow. The total acoustic energy flow down the duct, $\mathcal{P}_a^P$, is the sum of the integrated flux $\overline{J}_s^P$ for each mode considered separately. Furthermore, the source term in the physical energy equation is zero when each mode is considered separately, and is only nonzero for cross-mode terms, in which case it cancels with $\mathcal{P}_b^P$, giving the physically satisfying result that the cross-mode terms do not enter into the energy flow expression.

4.4. Acoustic Energy Flow Expressions Based on the Conservation Equations of Blockhintsev and Möhring

In this section acoustic energy flow expressions based on the work of Blockhintsev and Möhring will be derived for the case of an axisymmetric, sheared mean flow in a circular pipe.

The Blockhintsev type energy flux is given by Eqn. (4-5). Specializing this expression to the case under consideration, the axial acoustic energy flux can be written as

$$< J_{s_z}^B > = < p'u_z' > (1+M^2) + M\left(\rho_o a_o < u_z'^2 > + \frac{< p'^2 >}{\rho_o a_o}\right) \quad (4\text{-}31)$$

Integrating this energy flux across the duct cross section in the same manner as in the previous section*, we obtain

$$\int_s < J_{s_z}^B > ds = \frac{\pi r_o^2}{\rho_o a_o} \sum_{m,n} \sum_c \frac{C_{mn} C_{mc} \cos(\phi_{mc} - \phi_{mn})}{2(1+\varepsilon_m)} \int_0^1 \Bigg\{ R_{mn} \left[\frac{\overline{k}_{mc} R_{mc}}{K_{mc}} - \frac{\frac{dR_{mc}}{d\overline{r}} \frac{dM}{d\overline{r}}}{\gamma^2 K_{mc}^2} \right] (1+M^2) + M \left(\frac{\overline{k}_{mn} R_{mn}}{K_{mn}} - \frac{\frac{dR_{mn}}{d\overline{r}} \frac{dM}{d\overline{r}}}{\gamma^2 K_{mn}^2} \right) \left(\frac{\overline{k}_{mc} R_{mc}}{K_{mc}} - \frac{\frac{dR_{mc}}{d\overline{r}} \frac{dM}{d\overline{r}}}{\gamma^2 K_{mc}^2} \right)$$

$$+ M R_{mn} R_{mc} \Bigg\} 2\overline{r} d\overline{r} \cos(\overline{k}_{mc} - \overline{k}_{mn}) \overline{z} \quad (4\text{-}32)$$

*Details are given in Appendix A9.

Again, the integrated power flow can be separated into two parts, $\mathcal{P}_a^B$ and $\mathcal{P}_b^B$, where $\mathcal{P}_a^B$ is independent of $\bar{z}$ and $\mathcal{P}_b^B$ has a cosine dependence on $\bar{z}$. The results are

$$\mathcal{P}_a^B = \frac{\pi r_o^2}{\rho_o a_o} \sum_{m,n} \overline{P_{mn}^2} \int_0^1 \left\{ \left[\frac{M}{K_{mn}} + \frac{\bar{k}_{mn}}{K_{mn}^2} \right] R_{mn}^2 \right. \tag{4-33a}$$

$$\left. - \left[1 + M^2\left(K_{mn}^2 - \bar{k}_{mn}^2\right)\right] \frac{R_{mn} \dfrac{dR_{mn}}{d\bar{r}} \dfrac{dM}{d\bar{r}}}{\gamma^2 K_{mn}^4} + \frac{\left(\dfrac{dR_{mn}}{d\bar{r}}\right)^2 \left(\dfrac{dM}{d\bar{r}}\right)^2 M}{\gamma^4 K_{mn}^4} \right\} 2\bar{r}d\bar{r}$$

and

$$\mathcal{P}_b^B = \frac{\pi r_o^2}{\rho_o a_o} \sum_{m,n} \sum_{c<n} \frac{C_{mn} C_{mc} \cos(\phi_{mc} - \phi_{mn})}{2(1+\varepsilon_m)} \int_0^1 \left\{ \left(\frac{2M + (\bar{k}_{mn} + \bar{k}_{mc})(1-M^2)}{K_{mc} K_{mn}} \right) R_{mn} R_{mc} \right.$$

$$- \frac{\dfrac{dM}{d\bar{r}}}{\gamma^2 K_{mc}^2 K_{mn}^2} \left[R_{mc} \frac{dR_{mn}}{d\bar{r}} \left(1 + M^2\left(K_{mc}^2 - \bar{k}_{mc}^2\right)\right) + R_{mn} \frac{dR_{mc}}{d\bar{r}} \left(1 + M^2\left(K_{mn}^2 - \bar{k}_{mn}^2\right)\right) \right]$$

$$\left. + 2 \frac{\dfrac{dR_{mc}}{d\bar{r}} \dfrac{dR_{mn}}{d\bar{r}} \left(\dfrac{dM}{d\bar{r}}\right)^2 M}{\gamma^4 K_{mc}^2 K_{mn}^2} \right\} 2\bar{r}d\bar{r} \cos(\bar{k}_{mc} - \bar{k}_{mn})\ \bar{z} \tag{4-33b}$$

The equivalent energy flow expressions based on the work of Möhring will now be derived. In his 1971 paper, Möhring presents an acoustic energy flux, derived from his conservation principle, for the case of a two-dimensional duct containing a sheared mean flow. The acoustic energy flow can be divided into two parts. The first part, $\mathcal{P}_a^M$, is the sum of the energy flows for each mode interacting only with itself. This part of the acoustic energy flow is independent of the axial coordinate, $\bar{z}$. The second part of the acoustic energy flow, $\mathcal{P}_b^M$, contains the cross-mode terms and has a cosine dependence on $\bar{z}$. When the results of Möhring's analysis are rederived for the case of a circular duct, the following expressions are obtained.

$$\mathcal{P}_a^M = \frac{\pi r_o^2}{\rho_o a_o} \sum_{m,n} \overline{P_{mn}^2} \int_0^1 \left\{ \left[\frac{M}{K_{mn}} + \frac{\bar{k}_{mn}}{K_{mn}^2} \right] R_{mn}^2 - \frac{R_{mn} \dfrac{dR_{mn}}{d\bar{r}} \dfrac{dM}{d\bar{r}}}{\gamma^2 K_{mn}^4} \right\} 2\bar{r}d\bar{r} \tag{4-34a}$$

and

$$\mathscr{P}_b^M = \frac{\pi r_o^2}{\rho_o a_o} \sum_{m,n} \sum_{c<n} \frac{C_{mn} C_{mc} \cos(\phi_{mc} - \phi_{mn})}{2(1+\varepsilon_m)} \int_0^1 \left\{ \left[\frac{2M + (\bar{k}_{mn} + \bar{k}_{mc})(1-M^2)}{K_{mc} K_{mn}} \right] R_{mn} R_{mc} \right.$$

$$\left. - \frac{\left(R_{mn} \dfrac{dR_{mc}}{d\bar{r}} + R_{mc} \dfrac{dR_{mn}}{d\bar{r}} \right)}{\gamma^2 K_{mc}^2 K_{mn}^2} \right\} 2\bar{r} d\bar{r} \cos(\bar{k}_{mc} - \bar{k}_{mn}) \bar{z} \qquad (4\text{-}34b)$$

Comparing Eqns. (4-33a) and (4-34a), and (4-33b) and (4-34b), it is seen that the terms not involving derivatives of the mean flow profile are the same for the Blockhintsev and Möhring fluxes. Thus these expressions reduce to the same limit for a uniform flow. Furthermore, the coefficient of the terms linear in $dM/d\bar{r}$ in the Blockhintsev acoustic energy flow is proportional to $\frac{1}{\gamma^2}\left(1 + M^2\left(K_{mn}^2 - \bar{k}_{mn}^2\right)\right)$, whereas the proportionality constant of Möhring is simply $1/\gamma^2$. Thus these terms also agree closely for low-speed mean flow $(M << 1)$. For sufficiently high reduced frequency, γ, the terms linear in $dM/d\bar{r}$ are negligible. The Blockhintsev energy flow expressions also contain a term quadratic in the derivative of the mean flow profile, with a coefficient proportional to M/γ^4. Thus these terms are also negligible for high values of γ, and the Blockhintsev expressions reduce to the results of Möhring for sufficiently high frequency and low mean shear.

The total acoustic energy flow defined by Möhring, $\mathscr{P}_a^M + \mathscr{P}_b^M$, must be conserved for acoustic propagation inside a hard-walled duct. $\mathscr{P}_a^M$ is independent of $\bar{z}$. However, $\mathscr{P}_b^M$ is a sum of terms each of which has a cosine dependence on $\bar{z}$. Thus, for the total energy flow to be constant at all $\bar{z}$, we require $\mathscr{P}_b^M = 0$. For this to be true in general, the integral in Eqn. (4-34b) must equal zero. This is an orthogonality condition for the eigenfunctions R_{mn} and R_{mc}. Although it is considerably simpler than the orthogonality condition derived from the physical energy equation, the expression still contains the eigenvalues and derivatives of the eigenfunctions.

The total acoustic energy flow calculated from the Blockhintsev flux expression is conserved in the geometric acoustics limit, i.e., for sufficiently high frequency and low mean shear, and agrees with the Möhring energy flux in this limit. However, the extent to which the Blockhintsev flux reduces to the Möhring flux, i.e., the extent to which the geometric acoustics limit is valid, also depends on the behavior of the eigenfunctions. In order to quantitatively assess the conditions under which the Blockhintsev energy flux is a conserved quantity, the values of the integrals containing

$$\frac{M^2}{\gamma^2}\frac{dM}{d\bar{r}} \quad \text{and} \quad \frac{M}{\gamma^4}\left(\frac{dM}{d\bar{r}}\right)^2$$

must be compared to the values of the other integrals in the Blockhintsev flux. Since analytical solutions for R_{mn} are not available for general $M(\bar{r})$, this comparison must be done using numerical techniques.

Following the approach used for the physical energy flux, the Möhring and Blockhintsev energy flow expressions can be written as

$$\mathbb{P}_a^{\binom{M}{B}} = \frac{\pi r_o^2}{\rho_o a_o} \sum_{m,n} \overline{P_{mn}^2}\; EWF_{m,n}^{\binom{M}{B}} \tag{4-35a}$$

where the Möhring and Blockhintsev energy weighting functions are given by

$$EWF_{m,n}^{M} = \int_0^1 \left\{ \left[\frac{M}{K_{mn}} + \frac{\bar{k}_{mn}}{K_{mn}^2}\right] R_{mn}^2 - \frac{R_{mn}\dfrac{dR_{mn}}{d\bar{r}}\dfrac{dM}{d\bar{r}}}{\gamma^2 K_{mn}^4} \right\} 2\bar{r}d\bar{r} \tag{4-35b}$$

$$\begin{aligned} EWF_{m,n}^{B} = \int_0^1 \Bigg\{ & \left[\frac{M}{K_{mn}} + \frac{\bar{k}_{mn}}{K_{mn}^2}\right] R_{mn}^2 - \left[1 + M^2\left(K_{mn}^2 - \bar{k}_{mn}^2\right)\right] \frac{R_{mn}\dfrac{dR_{mn}}{d\bar{r}}\dfrac{dM}{d\bar{r}}}{\gamma^2 K_{mn}^4} \\ & + \frac{\left(\dfrac{dR_{mn}}{d\bar{r}}\right)^2 \left(\dfrac{dM}{d\bar{r}}\right)^2 M}{\gamma^4 K_{mn}^4} \Bigg\} 2\bar{r}d\bar{r} \end{aligned} \tag{4-35c}$$

In the next section, the Möhring and Blockhintsev energy weighting functions are numerically evaluated to determine the frequency and flow-rate range over which they give essentially the same results. This defines the validity of the geometric acoustics limit.

4.5 Numerical Results

This section presents numerical results for the energy weighting functions developed in the previous sections. The objectives of the numerical study were (i) to gain quantitative information on the flowrate and frequency range over which the Blockhintsev and Möhring energy flow expressions give essentially the same result, and (ii) to examine the accuracy with which the energy flow can be approximated by the use of a uniform mean flow (slug flow*) assumption. The calculations are considerably simplified by this assumption, since the energy weighting functions are given by analytical expressions for the slug flow case. To facilitate comparisons, the energy weighting functions for the (0,0), (1,0), (2,0), and (0,1) modes were calculated for the case of a one-seventh power mean flow profile $\left(M(\bar{r}) = M_{max}(1-\bar{r})^{1/7}\right)$, representative of turbulent pipe flow. The frequency range from mode cuton to $\gamma = 20$ and mean flows with centerline Mach numbers up to 0.9 were covered in the calculations.

4.5.1 Numerical Technique

In order to evaluate the energy weighting functions, the radial mode shape function, R_{mn}, and the axial wavenumber, $\bar{k}_{mn}$, must be determined. The differential equation for the mode shape function, Eqn. (2-3), is

$$\frac{d}{d\bar{r}}\left[\frac{\bar{r}}{(1-\bar{k}M)^2}\frac{dR}{d\bar{r}}\right] + \left[\left(\gamma^2\bar{r} - \frac{m^2}{\bar{r}(1-\bar{k}M)^2}\right) - \bar{k}^2\frac{\gamma^2\bar{r}}{(1-\bar{k}M)^2}\right]R = 0$$

with the hard-wall boundary condition $dR/d\bar{r} = 0$ at $\bar{r} = 1$. Eqn. (2-3) is an eigenvalue equation which, for given values of γ, m and $M(\bar{r})$, has solutions only for particular values of $\bar{k}$. The eigenvalue $\bar{k}$ appears in the parameter $(1-\bar{k}M)$ as well as in the standard position for a Sturm Liouville type equation. The eigenvalues and eigenfunctions are real for propagating modes, for the case of a hard-walled duct.

The differential equation was solved by an iterative technique. An initial estimate for the eigenvalue, $\bar{k}_{est}$, was substituted into the

*The slug flow approximation is a constant Mach number profile ($M(\bar{r})$ = constant) which has the same flowrate, when integrated across the duct cross-sectional area, as that obtained for the 1/7th power mean flow profile.

$(1-\bar{k}M)$ terms. We then have a Sturm Liouville type system. The equation was finite-differenced in self-adjoint form (see Dahlquist and Bjorck, 1974), using an evenly spaced mesh and a second-order accurate numerical scheme. Normally, 512 mesh points were used across the duct radius ($\bar{r}$ = 0 to 1). The Choleski decomposition (see Hornbeck, 1975) was then applied to the system, resulting in a matrix equation of the form $(\underset{\sim}{A} - \bar{k}^2 \underset{\sim}{I})\, \bar{X} = 0$. The eigenvalue of this system nearest to $\bar{k}^2_{est}$ was then found, and the system iterated to convergence. Normally only two or three iterations were necessary for a reasonably good first estimate of the eigenvalue.

After the mode shape function R_{mn} and axial wavenumber $\bar{k}_{mn}$ were determined, the energy weighting functions derived from the physical energy equation (4-24b) and the Möhring and Blockhintsev energy flow expressions (Eqns. (4-35b) and (4-35c)) were calculated. Each term in the energy weighting function was integrated separately, to allow a comparison of the relative importance of the different terms. A Romberg (see Hornbeck, 1975) integration scheme was used for evaluation of the integrals. Details of the numerical analysis are given in Appendix A10, where the computer program, MODE, and a sample of the output are listed.

4.5.2 Comparison of Blockhintsev and Möhring Energy Weighting Functions

The results of the numerical calculation showed a remarkable agreement between the values of the Blockhintsev and Möhring energy weighting functions. Representative values of the differences between EWF^B and EWF^M are given in Table 1. For the (0,0) mode, the differences were always less than 0.03% for the full frequency and Mach number range covered. For the higher modes, the differences between the Möhring and Blockhintsev energy weighting functions were greatest at values of γ close to cutoff. The largest differences observed in all the cases for which calculations were made was 5% for the (1,0) mode at $\gamma = 2$, $M_{max} = 0.9$, $\bar{k}_{10} = 0.096$. For the same value of γ with $M_{max} = 0.5$, this difference was reduced to 1%. The largest difference observed for the (2,0) mode was 3% at $\gamma = 3.5$, $M_{max} = 0.9$, $\bar{k}_{20} = 0.155$. In general, the (1,0) and (2,0) modes showed similar behavior for the differences between the values of the Blockhintsev and Möhring energy weighting functions. For both of these modes, at values of γ greater than twice the zero mean flow cutoff frequency, the difference was less than 1% for the $M_{max} = 0.9$ case and less than 0.1% for the $M = 0.5$ case. For the highest values of γ the differences approached those found for the (0,0) mode.

The differences between the values of the Blockhintsev and Möhring energy weighting functions were much less significant for the (0,1) mode than for the other higher modes. The largest difference for all the (0,1) mode calculations was 0.7% at $\gamma = 4$, $M_{max} = 0.9$, $\bar{k}_{01} = 0.0513$. The differences between the two energy weighting functions were also correspondingly smaller for larger values of γ.

The higher modes displayed the type of behavior expected for the comparison between the Möhring and Blockhintsev energy weighting functions, i.e., good agreement at high frequencies and poorer agreement closer to cutoff. The closer agreement near cutoff for the (0,1) mode than for the (1,0) and (2,0) modes is due to the fact that $R_{01}(\bar{r})$ changes sign across the duct radius, while R_{10} and R_{20} do not. The dominant term of the two additional terms in the Blockhintsev energy weighting function is the one containing

$$M^2 R_{mn} \frac{dR_{mn}}{d\bar{r}} \frac{dM}{d\bar{r}}$$

for the higher modes with a one-seventh power mean flow profile. At values of γ near cutoff,

$$M^2 \frac{dR_{mn}}{d\bar{r}} \frac{dM}{d\bar{r}}$$

is always positive across the duct radius, for these three modes. Thus the contributions to this integral for R_{01} positive and R_{01} negative nearly cancel, giving much better agreement between the Möhring and Blockhintsev energy weighting functions for the (0,1) mode than for the (1,0) and (2,0) modes.

A more surprising result is that the (0,0) mode Blockhintsev and Möhring energy weighting functions agree almost uniformly for low as well as high frequency. This can be explained by noting that both additional terms in the Blockhintsev energy weighting function involve

$$\frac{1}{\gamma^2} \frac{dR_{mn}}{d\bar{r}} \frac{dM}{d\bar{r}}$$

These terms are insignificant for large values of γ, as expected. Examining these terms for lower values of γ, we find that as γ decreases, $dR_{00}/d\bar{r}$ also decreases. Since mode shape changes due to mean shear are mainly a high frequency effect, $R_{00}(\bar{r})$ approaches its uniform mean flow shape (a constant) for low values of γ. Thus these two effects cancel, and the additional terms in the Blockhintsev energy weighting function are unimportant in the (0,0) mode case for the full range of parameters studied.

4.5.3 General Characteristics of the Möhring Energy Weighting Functions and Comparison to Slug Flow Approximations

The calculated values of the Möhring energy weighting function, for the case of a 1/7 power mean flow profile, are shown in Figs. 26a, b, c, and d. The values obtained using the slug flow approximation are also shown. In order to compare the effect of different profile shapes, the energy weighting functions were also calculated for a laminar flow profile $\left(M(\bar{r}) = M_{max}(1 - \bar{r}^2)\right)$, with M_{max} chosen to produce the same flowrate as that obtained for the $M_{max} = 0.1$ 1/7th power profile case.

Although only the Möhring energy weighting functions will be discussed in detail in this subsection, the physical energy weighting functions display similar characteristics. The values of the Mohring and physical energy weighting functions are compared in Subsection 4.5.4. Detailed results are presented in tabular form in Appendix A11.

Referring to Fig. 26a it is seen that, at low values of γ, the (0,0) mode energy weighting functions are slightly higher than those obtained with the slug flow approximation. This difference increases as mean flow Mach number increases. The values of the (0,0) mode energy weighting function fall off rapidly with increasing γ, due to mean flow refraction effects which decrease the acoustic pressure in the central region of the pipe. These refractive effects increase with increase of frequency, for a given mean flow profile. The energy weighting functions fall off more rapidly, with increasing frequency, for higher mean flow Mach numbers. The effect of the mean shear is quite substantial. Even in the $M_{max} = 0.1$ case, the 1/7th power profile reduces the energy weighting function by approximately 50% at $\gamma = 20$. A comparison of the laminar flow profile results to the 1/7th power profile, $M_{max} = 0.1$, case shows that the laminar flow profile shape produces an even greater change from the uniform flow results than that produced by the 1/7th power profile.

The Möhring energy weighting functions for the (1,0) and (2,0) modes are shown in Figs. 23b and -c. The behavior of the energy weighting functions for the (1,0) and (2,0) modes is very similar to that for the (0,0) mode. The agreement with the uniform mean flow assumption is very good at values of γ near cutoff, but the actual energy weighting functions fall far below the uniform flow approximations as γ increases. Again, the laminar flow profile shows a stronger effect than the equivalent 1/7th power profile.

The calculated values of the Möhring energy weighting function for the (0,1) mode agree well with the uniform flow approximations near cutoff, but lie substantially above these curves for higher values of γ, in contrast to the behavior of the other three modes. The reason for this is that the mode shape function R_{01} attains its highest values (approximately 2.5) in the central region of the pipe, where the mean flow Mach number is also the highest. The mode shape function R_{01} is affected little by the mean shear, at high frequencies, compared to the other three modes. Thus, as $\bar{k}_{01}$ increases, for frequencies higher above cutoff, the integral of $\left(R_{01}/(1-\bar{k}_{01}M)\right)^2$ becomes much larger than the equivalent integral for the slug flow approximation. The convected energy term, i.e., the integral of $MR_{01}^2/(1-\bar{k}_{01}M)$, also displays this same effect.

In order to check if refractive effects eventually reduced the extremely high values obtained for the (0,1) mode energy weighting functions, the calculations for the $M_{max} = 0.5$ case were extended up to a value of $\gamma = 40$ (see inset, Fig. 25d). It was found that the energy weighting function reached a peak at around $\gamma = 20$, and decreased for higher γ. For the laminar flow case, the (0,1) mode energy weighting function reached a maximum at approximately $\gamma = 15$. The laminar flow profile in general produces stronger refractive effects than the one-seventh power profile.

4.5.4 Comparison of the Möhring and Physical Energy Weighting Functions

Representative values of the Möhring and physical energy weighting functions are compared in Table 2. In all cases shown, the Möhring energy weighting function is larger than the physical energy weighting function. The differences are greater for higher Mach numbers, and for a given Mach number the differences are smallest for the higher modes near cutoff. For the higher modes, as γ increases, the differences (on a per-cent basis) approach those found for the (0,0) mode.

The behavior described above can be explained by noting that the dominant terms in the Möhring energy weighting function are the same as those in the physical energy weighting function, but multiplied by $1/(1-\bar{k}M)$. The axial wavenumber, $\bar{k}$, was positive for all cases shown in Table 2. Thus the factor $1/(1-\bar{k}M)$ is always greater than 1, and is larger for higher values of the Mach number. In the higher mode cases shown in Table 2, $\bar{k}$ is small for values of γ near cutoff and increases with increasing γ, approaching the values of $\bar{k}$ found for the (0,0) mode at high γ. Thus the behavior of the factor $1/(1-\bar{k}M)$ explains why, for the higher modes, the differences between the Möhring and physical energy weighting functions are small for values of γ near cutoff, and on a per-cent basis approach those found for the (0,0) mode at high γ.

The large differences between the physical and Möhring energy weighting functions raise the question of which flux expression is the appropriate definition of acoustic energy flow. The utility of a particular definition depends on the application in mind. For example, suppose we are interested in the total acoustic energy propagating out of a duct inlet, as shown in Fig. 25. If the mean velocity is negligible at distances far from the duct inlet, the Blockhintsev flux reduces to the actual acoustic energy $\langle p'\bar{v}' \rangle$ crossing surface S_2. Then, at least in the high frequency limit, a measurement of the Möhring/Blockhintsev energy flux crossing surface S_1 inside the duct can be substituted for the measurement at S_2. If the physical energy flux definition were used in this case, the source term in the physical energy equation would have to be evaluated over the region which lies between S_1 and S_2, and a simple measurement across S_1 would not suffice to determine the acoustic energy crossing surface S_2. Thus the Blockhintsev approach is clearly more useful in this case. However, although the Blockhintsev flux is more useful in the above example, we believe that the physically appropriate time-averaged acoustic energy crossing surface S_1 is not the Möhring/Blockhintsev flux, but rather the physical energy flux. If this viewpoint is accepted, the conclusion must be drawn that acoustic energy is not conserved in a general nonuniformly moving medium. Since even the Blockhintsev flux is not conserved except for the high frequency limit (geometric acoustics), this viewpoint seems appropriate. The analysis of Section 4.3 then leads to the conclusion that not only is the Möhring flux conserved for acoustic propagation in a constant area duct containing a parallel sheared mean flow, but the physical energy flux is also conserved. This is discussed in detail in Subsection 4.3.2.

4.5.5 Importance of the Terms Containing $dM/d\bar{r}$ in the Möhring and Physical Energy Weighting Functions

The Möhring, Blockhintsev and physical energy weighting functions (Eqns. (4-35b, -35c, and -24b)) would be simplified substantially if the terms involving derivatives of the mean flow were neglected. This section examines the accuracy of such an assumption.

The percentage contributions of the terms containing $dM/d\bar{r}$ to the physical and Mohring energy weighting functions are shown in Table 3. For the (0,0) mode, these terms never contribute more than 2% to the Möhring energy weighting function and 3% to the physical energy weighting function, even for Mach numbers up to 0.9. In the $M_{max} = 0.5$ case, the shear terms never contributed more than 1% to the (0,0) mode energy weighting functions. The contributions of the mean shear were approximately ten times as large for the laminar flow profile case as for the equivalent flowrate 1/7th power profile case.

For the higher modes, the contributions of the terms involving $dM/d\bar{r}$ were most important near cutoff. The importance of these terms gradually decreased with increasing frequency, approaching the percentage level contributions found for the (0,0) mode at high frequencies. In all the cases for which calculations were made, the highest percentage contributions were for the (1,0) mode at $\gamma = 2$, $M_{max} = 0.9$. The terms involving $dM/d\bar{r}$ contributed 10% to the Möhring energy weighting function and

14% to the physical energy weighting function in this case. The contributions to the (0,1) mode were much smaller than to the (1,0) and (2,0) modes, which is explained by the fact the R_{01} changes sign across the duct radius, while R_{10} and R_{20} do not. Thus the $dM/d\bar{r}$ term cancels to a certain extent when the (0,1) mode integral is evaluated. This does not happen for the (1,0) and (2,0) modes.

Compared to the large effect that the introduction of mean shear has on the energy weighting functions, as displayed in Fig. 26, the contributions of the terms which contain $dM/d\bar{r}$ explicitly are relatively small. The addition of mean shear changes the value of the energy weighting functions principally through changes in the mode shape function. Thus the physical energy weighting function and the Möhring and Blockhintsev energy weighting functions can be approximated by

$$EWF^{P}_{m,n} = \int_0^1 \left[M + \frac{\bar{k}_{mn}}{(1 - \bar{k}_{mn} M)} \right] R^2_{mn} \; 2\bar{r}d\bar{r} \qquad (4\text{-}36a)$$

and

$$EWF^{M}_{m,n} = EWF^{B}_{m,n} = \int_0^1 \left[\frac{M}{(1 - \bar{k}_{mn} M)} + \frac{\bar{k}_{mn}}{(1 - \bar{k}_{mn} M)^2} \right] R^2_{mn} \; 2\bar{r}d\bar{r} \qquad (4\text{-}36b)$$

with little error, except very near the mode cutoff frequency.

4.5.6 Orthogonality of the Mode Shape Function

In order to numerically check the orthogonality expressions derived from the physical energy equation and Möhring's conservation equation (the integrals in Eqns. (4-30) and (4-35b)), these integrals were evaluated numerically* for two typical cases. In addition, the Blockhintsev cross-mode energy weighting function (i.e., the integral in Eqn. (4-33b)) was also evaluated. This cross-mode energy weighting function should approach zero in the geometric acoustics limit.

The first case considered was that of the (0,0) and (0,1) modes, for a laminar flow profile with $M_{max} = 0.3$ and $\gamma = 5$. The calculated values of the integrals in the physical energy equation and Möhring orthogonality relationships were less than 4×10^{-6}, which is smaller than the uncertainty associated with the numerical integration. The Blockhintsev cross-mode flux was only slightly larger than the integrated value of the Möhring orthogonality relationship.

*Details are given in Appendix A10.

The same functions were also evaluated for a one-seventh power profile with $M_{max} = 0.5$ and $\gamma = 5$. The values of the orthogonality relationships were again within the uncertainty of the numerical integration. The Blockhintsev cross-mode energy weighting function was also negligible in this case.

Thus the numerical results verified the orthogonality properties derived earlier in this chapter, and also showed that the Blockhintsev cross-mode flux was approximately zero for these typical cases.

4.6 Summary

Two types of acoustic energy flow relationships have been examined for the case of acoustic propagation inside a circular duct containing a sheared mean flow. The first type of acoustic energy flow expression is derived from the thermodynamic energy equation, while the second type is derived from conservation equations presented by Blockhintsev and Möhring.

In the case of a nonuniformly moving medium, the acoustic energy equation derived from the thermodynamic energy equation in general contains source terms. For this reason, applications of the acoustic energy flow derived from the thermodynamic energy equation to propagation inside ducts have been criticized as being applicable only to flows with very small shear. In the present research, this type of energy flow expression has been found to be generally applicable to acoustic propagation inside a constant area duct containing a nonuniform mean flow, with no restriction to the case of small shear. The source term in the acoustic energy equation combines with the cross-mode flux term to present an orthogonality relationship for the radial mode shape functions R_{mn} and R_{mc}. The acoustic energy flow developed from the thermodynamic energy equation is called the physical energy flow, because of its interpretation as the sum of the flow work of the acoustic wave and the acoustic energy density convected by the mean flow, i.e., $< p'\overline{v}' > + < \xi_s > \overline{V}_o$.

The energy flow expressions derived from the work of Blockhintsev and Möhring satisfy conservation equations, i.e., energy equations with no source terms, but these energy flow expressions are not necessarily the thermodynamic energy associated with the acoustic wave. The energy flux defined by Blockhintsev is a conserved quantity only in the geometric acoustics limit, where the wavelength is short compared to the distance over which substantial changes in the mean flow occur. Möhring's energy flow is a conserved quantity for the case of a constant area duct containing a parallel shear flow, and reduces to the Blockhintsev result for sufficiently high frequency. Since the Möhring energy flux is not defined in general outside of the duct, the usefulness of his result is somewhat limited. However, a comparison of the Möhring and Blockhintsev energy flow expressions inside the duct not only allows one to assess the validity of the geometric acoustics limit in this particular case, but also relates the Möhring flux to an acoustic energy flux defined outside the duct.

The Möhring and Blockhintsev acoustic energy flow expressions were compared for the case of a circular duct containing a one-seventh power mean flow profile, with Mach numbers up to 0.9. The agreement between the two acoustic energy flows for the (0,0) mode was extremely good over the whole frequency and flowrate range, although the Blockhintsev analysis is essentially a high frequency limit. The surprisingly good agreement at low frequencies is due to the fact that the (0,0) mode shape function is affected very little by mean shear at low frequencies.

The agreement bweteen the Möhring and Blockhintsev energy flows for the higher modes was poorest at frequencies very close to cutoff. However, the largest difference observed between the Möhring and Blockhintsev energy flows was only 5%, for the (1,0) mode at γ equal to 2, with a centerline Mach number of 0.9. At higher frequencies the differences between the Blockhintsev and Möhring energy flows approached those found for the (0,0) mode. Thus, for energy flow calculations, the geometric acoustics limit appears to be valid for duct propagation over a very wide range of frequencies, even for cases with very highly sheared mean flow.

The energy weighting functions for the one-seventh power mean flow profile were compared to approximate values obtained assuming a uniform flow profile with the same overall flowrate. The agreement was very good for the (0,0) mode at low frequencies and for the higher modes very close to cutoff. However, for higher frequencies the agreement was much worse. The (0,0), (1,0) and (2,0) mode acoustic energy flows (normalized by the wall acoustic pressure) were much lower than the uniform flow approximations, due to mean flow refractive effects, which increased with frequency. However, for the (0,1) mode, the actual acoustic energy flow became much larger than the uniform flow approximation, as the frequency increased beyond cutoff. At very high frequencies, refractive effects began to dominate, lowering the normalized acoustic energy flow.

The exact acoustic energy flow expressions are fairly complicated for the case of acoustic propagation inside a pipe containing a sheared mean flow. However, it was found that under a wide range of conditions these expressions can be simplified considerably, with the approximation causing little loss in accuracy.

Chapter 5

CONCLUSIONS AND RECOMMENDATIONS

5.1 Conclusions

•• Two new experimental techniques have been developed for separating acoustic waves propagating inside circular ducts into the acoustic duct modes. The instantaneous technique uses four wall-mounted microphones to separate the first three acoustic duct modes, the (0,0), (1,0), and (2,0) modes, below the frequency at which the fourth mode starts propagating. The time averaged technique uses only three microphones to separate the first three acoustic duct modes, but requires the additional assumption that the modes be uncorrelated. Comparison of the results of the two techniques shows that this is in fact the case, for the type of noise source examined in this study. Both techniques can in principle be extended to measure a greater number of modes.

•• Downstream modal pressure spectra (200-6000 Hz frequency range) were measured for noise generated by flow through coaxial restrictions in a 97 mm pipe. Four orifices (12.7, 19.0, 31.8, and 50.8 mm diameters) and three nozzles (a 3.18 mm diameter nozzle and 16.2 mm diameter nozzles with throat length-to-diameter ratios of 1 and 8) were tested, at exit jet Mach numbers ranging from 0.15 to slightly super-critical flow.

The shape of the frequency spectrum was found to be scaled by the frequency ratio, $f_r = \frac{\gamma}{\pi St} = \frac{U_j D}{a_o d}$. f_r is the ratio of two non-dimensional frequencies: (i) γ, the nondimensional frequency governing acoustic propagation inside ducts, and (ii) St, the Strouhal number, which scales the jet noise spectrum shape. The experimental results showed that the higher modes dominate the pressure spectrum above their cutoff frequencies for low values of f_r (<3), while all modes are of approximately equal strength for higher values of f_r. This result is related to the behavior of the large-scale flow structures in the region of the jet near the nozzle exit.

•• The measured modal pressure spectra were converted to acoustic power spectra and integrated to determine overall downstream acoustic power. The acoustic efficiency levels (sound power normalized by jet kinetic energy flow) were plotted vs. M_i, the indicated Mach number of the jet that issues from the orifice or nozzle. The acoustic efficiencies were of the same order of magnitude as for the free jet case.

The acoustic efficiency levels for the 19.0 mm orifice and 16.2 mm nozzles agreed closely, indicating very similar noise generation characteristics for nozzles and orifices when the comparison is made using orifice vena contracta and nozzle exit plane conditions.

The acoustic efficiency increased with the ratio of orifice to pipe diameter, $\left(\frac{d}{D}\right)$, for constant M_i. When the efficiency levels were divided by the area ratio, $\left(\frac{d}{D}\right)^2$, the data for the 12.7 and 19.0 mm orifices collapsed onto a single curve, $\frac{\eta}{(d/D)^2} = 3.47 \times 10^{-4} M_i^{4.6}$. The data the 31.8 and 50.8 mm orifices fell somewhat below that for the smaller orifices on this plot. This is believed to be caused by the increased effect of the confining pipe-wall on the hydrodynamic behavior of the jet, for larger $\left(\frac{d}{D}\right)$. The 3.18-mm nozzle data, when efficiency was divided by $\left(\frac{d}{D}\right)^2$, also fell somewhat below that for the 12.7 and 19.0 mm orifices. This is believed to have been caused by the neglect of the acoustic energy above 6000 Hz.

•• An approximate acoustic power measurement, which used one wall-mounted microphone and assumed that the total signal measured by the microphone was that of a plane wave, was compared to the exact acoustic power measurement. The one-microphone technique typically produced a sound power level approximately 1.5 dB above the exact value.

•• Acoustic energy flow expressions were developed for the case of a circular, constant-area, hard-walled duct containing a parallel sheared mean flow. Three different formulations were examined: (i) energy flow expressions derived from the thermodynamic energy equation, (ii) energy flow expressions derived from the conservation equation of Blockhintsev, i.e., the geometric acoustics limit, and (iii) energy flow expressions derived from the conservation principle of Möhring.

The acoustic energy flux derived from the thermodynamic energy equation consists of two terms. The first term is the flow work ($\langle p'\overline{v}' \rangle$) of the acoustic wave and the second is the convection of the acoustic energy density by the mean flow. This flux is conserved for the case of a hard-walled duct containing a parallel sheared mean flow, but is not conserved in a general nonuniformly moving medium.

The energy flux expressions derived from the results of Blockhintsev and Möhring agree for high frequencies and low mean shear, i.e., in the geometric acoustics limit. The Möhring flux is a conserved quantity for all frequency and flowrate conditions, while the Blockhintsev flux is conserved only in the geometric acoustics limit. Thus a comparision of the values of these two energy flux expressions defines the validity of the geometric acoustics limit.

The values of the (0,0) , (1,0) , (2,0) and (0,1) mode Blockhintsev and Möhring energy flux expressions were compared for a $1/7^{th}$ power mean flow profile with centerline Mach numbers up to 0.9. For the (0,0) mode, the difference between these two energy flow expressions was uniformly small for low and high frequency. For the higher modes, the differences were greatest at the frequencies near cut-off and approached those seen for the (0,0) mode at higher frequencies. The general validity of the geometric acoustics limit was remarkable.

The values of the energy flux expressions calculated for sheared mean flow profiles were compared to approximate values obtained by assuming a slug flow profile with the same overall flowrate. The agreement was very poor, except for the (0,0) mode at low frequencies and the higher modes very close to their cutoff frequencies.

The acoustic energy flow analysis based on the thermodynamic energy equation and on the results of Mohring both resulted in orthogonality properties for the eigenfunctions of the radial mode shape equation.

These could be of use in further developing the mathematical properties of this eigenvalue equation.

5.2 Recommendations

•• The approximate scaling law suggested in the present investigation, $\frac{\eta}{(d/D)^2} = f(M_1)$ is a potentially very useful result. In order to further substantiate this result, experiments with a greater number of restriction sizes should be made. Increasing the frequency range over which the measurements are made would also improve the confidence in this result. The mode separation techniques could be extended to separate a greater number of modes, thus allowing measurements over a wider frequency range.

•• The present research considered only circular shaped restrictions mounted concentrically in the pipe. For these types of restrictions the higher mode nodal diameters varied randomly. As an extension of the present research the behavior of noncircular restrictions could be examined. In particular, two issues are of interest: (i) do the higher mode nodal diameters have a preferred direction for noncircular restrictions, and (ii) can the acoustic power output of noncircular restrictions be correlated in the same manner as the results for circular obstructions?

•• The experimental results of the present investigation show that in most cases the (0,1) mode dies off rapidly above its cutoff frequency, in contrast to the behavior of the (1,0), (2,0) and (3,0) modes. It would be interesting to see if the behavior of the (1,1) and (2,1) modes is similar to that of the (0,1) mode. The (1,1) and (2,1) modes could be examined by simply measuring the spectra with the instantaneous mode separation technique over a wider frequency range. The (1,1) mode would combine with the (1,0) mode and the (2,1) mode would combine with the (2,0) mode. If the (1,1) and (2,1) modes also die off rapidly above their cutoff frequencies, this may indicate that the modes with the nodal circles (i.e., (m,n) modes with $n > 0$) are less important than the (m,0) modes.

•• The extent to which the higher acoustic duct modes contribute to the noise transmitted through the pipewall is influenced strongly by the flexibility of the pipe to these particular modes. The present research indicates that the higher modes may make a significant contribution to the noise transmitted through the pipewall. Further research on the pipewall vibration caused by the higher acoustic duct modes and the far field noise resulting from such pipewall vibration might clarify this issue.

•• The Möhring and Blockhintsev acoustic energy flow expressions give essentially the same results for the case of a hard-walled duct containing a parallel shear flow. However, in many practical applications the duct walls are acoustically treated. Thus a similar comparision for the case of a duct with acoustically treated walls would be useful.

Table 1

Accuracy of Geometric Acoustics Limit
for $1/7^{th}$ Power Mean Flow Profile.
Tabulated Values are $(EWF^B - EWF^M)/EWF^M$
in Per Cent

(0,0) Mode

γ	$M_{max} = 0.5$	$M_{max} = 0.9$
0.5	0.002	0.018
6	0.002	0.022
10	0.002	0.026
20	0.002	0.029

(1,0) Mode

γ	$M_{max} = 0.5$	$M_{max} = 0.9$
2	1.23	5.05
4	0.092	0.70
10	0.006	0.06
20	0.003	0.03

(2,0) Mode

γ	$M_{max} = 0.5$	$M_{max} = 0.9$
3.5	0.63	2.95
6	0.087	0.68
10	0.014	0.15
20	0.004	0.04

(0,1) Mode

γ	$M_{max} = 0.5$	$M_{max} = 0.9$
4	0.18	0.68
6	0.040	0.25
10	0.009	0.07
20	0.002	0.017

Table 2

A Comparison of the Möhring and Physical Energy Weighting Functions for 1/7th Power Mean Flow Profiles

(0,0) Mode

γ	$M_{max} = 0.1$		$M_{max} = 0.5$		$M_{max} = 0.9$	
	EWF^M	EWF^P	EWF^M	EWF^P	EWF^M	EWF^P
0.5	1.168	1.080	1.995	1.413	3.086	1.765
6	1.061	.9825	1.525	1.088	2.244	1.305
10	.9113	.8447	1.075	.7787	1.501	.8955
20	.5732	.5340	.5544	.4117	.7333	.4566

(1,0) Mode

γ	$M_{max} = 0.1$		$M_{max} = 0.5$		$M_{max} = 0.9$	
	EWF^M	EWF^P	EWF^M	EWF^P	EWF^M	EWF^P
2	.2945	.2902	.4462	.4347	.6657	.6503
4	.6985	.6556	1.035	.7978	1.422	.9705
10	.7042	.6556	.9259	.6813	1.292	.7921
20	.5315	.4957	.5467	.4066	.7237	.4519

(2,0) Mode

γ	$M_{max} = 0.1$		$M_{max} = 0.5$		$M_{max} = 0.9$	
	EWF^M	EWF^P	EWF^M	EWF^P	EWF^M	EWF^P
3.5	.2985	.2908	.4126	.3843	.5732	.5289
6	.5399	.5088	.7659	.6018	1.024	.7210
10	.5733	.5362	.7805	.5863	1.070	.6841
20	.4830	.4513	.5278	.3943	.6988	.4397

(0,1) Mode

γ	$M_{max} = 0.1$		$M_{max} = 0.5$		$M_{max} = 0.9$	
	EWF^M	EWF^P	EWF^M	EWF^P	EWF^M	EWF^P
4	.3089	.3042	.5450	.5300	.8711	.8480
6	.8742	.8224	1.257	1.001	1.626	1.190
10	1.163	1.077	2.046	1.481	2.749	1.679
20	1.832	1.684	3.760	2.618	4.841	2.741

C-2

Table 3

Percentage Contributions of the Terms Containing $(dM/d\bar{r})$ to the Total Values of EWF^P and EWF^M

(0,0) Mode

γ	1/7 Power Profile $M_{max} = 0.9$ Möhring Flux	1/7 Power Profile $M_{max} = 0.9$ Physical Flux	1/7 Power Profile $M_{max} = 0.5$ Möhring Flux	1/7 Power Profile $M_{max} = 0.5$ Physical Flux	1/7 Power Profile $M_{max} = 0.1$ Möhring Flux	1/7 Power Profile $M_{max} = 0.1$ Physical Flux	Lam. Flow Profile $M_{max} = 0.163$ Möhring Flux	Lam. Flow Profile $M_{max} = 0.163$ Physical Flux
0.5	1.80	2.42	0.61	0.85	0.03	0.04	0.44	0.65
6	1.97	2.65	0.66	0.92	0.03	0.04	0.43	0.62
10	2.13	2.85	0.71	0.98	0.03	0.04	0.36	0.53
20	2.09	2.79	0.70	0.97	0.03	0.05	0.20	0.29

(1.0) Mode

2	9.78	13.64	7.84	11.08	2.01	2.96	9.39	13.28
4	5.50	7.12	2.36	3.22	0.27	0.39	1.47	2.11
10	2.58	3.40	0.90	1.24	0.06	0.09	0.42	0.60
20	2.11	2.81	0.71	0.99	0.04	0.05	0.20	0.29

(2,0) Mode

3.5	7.14	9.98	5.09	7.22	1.07	1.57	4.64	6.68
6	4.64	6.12	2.05	2.82	0.24	0.35	1.15	1.65
10	3.00	3.95	1.12	1.54	0.10	0.14	0.50	0.72
20	2.16	2.88	0.74	1.03	0.04	0.06	0.21	0.30

(0,1) Mode

4	1.81	2.72	1.59	2.40	0.53	0.80	-0.16	-0.09
6	0.88	1.63	0.52	0.89	0.10	0.15	-0.22	-0.22
10	0.15	0.51	0.11	0.24	0.03	0.04	-0.17	-0.22
20	0.02	0.13	0.01	0.04	0.003	0.005	-0.04	-0.05

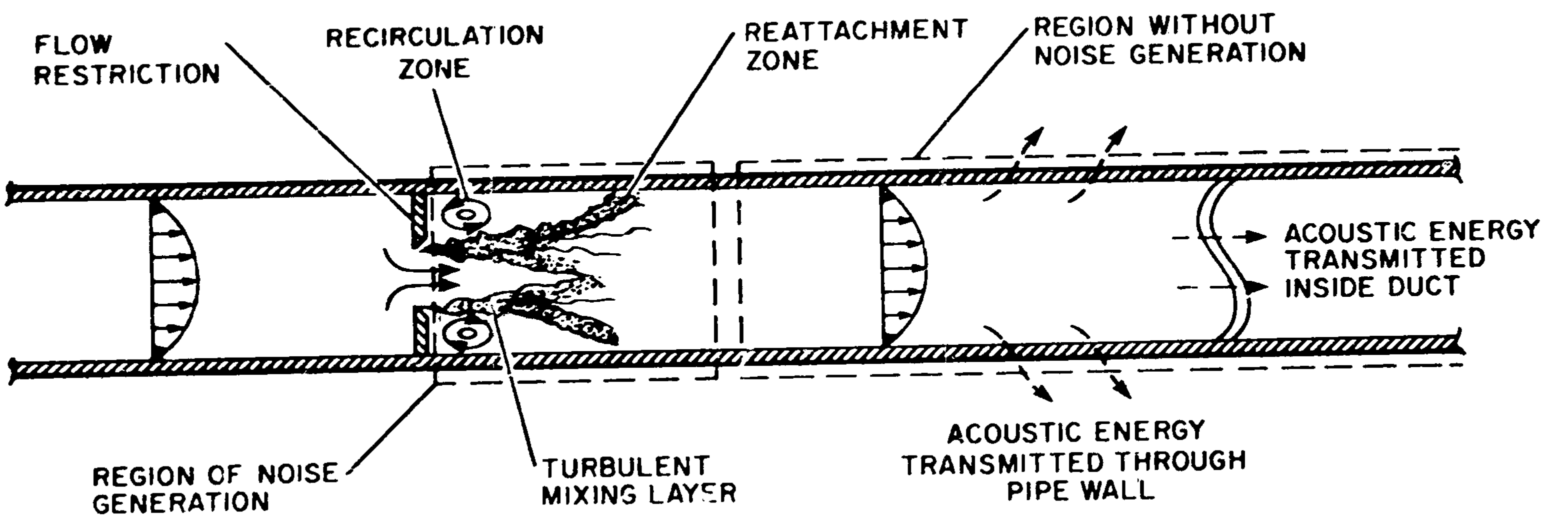

Fig. 1. An illustration of the physical characteristics of flow-generated noise.

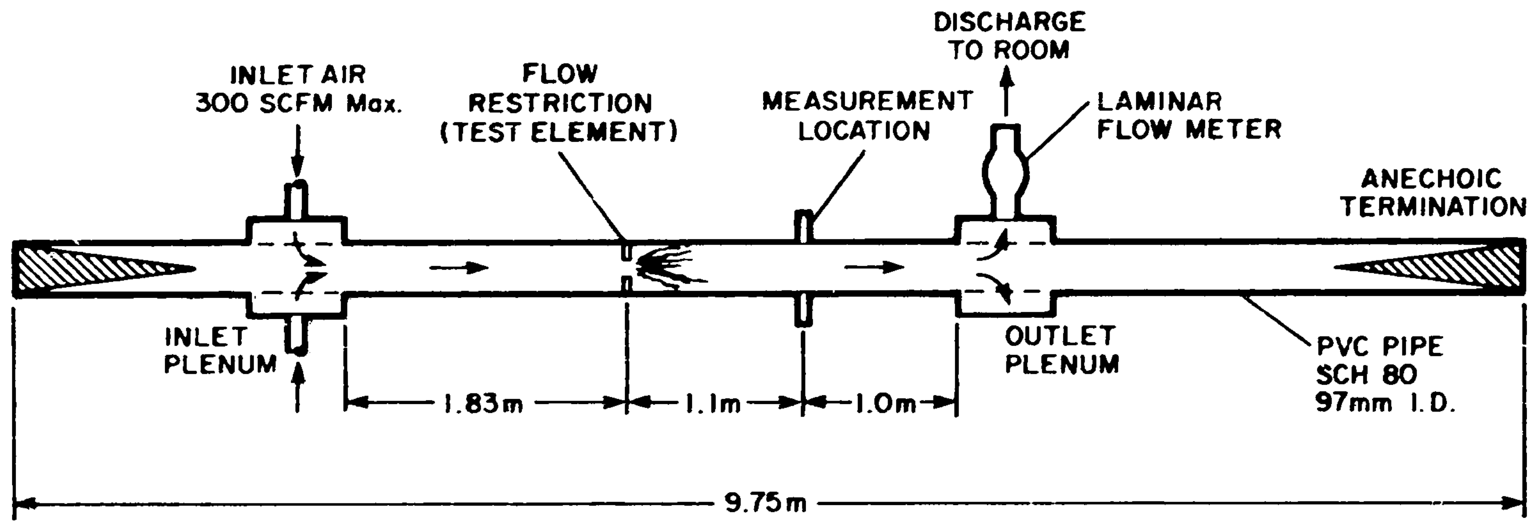

Fig. 2. Schematic of the experimental apparatus.

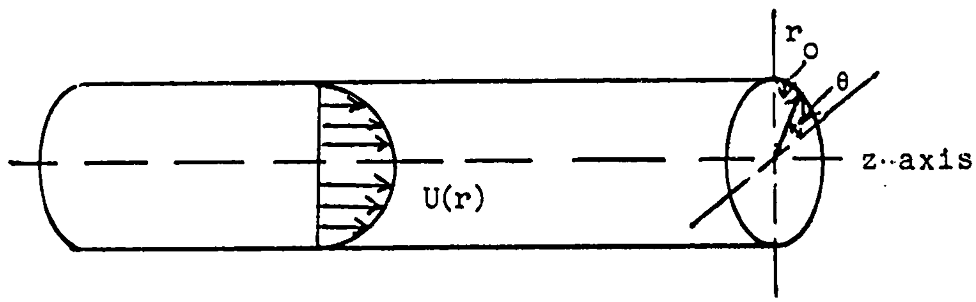

Fig. 3. Duct geometry and coordinate system.

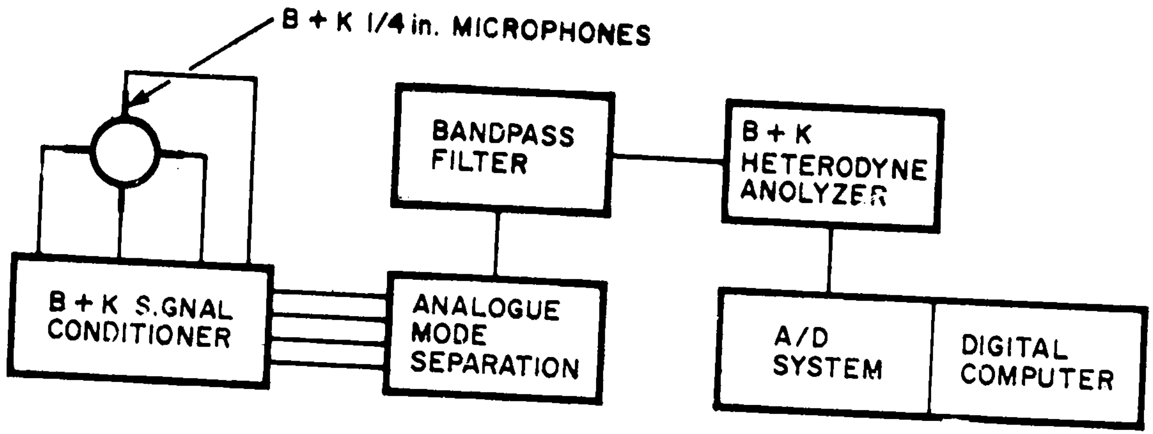

Fig. 4a. Line diagram of instrumentation for the instantaneous mode separation technique.

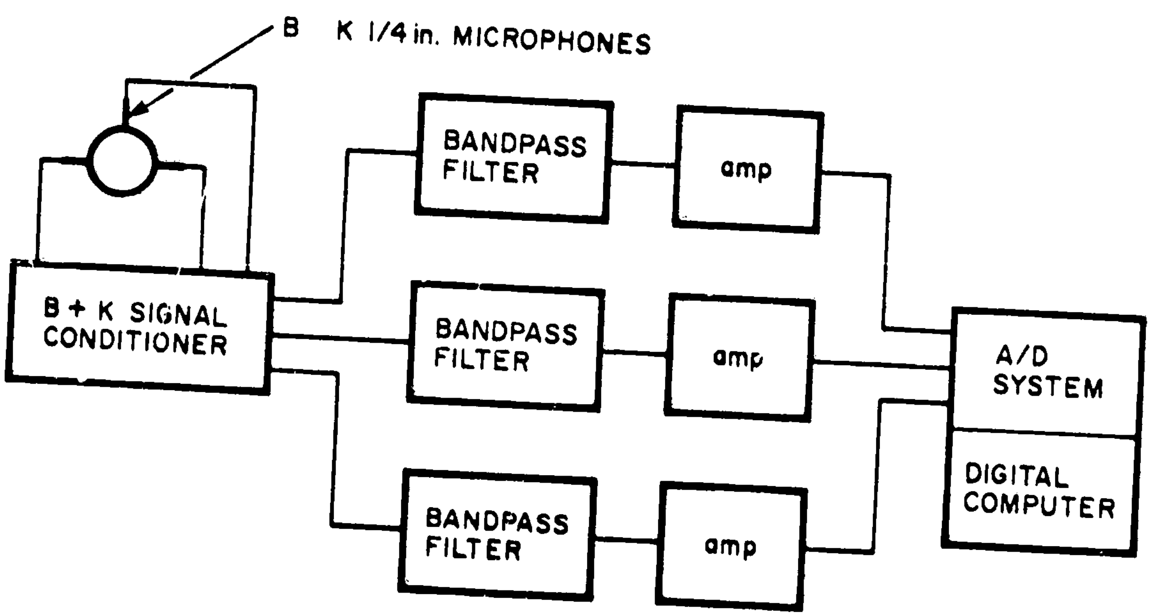

Fig. 4b. Line diagram of instrumentation for the time-averaged mode separation technique.

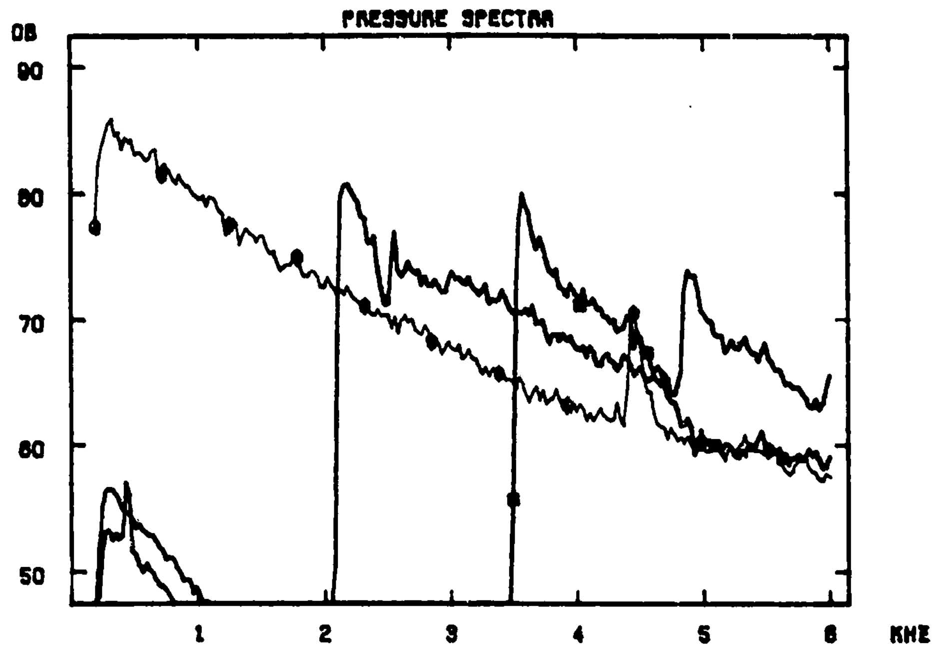

Fig. 5. Modal pressure spectra measured with the instantaneous mode separation technique.
—⊕— (0,0) mode, ——— (1,0) mode,
—■— (2,0) mode.

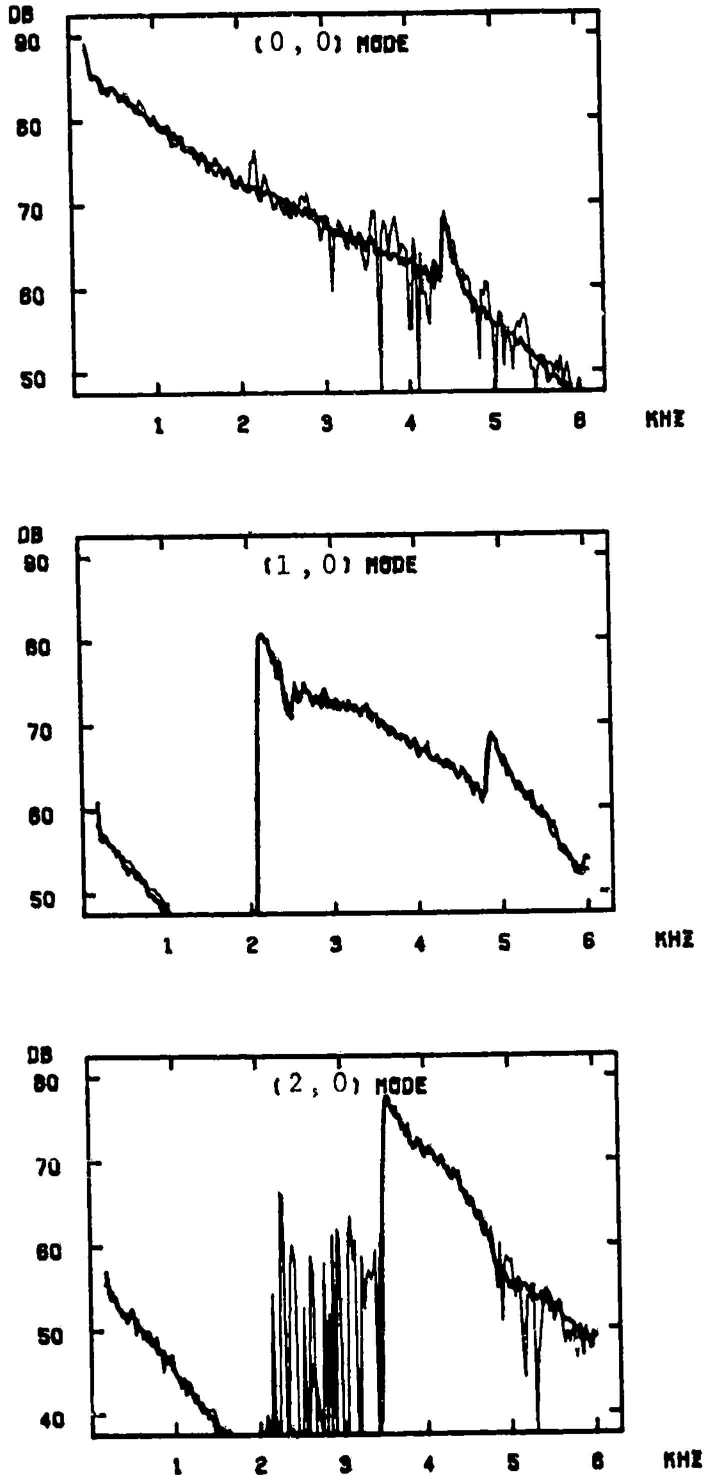

Fig. 6. Modal pressure spectra measured with the time-averaged mode separation technique using 64 ensembles (light line). Output of the instantaneous technique (heavy line) shown for comparison.

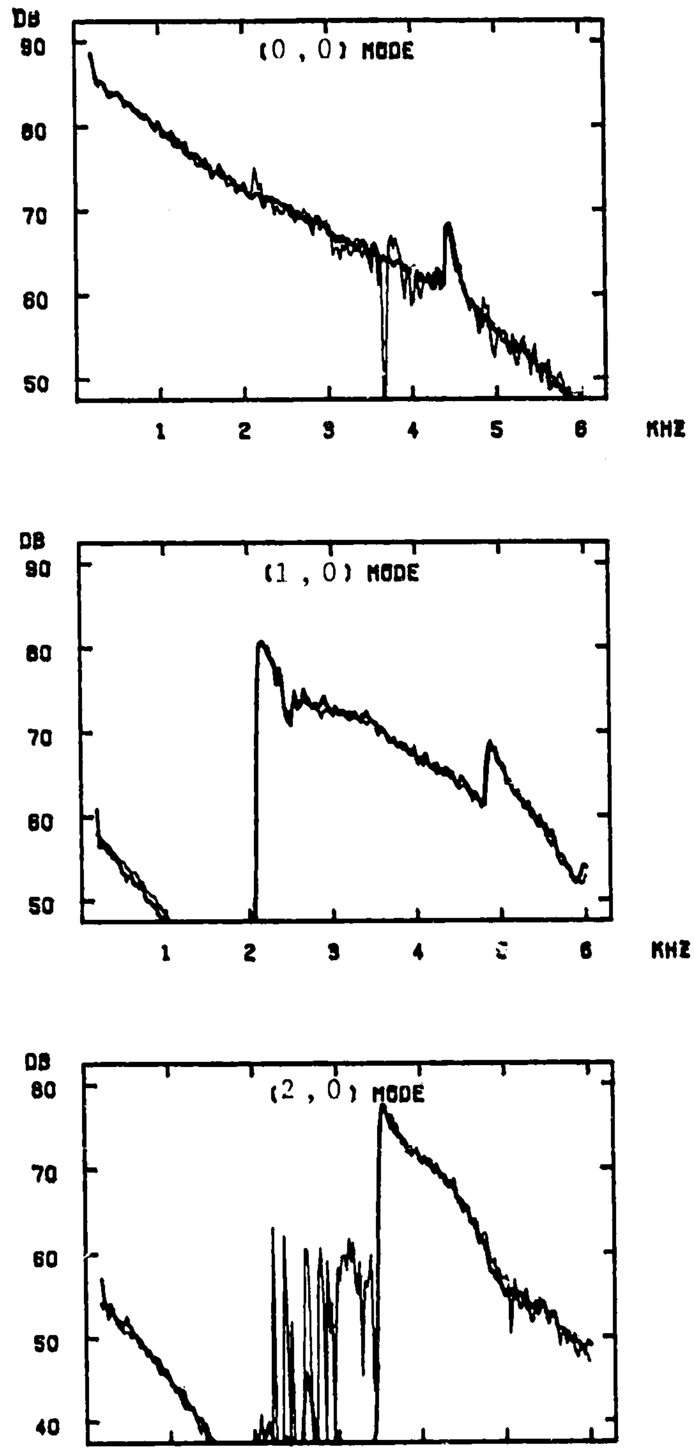

Fig. 7. Modal pressure spectra measured with the time-averaged mode separation technique using 256 ensembles (light line). Output of the instantaneous technique (heavy line) shown for comparison.

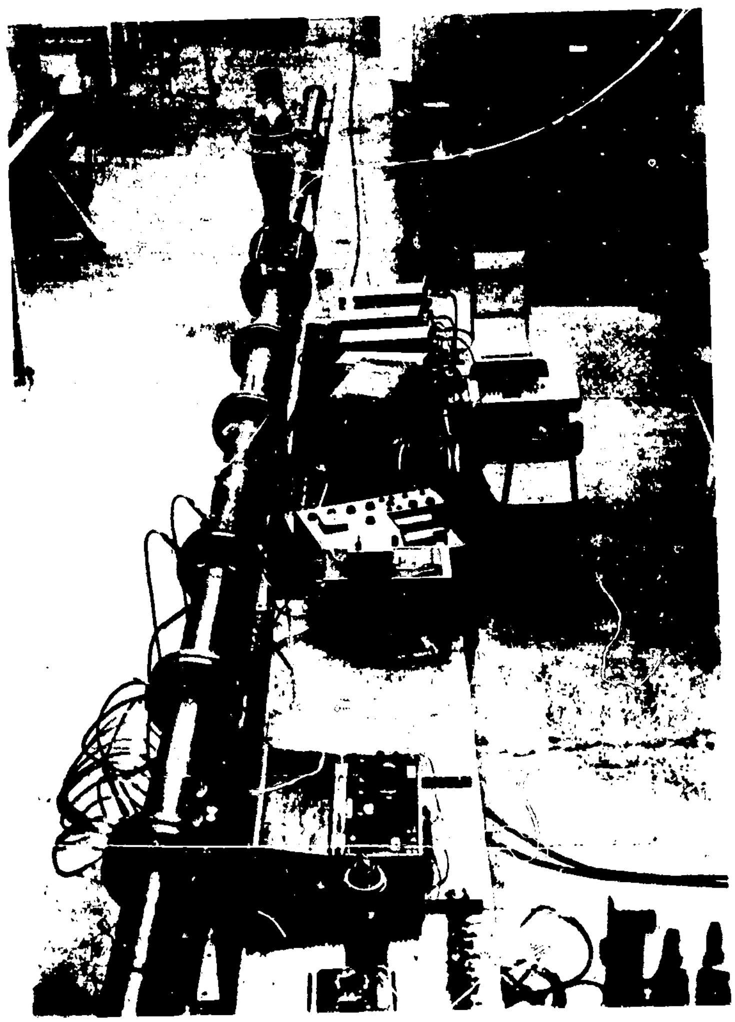

Fig. 8. Photograph of experimental apparatus.

Fig. 9. Photograph of microphone assembly.

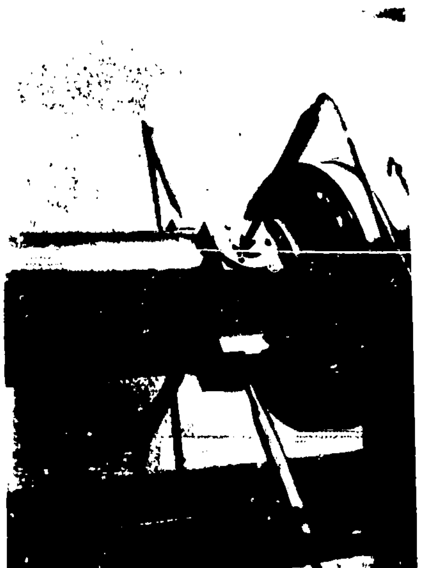

Fig. 10. Photograph showing microphones mounted in the pipe.

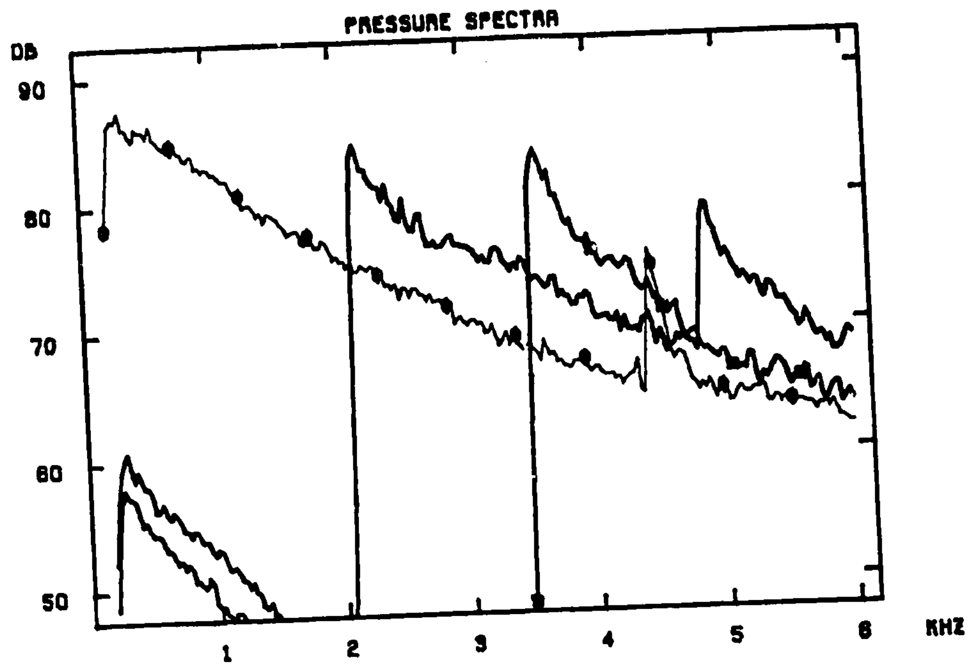

Fig. 11. Typical modal pressure spectra for a low value of the frequency ratio, $f_r = 1.19$. $(d/D) = 0.327$, $M_1 = 0.397$, $f_{St} = 850$ Hz. —ф— (0,0) mode, ——— (1,0) mode, —■— (2,0) mode.

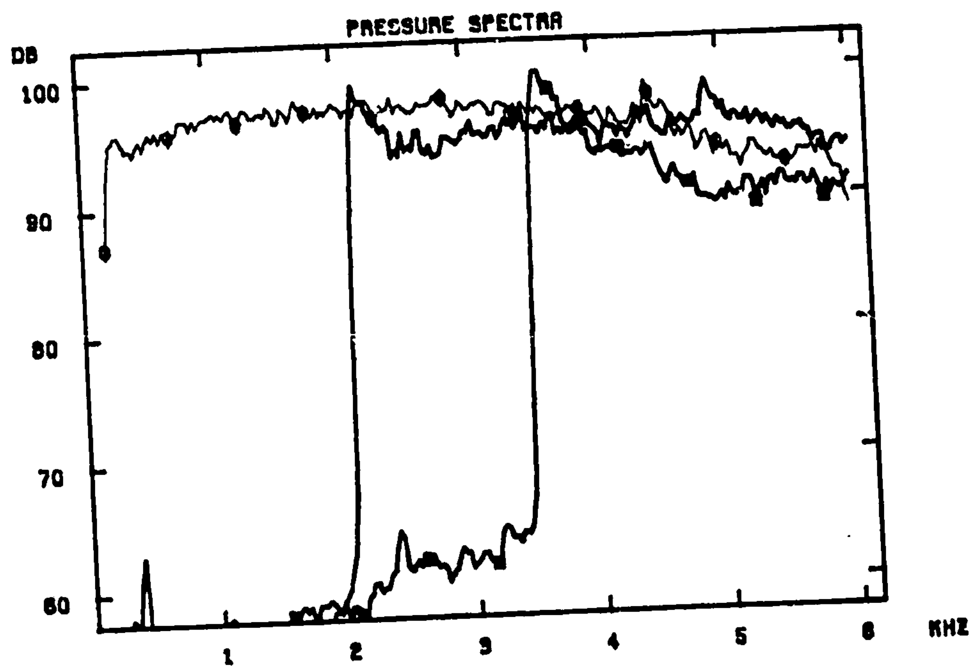

Fig. 12. Typical modal pressure spectra for a high value of the frequency ratio, $f_r = 7.42$. $(d/D) = 0.131$, $M_1 = 1.08$, $f_{St} = 5290$ Hz. —ф— (0,0) mode, ——— (1,0) mode, —■— (2,0) mode.

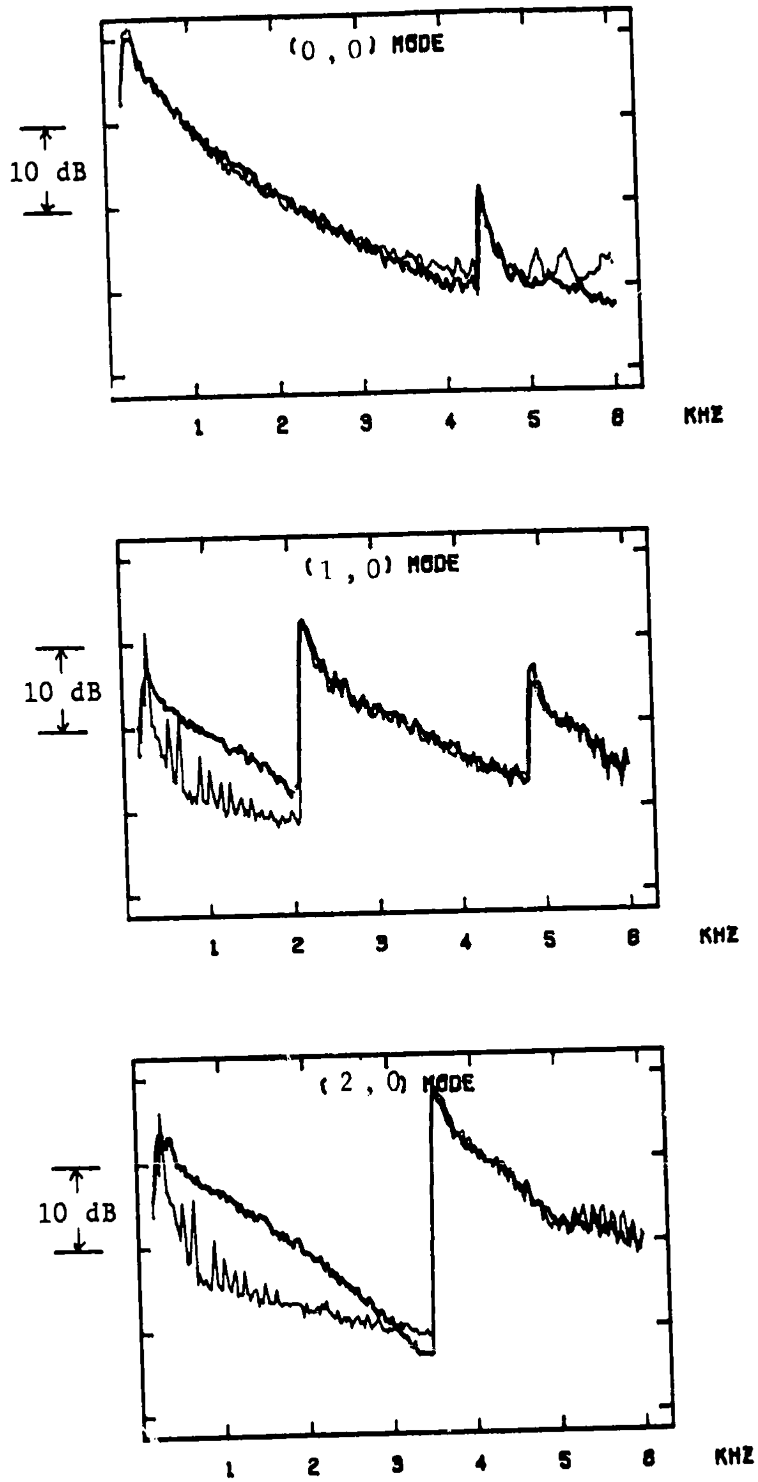

Fig. 13. A comparison of two sets of modal pressure spectra with closely matching frequency ratio. Light line: (d/D) = 0.327, M_i = 0.149, f_r = 0.455, f_{St} = 325 Hz. Heavy line: (d/D) = 0.523, M_i = 0.225, f_r = 0.428, f_{St} = 305 Hz.

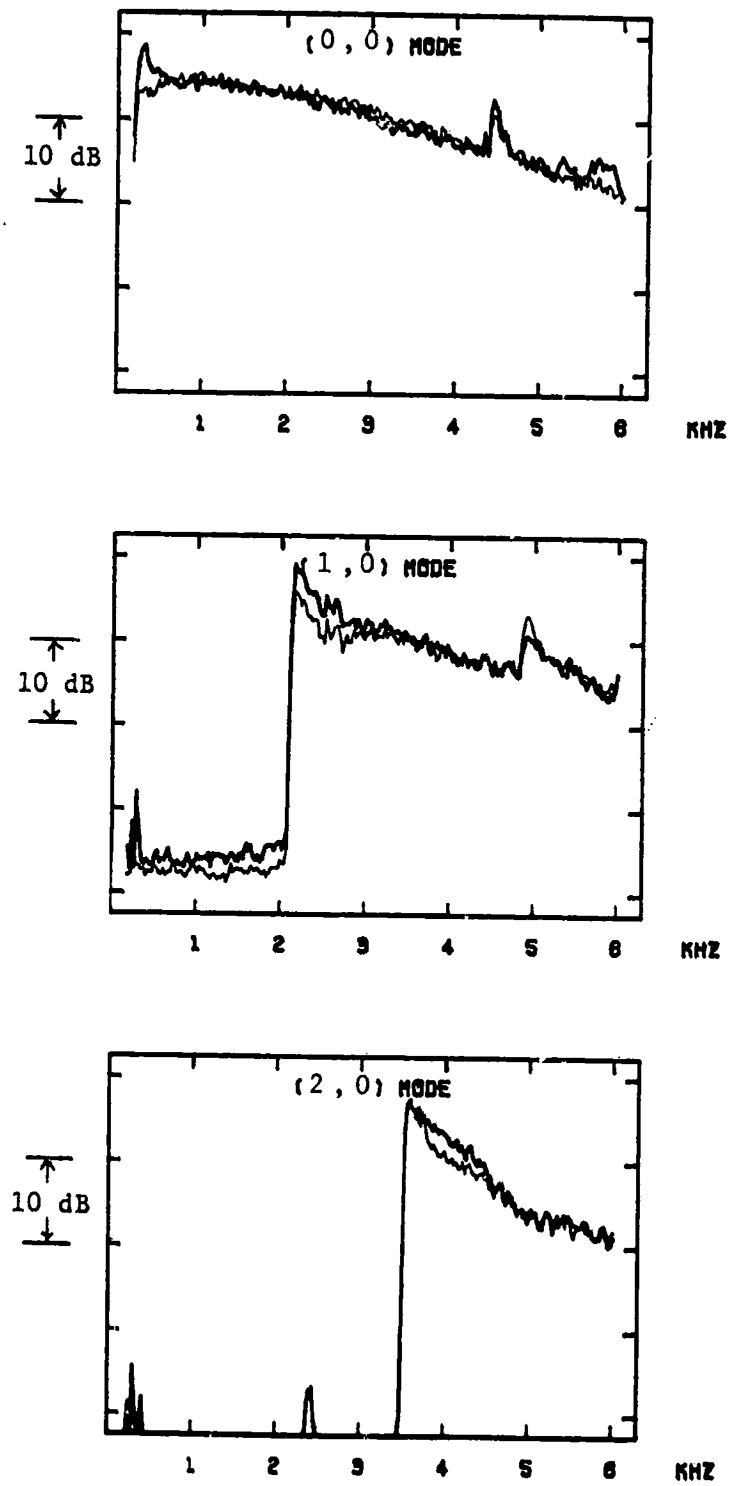

Fig. 14. A comparison of two sets of modal pressure spectra with closely matching frequency ratio. Light line: $(d/D) = 0.196$, $M_i = 0.755$, $f_r = 3.65$, $f_{St} = 2610$ Hz. Heavy line: $(d/D) = 0.131$, $M_i = 0.499$, $f_r = 3.72$, $f_{St} = 2660$ Hz.

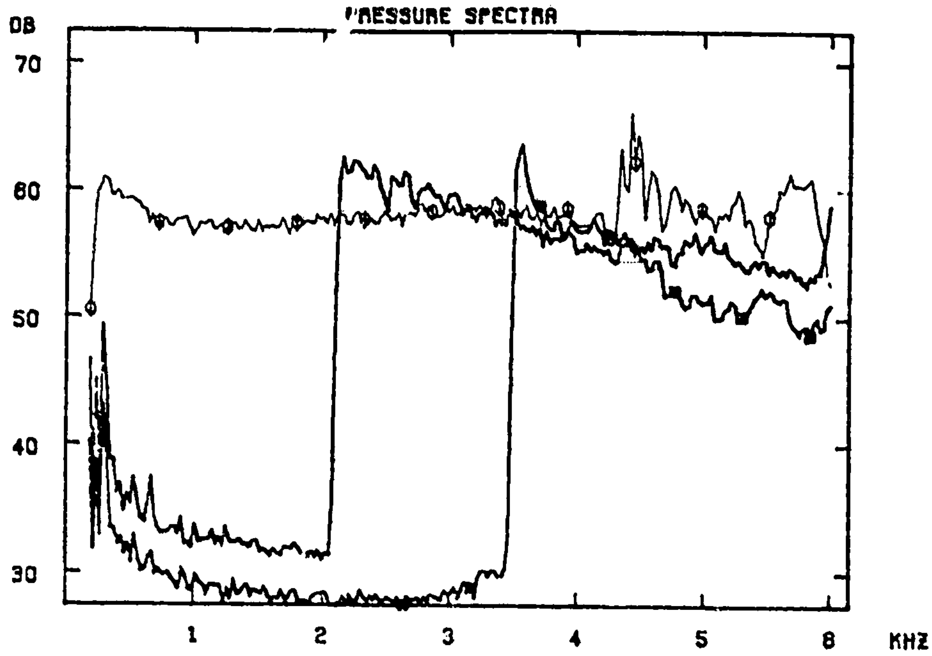

Fig. 15. Typical modal pressure spectra for the 3.18 mm diameter nozzle. (d/D) = 0.033, M_j = 0.75, f_T = 21.8. —◆— (0,0) mode, ——— (1,0) mode, —■— (2,0) mode.

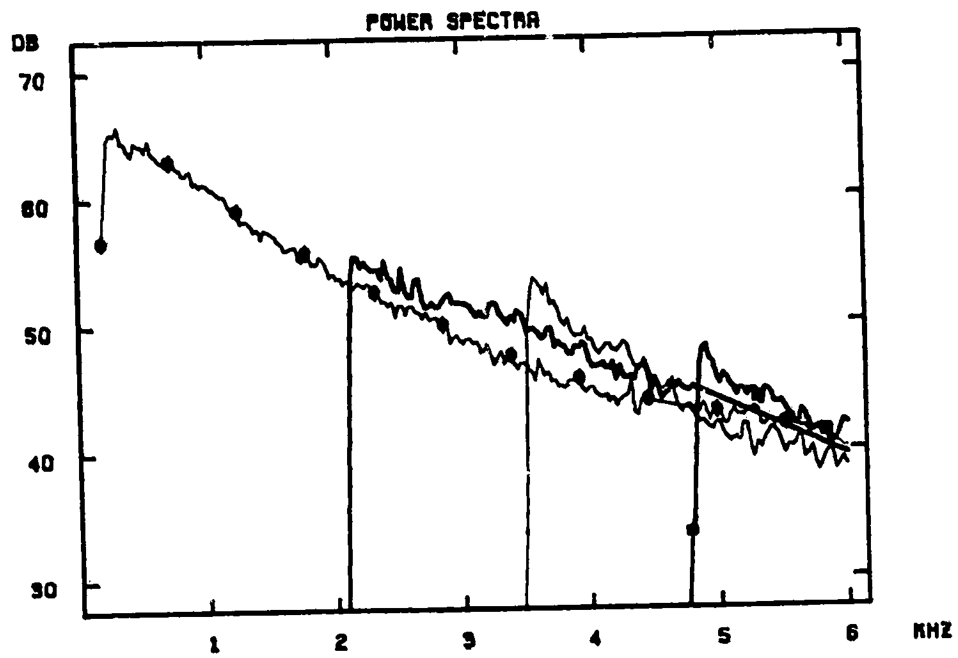

Fig. 16. Modal power spectra calculated using the modal pressure spectra shown in Fig. 11. ——— (0,0) mode, ——— (1,0) mode, ——— (2,0) mode, —■— (3,0) mode.

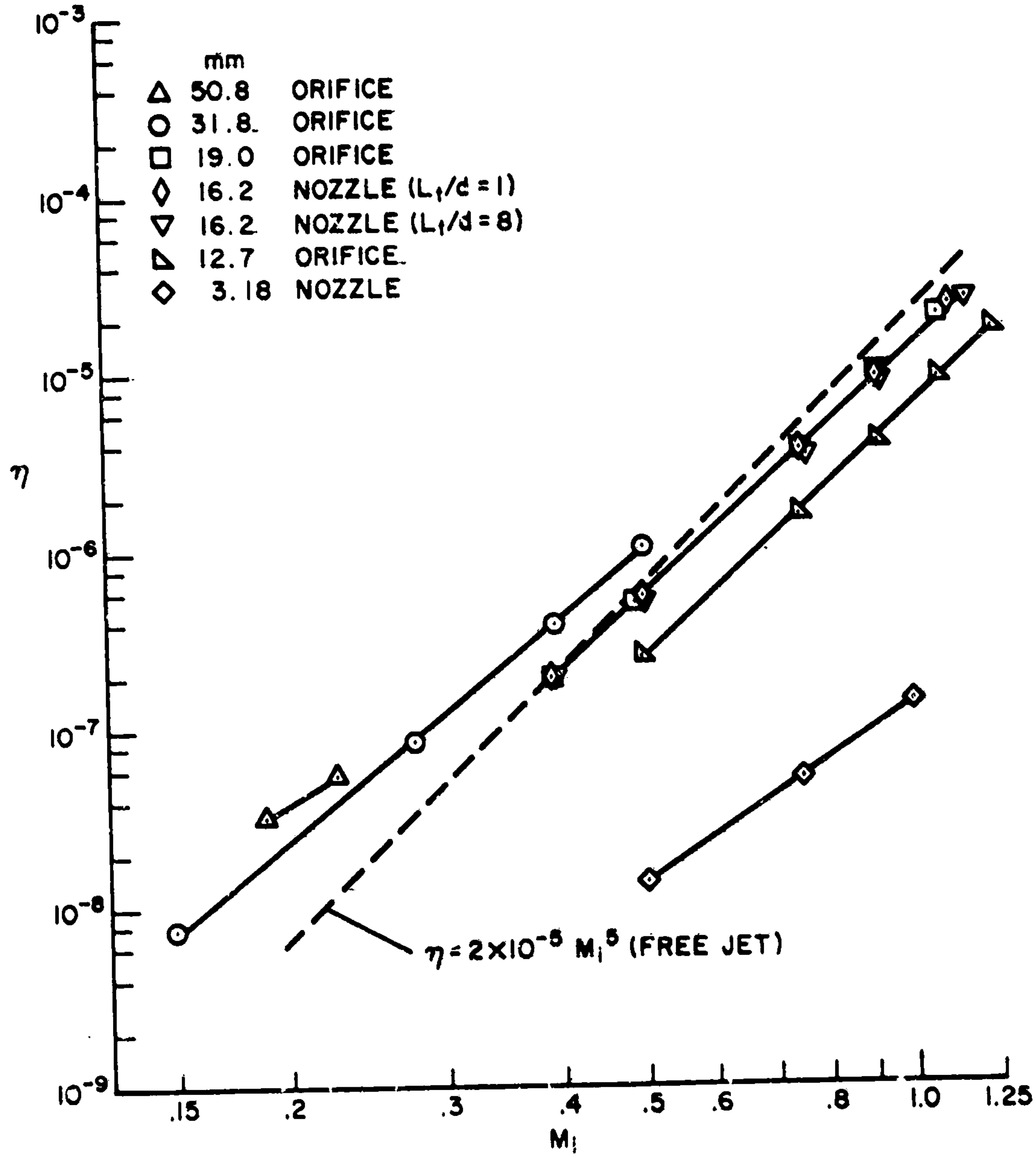

Fig. 17. Overall noise generation efficiency plotted as a function of jet indicated Mach number.

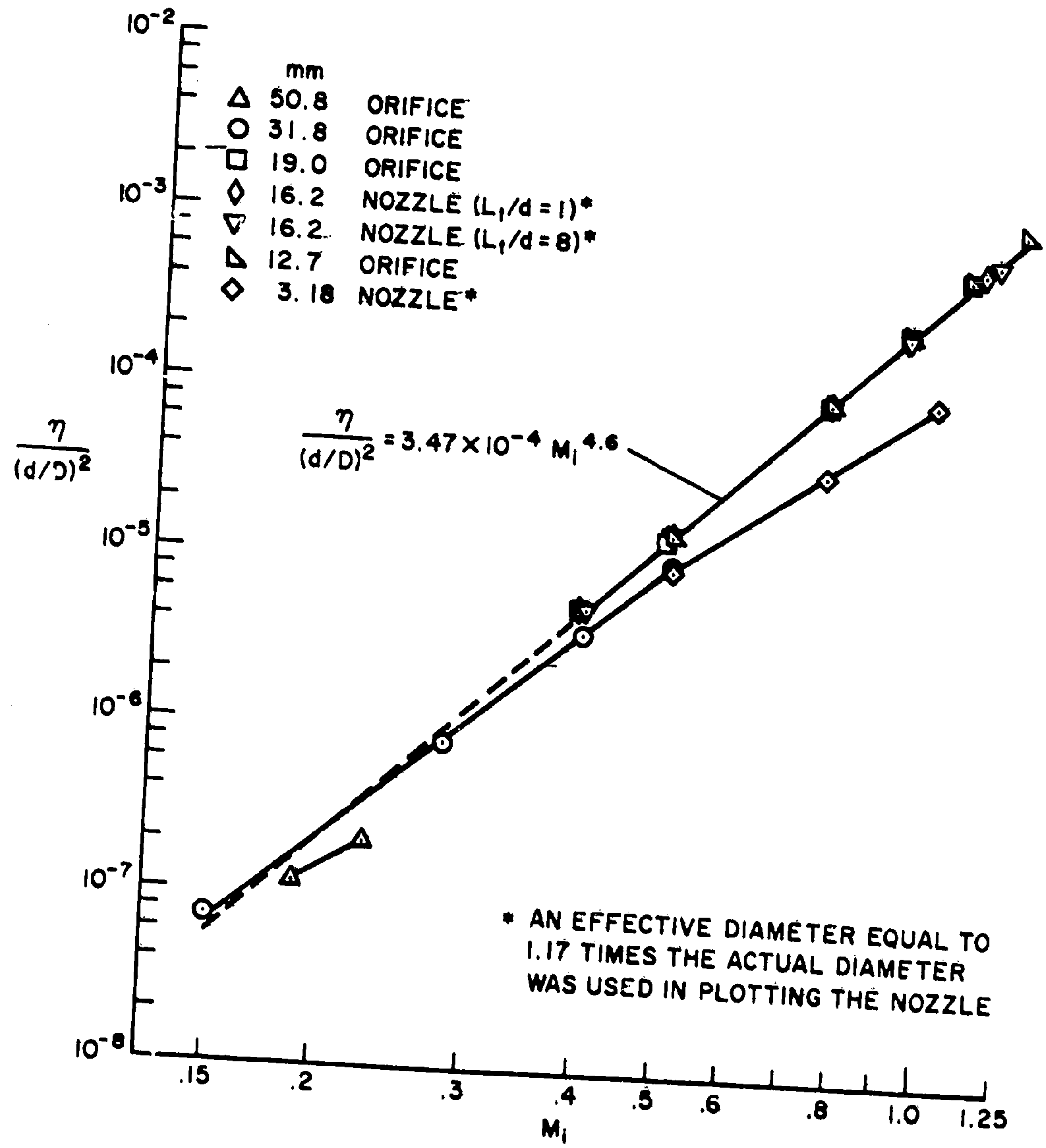

Fig. 18. Overall noise generation efficiency divided by area ratio plotted as a function of jet indicated Mach number.

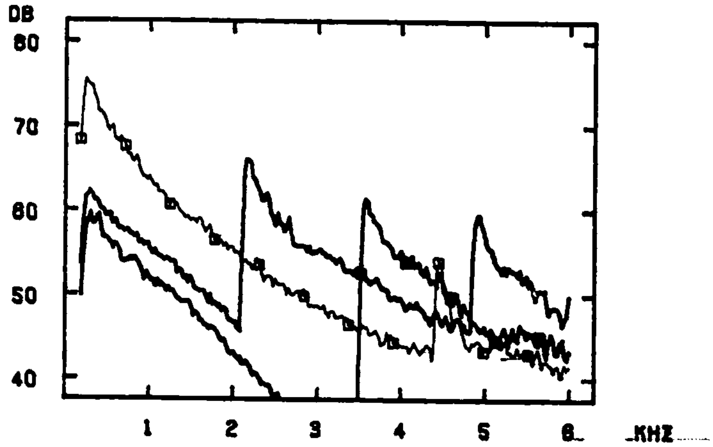

50.8 mm Orifice

(d/D) = 0.523

M_i = 0.187

f_r = 0.356

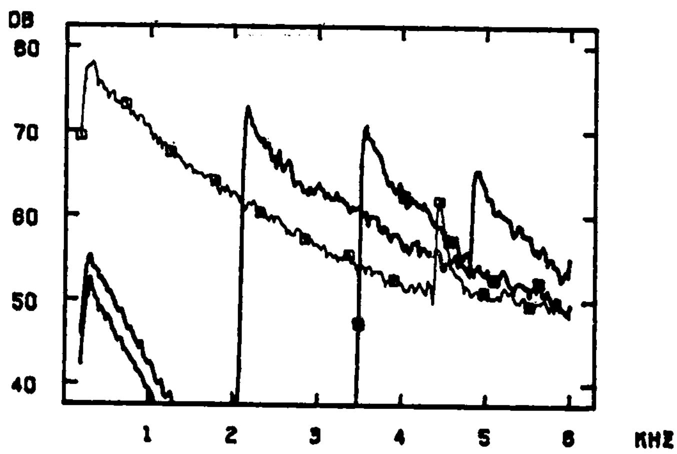

31.8 mm Orifice

(d/D) = 0.327

M_i = 0.277

f_r = 0.841

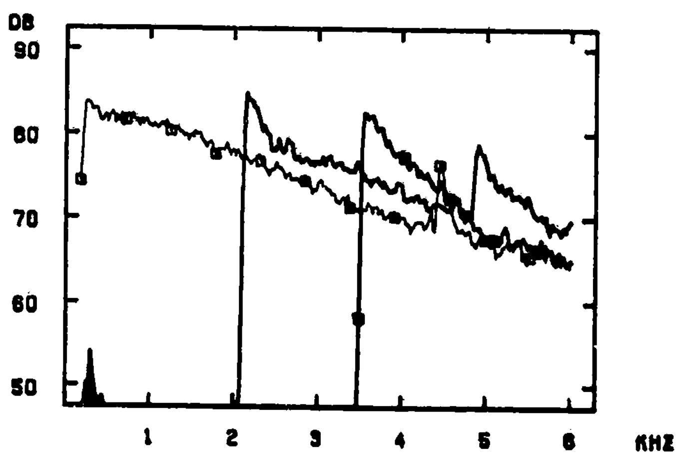

19.0 mm Orifice

(d/D) = 0.196

M_i = 0.492

f_r = 2.45

Fig. 19. Modal pressure spectra illustrating the relative levels of acoustic and hydrodynamic pressure fluctuations at the measurement station. —⊕— (0,0) mode, ——— (1,0) mode, —■— (2,0) mode.

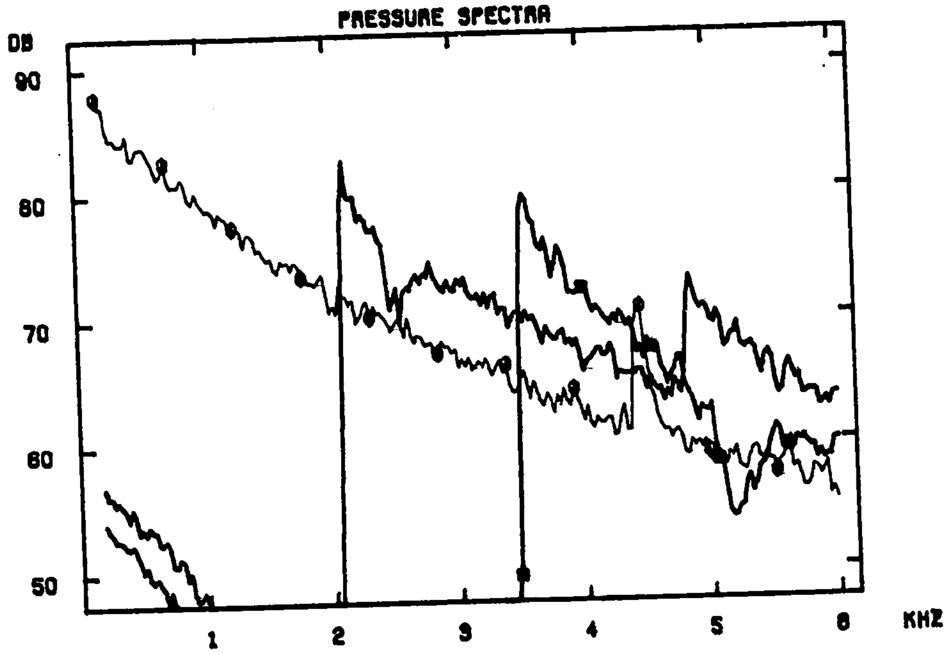

Fig. 20. Modal pressure spectra measured 2.2 meters downstream of the restriction. Note dip in the (1,0) mode at 2500 Hz and in the (2,0) mode at 5000 Hz.
(0,0) mode, (1,0) mode, (2,0) mode.

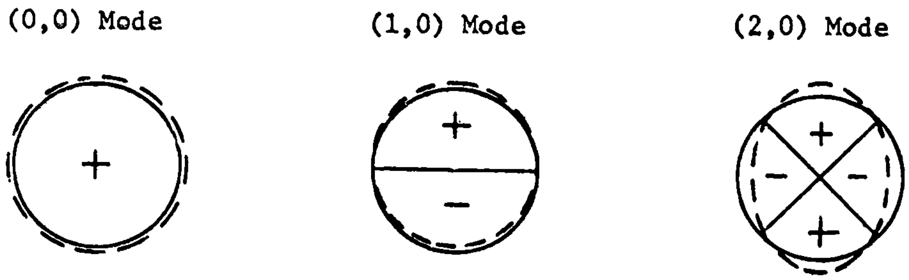

Fig. 21. Cross-sectional pressure patterns for the first three acoustic duct modes. Dashed lines indicate type of pipe wall vibration caused by each mode.

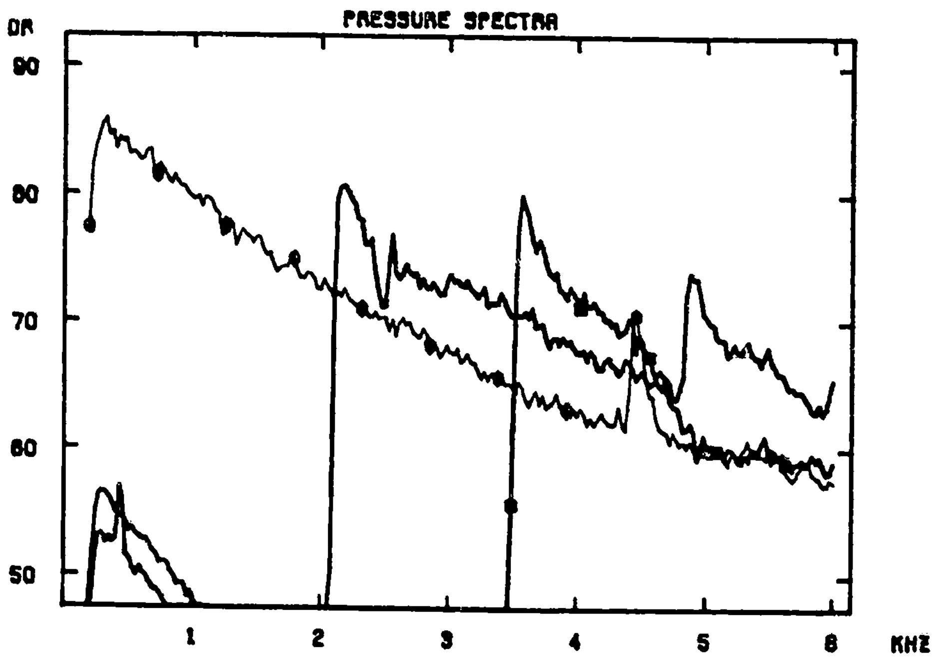

Fig. 22. Modal pressure spectra measured 2.36 meters downstream of the restriction with stiffened pipe configuration. Experimental conditions (M_1 and (d/D)) are identical to those for Fig. 20. —⊕— (0,0) mode, ——— (1,0) mode, —■— (2,0) mode.

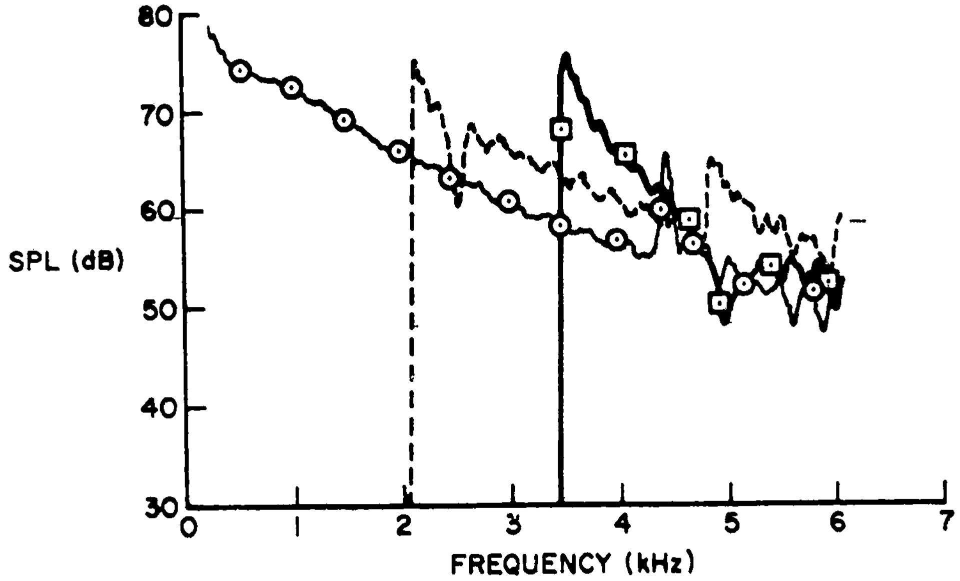

Fig. 23a. Modal pressure spectra measured upstream of the outlet plenum (2.2 meters downstream of the restriction). Experimental conditions ((d/D) and M_i) are identical to those for Fig. 23b. —⊙— (0,0) mode, – – – – (1,0) mode, —⊡— (2,0) mode.

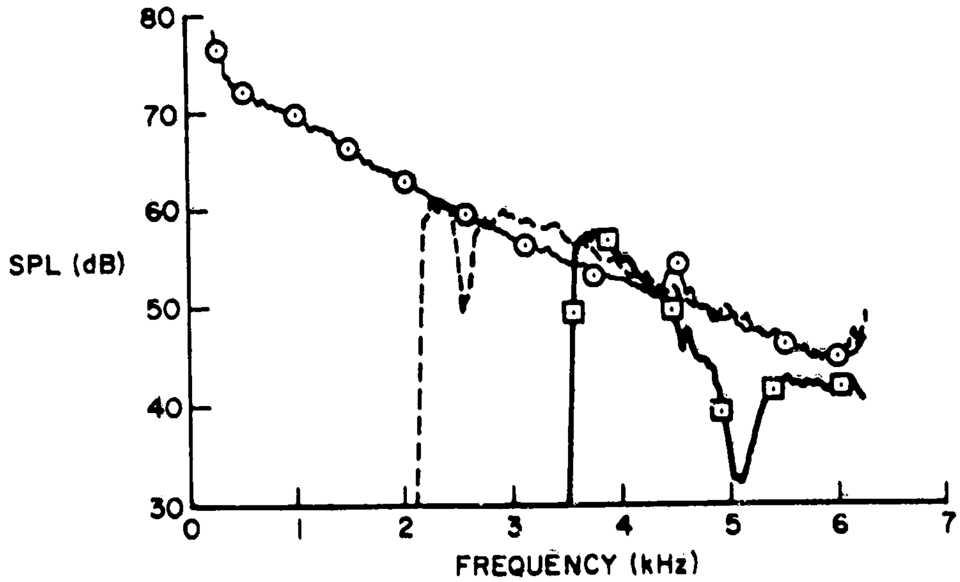

Fig. 23b. Modal pressure spectra measured in the downstream no-flow zone. Experimental conditions ((d/D) and M_i are identical to those for Fig. 23a. —⊙— (0,0) mode, – – – – (1,0) mode, —⊡— (2,0) mode.

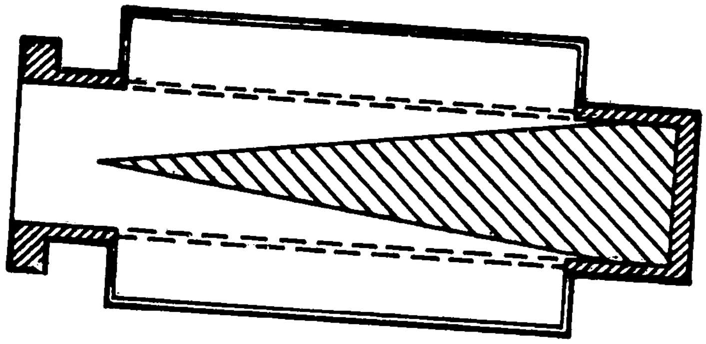

Fig. 24. Proposed modification to outlet plenum section of experimental apparatus.

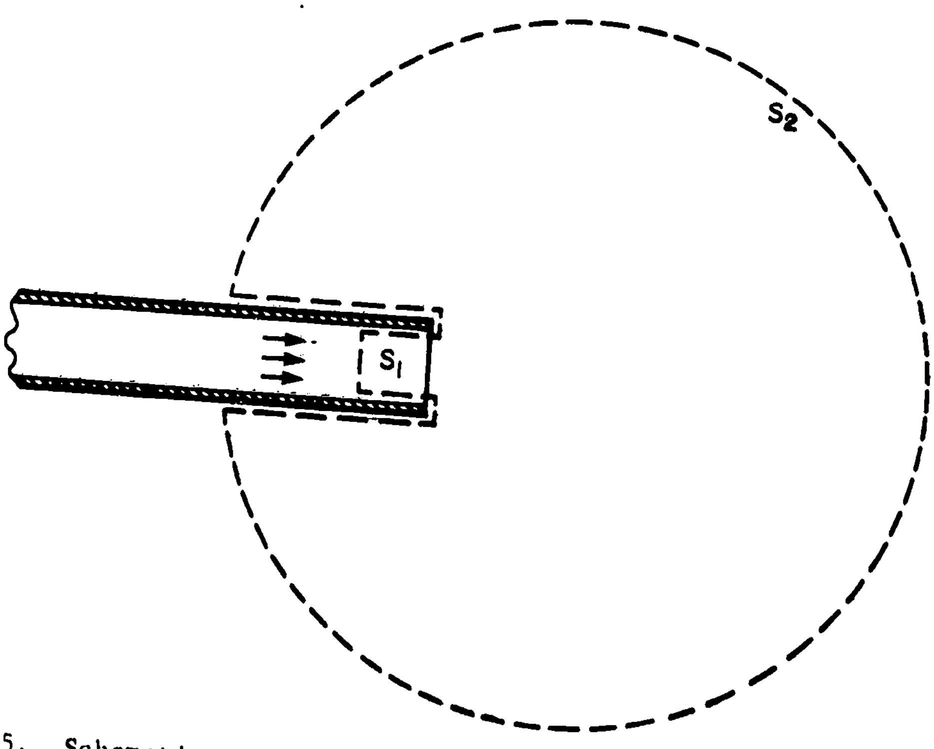

Fig. 25. Schematic of possible surfaces for measurement for acoustic energy flow from duct end.

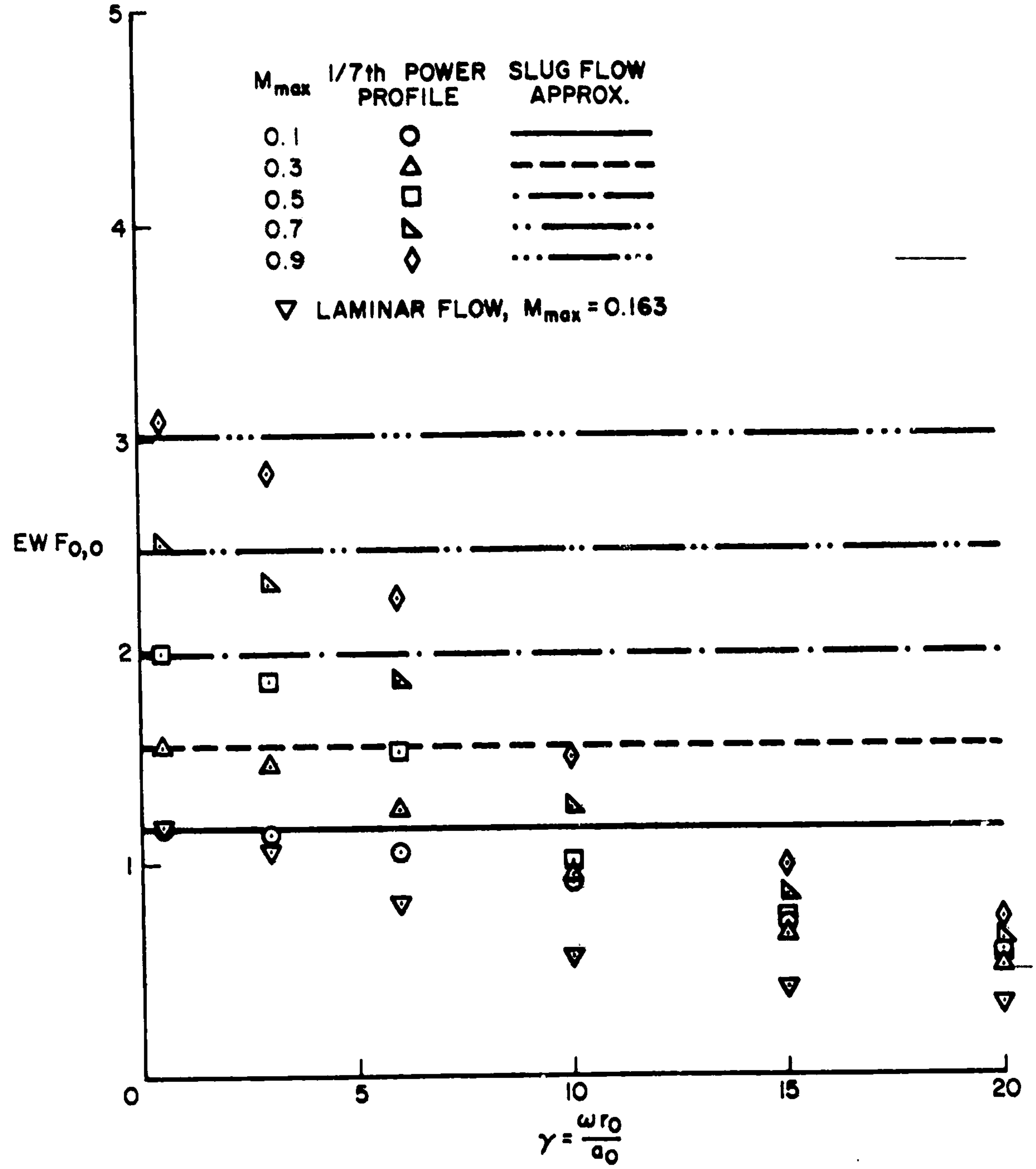

Fig. 26a. (0,0) mode energy weighting functions for sheared mean flow profiles and comparison to slug flow approximations.

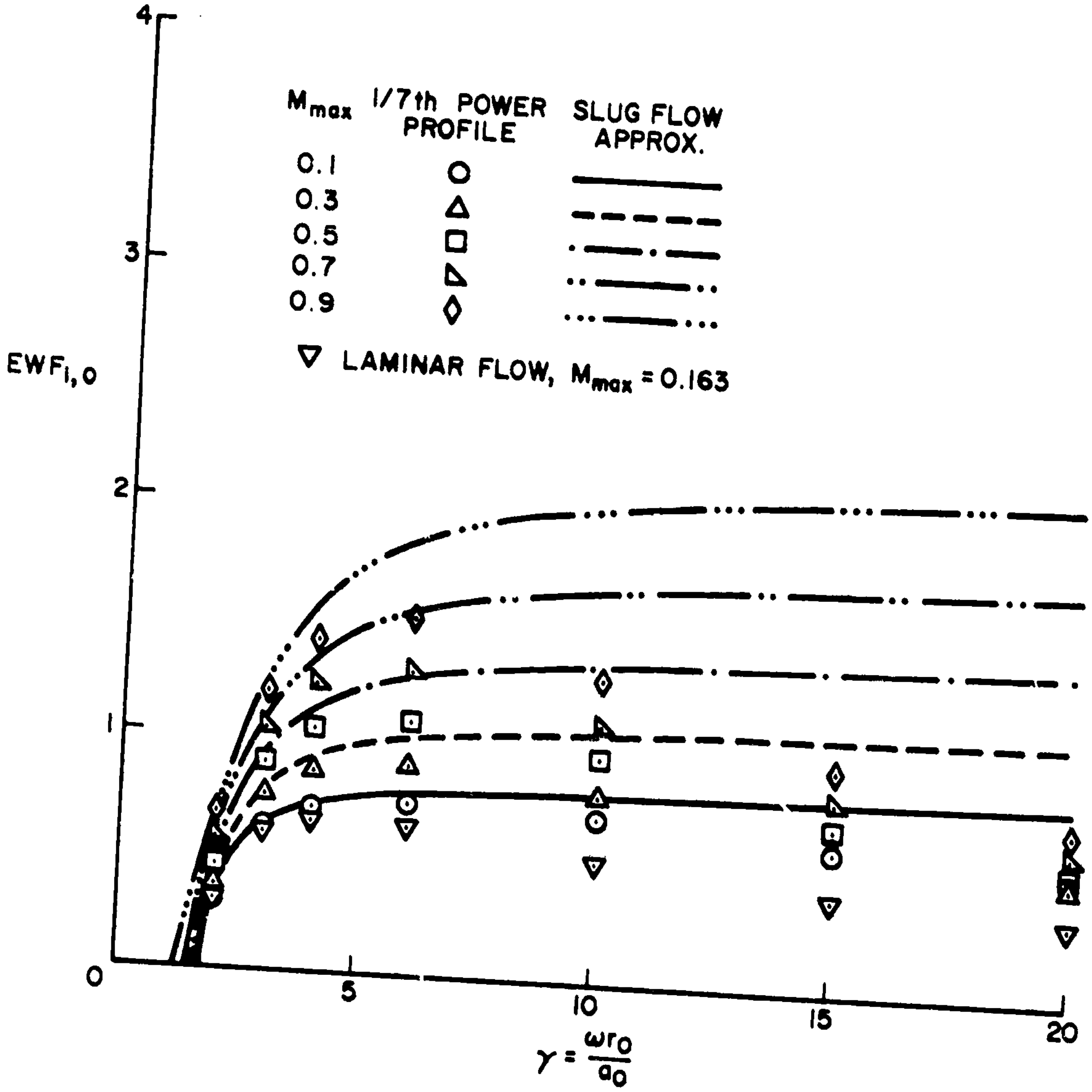

Fig. 26b. (1,0) mode energy weighting functions for sheared mean flow profiles and comparison to slug flow approximations.

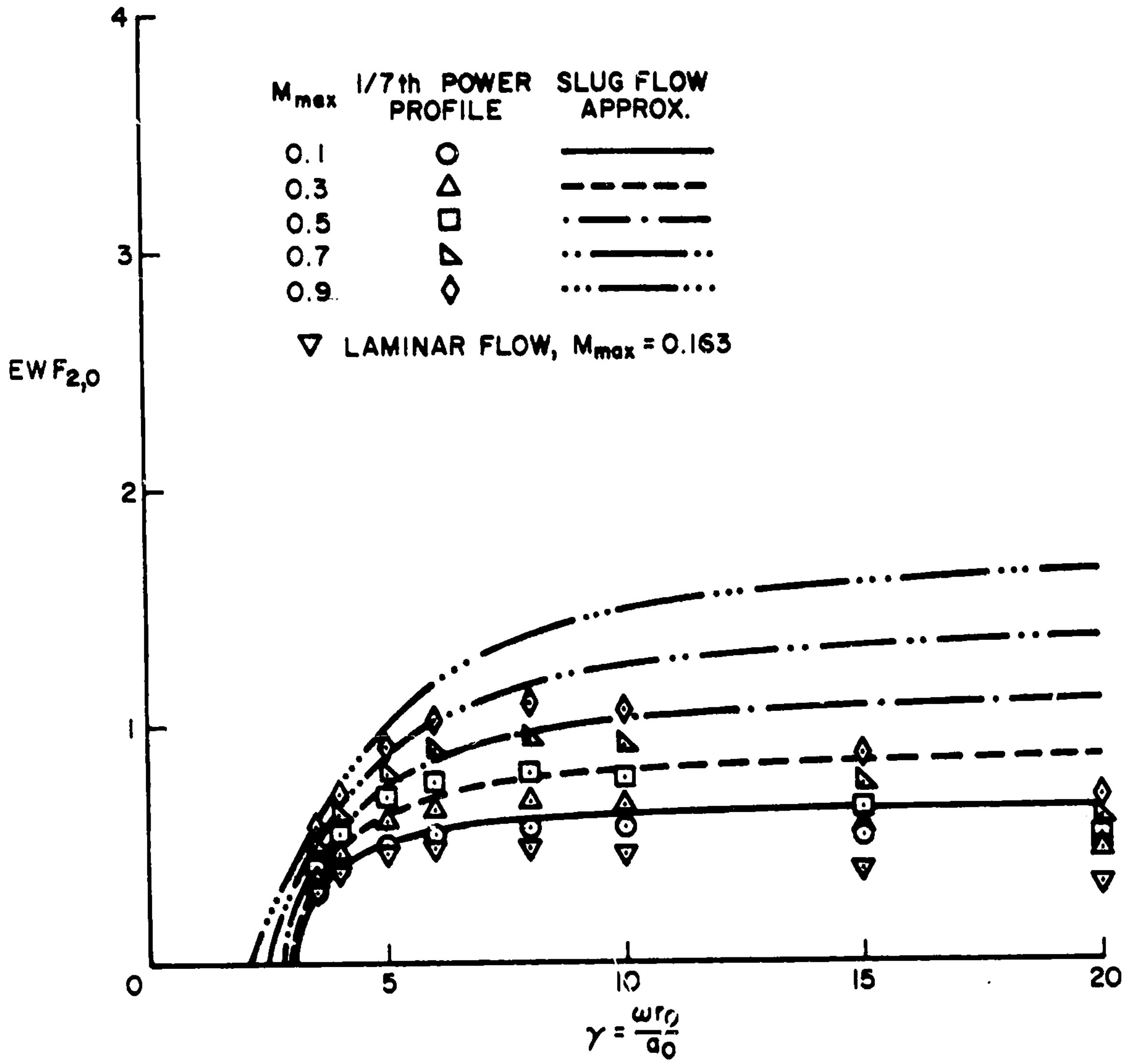

Fig. 26c. (2,0) mode energy weighting functions for sheared mean flow profiles and comparison to slug flow approximations.

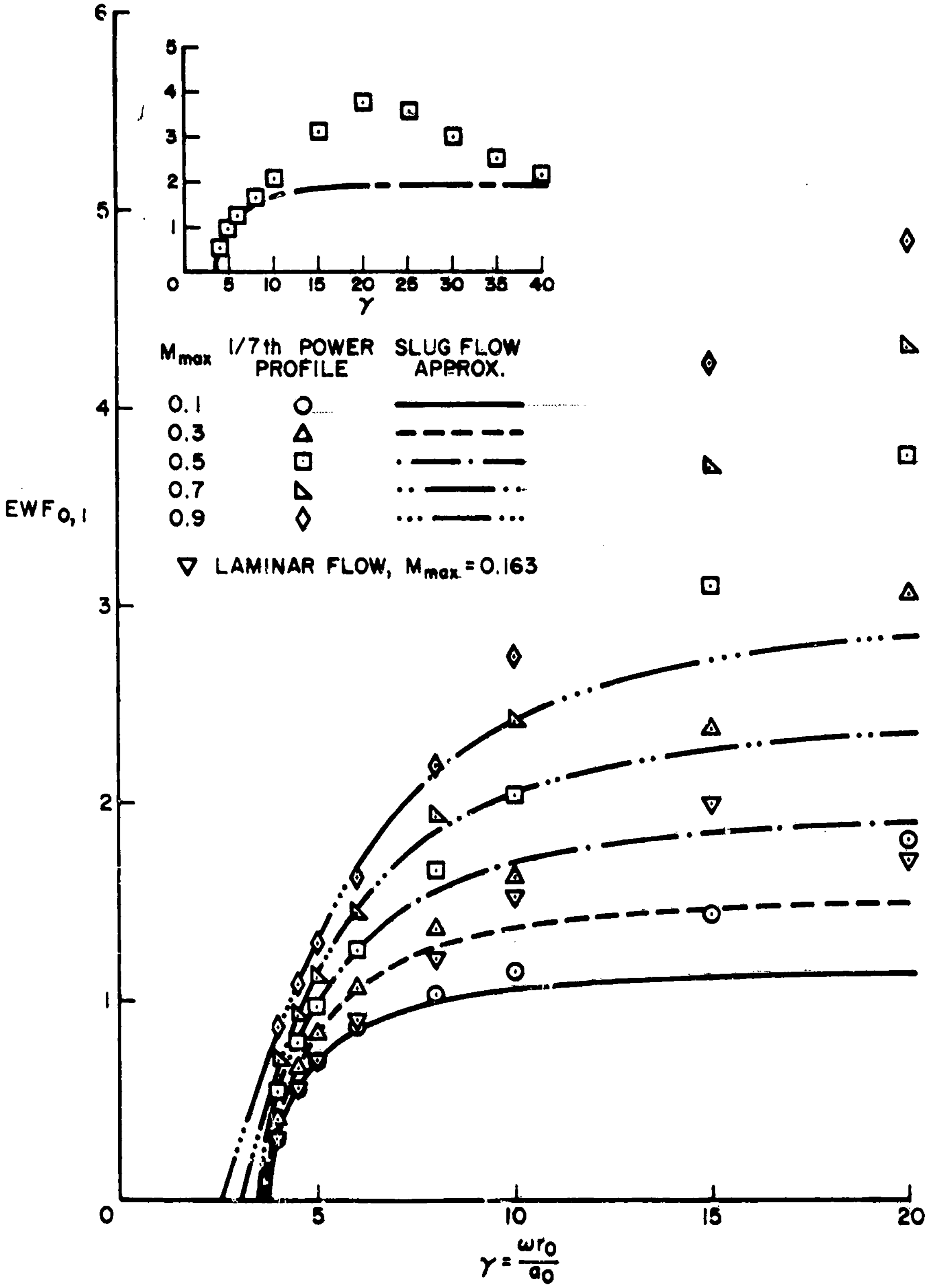

Fig. 26d. (0,1) mode energy weighting functions for sheared mean flow profiles and comparison to slug flow approximations

References

Allen, E. E., "Prediction and Abatement of Control Valve Noise," 1969 Instrument Society of America Annual Conference, Paper No. 69-535.

Banerian, Gordon, "Jet Noise -- The State-of-the-Art," Sound and Vibration, February 1974, pp. 30-34.

Baumann, H. O., "On the Prediction of Aerodynamically Created Sound Pressure Level of Control Valves," Paper No. WA/FE-28, ASME Winter Annual Meeting, New York, Nov. 29-Dec. 3, 1970.

Blockhintsev, D. I., "Acoustics of a Nonhomogeneous Moving Medium," NACA Technical Memo 1399, 1946.

Bolleter, U., and M. J. Crocker, "Theory and Measurement of Modal Spectra in Hard-Walled Cylindrical Ducts," The Journal of the Acoustical Society of America, Vol. 51, No. 5 (Part 1), 1972, pp. 1439-47.

Bretherton, F. P., and C. J. R. Garrett, "Wavetrains in Inhomogeneous Moving Media," Proc. Roy. Soc., A. 302, 1969, pp. 529-554.

Candel, S. M., "Acoustic Conservation Principles and an Application to Plane and Modal Propagation in Nozzles and Diffusers," Jour. of Sound and Vibration, Vol. 41, No. 2, 1975, pp. 207-232.

Cantrell, R. H., and R. W. Hart, "Interaction between Sound and Flow in Acoustic Cavities: Mass, Momentum, and Energy Considerations," The Jour. of the Acoustical Society of America, Vol. 36, No. 4, April 1964, pp. 697-706.

Cumpsty, N. A., "A Critical Review of Turbomachinery Noise," Trans. ASME, Jour. of Fluids Engrg., Vol. 99(I), No. 2, June 1977, pp. 278-293.

Dahlquist, Germund, and A. Bjorck, Numerical Methods (translated by Ned Anderson), Prentice-Hall, Englewood Cliffs, N. J. (1974).

Eversman, Walter, "Energy Flow Criteria for Acoustic Propagation in Ducts with Flow," Jour. of the Acoustical Soc. of America, Vol. 49, No. 6 (Part 1), 1971, pp. 1717-1721.

Fuchs, H. V., "Space Correlations of the Fluctuating Pressure in Subsonic Turbulent Jets," Jour. of Sound and Vibration, Vol. 23, No. 1, 1972, pp. 77-99.

Guiraud, J. P., "Geometric Acoustics and Ballistic Shock Waves," Comptes Rendus Academie des Sciences, Paris 258, 1964, pp. 4425-4428.

Harel, P., and M. Perulli, "Measurement, in a Duct, of the Space-Structure of the Discrete-Frequency Noise Generated by an Axial Compressor," Jour. of Sound and Vibration, Vol. 22, No. 4, 1972, pp. 487-506.

Hayes, Wallace D., "Energy Invariant for Geometric Acoustics in a Moving Medium," The Physics of Fluids, Vol. 11, No. 8, August 1968, pp. 1654-1656.

Heymann, Frank J., "Some Experiments Concerning Control Valve Noise," Noise-Con 73 Proceedings.

Hornbeck, Robert W., Numerical Methods, Quantum Publishers, Inc., New York, 1975, p. 309.

Karvelis, A. V., "An Experimental Investigation of the Wall Pressure Fluctuations in Piping Containing Simple Control Devices," Ph.D. thesis, The Pennsylvania State University Graduate School, Aug. 1975.

Kline, S. J., and F. A. McClintock, "The Description of Uncertainties in Single-Sample Experiments," Mechanical Engineering, Jan. 1953.

Kuhn, G. F., "Sound Transmission through Ducts with and without Flow," Inst. of Sound and Vibration Research, TR 65, Southampton Univ., England, Feb. 1974.

Lau, J. C., M. J. Fisher, and H. V. Fuchs, "The Intrinsic Structure of Turbulent Jets," Jour. of Sound and Vibration, Vol. 22, No. 4, 1972, pp. 379-406.

Michalke, A., and H. V. Fuchs, "On Turbulence and Noise of an Axi-symmetric Shear Flow," Jour. Fluid Mechanics, Vol. 70, Part 1, 1975, pp. 179-205.

Möhring, W., "Energy Flux in Duct Flow," Jour. of Sound and Vibration, Vol. 18, No. 1, 1971, pp. 101-109.

Mollo-Christensen, E., "Jet Noise and Shear Flow Instability Seen from an Experimenter's Viewpoint," Jour. Appl. Mechanics, Vol. 34, 1967, pp. 1-7.

Moore, C. J., "In-Duct Investigation of Subsonic Fan 'Rotor Alone' Noise," Jour. of the Acoustical Society of America, Vol. 51, No. 5 (part 1), 1972, pp. 1471-82.

Moore, C. J., "The Role of Shear-Layer Instability Waves in Jet Exhaust Noise," Jour. Fluid Mech., Vol. 80, Part 2, 1977, pp. 321-367.

Morfey, C. L., "Acoustic Energy in Non-Uniform Flows," Jour. of Sound and Vibration, Vol. 14, No. 2, 1971a, pp. 159-170.

Morfey, C. L., "Sound Transmission and Generation in Ducts with Flow," Jour. of Sound and Vibration, Vol. 14, No. 1, 1971b, pp. 37-55.

Mugridge, B. D., "The Measurement of Spinning Acoustic Modes Generated in an Axial Flow Fan," Jour. of Sound and Vibration, Vol. 10, No. 2, 1969, pp. 227-246.

Munger, P., and H. E. Plumblee, "Propagation and Attenuation of Sound in a Soft-Walled Annular Duct Containing a Sheared Flow," Basic Noise Research Conference, NASA SP-207, 1969, pp. 305-327.

Nakano, A., "Characteristics of Noise Emitted by Valves," The 6th Internatioanl Congress on Acoustics, Japan, Aug. 21-28, 1968, pp. 169-172.

Pridmore-Brown, D. C., "Sound Propagation in a Fluid Flowing through an Attenuating Duct," Jour. Fluid Mech., Vol. 4, 1958, pp. 393-406.

Rabiner, L. R., and Bernard Gold, Theory and Application of Digital Signal Processing, Prentice-Hall, Englewood Cliffs, N. Y. (1975), 414-418.

Ribner, H. S., "The Generation of Sound by Turbulent Jets," Advances in Appl. Mechanics, Vol. 8, Academic Press, 1964.

Roberts, D. W., and J. P. Johnston, "Development of a New Internal Flow Aeroacoustic Facility--Aerodynamic and Acoustic Experiments on Square-Edged Orifices," Thermosciences Div., Mech. Engrg. Dept., Stanford University, PD-18, Sept. 1974.

Ryshov, O. F., and G. M. Shefter, "On the Energy of Acoustic Waves Propagating in Moving Media," Jour. of Appl. Math. and Mech., 26, 1962, pp. 1293-1309.

Savkar, S. D., "Propagation of Sound in Ducts with Shear Flow," Jour. of Sound and Vibration, Vol. 19, No. 3, 1971, pp. 355-372.

Seebold, J. G., "Process Plant Noise Control at the Design Engineering Stage," Jour. of Engrg. for Industry, Nov. 1970, pp. 779-784.

Seliger, R. L., and G. B. Whitham, F.R.S., "Variational Principles in Continuum Mechanics," Proceedings of the Royal Society, A. 305, 1968, pp. 1-25.

Shankar, P. N., "Sound Propagation in Duct Shear Layers," Jour. of Sound and Vibration, Vol. 22, No. 2, 1972, pp. 221-232.

Thompson, P. A., Compressible-Fluid Dynamics, McGraw-Hill Book Co., New York, 1972.

Witczak, Krystyna J., "Flow Patterns and Noise of a Choked Gas Jet Expanding into a Duct," Archives of Acoustics, 1, 3, 1976, pp. 181-200.

Whitham, G. B., "A General Approach to Linear and Nonlinear Dispersive Waves Using a Lagrangian," Jour. Fluid Mech., 22, 1965, pp. 273-283.

Yardley, P. D., "Measurement of Noise and Turbulence Generated by Rotating Machines," Univ. of Southampton, Ph.D. thesis, 1975.

Yule, A. J., "Large-Scale Structure in Mixing Layer of a Round Jet," submitted to Jour. Fluid Mech., June 1977.

Appendix A1

COMPUTER PROGRAMS FOR THE MODE SEPARATION TECHNIQUES

The programs in this appendix are Fortran programs written for use with the Hewlett-Packard HP-2100A computer.

A1.1. Program PIPE

The computer program PIPE performs an on-line spectral analysis of an analogue input signal using digital spectral analysis techniques. The program is usually run from a remote teletype terminal located near the experimental apparatus. The plotted spectrum is displayed on the oscilloscope plotter. Results are printed on the line printer and stored on digital magnetic tape.

The program operates in an interactive fashion, with the computer stopping and asking for input and control variables at various points in the execution. The definitions of the input variables are included in the program listing on the following page.

A1.1. Listing of PIPE

```
FTN,L
      PROGRAM PIPE
C              2/3/77
C              E. KERSCHEN
C
C   THIS PROGRAM USES THE METHOD OF AVERAGED PERIODOGRAMS TO DETERMINE THE
C   POWER SPECTRUM OF A MICROPHONE SIGNAL.  THE SPECTRUM IS DISPLAYED ON THE
C   OSCILLOSCOPE PLOTTER. PARAMETERS &FINAL RESULTS ARE STORED ON MAG TAPE.
C
C   INPUT IS:  MICROPHONE SIGNAL INTO A/D CHANNEL 16
C         OR:  MAG TAPE PRODUCED BY:  PROGRAM UNOYS (7/2/76)
C
C   NOTE:  PROGRAM PARAMETERS ASSUME INPUT MICROPHONE SIGNAL IS
C          AMPLITUDE SCALED BY AMPLIFIER SECTION OF B&K 2010.
C
C   TTY COMMUNICATION IS PROMPTED AT STATEMENTS # 5, 6, 10, 12, 17, 111, 729.
C
C   OUTPUT IS:  SPECTRUM ON OSCILLOSCOPE PLOTTER
C               DOCUMENTATION ON LINE PRINTER
C               PARAMETER AND RESULTS STORAGE ON MAG TAPE
C
C
      COMMON IPT1(1300),IBF(4096),RMIKE(4096),AMIKE(1024),ALPLT(256),
     $FRQ(256)
      DIMENSION IDATE(40),IA(40),LINE(30),W(2048),IPT3(2000),CMIKE(2048)
      DIMENSION TCOEF(1024),ITBF(128),LABEL(10),IIY(256),YDB(256)
      DIMENSION ITIMES(5),ITIMEF(5)
      EQUIVALENCE (IBF(1),TCOEF(1),W(1),IPT3(1)),(RMIKE(1),CMIKE(1))
      EQUIVALENCE (IBF(2600),IIY(1)),(IBF(3000),YDB(1))
      EQUIVALENCE (ALPLT(1),ITBF(1)),(IA(30),LABEL(1))
C
C  DETERMINE DATA ACQUISITION MODE & SET PARAMETERS FOR THIS RUN
C  IDAQ = FLAG FOR DATA ACQUISITION MODE
C  IFILE = 'PIPE TAPE' FILE # FOR STORAGE OF RESULTS
C  DATE & COMMENTS ARE FOR DOCUMENTATION
C  NMODE = RADIAL MODE NUMBER
C  MMODE = CIRCUMFERENTIAL MODE NUMBER
C  GAIN = DB LEVEL OF B&K 2010 "METER ZERO"
C  NENSB = NUMBER OF PERIODOGRAM AVERAGES TO BE MADE
C
    4 WRITE (1,5)
    5 FORMAT("INPUT 'FLOWYS TAPE' FILE #.")
C NOTE: '.' IN PREVIOUS FORMAT STATEMENT IS TTY "BELL" SYMBOL
      READ (1,*) IFILE
      IF (IFILE.LE.0) GO TO 4
      WRITE (1,6)
    6 FORMAT("TYPE '1' FOR DATA TO BE ACQUIRED REAL TIME BY A/D SYSTEM"/
     1,"... '-1' FOR DATA TO BE READ FROM MAG TAPE.")
      READ (1,*) IDAQ
      IF (IDAQ.LT.0) GO TO 15
      WRITE (1,10)
   10 FORMAT(/"INPUT: DATE & A LINE OF COMMENTS FOR THIS RUN"/
     2"E.G.:  2/3/77"/
     3"      3/4 IN. NOZZLE, DELPLFM = 3.0 IN. H2O, 60 IN. DOWNSTREAM.")
      READ (1,11) IDATE,IA
   11 FORMAT (40A2,/,40A2)
      WRITE (1,12)
   12 FORMAT(//"INPUT: MMODE, NMODE, GAIN, NENSB.")
      READ (1,*) MMODE,NMODE,GAIN,NENSB
      GO TO 20
```

```
   15 READ (8,11) IDATE,IA
      READ (8,16) MMODE,NMODE,GAIN
   16 FORMAT(3E20.10)
      WRITE (1,17) IDATE,IA,MMODE,NMODE,GAIN
   17 FORMAT (2(40A2,/),"(",I1,",",I1,") MODE",5X,"GAIN:",F5.1," DB"/
     1/"TYPE IN 'NENSB'.")
      READ (1,*) NENSB
   20 CONTINUE
C
C
C    INITIALIZE ENSEMBLE COUNTER "NE"  &  SET PARAMETERS
C    BWD = BANDWIDTH FOR USE IN SPECTRA PLOT (HZ)
C    ISRP = PERIOD OF DIGITAL SAMPLING RATE (MICRO-SEC.)
C                        ISRP = 50    => 20 KHZ
C    NBINS = NUMBER OF POINTS PER DATA SET
C    APER = BASIC SAMPLE LENGTH (SEC.)
C    FREQ = SPECTRAL RESOLUTION (HZ/HARMONIC)
C    NSP = NUMBER OF POINTS OBTAINED BY A/D SYSTEM
C    NFC = A/D CHANNEL 16
C    "LABEL" ADDS DOCUMENTATION TO "IA"
C
      NE = 2
      BWD = 10.**1.5
      ISRP = 50
      NBINS = 2048
      APER = FLOAT(NBINS)*1.E-6*FLOAT(ISRP)
      FREQ = 1./APER
      FMAX = FREQ*FLOAT(NBINS/2)
      NSP = 2*NBINS
      NFC = 16 + 2008
C
C
C    HAMMING DATA WINDOW WILL BE USED TO TAPER MICROPHONE SAMPLES.
C    THE FOLLOWING STATEMENTS COMPUTE THE WEIGHTING COEFFICIENTS
C    TPOW = WINDOW POWER CORRECTION FACTOR
C
      PI = 3.14159265
      NCOEF = NBINS/2
      TPOW = 0.
      DO 50 I=1,NCOEF
      TCOEF(I) = 0.54  -  0.46*COS(PI*FLOAT(I-1)/1023.)
   50 TPOW = TPOW + TCOEF(I)**2
      TPOW = 2.*TPOW
C
C    TWO CORRECTION FACTORS ARE NEEDED TO CALCULATE SPECTRA FROM
C    DATA SAMPLES.
C    SNORM NORMALIZES FFT OUTPUT.
C    CRCT COMPENSATES FOR FACTORS INTRODUCED BY THE MODE SEPARATION
C    TECHNIQUE.
C
      SNORM = 1./(TPOW*NBINS*10.0)
      CRCT = 16.0
      IF (MMODE.EQ.1) CRCT = 4.0
      IF (MMODE.GT.5) CRCT = 1.0
C
C    TO CONSERVE MEMORY, STORE "TCOEF" ON DISC
C
      CALL EXEC(17,IFTK,ILTK,ISIZ)
      CALL EXEC(2,2,TCOEF,2048,IFTK,0)
C
```

```
C
C.  INITIALIZE "W" ARRAY FOR FFT & STORE ON DISC
      CALL IFFT(W,2048,0)
      CALL EXEC(2,2,W,4096,IFTK,16)
C
C
C
C    INITIALIZE AMIKE - THIS ARRAY WILL CONTAIN CURRENT PSD AVERAGE
C      AMIKE = NORMALIZED MAGNITUDE SQUARE (PEAK) OF SPECTRA
C                => VOLTS**2. REF. B&K 2010
      DO 60 I=1,1024
   60 AMIKE(I) = 0.0
C
C
C    OBTAIN MICROPHONE SAMPLE
C    NOTE THAT TWO DATA SETS ARE OBTAINED SEQUENTIALLY.
C    COMPLEX FFT WILL TRANSFORM TWO DATA SETS SIMULTANEOUSLY IN SAME TIME
C    AS SINGLE DATA SET.
C
      IF (IDAQ.LE.0) GO TO 110
C
C
C    IF THIS BRANCH ENTERED, SET UP A/D SYSTEM & GET DATA
C    BUT FIRST, GET STARTING TIME FROM SYSTEM DISC FOR LATER COMPUTATION
C    OF 'EFFECTIVE AVERAGING TIME' (TBAR).
C
      CALL EXEC(11,ITIMES)
   99 CALL I2313(7,0)
      CALL I2313(7,6,0,0,5,4)
      CALL I2313(7,6,-1,0,ISRP,0)
      CALL I2313(7,2,-1,0,NFC,NSP,IBF,0)
C    WAIT UNTIL DATA ARE READ IN
  100 CALL I2313(7,1,ISTAT,ILOG)
      IF (ISTAT.LT.0) GO TO 100
      CALL I2313(7,0)
C    IF LAST ENSEMBLE, GET FINISH TIME FROM SYSTEM DISC.
      IF (NE.EQ.NENSB) CALL EXEC(11,ITIMEF)
C    CHECK FOR A/D TIMING ERRORS
      IF(IDTST(IBF,NSP).GE.0) GO TO 104
      WRITE (1,101) NE
  101 FORMAT(I8,"TH SAMPLE RETAKEN - PACING ERROR DETECTED")
      GO TO 99
C    CHECK THAT DATA IS WITHIN  +-10 VOLT DYNAMIC RANGE
C    NOTICE IS GIVEN IF OVERLOAED POINTS EXCEED  10% OF SAMPLE
  104 CALL OVLOD(IBF,NSP,NPOLD,NNOLD,1)
      IF(NPOLD+NNOLD.LT.409) GO TO 140
      WRITE(1,105) NE,NPOLD,NNOLD
  105 FORMAT("SAMPLE",I5,":",10X,I4," +OVERLOADS,",10X,I4," -OVERLOADS")
      GO TO 140
C
C
C    IF THIS BRANCH ENTERED, GET DATA FROM MAG TAPE
C    NOTE THAT SYNCHRONIZATION SIGNAL, INTERLEAVED WITH MIKE SIGNAL, IS DISCARDED
C
  110 WRITE (1,111)
  111 FORMAT(/"TYPE IN AVERAGING TIME (SEC.).")
      READ (1,*) TBAR
      TMIN = FLOAT(NENSB)*FLOAT(NBINS)*FLOAT(ISRP)*1.E-6
      IF (TBAR.LT.TMIN) TBAR=TMIN
      TMAX = 12./SPEED*FLOAT(NRR)
```

```
      IF(IBAR.GT.IMAX) TBAR=TMAX
      WRITE (6,112) TBAR
  112 FORMAT('TBAR TO BE USED:',F6.2,' SEC.'//)
      NDBLK = NSP/64
      SBLK = (((TBAR/(ISRP*1.E-6))-NSP)/(NENSB-2)/64.) - FLOAT(NDBLK)
      GO TO 121
  120 NSBLK = IFIX(SBLK*FLOAT(NE-2))/(NE-2)
      CALL PTAPE(8,0,NSBLK)
  121 DO 130 J=1,NDBLK
      IO = 64*(J-1)
      CALL EXEC(1,8,ITBF,128)
      IF (IEOF(6).GE.0) GO TO 129
C  IF EOF HAS BEEN READ, RECOMPUTE TBAR AND END DATA ACQUISITION
      TBAR = ((NE-4)*(SBLK+NDBLK)+NDBLK)*ISRP*1.E-6
      GO TO 260
  129 DO 130 I=1,64
  130 IBF(I+IO) = ITBF(2*I-1)
C
C
C   CONVERT DATA TO FLOATING POINT (VOLTAGE) FORM,  INTERLEAVE
C   FOR USE IN FFT, & STORE IN ARRAY "RMIKE"
  140 DO 150 I=1,2048
      I2 = 2*I
      RMIKE(I2-1) = IAND(IBF(I),177760B)*0.0003125
      RMIKE(I2) = IAND(IBF(2048+I),177760B)*0.0003125
  150 CONTINUE
C
C
C
C   RECALL "TCOEF" FROM DISC & APPLY DATA TAPER
      CALL EXEC(1,2,TCOEF,2048,IFTK,0)
      DO 160 I=1,1024
      I2 = 2*I
      RMIKE(I2-1) = TCOEF(I) * RMIKE(I2-1)
      RMIKE(I2)   = TCOEF(I) * RMIKE(I2)
      RMIKE(4098-I2) = TCOEF(I) * RMIKE(4098-I2)
  160 RMIKE(4097-I2) = TCOEF(I) * RMIKE(4097-I2)
C
C   COMPUTE & REMOVE RESIDUAL MEAN FROM DATA
C   F(X) <= F(X) - FBAR
      SUM1=0.
      SUM2=0.
      DO 190 I=1,NSP,2
      SUM1=SUM1+RMIKE(I)
  190 SUM2=SUM2+RMIKE(I+1)
      FBAR1=SUM1/FLOAT(NBINS)
      FBAR2=SUM2/FLOAT(NBINS)
      DO 195 I=1,NSP,2
      RMIKE(I)=RMIKE(I)-FBAR1
  195 RMIKE(I+1)=RMIKE(I+1)-FBAR2
C
C   RECALL "W" FROM DISC & COMPUTE FOURIER TRANSFORM
      CALL EXEC(1,2,W,4096,IFTK,16)
      CALL FFT(RMIKE)
C
C
C   SUM POWER INTO EACH FREQUENCY IN RUNNING AVERAGE
      DO 210 I=2,1025
      J = I-1
      I2 = 2*I
```

```
      NM12 = 4100 - I2
      XSPYS=(RMIKE(I2-1)**2+RMIKE(NM12-1)**2+RMIKE(I2)**2+
     $RMIKE(NM12)**2)/CRCT
      AMIKE(J) = AMIKE(J) + (SNORM*XSPYS - AMIKE(J) - AMIKE(J))/NE
  210 CONTINUE
C
C
C   COMPUTE CURRENT ESTIMATE OF NORMALIZED STATISTICAL ERROR
      STERR = 1.00/SQRT(FLOAT(NE))
      STERP = 1.0/SQRT(NE*BWD/FREQ)
C
C   COMPUTE CURRENT R.M.S. PRESSURE & SPL
C   THIS MUST BE NORMALIZED FOR B&K 2010
      SS = 0.
      DO 220 I=1,1024
  220 SS = SS + AMIKE(I)
      DB = 10.*ALOG10(SS)  + GAIN
      EMRMS = SQRT(SS)
C
C   WRITE OUT CURRENT VALUES ON TERMINAL
      WRITE (1,250) NE,STERR,STERP,DB
  250 FORMAT("AFTER",I3," ENSEMBLES  (",F3.2,"/",F3.2," STATISTICAL ERRO
     2RS), SPL =",F5.1," DB")
C
C   TEST ENSEMBLE COUNTER
      NE = NE + 2
      IF(NE.LE.NENSB) IF(IDAQ)120,99
  260 NE = NE - 2
      NENSB = NE
C
C   DETERMINE EFFECTIVE AVERAGING TIME, IF NOT PREVIOUSLY SPECIFIED.
C
      IF (IDAQ.LE.0) GO TO 600
      TH = ITIMEF(4) - ITIMES(4)
      TM = ITIMEF(3) - ITIMES(3)
      TS = ITIMEF(2) - ITIMES(2)
      TF = ITIMEF(1) - ITIMES(1)
      TBAR = TF/100. + TS + 60.*(TM + 60.*TH)
C
C   CALCULATE THE POWER SPECTRAL DENSITY BASED ON "BWD" BANDWIDTH.
C
      AGAIN = 10.**(GAIN /10.)
      DO 640 IX=1,256
      YDB(IX) = 0.
      ITY(IX) = 0
  640 ALPLT(IX) = 0.
      DO 680 IX=32,250
      FRQ(IX) = 6000.*(IX-25)/225.
      FL = FRQ(IX) - BWD/2.
      FU = FRQ(IX) + BWD/2.
      RJL = FL/FREQ
      JL = RJL
      IF(RJL-JL.GT.0.5) JL = JL+1
      RJU = FU/FREQ
      JU = RJU
      IF(RJU-JU.GT.0.5) JU = JU+1
      AREA = 0.0
      DO 670 J=JL,JU
  670 AREA = AREA + AMIKE(J)
      AREA=AREA-AMIKE(JL)*(RJL-JL+0.5)-AMIKE(JU)*(JU+0.5-RJU)
```

```
      ALPLT(IX) = AGAIN*AREA/BWD
  600 YDB(IX) = 10.*ALOGT(ALPLT(IX))
C
C   SET UP SCOPE 'GRAPH PAPER'
C   HORIZONTAL AXIS IS FREQUENCY PLOTTED LINEARLY ( 0 TO 6000 HZ )
C   VERTICAL AXIS IS POWER SPECTRAL DENSITY PLOTTED LOGARITHMICALLY.
C
C   FIND MAXIMUM SIGNAL AND SCALE GRAPH ACCORDINGLY.
C
      ALMAX = ALPLT(32)
      DO 500 I=33,250
      IF (ALPLT(I).GT.ALMAX) ALMAX = ALPLT(I)
  500 CONTINUE
      DBMAX = 10*ALOGT(ALMAX)
      MSCALE = (INT(DBMAX)/10)*10 + 10
      NGAIN = MSCALE - 20
C
  600 YGAIN = 5.0
      CALL SETUP(1,IPT1(1),IPT1(1300),1300,ISTA)
      CALL XAXIS(25,255,2,20)
      CALL XAXIS(25,255,2,255)
      CALL YAXIS(25,20,255,2)
      CALL YAXIS(255,20,255,2)
      DO 610 L=1,9
      K = 5-L
      IYTIC = 132. +K*5*YGAIN
      CALL XAXIS(26,29,1,IYTIC)
  610 CALL XAXIS(252,254,1,IYTIC)
      DO 615 L=1,6
      IX = 25. + 37.5*L
      CALL YAXIS(IX,20,23,1)
      CALL YAXIS(IX,252,254,1)
      CALL CODE
      WRITE(LINE,612) L
  612 FORMAT(I1)
      IX = IX - 3
      CALL STLIN(IX,6,LINE,-1)
  615 CONTINUE
      CALL CODE
      WRITE(LINE,621)
  621 FORMAT("DB")
      CALL STLIN(8,245,LINE,-2)
      DO 625 L=1,5
      N = NGAIN + (L-3)*10
      M = 129. + (L-3)*10*YGAIN
      CALL CODE
      WRITE(LINE,624) N
  624 FORMAT(I3)
  625 CALL STLIN(3,M,LINE,-3)
      CALL CODE
      WRITE(LINE,626)
  626 FORMAT("KHZ")
      CALL STLIN(140,2,LINE,-3)
      CALL CODE
      WRITE(LINE,630) MMODE,NMODE
  630 FORMAT("(",I1,",",I1,") MODE")
      CALL STLIN(100,240,LINE,-10)
C
C   NOW PLOT THE SPECTRUM
C
```

```
      CALL SETUP(2,IPT3(1),IPT3(2000),2000,ISTC)
      DO 685 IX=32,250
      IY = 132. + YGAIN*(YDB(IX)-NGAIN)
      IF (IY.LT.20) GO TO 685
      CALL ISTPN(IX,IY)
      IIY(IX) = IY
  685 CONTINUE
C
C   NOW ADD PSEUDO-CONNECTING LINES SO SPECTRA PLOT APPEARS CONTINUOUS
C
  690 DO 695 IX=33,249
      IYM1 = IIY(IX) - 1
      IF (IYM1.LT.20) GO TO 695
      IB = MINO(IIY(IX-1),IIY(IX+1))
      IF (IB.LT.20) IB=20
      IF (IB.GE.IYM1) GO TO 695
      CALL YAXIS(IX,IB,IYM1,2)
  695 CONTINUE
C
C
C   LIST IMPORTANT PARAMETERS ON LINE PRINTER
C
      WRITE (6,721) IDATE,MMODE,NMODE,IA,NENSB,STERR,STERP,TBAR
      WRITE (6,722) APER,FMAX,FREQ,BWD
      WRITE (6,723) GAIN,EMRMS,DB
      WRITE (6,724) IFILE
  721 FORMAT("1",40A2,//,1X,"(",I1,",",I1,") MODE",//,1X,40A2,///
     $" AVERAGED PERIODOGRAM SPECTRA:",/,1X
     1,I5," SAMPLES TAKEN  =>  NORMALIZED STATISTICAL ERRORS =",F4.2,"/"
     2,F5.2,/,1X,F7.1," SEC. AVERAGING TIME",/)
  722 FORMAT(11X,"SAMPLE LENGTH:",F26.5," SEC.",/11X,"MAXIMUM FREQUENCY:
     1",F17.0,"   HZ",/,11X,"MAXIMUM SPECTRAL RESOLUTION:",F9.2," HZ",/,
     211X,"PLOT EQUIVALENT BANDWIDTH:",F6.1,"  HZ",/)
  723 FORMAT(" B&K 2010 AMPLIFIER 'METER ZERO':",F5.1," DB",/," R.M.S. V
     1OLTAGE OF AVERAGED PRESSURE SIGNAL:",F6.2," VOLTS",/," FOR SPL OF:
     2",F6.2," DB",////)
  724 FORMAT(" DATA STORAGE:  'PIPE TAPE' FILE #",I4,/," SOURCE PROGRAM
     1:  PIPE (2/3/77)")
C
      WRITE (6,725) IFILE
  725 FORMAT ("1",25X,"FILE #",I4,/" ",4(4X,"FREQ.   DB "))
      WRITE (6,728)
  728 FORMAT ("      ")
      DO 726 IX=32,85
      IX1 = IX + 55
      IX2 = IX1 + 55
      IX3 = IX2 + 55
  726 WRITE (6,727) FRQ(IX),YDB(IX),FRQ(IX1),YDB(IX1),FRQ(IX2),
     $YDB(IX2),FRQ(IX3),YDB(IX3)
  727 FORMAT (" ",4(4X,F5.0,1X,F5.1))
      WRITE (6,727) FRQ(86),YDB(86),FRQ(141),YDB(141),FRQ(196),
     $YDB(196)
C
C
C
C   DISPLAY SPECTRA AND LIST ON TERMINAL IF DESIRED.
C
      CALL DSPLY(1,2,0)
      WRITE (1,730)
  730 FORMAT ("TYPE '1' IF LISTING IS DESIRED ON TERMINAL,"/
```

```
     $,"OTHERWISE TYPE '-1'")
      READ (1,*) LIST
      IF (LIST.EQ.-1) GO TO 735
      WRITE (1,736)
  736 FORMAT ("0",4(4X,"FREQ.   DB ")/)
      DO 737 IX=32,85
      IX1 = IX + 55
      IX2 = IX1 + 55
      IX3 = IX2 + 55
  737 WRITE (1,738) FRQ(IX),YDB(IX),FRQ(IX1),YDB(IX1),FRQ(IX2),
     $YDB(IX2),FRQ(IX3),YDB(IX3)
  738 FORMAT (" ",4(4X,F5.0,1X,F5.1))
      WRITE (1,738) FRQ(86),YDB(86),FRQ(141),YDB(141),FRQ(196),
     $YDB(196)
  735 CONTINUE
      WRITE (1,739)
  739 FORMAT (" TYPE '1' TO STORE OUTPUT ON MAG TAPE,"/
     $" OTHERWISE TYPE '-1'")
      READ (1,*) STORE
      CALL DSPLY(-1,0,0)
      IF(STORE.EQ.-1) GO TO 1000
C
C   STOREINFORMATION ON MAG TAPE.
C
C
      REWIND 8
      NFILE = IFILE - 1
      CALL PTAPE(8,NFILE,0)
      WRITE (8,731) IDATE
      WRITE (8,731) IA
      WRITE (8,732) IFILE,NBINS,NENSB,MMODE,NMODE
      WRITE (8,733) APER,FMAX,FREQ,STERR,STERP
      WRITE (8,733) EMRMS,DB,GAIN,BWD,TBAR
      WRITE (8,734)
  731 FORMAT(40A2)
  732 FORMAT(3I20,2I1)
  733 FORMAT(5E20.7)
  734 FORMAT(" THIS RECORD INTENTIONALLY LEFT BLANK")
      CALL EXEC(2,8,AMIKE,2048)
      CALL EXEC(2,8,ALPLT,512)
      END FILE 8
      END FILE 8
      REWIND 8
C
C   THIS SECTION EXITS PROGRAM
C
 1000 CONTINUE
      STOP
      END
$
LIST END ****
```

A1.2. Program PIPE4

The computer program PIPE4 digitally samples three microphone outputs ($P_w(0)$, $P_w(\frac{\pi}{2})$, and $P_w(\pi)$), performs the subtractions ($P_w(0) - P_w(\pi)$) and ($P_w(0) - P_w(\frac{\pi}{2})$), and calculates the frequency spectra of $P_w(0)$, ($P_w(0) - P_w(\pi)$) and $P_w(0) - P_w(\frac{\pi}{2})$). The spectra are displayed on the oscilloscope plotter and stored on magnetic tape for later use. Results are listed on the line printer.

This program also operates in an interactive fashion and is usually controlled from a remote teletype terminal. Input and control variables are explained in the comment lines included in the listing.

A1.2. Listing of PIPE4

```
FIN,L
      PROGRAM PIPE4
C           6/17/77
C           E. KERSCHEN
C
C   THIS PROGRAM TAKES SIMULTANEOUS SAMPLES OF P(0), P(90) AND P(180) TO
C   FORM THE TIME AVERAGED SPECTRA <P(0)**2>, <(P(0) - P(180))**2> AND
C   <(P(0) - P(90))**2> NECESSARY FOR TIME AVERAGED MODE SEPARATION.  THE
C   TIME AVEAGED OUTPUTS ARE STORED ON TAPE FOR USE WITH PIPE3.
C
C   INPUT IS:  MICROPHONE P(0) INTO CHAN. 16, P(90) INTO CHAN. 17 AND
C              P(180) INTO CHAN. 18.
C
C
C   OUTPUT IS:  SPECTRUM ON OSCILLOSCOPE PLOTTER
C               DOCUMENTATION ON LINE PRINTER
C               PARAMETER AND RESULTS STORAGE ON MAG TAPE
C
C
      COMMON IBF(6144),IMIKE(2048,3),AMIKE(512,3)
      DIMENSION IDATE(40),IA(40),LINE(30),W(1024),IPT3(2000),IFILE(3)
      DIMENSION ICOEF(512),IIY(256),YDB(256),ALPLT(256),FRQ(256)
      DIMENSION ITIMES(5),ITIMEF(5),NPOLD(3),NNOLD(3),EMRMS(3),DB(3)
      DIMENSION RMIKE(2048),CMIKE(512),IPT1(1300)
      EQUIVALENCE (IBF(1),ICOEF(1),W(1),YDB(1)),(IBF(2049),RMIKE(1))
      EQUIVALENCE (IBF(513),IIY(1)),(IBF(769),ALPLT(1))
      EQUIVALENCE (IBF(1281),FRQ(1)),(IBF(1793),IPT1(1))
      EQUIVALENCE (IBF(3093),IPT3(1)),(IBF(5121),CMIKE(1))
C
C  SET PARAMETERS FOR THIS RUN
C  IFILE = 'PIPE TAPE' FILE # FOR STORAGE OF RESULTS
C  DATE & COMMENTS ARE FOR DOCUMENTATION
C  NMODE IS SET TO '6' FOR THIS PROGRAM
C  MMODE IS SET TO '6' FOR THIS PROGRAM
C  GAIN1 = DB LEVEL OF B&K 222 GAIN SETTING
C  GAIN = 130 - GAIN1 , FOR CONSISTENCY WITH OTHER PROGRAMS.
C  NENSB = NUMBER OF PERIODOGRAM AVERAGES TO BE MADE
C
      WRITE (1,5)
    5 FORMAT("INPUT 'FLONYS TAPE' FILE NUMBERS FOR STORAGE OF"/
     $"<P(0)**2>, <(P(0) - P(180))**2> AND <(P(0) - P(90))**2>")
C
      READ (1,*) IFILE(1),IFILE(2),IFILE(3)
      WRITE (1,10)
   10 FORMAT(/"INPUT: DATE & A LINE OF COMMENTS FOR THIS RUN"/
     2"E.G.:  2/3/77"/
     3"     3/4 IN. NOZZLE, DELPLFM = 3.0 IN. H2O, 60 IN. DOWNSTREAM.")
      READ (1,11) IDATE,IA
   11 FORMAT (40A2,/,40A2)
      WRITE (1,12)
   12 FORMAT(//"INPUT:  GAIN1, NENSB.")
      READ (1,*) GAIN1,NENSB
      MMODE = 6
      NMODE = 6
      GAIN = 130 - GAIN1
C
C
C   INITIALIZE ENSEMBLE COUNTER "NE"  &  SET PARAMETERS
C   BWD = BANDWIDTH FOR USE IN SPECTRA PLOT (HZ)
C   ISRP = PERIOD OF DIGITAL SAMPLING RATE (MICRO-SEC.)
```

```
C   NBINS = NUMBER OF POINTS PER DATA SET
C   APER = BASIC SAMPLE LENGTH (SEC.)
C   FREQ = SPECTRAL RESOLUTION (HZ/HARMONIC)
C   NSP = NUMBER OF POINTS OBTAINED BY A/D_SYSTEM
C   NFC = A/D CHANNEL 16
C
      NE = 2
      BWD = 10.**1.5
      ISRP = 71
      NBINS = 1024
      APER = FLOAT(NBINS)*1.E-6*FLOAT(ISRP)
      FREQ = 1./APER
      FMAX = FREQ*FLOAT(NBINS/2)
      NSP = (2*NBINS)*3
      NFC = 16 + 2008
      NLC = 18 + 2008
C
C
C    HAMMING DATA WINDOW WILL BE USED TO TAPER MICROPHONE SAMPLES.
C    THE FOLLOWING STATEMENTS COMPUTE THE WEIGHTING COEFFICIENTS
C    TPOW = WINDOW POWER CORRECTION FACTOR
C
      PI = 3.14159265
      NCOEF = NBINS/2
      TPOW = 0.
      DO 50 I=1,NCOEF
      TCOEF(I) = 0.54  -  0.46*COS(PI*FLOAT(I-1)/511.)
   50 TPOW = TPOW + TCOEF(I)**2
      TPOW = 2.*TPOW
C
C    SNORM NORMALIZES FFT OUTPUT.
C
      SNORM = 1./(TPOW*NBINS)
C
C    TO CONSERVE MEMORY, STORE "TCOEF" ON DISC
C
      CALL EXEC(17,IFTK,ILTK,ISIZ)
      CALL EXEC(2,2,TCOEF,1024,IFTK,0)
C
C
C    INITIALIZE "W" ARRAY FOR FFT & STORE ON DISC
      CALL IFFT(W,1024,0)
      CALL EXEC(2,2,W,2048,IFTK,8)
C
C
C    INITIALIZE AMIKE.  AMIKE WILL CONTAIN CURRENT PSD
C    AVERAGES (RELATIVE TO 'GAIN').
C
      DO 60 J=1,3
      DO 60 I=1,512
   60 AMIKE(I,J) = 0.0
C
C
C    OBTAIN MICROPHONE SAMPLE
C    NOTE THAT TWO DATA SETS ARE OBTAINED SEQUENTIALLY.
C    COMPLEX FFT WILL TRANSFORM TWO DATA SETS SIMULTANEOUSLY IN SAME TIME
C    AS SINGLE DATA SET.
C
      WRITE(1,70)
   70 FORMAT(/" NENSB",3X,"STAT. ERR.",3X,"<P(0)**2>",3X,
```

```
     $"<(P(0)-P(180))**2>",3X,"<(P(0)-P(90))**2>")
C
C
C     SET UP A/D SYSTEM & GET DATA.
C     BUT FIRST, GET STARTING TIME FROM SYSTEM DISC FOR LATER COMPUTATION
C     OF 'EFFECTIVE AVERAGING TIME' (TBAR).
C
      CALL EXEC(11,ITIMES)
   99 CALL I2313(7,0)
      CALL I2313(7,7,0,3,140B,NLC)
      CALL I2313(7,6,0,0,5,5)
      CALL I2313(7,6,-1,0,ISRP,0)
      CALL I2313(7,2,-1,2,NFC,NSP,IBF,0)
C     WAIT UNTIL DATA ARE READ IN
  100 CALL I2313(7,1,ISTAT,ILOG)
      IF (ISTAT.LT.0) GO TO 100
      CALL I2313(7,0)
C     IF LAST ENSEMBLE, GET FINISH TIME FROM SYSTEM DISC.
      IF (NE.EQ.NENSB) CALL EXEC(11,ITIMEF)
C     CHECK FOR A/D TIMING ERRORS
      IF(IDIST(IBF,NSP).GE.0) GO TO 104
      WRITE (1,101) NE
  101 FORMAT(I8,"TH SAMPLE RETAKEN - PACING ERROR DETECTED")
      GO TO 99
C     CHECK THAT DATA IS WITHIN  +-10 VOLT DYNAMIC RANGE
C     NOTICE IS GIVEN IF OVERLOADED POINTS EXCEED  5% OF SAMPLE
  104 CALL OVLOD(IBF,NSP,NPOLD,NNOLD,3)
      MPOLD = NPOLD(1) + NPOLD(2) + NPOLD(3)
      NOLD = NNOLD(1) + NNOLD(2) + NNOLD(3)
      IF(MPOLD+NOLD.LT.(NSP/20)) GO TO 130
      WRITE(1,105) NE,MPOLD,NOLD
  105 FORMAT("SAMPLE",I3,":",10X,I4," +OVERLOADS,",10X,I4," -OVERLOADS")
C
C     SEPARATE DATA INTO P(0)=IMIKE(I,1), (P(0)-P(180))=IMIKE(I,2)
C     AND (P(0)-P(90))=IMIKE(I,3).  DATA WILL BE CONVERTED TO FLOATING
C     POINT VOLTAGE FORM LATER.
C
C
  130 DO 140 I=1,2048
      IMIKE(I,1) = IAND(IBF(3*I-2),177760B)/4
      IMIKE(I,2) = IMIKE(I,1) - IAND(IBF(3*I),177760B)/4
  140 IMIKE(I,3) = IMIKE(I,1) - IAND(IBF(3*I-1),177760B)/4
C
C     CALCULATE FOURIER TRANSFORMS OF P(0), (P(0)-P(180)) AND (P(0)-P(90)).
C
      DO 250 J=1,3
C
C     INTERLEAVE FOR USE IN FFT, STORE IN ARRAY "RMIKE", AND CONVERT
C     TO FLOATING POINT VOLTAGE FORM.
C
      DO 150 I=1,1024
      I2 = 2*I
      RMIKE(I2-1) = IMIKE(I,J)*0.00125
      RMIKE(I2) = IMIKE(NBINS+I,J)*0.00125
  150 CONTINUE
C
C
C
C     RECALL "TCOEF" FROM DISC & APPLY DATA TAPER
      CALL EXEC(1,2,TCOEF,1024,IFTK,0)
```

```
      DO 180 I=1,512
      I2 = 2*I
      RMIKE(I2-1) = TCOEF(I) * RMIKE(I2-1)
      RMIKE(I2)   = TCOEF(I) * RMIKE(I2)
      RMIKE(2050-I2) = TCOEF(I) * RMIKE(2050-I2)
  180 RMIKE(2049-I2) = TCOEF(I) * RMIKE(2049-I2)
C
C    COMPUTE & REMOVE RESIDUAL MEAN FROM DATA
C    F(X) <= F(X) - FBAR
      SUM1=0.
      SUM2=0.
      DO 190 I=1,NBINS
      I2 = 2*I
      SUM1=SUM1+RMIKE(I2-1)
  190 SUM2=SUM2+RMIKE(I2)
      FBAR1=SUM1/FLOAT(NBINS)
      FBAR2=SUM2/FLOAT(NBINS)
      DO 195 I=1,NBINS
      I2 = 2*I
      RMIKE(I2-1)=RMIKE(I2-1)-FBAR1
  195 RMIKE(I2)=RMIKE(I2)-FBAR2
C
C    RECALL "W" FROM DISC & COMPUTE FOURIER TRANSFORM
      CALL EXEC(1,2,W,2048,IFTK,8)
      CALL FFT(RMIKE)
C
C
C    SUM POWER INTO EACH FREQUENCY IN RUNNING AVERAGE
      DO 210 I=2,513
      I1 = I-1
      I2 = 2*I
      NMI2 = 2052 - I2
      XSPYS=(RMIKE(I2-1)**2+RMIKE(NMI2-1)**2+RMIKE(I2)**2+
     $RMIKE(NMI2)**2)
      AMIKE(I1,J) = AMIKE(I1,J) + (SNORM*XSPYS - AMIKE(I1,J)
     $ - AMIKE(I1,J))/NE
  210 CONTINUE
C
C
C    COMPUTE CURRENT ESTIMATE OF NORMALIZED STATISTICAL ERROR
      STERR = 1.00/SQRT(FLOAT(NE))
      STERP = 1.0/SQRT(NE*BWD/FREQ)
C
C    COMPUTE CURRENT R.M.S. PRESSURE & SPL
C    THIS MUST BE NORMALIZED FOR B&K 222
      SS = 0.
      DO 220 I=1,512
  220 SS = SS + AMIKE(I,J)
      DB(J) = 10.*ALOG1(SS)  + GAIN
      EMRMS(J) = SQRT(SS)
  230 CONTINUE
C
C    WRITE OUT CURRENT VALUES ON TERMINAL
      WRITE (1,250) NE,STERR,STERP,DB(1),DB(2),DB(3)
  250 FORMAT("  ",I2,6X,F3.2,"/",F3.2,6X,F5.1," DB",10X,F5.1," DB",
     $10X,F5.1," DB")
C
C    TEST ENSEMBLE COUNTER
      NE = NE + 2
      IF(NE.LE.NENDB) GO TO 99
```

```
  260 NE = NE - 2
      NENSB = NE
C
C   DETERMINE EFFECTIVE AVERAGING TIME, IF NOT PREVIOUSLY SPECIFIED.
C
      IH = ITIMEF(4) - ITIMES(4)
      TM = ITIMEF(3) - ITIMES(3)
      TS = ITIMEF(2) - ITIMES(2)
      TF = ITIMEF(1) - ITIMES(1)
      TBAR = TF/100. + TS + 60.*(TM + 60.*IH)
C
C   CALCULATE THE POWER SPECTRAL DENSITY BASED ON "BWD" BANDWIDTH.
C
      REWIND 8
      NFILE = 1
C
      DO 1000 J=1,3
C
      AGAIN = 10.**(GAIN /10.)
      DO 640 IX=1,256
      YDB(IX) = 0.
      IIY(IX) = 0
  640 ALPLT(IX) = 0.
      DO 680 IX=32,250
      FRQ(IX) = 6000.*(IX-25)/225.
      FL = FRQ(IX) - BWD/2.
      FU = FRQ(IX) + BWD/2.
      RJL = FL/FREQ
      JL = RJL
      IF(RJL-JL.GT.0.5) JL = JL+1
      RJU = FU/FREQ
      JU = RJU
      IF(RJU-JU.GT.0.5) JU = JU+1
      AREA = 0.0
      DO 670 I=JL,JU
  670 AREA = AREA + AMIKE(I,J)
      AREA=AREA-AMIKE(JL,J)*(RJL-JL+0.5)-AMIKE(JU,J)*(JU+0.5-RJU)
      ALPLT(IX) = AGAIN*AREA/BWD
  680 YDB(IX) = 10.*ALOG10(ALPLT(IX))
C
C   SET UP SCOPE 'GRAPH PAPER'
C   HORIZONTAL AXIS IS FREQUENCY PLOTTED LINEARLY ( 0 TO 6000 HZ )
C   VERTICAL AXIS IS POWER SPECTRAL DENSITY PLOTTED LOGARITHMICALLY.
C
C   FIND MAXIMUM SIGNAL AND SCALE GRAPH ACCORDINGLY.
C
      ALMAX = ALPLT(32)
      DO 500 I=33,250
      IF (ALPLT(I).GT.ALMAX) ALMAX = ALPLT(I)
  500 CONTINUE
      DBMAX = 10*ALOG10(ALMAX)
      MSCALE = (INT(DBMAX)/10)*10 + 10
      NGAIN = MSCALE - 20
C
      YGAIN = 5.0
      CALL SETUP(1,IPT1(1),IPT1(1300),1300,ISTA)
      CALL XAXIS(25,255,2,20)
      CALL XAXIS(25,255,2,255)
      CALL YAXIS(25,20,255,2)
      CALL YAXIS(255,20,255,2)
```

```
      DO 610 L=1,9
      K = 5-L
      IYTIC = 132. +K*5*YGAIN
      CALL XAXIS(26,29,1,IYTIC)
  610 CALL XAXIS(252,254,1,IYTIC)
      DO 615 L=1,6
      IX = 25. + 37.5*L
      CALL YAXIS(IX,20,23,1)
      CALL YAXIS(IX,252,254,1)
      CALL CODE
      WRITE(LINE,612) L
  612 FORMAT(I1)
      IX = IX - 3
      CALL STLIN(IX,8,LINE,-1)
  615 CONTINUE
      CALL CODE
      WRITE(LINE,621)
  621 FORMAT("DB")
      CALL STLIN(8,245,LINE,-2)
      DO 625 L=1,5
      N = NGAIN + (L-3)*10
      M = 129. + (L-3)*10*YGAIN
      CALL CODE
      WRITE(LINE,624) N
  624 FORMAT(I3)
  625 CALL STLIN(3,M,LINE,-3)
      CALL CODE
      WRITE(LINE,628)
  628 FORMAT("KHZ")
      CALL STLIN(148,2,LINE,-3)
      CALL CODE
      WRITE(LINE,630) MMODE,NMODE
  630 FORMAT("(",I1,",",I1,") MODE")
      CALL STLIN(100,240,LINE,-10)
C
C   NOW PLOT THE SPECTRUM
C
      CALL SETUP(2,IPT3(1),IPT3(2000),2000,ISTC)
      DO 685 IX=32,250
      IY = 132. + YGAIN*(YDB(IX)-NGAIN)
      IF (IY.LT.20) GO TO 685
      CALL ISTPH(IX,IY)
      IIY(IX) = IY
  685 CONTINUE
C
C   NOW ADD PSEUDO-CONNECTING LINES SO SPECTRA PLOT APPEARS CONTINUOUS
C
  690 DO 695 IX=33,249
      IYM1 = IIY(IX) - 1
      IF (IYM1.LT.20) GO TO 695
      IB = MIN0(IIY(IX-1),IIY(IX+1))
      IF (IB.LT.20) IB=20
      IF (IB.GE.IYM1) GO TO 695
      CALL YAXIS(IX,IB,IYM1,2)
  695 CONTINUE
C
C
C   LIST IMPORTANT PARAMETERS ON LINE PRINTER
C
      IF(J.GT.1) GO TO 714
```

```
      WRITE(6,716)
      GO TO 719
  714 IF(J.GT.2) GO TO 715
      WRITE(6,717)
      GO TO 719
  715 WRITE(6,718)
  716 FORMAT("1 INSTANTANEOUS SAMPLING PROGRAM:  <P(0)**2>")
  717 FORMAT("1 INSTANTANEOUS SAMPLING PROGRAM:  <(P(0) - P(180))**2>")
  718 FORMAT("1 INSTANTANEOUS SAMPLING PROGRAM:  <(P(0) - P(90))**2>")
  719 WRITE (6,720) IDATE,IA,NENSB,STERR,STERP,TBAR
      WRITE (6,721) APER,FMAX,FREQ,BWD
      WRITE (6,722) GAIN1,EMRMS(J),DB(J)
      WRITE (6,723) IFILE(1),IFILE(2),IFILE(3)
      WRITE (6,724) IFILE(J)
  720 FORMAT(//" ",40A2,//,1X,40A2,///
     $" AVERAGED PERIODOGRAM SPECTRA:",/,1X
     1,I5," SAMPLES TAKEN  =>  NORMALIZED STATISTICAL ERRORS =",E4.2,"/"
     2,F3.2,/,1X,F7.1," SEC. AVERAGING TIME",/)
  721 FORMAT(11X,"SAMPLE LENGTH:",F26.5," SEC.",/11X,"MAXIMUM FREQUENCY:
     1",F17.0,"   HZ",/,11X,"MAXIMUM SPECTRAL RESOLUTION:",F9.2," HZ",/,
     211X,"PLOT EQUIVALENT BANDWIDTH:",F6.1,"  HZ",/)
  722 FORMAT(" B&K 222 GAIN SETTING:",F5.1," DB",/," R.M.S. V",
     1"OLTAGE OF AVERAGED PRESSURE SIGNAL:",F6.2," VOLTS",/," FOR SPL",
     2" OF: ",F6.2," DB",//)
  723 FORMAT("  FILE NUMBERS ",I4,", ",I4," AND ",I4," TAKEN SIM",
     $"ULTANEOUSLY")
  724 FORMAT(" DATA STORAGE:  'PIPE TAPE' FILE #",I4,/," SOURCE PROGRAM
     1:  PIPE4 (5/12/77)")
C
      WRITE (6,725) IFILE(J)
  725 FORMAT ("1",25X,"FILE #",I4,/" ",4(4X,"FREQ.    DB "))
      WRITE (6,728)
  728 FORMAT ("      ")
      DO 726 IX=32,85
      IX1 = IX + 55
      IX2 = IX1 + 55
      IX3 = IX2 + 55
  726 WRITE (6,727) FRQ(IX),YDB(IX),FRQ(IX1),YDB(IX1),FRQ(IX2),
     $YDB(IX2),FRQ(IX3),YDB(IX3)
  727 FORMAT (" ",4(4X,F5.0,1X,F5.1))
      WRITE (6,727) FRQ(86),YDB(86),FRQ(141),YDB(141),FRQ(196),
     $YDB(196)
C
C
C
C   DISPLAY SPECTRA AND LIST ON TERMINAL IF DESIRED.
C
      CALL DSPLY(1,2,0)
      WRITE (1,730)
  730 FORMAT ("TYPE '1' IF LISTING IS DESIRED ON TERMINAL,"/
     $,"OTHERWISE TYPE '-1'")
      READ (1,*) LIST
      CALL DSPLY(-1,0,0)
      IF (LIST.EQ.-1) GO TO 735
      WRITE (1,736)
  736 FORMAT ("0",4(4X,"FREQ.   DB ")/)
      DO 737 IX=32,85
      IX1 = IX + 55
      IX2 = IX1 + 55
      IX3 = IX2 + 55
```

```
  737 WRITE (1,738) FRQ(IX),YDB(IX),FRQ(IX1),YDB(IX1),FRQ(IX2),
     $YDB(IX2),FRQ(IX3),YDB(IX3)
  738 FORMAT (" ",4(4X,F5.0,1X,F5.1))
      WRITE (1,736) FRQ(86),YDB(86),FRQ(141),YDB(141),FRQ(196),
     $YDB(196)
  735 CONTINUE
      WRITE (1,739)
  739 FORMAT (" TYPE '1' TO STORE OUTPUT ON MAG TAPE,"/
     $" OTHERWISE TYPE '-1'")
      READ (1,*) STORE
      IF(STORE.EQ.-1) GO TO 1000
C
C   STORE INFORMATION ON MAG TAPE.
C
      DO 740 I=1,512
  740 CMIKE(I) = AMIKE(I,J)
C
      NFILE = IFILE(J)  - NFILE
      IF(NFILE.LE.0) NFILE = NFILE - 1
      CALL PTAPE(8,NFILE,0)
      NFILE = IFILE(J)
      WRITE (8,731) IDATE
      WRITE (8,731) IA
      WRITE (8,732) IFILE(J),NBINS,NENSB,MMODE,NMODE
      WRITE (8,733) APER,FMAX,FREQ,STERR,STERP
      WRITE (8,733) EMRMS(J),DB(J),GAIN,BWD,TBAR
      WRITE (8,734)
  731 FORMAT(40A2)
  732 FORMAT(3I20,2I1)
  733 FORMAT(5E20.7)
  734 FORMAT(" THIS RECORD INTENTIONALLY LEFT BLANK")
      CALL EXEC(2,8,CMIKE,1024)
      CALL EXEC(2,8,ALPLT,512)
      END FILE 8
      END FILE 8
      CALL PTAPE(8,-3,0)
C
 1000 CONTINUE
      REWIND 8
      STOP
      END
$
LIST END ****
```

A1.3 Program PIPE2

The computer program PIPE2 performs the subtractions of time-averaged data needed for the time-averaged mode separation technique. This program operates on frequency spectra of $P_w(0)$, $(P_w(0) - P_w(\pi))$, and $(P_w(0) - P_w(\frac{\pi}{2}))$ which have previously been calculated by program PIPE4.

The program PIPE2 first needs the frequency spectra of $P_w(0)$, $(P_w(0) - P_w(\pi))$ and $(P_w(0) - P_w(\frac{\pi}{2}))$ from magnetic tape. The time-averaged mode separation is then performed at each center frequency of the 31.6 Hz bandwidth data. The (0,0), (1,0), and (2,0) mode spectra are then sequentially displayed on the oscilloscope plotter. Results are listed on the line printer and stored on magnetic tape.

The program operates in an interactive mode, with the input information being provided when asked for over the CRT terminal. The input variables are explained in the program listing.

A1.3. Listing of PIPE2

```
FTN,L
      PROGRAM PIPE2
C              2/29/77
C
C              E. KERSCHEN
C
C   THIS PROGRAM PERFORMS MODE SEPARATION BY A MATRIX
C   OPERATION ON TIME AVERAGED DATA, AND PLOTS
C   SPECTRA ON THE OSCILLOSCOPE PLOTTER.
C
C   SOURCE SPECTRA MUST HAVE BEEN PREVIOUSLY DETERMINED & STORED ON
C   'PIPE TAPE' BY SOURCE PROGRAM: PIPE (2/3/77)
C
C
      COMMON ALPLT(256),IPT1(1300),ILY(256),YDB(256),IPT3(2000),
     $A(256,3),P(256,3),AMIKE(1024),FRQ(256)
      DIMENSION NDATE(40),IA(40),IDATE(40),LINE(30),MFILE(3),
     $JFILE(3)
C
      WRITE (1,8)
    8 FORMAT (//" INPUT THE DATE")
      READ (1,9) NDATE
    9 FORMAT (40A2)
      IERR = 0
      REWIND 8
      NFILE = 1
      WRITE (1,10)
   10 FORMAT(//" MATRIX MODE SEPARATION TECHNIQUE"//"TYPE IN"
     1," SOURCE 'PIPE TAPE' FILE NUMBERS FOR <(P(0))**2>,"/
     2" <(P(0)-P(180))**2> AND <(P(0)-P(90))**2>.")
      READ(1,*) MFILE(1),MFILE(2),MFILE(3)
      WRITE (1,11)
   11 FORMAT ("TYPE IN FILE NUMBERS FOR STORAGE OF MODAL SPECTRA")
      READ (1,*) JFILE(1),JFILE(2),JFILE(3)
C
C   READ DATA FROM MFILES.
C
      DO 20 I=1,3
      NFILE = MFILE(I) - NFILE
      IF (NFILE.LE.0) NFILE = NFILE - 1
      CALL PTAPE(8,NFILE,0)
      READ (8,15)IDATE
      READ (8,15)IA
      READ (8,16)IFILE,NBINS,NENSB,MMODE,NMODE
      READ (8,18) APER,FMAX,FREQ,STERR,STEMP
      READ (8,18)EMRMS,DB,GAIN,BWD,IBAN
   15 FORMAT(40A2)
   16 FORMAT(3I20,2I1)
   18 FORMAT(5E20.7)
      CALL PTAPE(8,0,2)
      CALL EXEC(1,8,ALPLT,512)
      DO 30 IX=1,250
   30 A(IX,1) = ALPLT(IX)
C
C   CHECK THAT PROPER DATA HAS BEEN READ IN
      NFILE = IFILE
      IF (MFILE(1).EQ.IFILE) GO TO 50
C
C   THIS BRANCH ENTERED ONLY IF DATA ERROR DETECTED
   45 WRITE (1,47) MFILE(I)
```

```
   47 FORMAT(//"DATA ERROR DETECTED IN READING FILE #",I4)
      IERR = 1
C
C     NORMAL PROGRAM CONTINUATION
C     WRITE OUT DOCUMENTATION
C
   50 WRITE(1,51)IFILE,IDATE,IA,DB
   51 FORMAT(//"FILE #",I3,/,40A2,/,40A2,/,"SPL =",F6.2," DB")
C
   20 CONTINUE
      IF(IERR.EQ.1) GO TO 1000
C
C
C     PERFORM MODE SEPARATION.
C
      DO 40 IX=1,250
      P(IX,1) = A(IX,1) - A(IX,2)/8.0 - A(IX,3)/4.0
      P(IX,2) = A(IX,2)/4.0
   40 P(IX,3) = A(IX,3)/4.0 - A(IX,2)/8.0
C
C     NOW PLOT SPECTRA ON OSCILLOSCOPE PLOTTER
C
      NMODE = 0
      DO 60 I=1,3
      DO 70 IX=32,250
   70 ALPLT(IX) = P(IX,I)
      MMODE = I - 1
C
C     SET UP SCOPE 'GRAPH PAPER'
C     HORIZONTAL AXIS IS FREQUENCY PLOTTED LINEARLY ( 0 TO 6000 HZ )
C     VERTICAL AXIS IS POWER SPECTRAL DENSITY PLOTTED LOGARITHMICALLY.
C
C     FIND MAXIMUM SIGNAL AND SCALE GRAPH ACCORDINGLY.
C
      ALMAX = ALPLT(32)
      DO 500 J=33,250
      IF (ALPLT(J).GT.ALMAX) ALMAX = ALPLT(J)
  500 CONTINUE
      DBMAX = 10*ALOGT(ALMAX)
      MSCALE = (INT(DBMAX)/10)*10 + 10
      NGAIN = MSCALE - 20
C
  600 YGAIN = 5.0
      CALL SETUP(1,IPT1(1),IPT1(1300),1300,ISTA)
      CALL XAXIS(25,255,2,20)
      CALL XAXIS(25,255,2,255)
      CALL YAXIS(25,20,255,2)
      CALL YAXIS(255,20,255,2)
      DO 610 L=1,9
      K = 5-L
      IYTIC = 132. +K*5*YGAIN
      CALL XAXIS(26,29,1,IYTIC)
  610 CALL XAXIS(252,254,1,IYTIC)
      DO 615 L=1,6
      IX = 25. + 37.5*L
      CALL YAXIS(IX,20,23,1)
      CALL YAXIS(IX,252,254,1)
      CALL CODE
      WRITE(LINE,612) L
  612 FORMAT(I1)
```

```
      IX = IX - 3
      CALL STLIN(IX,8,LINE,-1)
  615 CONTINUE
      CALL CODE
      WRITE(LINE,621)
  621 FORMAT("DB")
      CALL STLIN(8,245,LINE,-2)
      DO 625 L=1,5
      N = NGAIN + (L-3)*10
      M = 129. + (L-3)*10*YGAIN
      CALL CODE
      WRITE(LINE,624) N
  624 FORMAT(I3)
  625 CALL STLIN(3,M,LINE,-3)
      CALL CODE
      WRITE(LINE,628)
  628 FORMAT("KHZ")
      CALL STLIN(148,2,LINE,-3)
      CALL CODE
      WRITE (LINE,629) MMODE,NMODE
  629 FORMAT ("(",I1,",",I1,") MODE")
      CALL STLIN(100,240,LINE,-10)
C
C     NOW PLOT THE SPECTRUM
C
      CALL SETUP(2,IPT3(1),IPT3(2000),2000,ISTC)
      DO 640 IX=1,256
      YDB(IX) = 0.
  640 IIY(IX) = 0
      DO 680 IX=32,250
      FRQ(IX) = 6000.*(IX - 25)/225.
      IF(ALPLT(IX).LE.1.0E-30) GO TO 680
      YDB(IX) = 10.*ALOG10(ALPLT(IX))
      IY = 132. + YGAIN*(YDB(IX)-NGAIN)
      IF (IY.LT.20) GO TO 680
      CALL ISTPN(IX,IY)
      IIY(IX) = IY
  680 CONTINUE
C
C     NOW ADD PSEUDO-CONNECTING LINES SO SPECTRA PLOT APPEARS CONTINUOUS
C
  690 DO 695 IX=33,249
      IYM1 = IIY(IX) - 1
      IF (IYM1.LT.20) GO TO 695
      IB = MIN0(IIY(IX-1),IIY(IX+1))
      IF (IB.LT.20) IB=20
      IF (IB.GE.IYM1) GO TO 695
      CALL YAXIS(IX,IB,IYM1,2)
  695 CONTINUE
C
C     THIS IS A TEMPORARY FIX.
C
      GAIN = 0.0
      EMRMS = 0.0
      DB = 0.0
      DO 696 J=1,1024
  696 AMIRE(J) = 0.0
C
C
C
```

```
C     LIST IMPORTANT PARAMETERS ON LINE PRINTER
C
      WRITE (6,721) NDATE,MMODE,NMODE,IA,NENSB,STERR,STERP,TBAR
      WRITE (6,722) APER,FMAX,FREQ,BWD
      WRITE (6,723) GAIN,EMRMS,DB
      WRITE (6,729) MFILE(1),MFILE(2),MFILE(3)
      WRITE (6,724) JFILE(I)
  721 FORMAT("1",40A2,//,1X,"(",I1,",",I1,") MODE",//,1X,40A2,///
     $" AVERAGED PERIODOGRAM SPECTRA:",/,1X
     1,I5,"-SAMPLES TAKEN  => NORMALIZED STATISTICAL ERRORS =",F4.2,"/"
     2,F5.2,/,1X,F7.1," SEC. AVERAGING TIME",/)
  722 FORMAT(11X,"SAMPLE LENGTH:",F26.5," SEC.",/11X,"MAXIMUM FREQUENCY:
     1",F17.0,"   HZ",/,11X,"MAXIMUM SPECTRAL RESOLUTION:",F9.2," HZ",/,
     211X,"PLOT EQUIVALENT BANDWIDTH:",F6.1,"  HZ",/)
  723 FORMAT(" B&K 2010 AMPLIFIER 'METER ZERO':",F5.1," DB",/," R.M.S. V
     1OLTAGE OF AVERAGED PRESSURE_SIGNAL:",F6.2," VOLTS",/," FOR SPL OF:
     2",F6.2," DB",//)
  729 FORMAT(" DATA SOURCE:  FILES",I4,",",I4," AND",I4)
  724 FORMAT(" DATA STORAGE:  'PIPE TAPE' FILE #",I4,/," SOURCE PROGRAM
     1:  PIPE2 (3/1/77)")
C
      WRITE (6,725) JFILE(I)
  725 FORMAT ("1",25X,"FILE #",I4,/" ",4(4X,"FREQ.   DB "))
      WRITE (6,728)
  728 FORMAT ("      ")
      DO 726 IX=32,85
      IX1 = IX + 55
      IX2 = IX1 + 55
      IX3 = IX2 + 55
  726 WRITE (6,727) FRQ(IX),YDB(IX),FRQ(IX1),YDB(IX1),FRQ(IX2),
     $YDB(IX2),FRQ(IX3),YDB(IX3)
  727 FORMAT (" ",4(4X,F5.0,1X,F5.1))
      WRITE (6,727) FRQ(86),YDB(86),FRQ(141),YDB(141),FRQ(196),
     $YDB(196)
C
C
C
C     DISPLAY SPECTRA AND LIST ON TERMINAL IF DESIRED.
C
      CALL DSPLY(1,2,0)
      WRITE (1,730) MMODE,NMODE
  730 FORMAT (//" (",I1,",",I1,") MODE HAS BEEN CALCULATED"/
     $" TYPE '1' IF LISTING IS DESIRED ON TERMINAL,"/
     $" OTHERWISE TYPE '-1'.")
      READ (1,*) LIST
      CALL DSPLY(-1,0,0)
      IF (LIST.EQ.-1) GO TO 735
      WRITE (1,736)
  736 FORMAT ("0",4(4X,"FREQ.   DB ")/)
      DO 737 IX=32,85
      IX1 = IX + 55
      IX2 = IX1 + 55
      IX3 = IX2 + 55
  737 WRITE (1,738) FRQ(IX),YDB(IX),FRQ(IX1),YDB(IX1),FRQ(IX2),
     $YDB(IX2),FRQ(IX3),YDB(IX3)
  738 FORMAT (" ",4(4X,F5.0,1X,F5.1))
      WRITE (1,738) FRQ(86),YDB(86),FRQ(141),YDB(141),FRQ(196),
     $YDB(196)
  735 CONTINUE
      WRITE (1,739)
```

```
  739 FORMAT (//" TYPE '1' TO STORE OUTPUT ON MAG TAPE,"/
     $" OTHERWISE TYPE '-1'")
      READ (1,*) STORE
      IF(STORE.EQ.-1) GO TO 60
C
C   STOREINFORMATION ON MAG TAPE.
C
C
      NFILE = JFILE(1) - NFILE
      IF(NFILE.LE.0) NFILE = NFILE - 1
      CALL PTAPE(8,NFILE,0)
      NFILE = JFILE(1)
      WRITE (8,731) NDATE
      WRITE (8,731) IA
      WRITE (8,732) JFILE(1),NBINS,NENSB,MMODE,NMODE
      WRITE (8,733) APER,FMAX,FREQ,STERR,STERP
      WRITE (8,733) EMRMS,DB,GAIN,BND,IBAR
      WRITE (8,734)
  731 FORMAT(40A2)
  732 FORMAT(3I20,2I1)
  733 FORMAT(5E20.7)
  734 FORMAT(" THIS RECORD INTENTIONALLY LEFT BLANK")
      CALL EXEC(2,8,AMIKE,2048)
      CALL EXEC(2,8,ALPLT,512)
C
      END FILE 8
      END FILE 8
      CALL PTAPE(8,-3,0)
   60 CONTINUE
 1000 CONTINUE
      REWIND 8
      STOP
      END
$
C
LIST END ****
```

Appendix A2

COMPUTER PROGRAM FOR ACOUSTIC POWER ANALYSIS

The computer program PIPE5 was used to perform the acoustic energy analysis. PIPE5 is a FORTRAN program written for use with the Hewlett-Packard HP-2100A computer.

The computer program first reads the acoustic pressure frequency spectra of the (0,0), (1,0) and (2,0) modes from magnetic tape. These spectra had previously been obtained using the instantaneous mode separation technique and computer program PIPE. The required fluid dynamic information (P_{amb}, T_o, M_i and $\dot{m}$) and an estimate for the level of the (1,0) mode at 6 KHz were input through the terminal. The program then calculated the necessary fluid dynamic parameters and modified the pressure spectra to eliminate the influence of the (0,1) mode and approximately separate the (1,0) and (3,0) modes. The modal acoustic power spectra were calculated using the physical energy weighting function and a slug flow approximation to the mean flow. The acoustic power spectra of the (0,0), (1,0), (2,0) and (3,0) modes were then displayed sequentially on the oscilloscope plotter. The spectra and integrated results were stored on a floppy disk and listed on the line printer.

```
FTN,L
      PROGRAM PIPES
C              7/28/77
C
C              E. KERSCHEN
C
C   THIS PROGRAM CONVERTS MODAL PRESSURE SPECTRA TO
C   MODAL POWER SPRECTRA, CALCULATES MODAL POWER
C   PARAMETERS AND PLOTS RESULTS ON THE OSCILLOSCOPE
C   PLOTTER
C
C   SOURCE SPECTRA MUST HAVE BEEN PREVIOUSLY DETERMINED & STORED ON
C   'PIPE TAPE' BY SOURCE PROGRAM: PIPE (2/3/77)
C
C
      COMMON ALPLT(256),IPT1(3300),IIY(256),YDB(256),
     $A(256,4),POW(256,4),FRQ(256),AMI,M,AMACH,PSTODB,
     $PSPLDB,PRSDB(4),SPLDI,PWTODB,PIPLDB,PWPLDB,POWDB(4),
     $EFFTL,EFFIPL,EFFPL,EFF(4)
      DIMENSION NDATE(40),IA(40),IDATE(40),LINE(30),MFILE(3),
     $DB(3),GAIN(3),AND(4),AINT(4),PRSINT(4),POWINT(4),
     $FCR(4),FLO(3),PRESS(7),POWS(7),EF(7),IFF(3)
      EQUIVALENCE (FLO(1),AMI),(PRESS(1),PSTODB),(POWS(1),PWTODB),
     $(EF(1),EFFT)
      DATA IDISC/2H* /,IFF(3)/2H  /
C
      CALL EXEC(23,IDISC,3)
C
      WRITE (1,8)
    8 FORMAT (//" INPUT THE DATE")
      READ (1,9) NDATE
    9 FORMAT (40A2)
      IERR = 0
      REWIND 8
      NFILE = 1
   13 WRITE (1,10)
   10 FORMAT(//" POWER FLOW CALCULATION"//"TYPE IN"
     1," SOURCE 'PIPE TAPE' FILE NUMBERS FOR (0,0),(1,0)"/
     2" AND (2,0) MODES",/," '-1' TO STOP")
      READ(1,*) MFILE(1),MFILE(2),MFILE(3)
      IF (MFILE(1).LT.0) GO TO 1000
      WRITE (1,11)
   11 FORMAT ("TYPE IN FILE NUMBER FOR STORAGE ON FLOPPY, IE. 'FF01'")
      READ (1,7) IFF(1),IFF(2)
    7 FORMAT(2A2)
C
C   READ DATA FROM MAG TAPE.
C
      DO 12 I=1,3
      NFILE = MFILE(I) - NFILE
      IF (NFILE.LE.0) NFILE = NFILE - 1
      CALL PTAPE(8,NFILE,0)
      READ (8,15)IDATE
      READ (8,15)IA
      READ (8,16)IFILE,NBINS.NENSB,MMODE,NMODE
      READ (8,18) APER,FMAX,FREQ,STERR,STERP
      READ (8,18)EMRMS,DB(I),GAIN(I),BWD,IBAR
   15 FORMAT(40A2)
   16 FORMAT(3I20,2I1)
   18 FORMAT(5E20.7)
```

```
      CALL PTAPE(8,0,2)
      CALL EXEC(1,8,ALPLT,512)
      DO 30 IX=1,256
   30 A(IX,1) = ALPLT(IX)
C
C   CHECK THAT PROPER DATA HAS BEEN READ IN
      MFILE = IFILE
      IF (MFILE(1).EQ.IFILE) GO TO 50
C
C   THIS BRANCH ENTERED ONLY IF DATA ERROR DETECTED
   45 WRITE (1,47) MFILE(1)
   47 FORMAT(//"DATA ERROR DETECTED IN READING FILE #",I4)
      IERR = 1
C
C   NORMAL PROGRAM CONTINUATION
C   WRITE OUT DOCUMENTATION
C
   50 WRITE(1,51)IFILE,IDATE,IA,DB(1)
   51 FORMAT(//"FILE #",I3,/,40A2,/,40A2,/,"SPL =",F6.2," DB")
C
      IF(IERR.EQ.1) GO TO 1000
   12 CONTINUE
C
C     THIS IS A TEMPORARY FIX TO CORRECT ERROR IN INPUT OF
C     FILE NUMBER 179
C
      IF(MFILE(1).NE.179) GO TO 42
      DO 40 IX=1,256
   40 A(IX,1)=A(IX,1)/100.0
   42 CONTINUE
C     CALCULATE NECESSARY FLUID PROPERTIES
C
C     APOW CONTAINS CONVERSIONS TO GIVE THE ACOUSTIC POWER
C     RELATIVE TO 10E-12 WATTS. FLOWPOW GIVES THE FLOW
C     POWER IN WATTS.
C
C
      WRITE(1,55)
   55 FORMAT("INPUT VALUES OF PAMB,TEMP,AM1,W AND SPL ESTIMATE"/
     2" FOR (1,0) MODE AT 6KHZ")
      READ (1,*) PAMB,T,AM1,W,SPL01
      T1=(T + 459.6)/(1.0 + 0.2*AM1**2)
      A1=49.02*SQRT(T1)
      U12 = (AM1*A1)**2
      POW = 16.548*(W-0.01)
      P = (PAMB + POW)*70.729
      RHO = P/(53.35*(T + 459.6))
      AO = 49.02*SQRT(T + 459.6)
      FLPOW = W*U12/47.489
      RZERO = 0.1594
      APOW = 23.898*(RZERO**2)/(RHO*AO)
      UON = W/(RHO*3.1416*RZERO**2)
      AMACH = UON/AO
C
C   CALCULATE PARAMETERS NECESSARY FOR DETERMINATION
C   OF MODAL SPECTRA.
C
C
      ANU(1)= 0.0
      AINT(1) = 1.0
```

```
      ANU(2) = 1.841
      AINT(2) = 0.705
      ANU(3) = 3.054
      AINT(3) = 0.5711
      ANU(4) = 4.201
      AINT(4) = 0.4900
      DO 35 I=1,4
   35 FCR(I)=A0*SQRT(1.0-AMACH**2)*ANU(I)/(6.283*RZERO)
      DO 60 I=1,4
      DO 60 IX=1,256
   60 POW(IX,I) = 0.0
      DO 65 IX=32,250
   65 FRQ(IX)=6000.0*(IX-25)/225.0
C
C
C     MODIFY PRESSURE SPECTRA TO APPROXIMATELY SEPARATE (0,1)
C     AND (3,0) MODES
C
      PLO = (A(186,1)+A(187,1)+A(188,1)+A(189,1))/4.0
      PUO = (A(205,1)+A(206,1)+A(207,1)+A(208,1))/4.0
      PLODB=10.0*ALOGT(PLO)
      PUODB=10.0*ALOGT(PUO)
      DO 68 IX=190,204
   68 A(IX,1) =10.0**(((PUODB-PLODB)*(IX-190)/14.0 + PLODB)/10.0)
      DO 70 IX=1,256
   70 A(IX,4) = A(IX,2)
      PL1 = (A(201,2)+A(202,2)+A(203,2)+A(204,2))/4.0
      PL1DB=10.0*ALOGT(PL1)
      DO 75 IX = 205,250
   75 A(IX,2) = 10.0**(((SPLU1 - PL1DB)*(IX-205)/45.0 + PL1DB)/10.0)
C
C --  CALCULATE POWER SPECTRA.
C
C
      DO 90 I=1,4
      DO 90 IX=32,250
      IF (FRQ(IX)-FCR(I)) 89,89,88
   88 GAMMA = 6.283*RZERO*FRQ(IX)/A0
      AKAY = (-AMACH + SQRT(1.0 - (1.0 - AMACH**2)*(ANU(I)/
     $GAMMA)**2))/(1.0 - AMACH**2)
      POW(IX,I) = A(IX,I)*(AMACH + AKAY/(1.0 - AKAY*
     $AMACH))*AINT(I)*APOW
      GO TO 90
   89 A(IX,I)=0.0
   90 CONTINUE
C
C
C     INTEGRATE PRESSURE AND POWER SPECTRA.
C
      PSPLN = 0.0
      PWPLN = 0.0
      DO 100 IX=32,102
      PSPLN = PSPLN + A(IX,1)*26.667
  100 PWPLN = PWPLN + POW(IX,1)*26.667
      DO 110 I=1,4
      PRSINT(I) = 0.0
      POWINT(I) = 0.0
      DO 110 IX=32,250
      PRSINT(I) = PRSINT(I) + A(IX,I)*26.667
  110 POWINT(I) = POWINT(I) + POW(IX,I)*26.667
```

```
      EFFPL = PWPLN/(FLPOW*10.0**12)
      DO 120 I=1,4
  120 EFF(I) = POWINT(I)/(FLPOW*10.0**12)
      EFFT = EFF(1) + EFF(2) + EFF(3) + EFF(4)
      PSPLDB = 10.0*ALOG10(PSPLN)
      PWPLDB = 10.0*ALOG10(PWPLN)
      DO 130 I=1,4
      PRSDB(I) = 10.0*ALOG10(PRSINT(I))
  130 POWDB(I) = 10.0*ALOG10(POWINT(I))
      PRSTOT = PRSINT(1) + PRSINT(2) + PRSINT(3)+PRSINT(4)
      POWTOT = POWINT(1) + POWINT(2) + POWINT(3)+POWINT(4)
      PSTODB = 10.0*ALOG10(PRSTOT)
      PWTODB = 10.0*ALOG10(POWTOT)
      PWTOPL = PRSTOT*APOW*(1.0+AMACH)
      PTPLDB = 10.0*ALOG10(PWTOPL)
      EFFTPL = PWTOPL/(FLPOW*10.0**12)
C
C
C   NOW PLOT SPECTRA ON OSCILLOSCOPE PLOTTER
C
      DO 700 I=1,4
C
C
C   SET UP SCOPE 'GRAPH PAPER'
C   HORIZONTAL AXIS IS FREQUENCY PLOTTED LINEARLY ( 0 TO 6000 HZ )
C   VERTICAL AXIS IS POWER SPECTRAL DENSITY PLOTTED LOGARITHMICALLY.
C
C   FIND MAXIMUM SIGNAL AND SCALE GRAPH ACCORDINGLY.
C
      POWMX = POW(32,I)
      DO 500 J=33,250
      IF (POW(J,I).GT.POWMX) POWMX = POW(J,I)
  500 CONTINUE
      DBMAX = 10*ALOG10(POWMX)
      MSCALE = (INT(DBMAX)/10)*10 + 10
      NGAIN = MSCALE - 20
C
  600 YGAIN = 5.0
      CALL SETUP(1,IPT1(1),IPT1(3300),3300,ISTA)
      CALL XAXIS(25,255,2,20)
      CALL XAXIS(25,255,2,255)
      CALL YAXIS(25,20,255,2)
      CALL YAXIS(255,20,255,2)
      DO 610 L=1,9
      K = 5-L
      IYTIC = 132. +K*5*YGAIN
      CALL XAXIS(26,29,1,IYTIC)
  610 CALL XAXIS(252,254,1,IYTIC)
      DO 615 L=1,6
      IX = 25. + 37.5*L
      CALL YAXIS(IX,20,23,1)
      CALL YAXIS(IX,252,254,1)
      CALL CODE
      WRITE(LINE,612) L
  612 FORMAT(I1)
      IX = IX - 3
      CALL STLIN(IX,8,LINE,-1)
  615 CONTINUE
      CALL CODE
      WRITE(LINE,621)
```

```
  621 FORMAT("DB")
      CALL STLIN(8,245,LINE,-2)
      DO 625 L=1,5
      N = NGAIN + (L-3)*10
      M = 129. + (L-3)*10*YGAIN
      CALL CODE
      WRITE(LINE,624) N
  624 FORMAT(I3)
  625 CALL STLIN(3,M,LINE,-3)
      CALL CODE
      WRITE(LINE,628)
  628 FORMAT("KHZ")
      CALL STLIN(148,2,LINE,-3)
      MEMOD = I-1
      CALL CODE
      WRITE (LINE,629) MEMOD
  629 FORMAT ("(",I1,",0) MODE POWER")
      CALL STLIN(80,240,LINE,-16)
C
C   NOW PLOT THE SPECTRUM
C
      DO 640 IX=1,256
      YDB(IX) = 0.
  640 IIY(IX) = 0
      DO 680 IX=32,250
      IF(POW(IX,1).LE.1.0E-14) GO TO 680
      YDB(IX) = 10.*ALOGT(POW(IX,1))
      IY = 132. + YGAIN*(YDB(IX)-NGAIN)
      IF (IY.LT.20) GO TO 680
      CALL ISTPN(IX,IY)
      IIY(IX) = IY
  680 CONTINUE
C
C   NOW ADD PSEUDO-CONNECTING LINES SO SPECTRA PLOT APPEARS CONTINUOUS
C
  690 DO 695 IX=33,249
      IYM1 = IIY(IX) - 1
      IF (IYM1.LT.20) GO TO 695
      IB = MINO(IIY(IX-1),IIY(IX+1))
      IF (IB.LT.20) IB=20
      IF (IB.GE.IYM1) GO TO 695
      CALL YAXIS(IX,IB,IYM1,2)
  695 CONTINUE
C
      WRITE(1,696) MEMOD
  696 FORMAT(//,"  (",I1,",0) MODE HAS BEEN CALCULATED",/,
     2" TYPE A '1' TO CONTINUE.")
      CALL DSPLY(1,0,0)
      READ(1,*) ICNT
      CALL DSPLY(-1,0,0)
  700 CONTINUE
C
C     LIST OUTPUT ON LINE PRINTER.
C
      WRITE(6,1695)
 1695 FORMAT("1",//,25X,"-  MODAL POWER ANALYSIS")
      WRITE(6,1700) NDATE,IA
 1700 FORMAT(/,14X,40A2,//,14X,40A2,/)
      WRITE(6,1705) AMI,W,AMACH
 1705 FORMAT(20X," INDICATED MACH NUMBER:      ",F8.3,/,
```

```
     221X," FLOW RATE          :               ",F8.4," LBM/SEC",/,
     321X," MEAN FLOW MACH NUMBER:        ",F8.4,//)
      WRITE(6,1710) PSTODB,PSPLDB,(PRSDB(I),I=1,4),SPLDI
1710 FORMAT(19X," TOTAL ACOUSTIC PRESSURE :  ",F8.2," DB",/,
     119X," ACOUSTIC PRES.(200-2100HZ):",F8.2," DB",/,
     218X,"  (0,0) MODE ACOUSTIC PRES. :",F8.2,"  DB",/,
     318X,"  (1,0) MODE ACOUSTIC PRES. :",F8.2,"  DB",/,
     418X,"  (2,0) MODE ACOUSTIC PRES. :",F8.2,"  DB",/,
     518X,"  (3,0) MODE ACOUSTIC PRES. :",F8.2,"  DB",/,
     618X,"  (1,0) MODE SPL EST AT 6KHZ:",F8.2,"  DB",/)
      WRITE(6,1715) PWTODB,PTPLDB,PWPLDB,(POWDB(I),I=1,4)
1715 FORMAT(19X," TOTAL ACOUSTIC POWER - ",/,
     119X,"               EXACT:          ",F8.2," DB",/,
     219X,"      PLANE WAVE ASSUMPTION:  ",F8.2," DB",/,
     219X," ACOUSTIC POWER(200-2100HZ):",F8.2," DB",/,
     419X," (0,0) MODE ACOUSTIC POWER :",F8.2," DB",/,
     519X," (1,0) MODE ACOUSTIC POWER :",F8.2," DB",/,
     619X," (2,0) MODE ACOUSTIC POWER :",F8.2," DB",/,
     719X," (3,0) MODE ACOUSTIC POWER :",F8.2," DB",/)
      WRITE(6,1720)EFFT,EFFTPL,EFFPL
1720 FORMAT(19X," OVERALL EFFICIENCY -",/,
     123X,"EXACT:                    ",E11.4,/,
     223X,"PLANE WAVE ASSUMPTION:  ",E11.4,/,
     323X," EFFICIENCY(200-2100HZ):",E10.4)
      DO 1726 I=1,4
      I9=I-1
      WRITE(6,1725) I9,EFF(I)
1725 FORMAT(23X," (",I1,",0) MODE EFFICIENCY:",E11.4)
1726 CONTINUE
      WRITE(6,1730)(MFILE(I),I=1,3),(IFF(I),I=1,3)
1730 FORMAT(/,12X," DATA SOURCE:  PIPE TAPE FILES  ",I3,
     1",",I3," AND ",I3,/,
     212X," DATA STORAGE: FLOPPY DISC FILE  ",3A2,/,
     412X," SOURCE PROGRAM  :  PIPES (7/28/77)")
C
C     STORE INFORMATION ON FLOPPY DISC FOR LATER
C     RETURN TO MAG TAPE.
C
C
      CALL BOPEN
      CALL DWRIT(NDATE,40,IFL)
      CALL DWRIT( IA,  40,IFL)
      CALL DWRIT(FLO,   6,IFL)
      CALL DWRIT(PRESS,14,IFL)
      CALL DWRIT(POWS, 14,IFL)
      CALL DWRIT( EF,  14,IFL)
      CALL DWRIT(A,  2048,IFL)
      CALL DWRIT(POW,2048,IFL)
      CALL DWRIT(MFILE, 3,IFL)
      CALL DWRIT(JFILE, 4,IFL)
      CALL DCLOS(IFF,+1,IFL)
C
      GO TO 13
C
C
1000 CONTINUE
      CALL EXEC(23,IDISC,1)
      REWIND 8
      STOP
      END
```

Appendix A3

MODAL PRESSURE AND POWER SPECTRA

This appendix contains the modal pressure and power spectra at all experimental conditions for which data were obtained. The spectra have been normalized to a bandwidth of 1 Hz (after being averaged over a 31.6 Hz bandwidth), as discussed in Chapter 3.

The following symbols were used in plotting the modal pressure spectra:

(0,0) Mode:

(1,0) Mode:

(2,0) Mode:

The following symbols were used in plotting the modal power spectra:

(0,0) Mode:

(1,0) Mode:

(2,0) Mode:

(3,0) Mode:

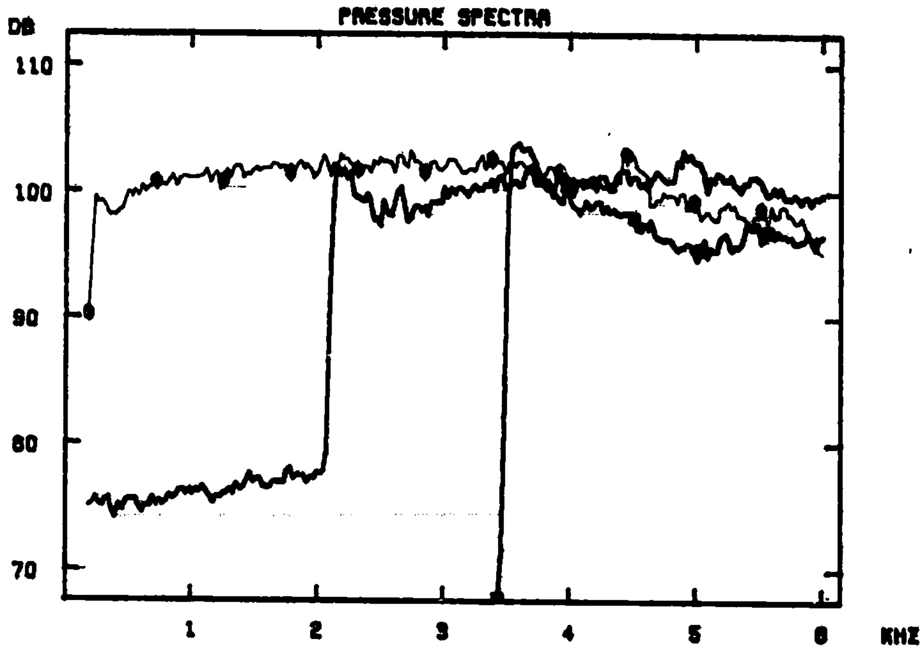

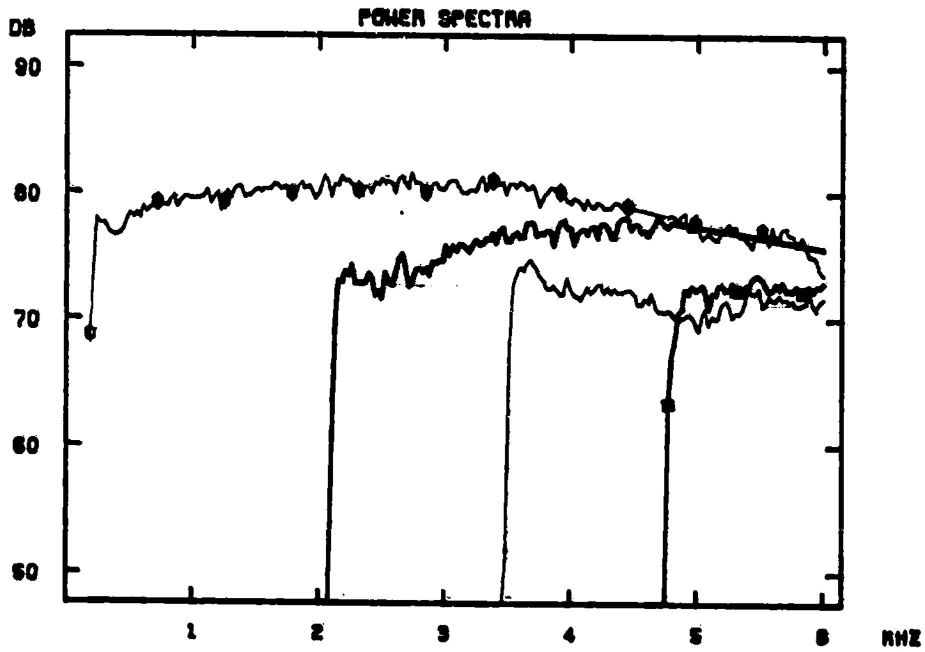

Fig. A3-1. 12.7 mm diameter orifice ($\frac{d}{D}$ = 0.131), M_i = 1.24, f_r = 8.25.

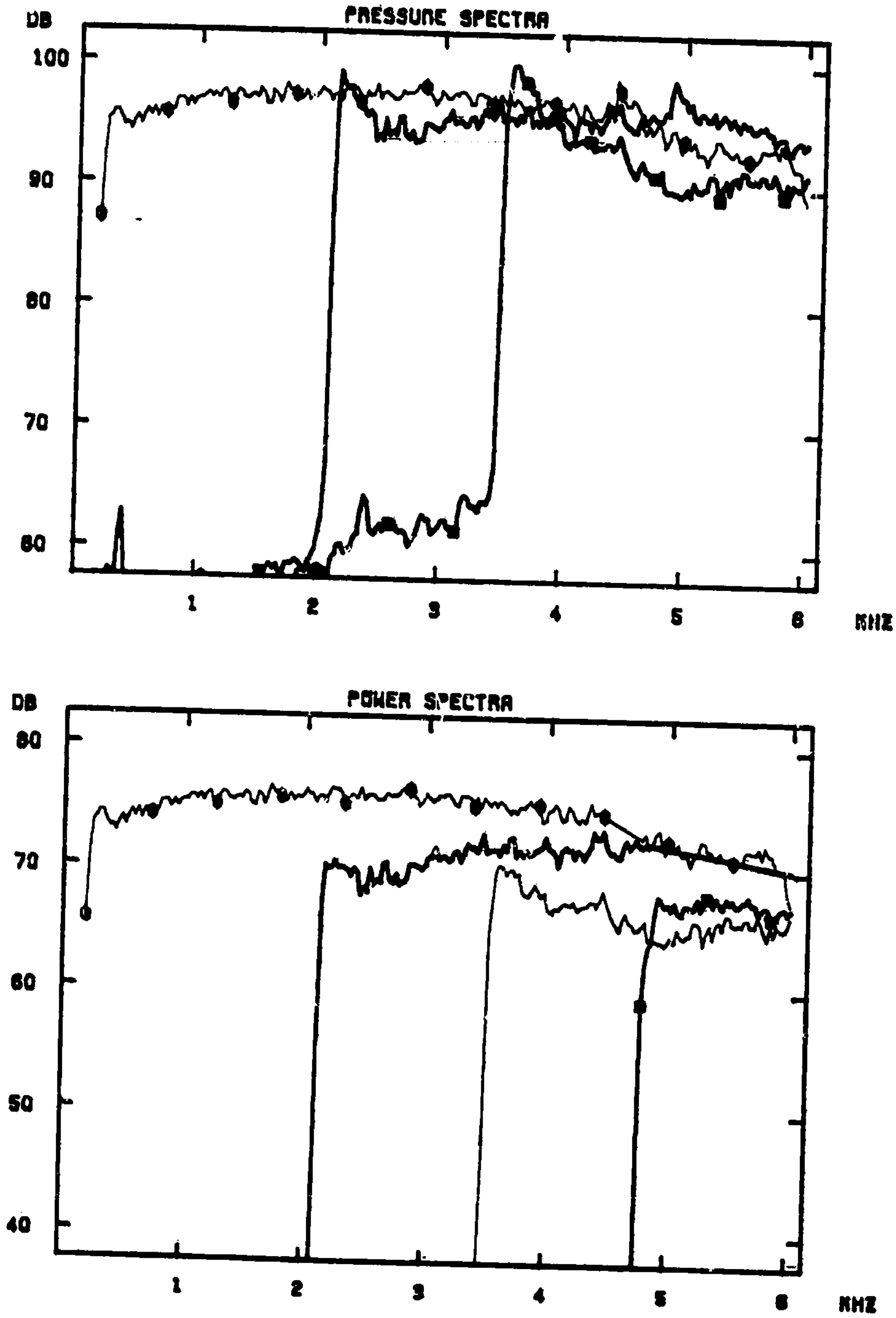

Fig. A3-2. 12.7 mm diameter orifice ($\frac{d}{D}$ = 0.131), M_i = 1.08, f_r = 7.42.

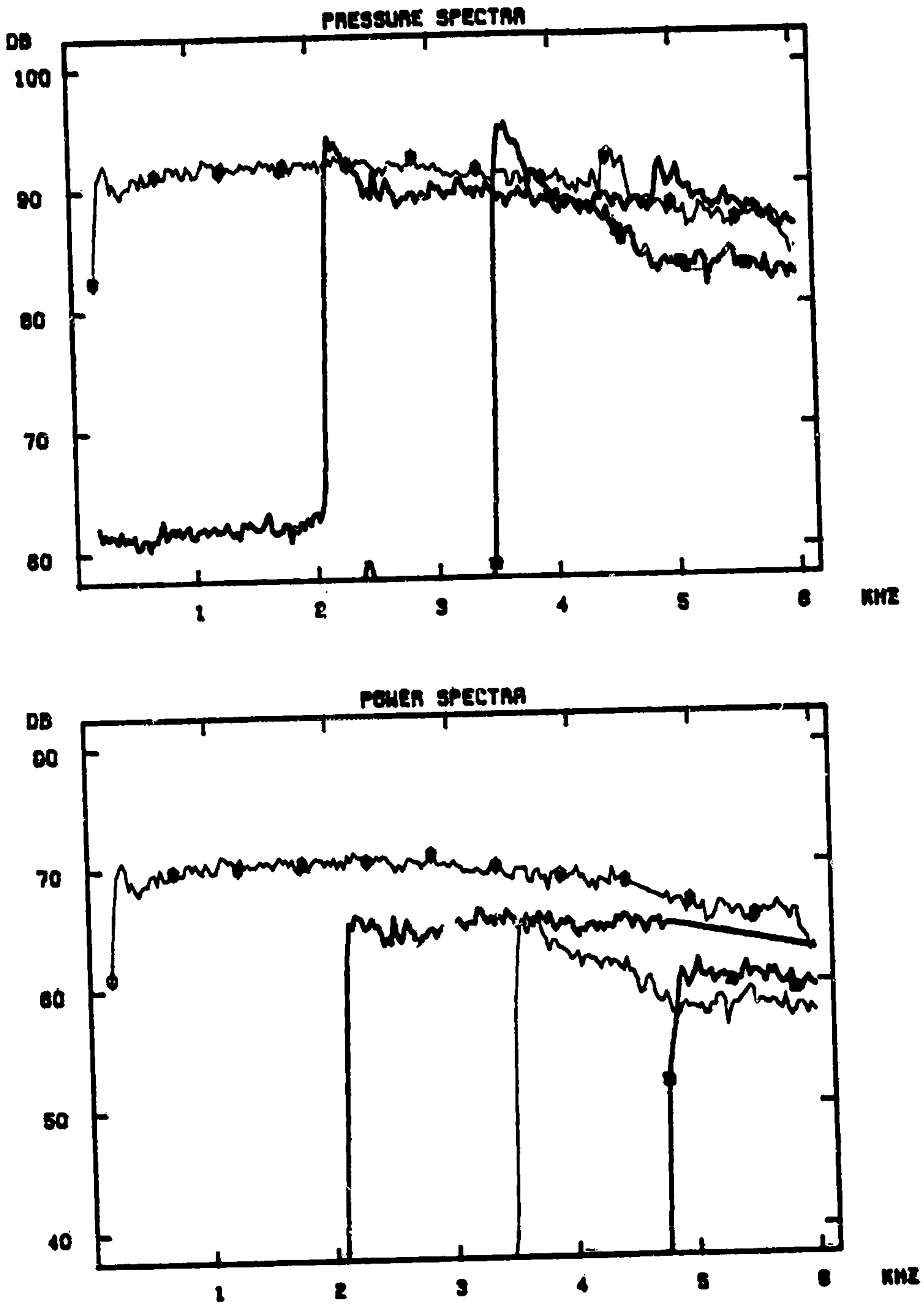

Fig. A3-3. 12.7 mm diameter orifice ($\frac{d}{D}$ = 0.131), M_i = 0.918, f_r = 6.48.

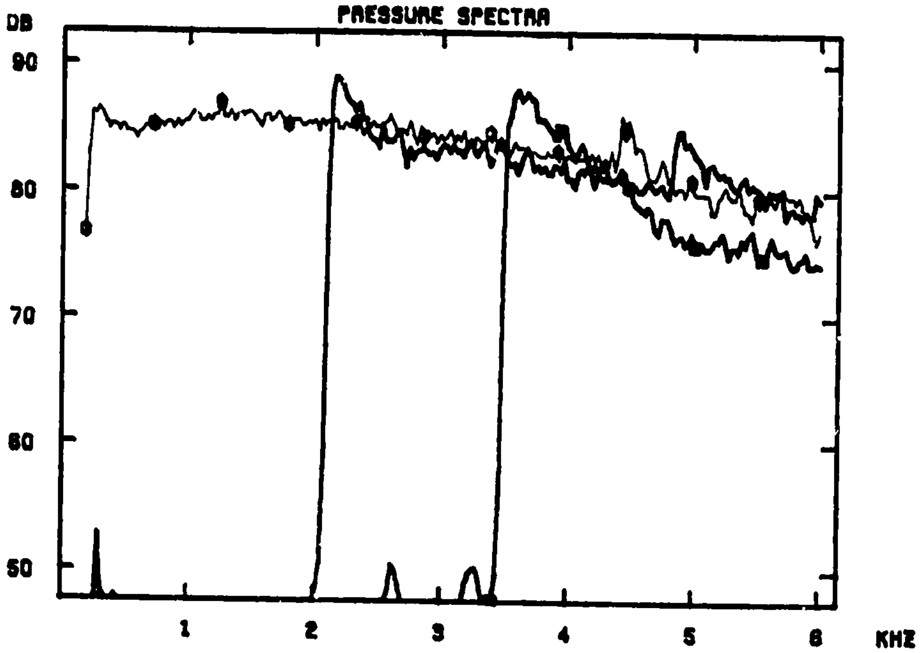

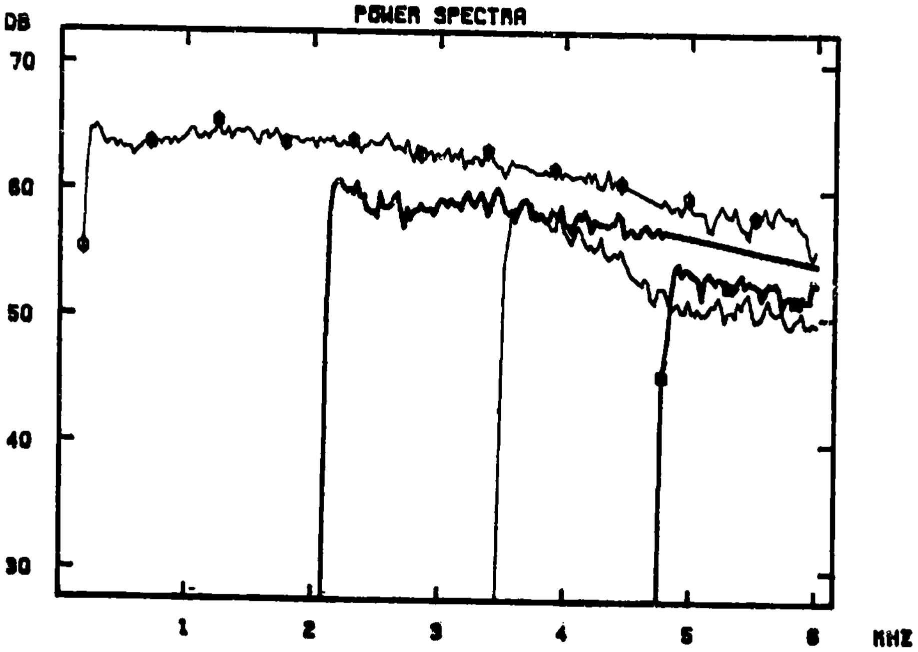

Fig. A3-4. 12.7 mm diameter orifice ($\frac{d}{D}$ = 0.131), M_1 = 0.752, f_r = 5.44.

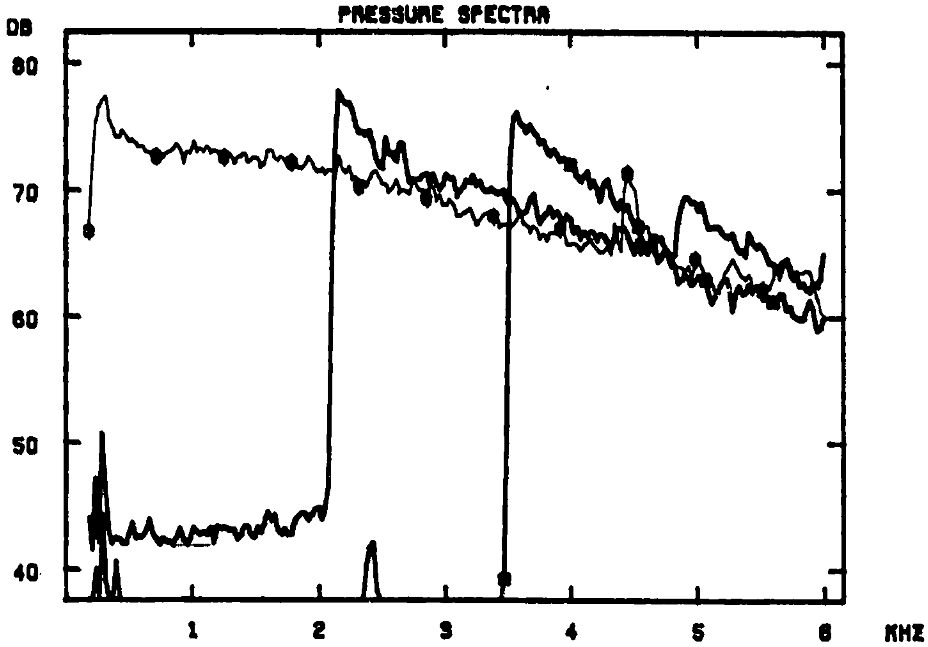

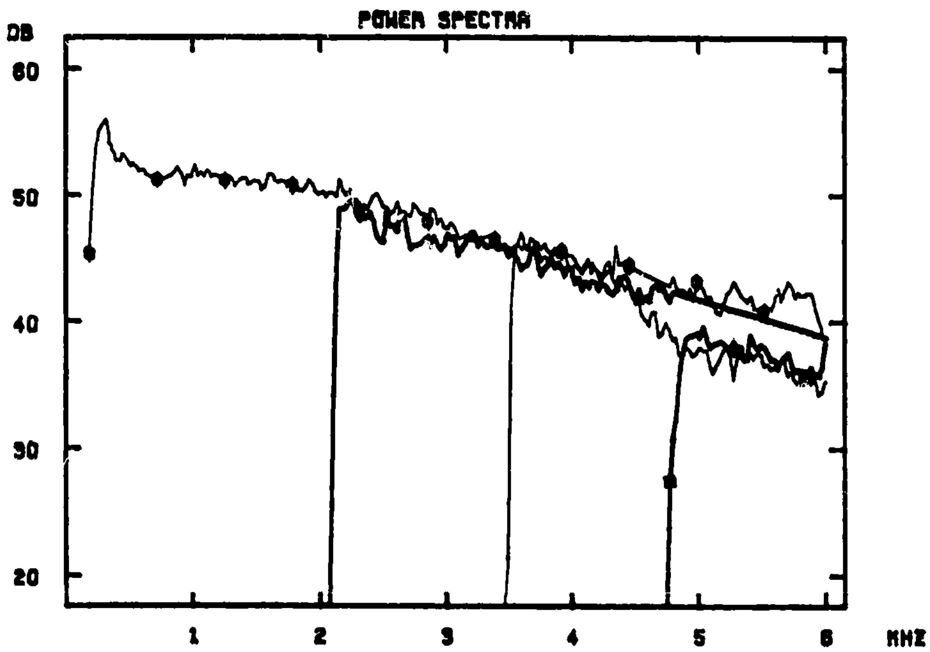

Fig. A3-5. 12.7 mm diameter orifice ($\frac{d}{D}$ = 0.131), M_1 = 0.499, f_r = 3.72.

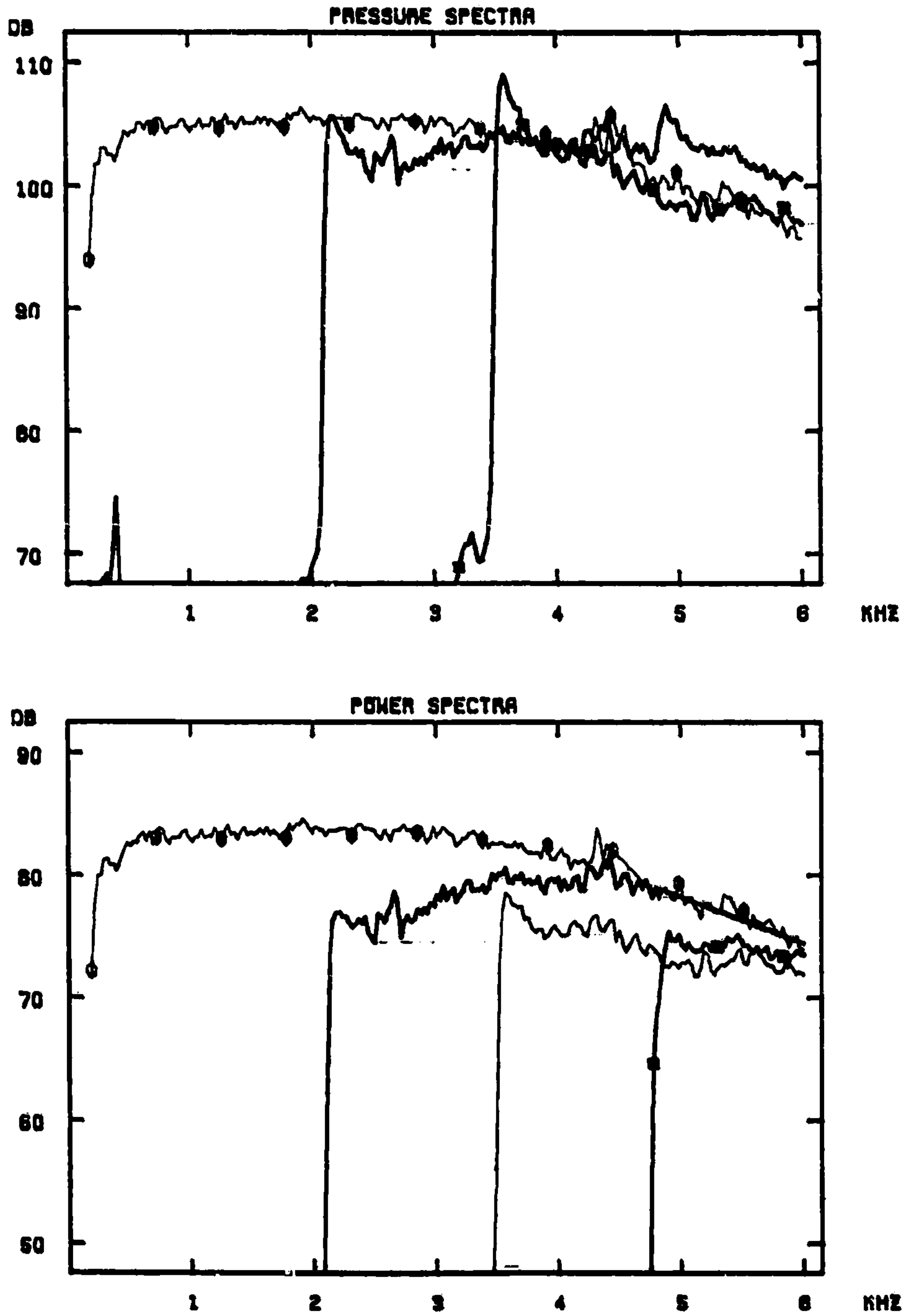

Fig. A3-6. 19.0 mm diameter orifice ($\frac{d}{D}$ = 0.196), M_1 = 1.07, f_r - 4.94.

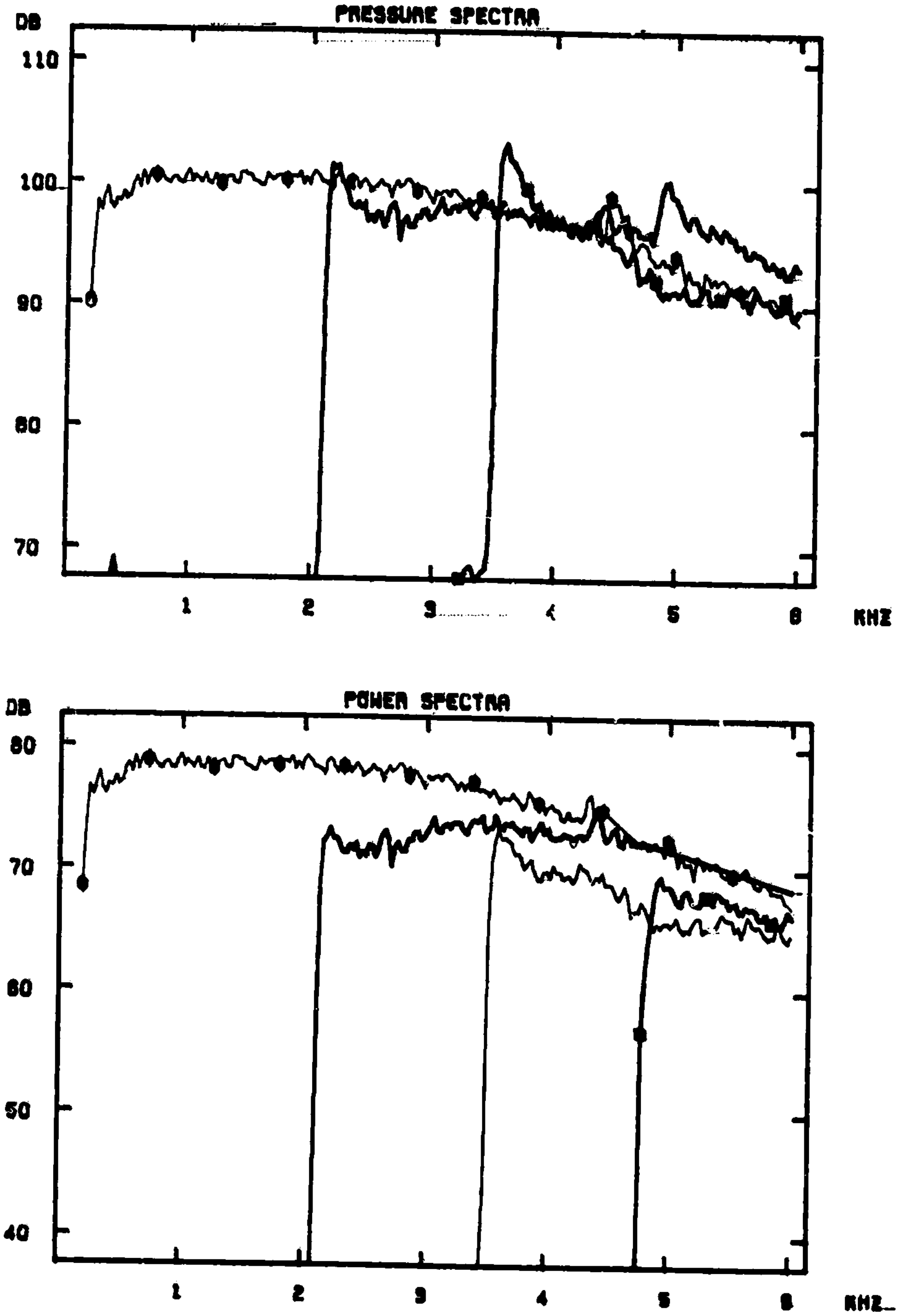

Fig. A3-7. 19.0 mm diameter orifice ($\frac{d}{D}$ = 0.196), M_i = 0.918, f_r = 4.33.

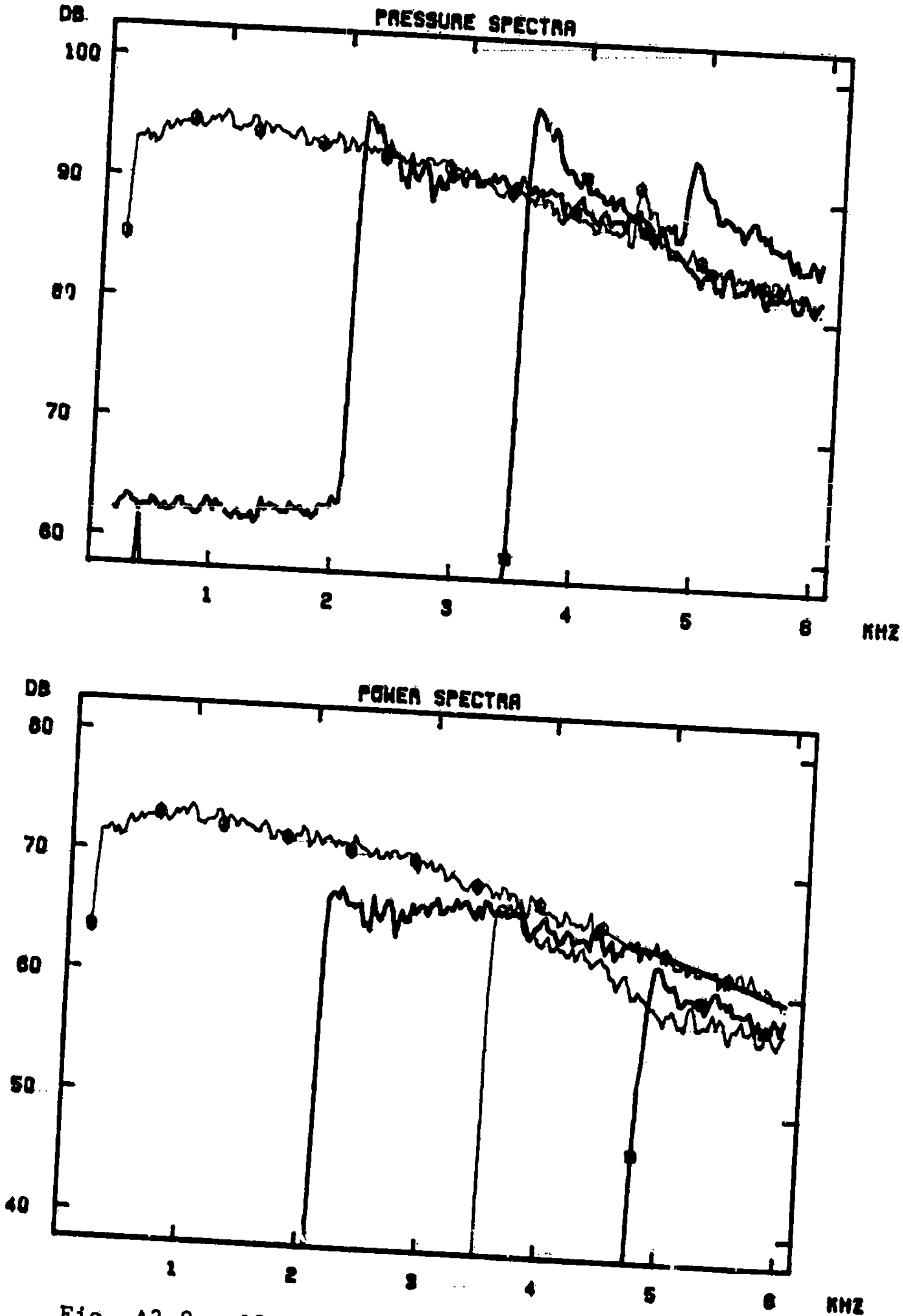

Fig. A3-8. 19.0 mm diameter orifice ($\frac{d}{D}$ = 0.196), M_1 = 0.755, f_r = 3.65.

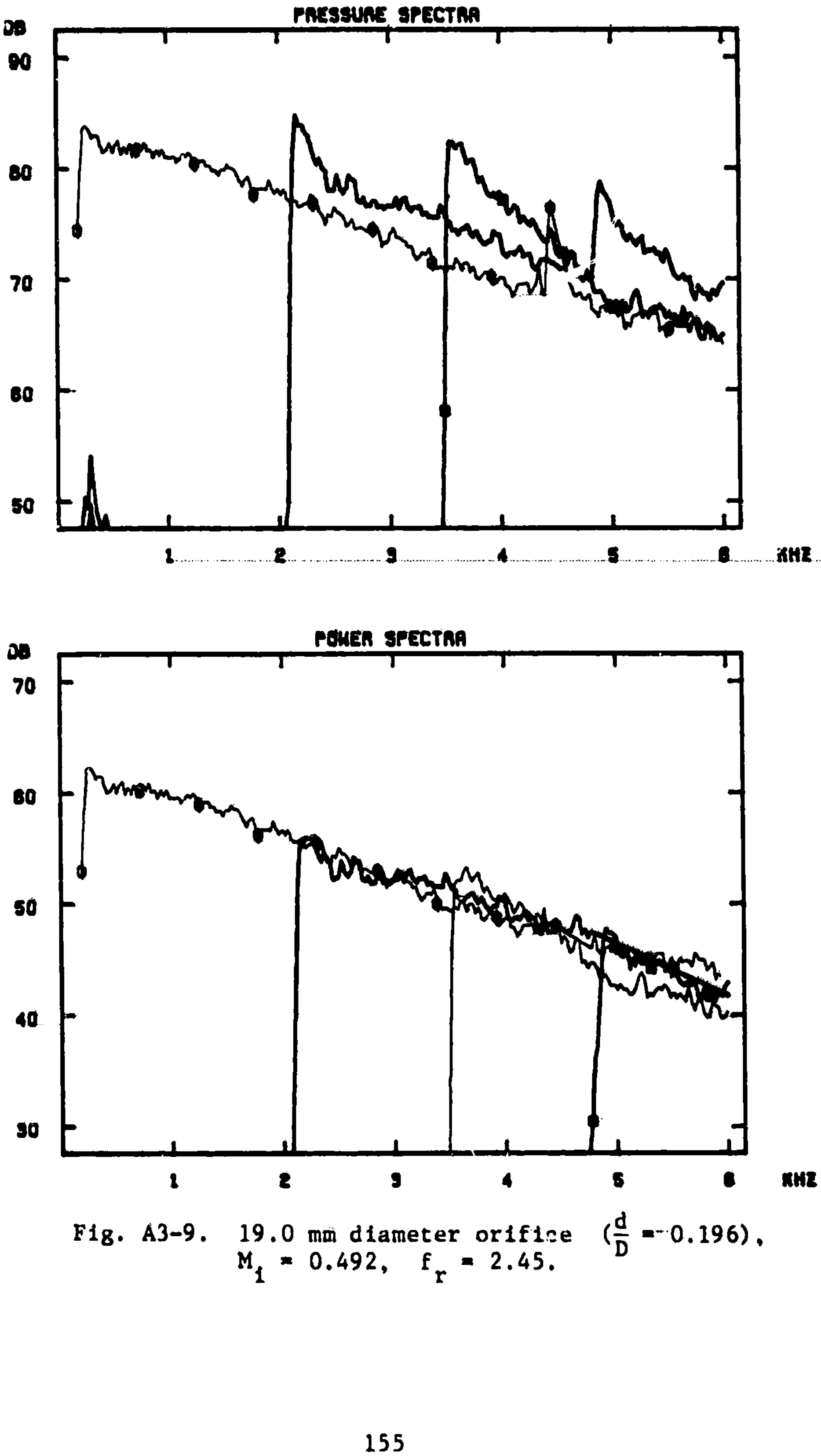

Fig. A3-9. 19.0 mm diameter orifice ($\frac{d}{D}$ = 0.196), M_i = 0.492, f_r = 2.45.

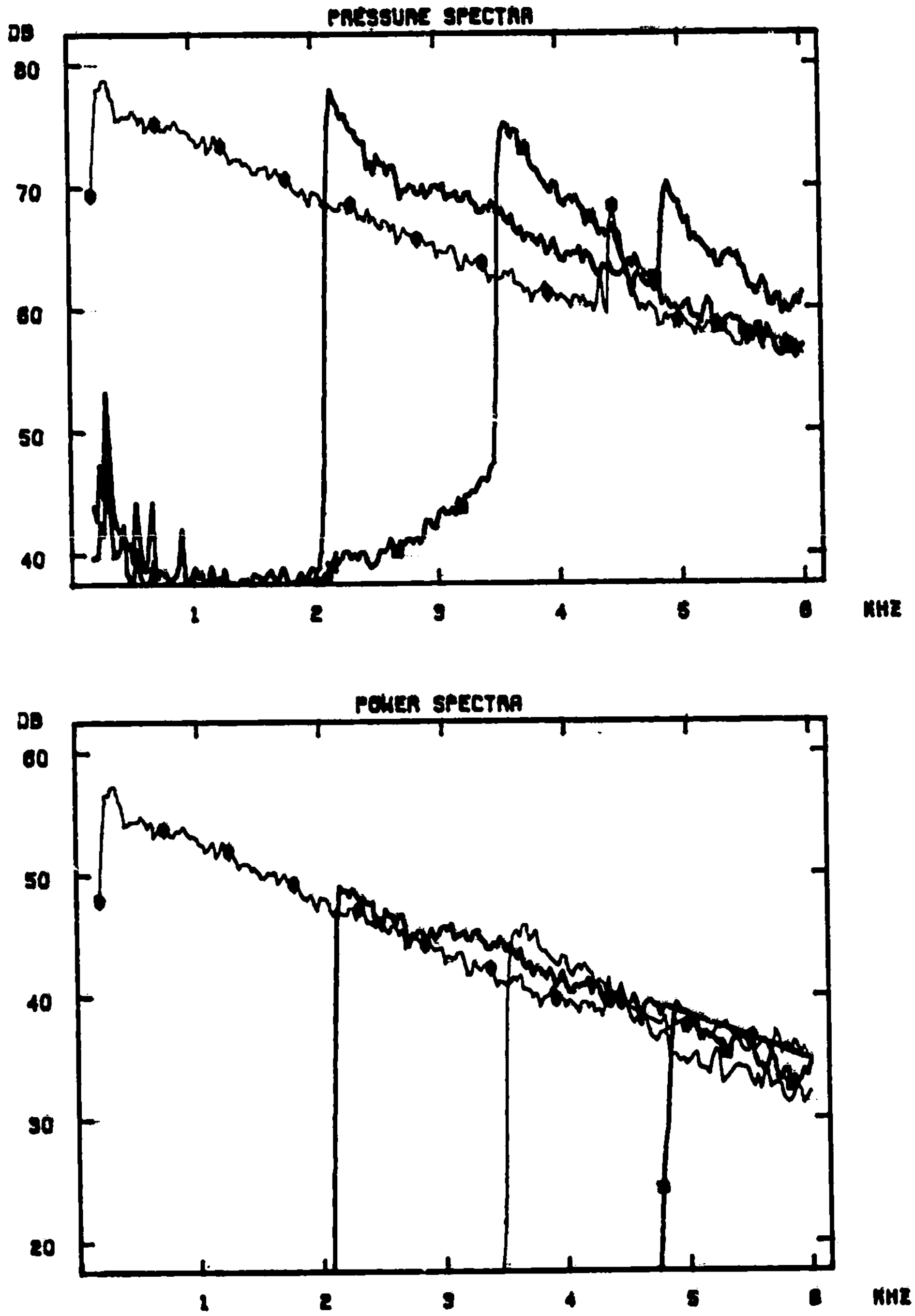

Fig. A3-10. 19.0 mm diameter orifice ($\frac{d}{D} = 0.196$), $M_i = 0.393$, $f_r = 1.97$.

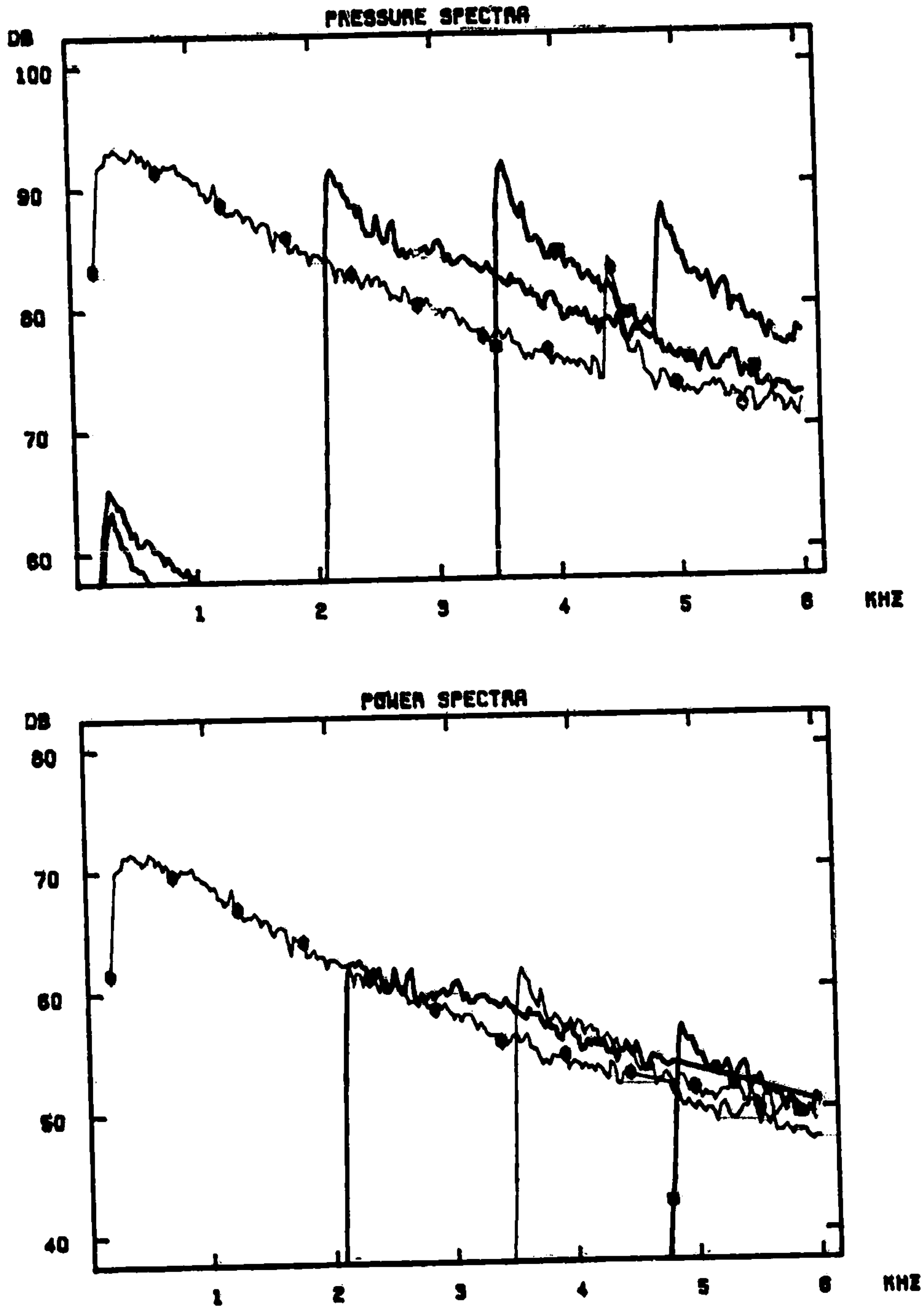

Fig. A3-11. 31.8 mm diameter orifice ($\frac{d}{D}$ = 0.327), M_i = 0.500, f_r = 1.49.

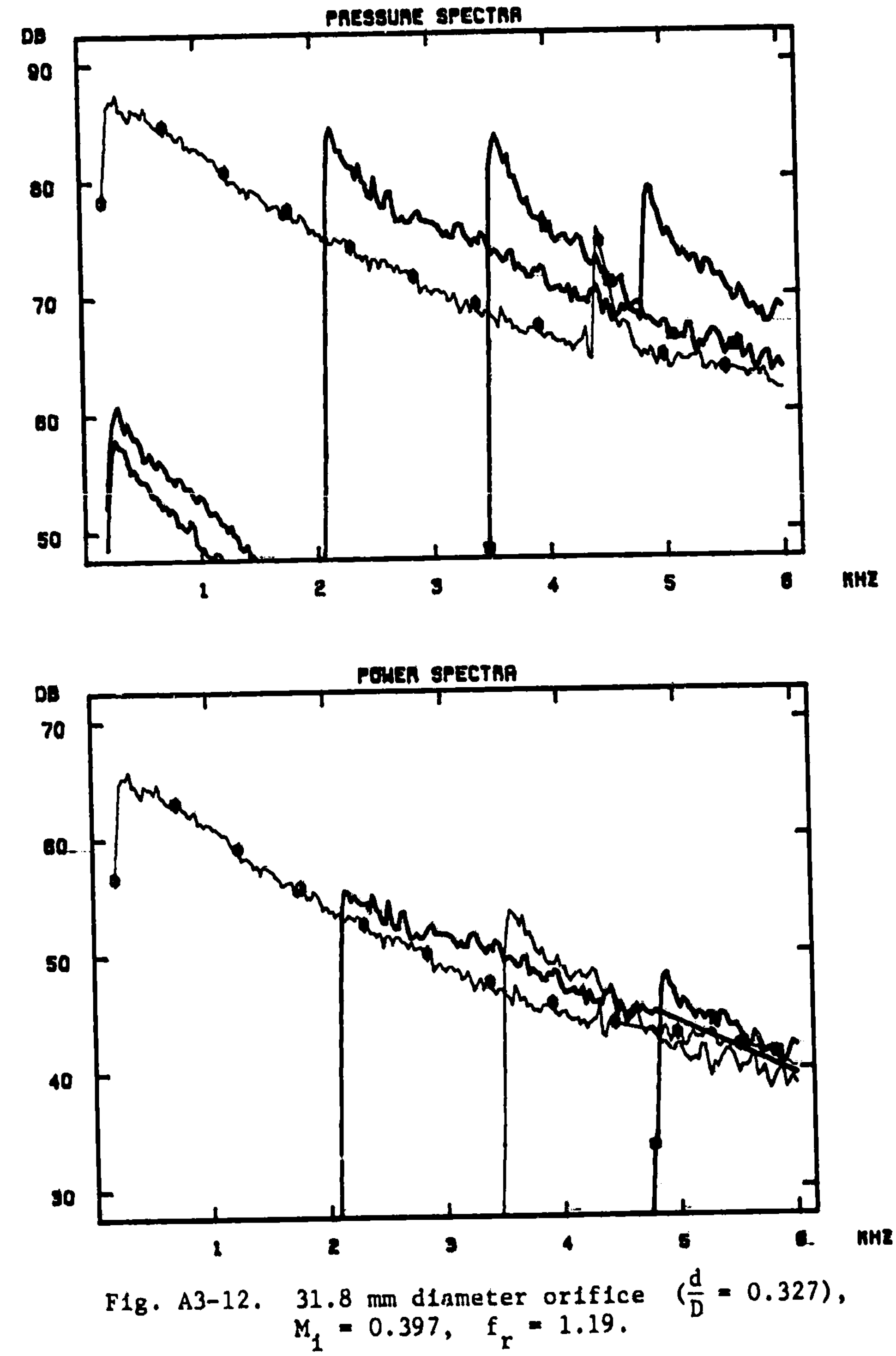

Fig. A3-12. 31.8 mm diameter orifice ($\frac{d}{D}$ = 0.327), M_1 = 0.397, f_r = 1.19.

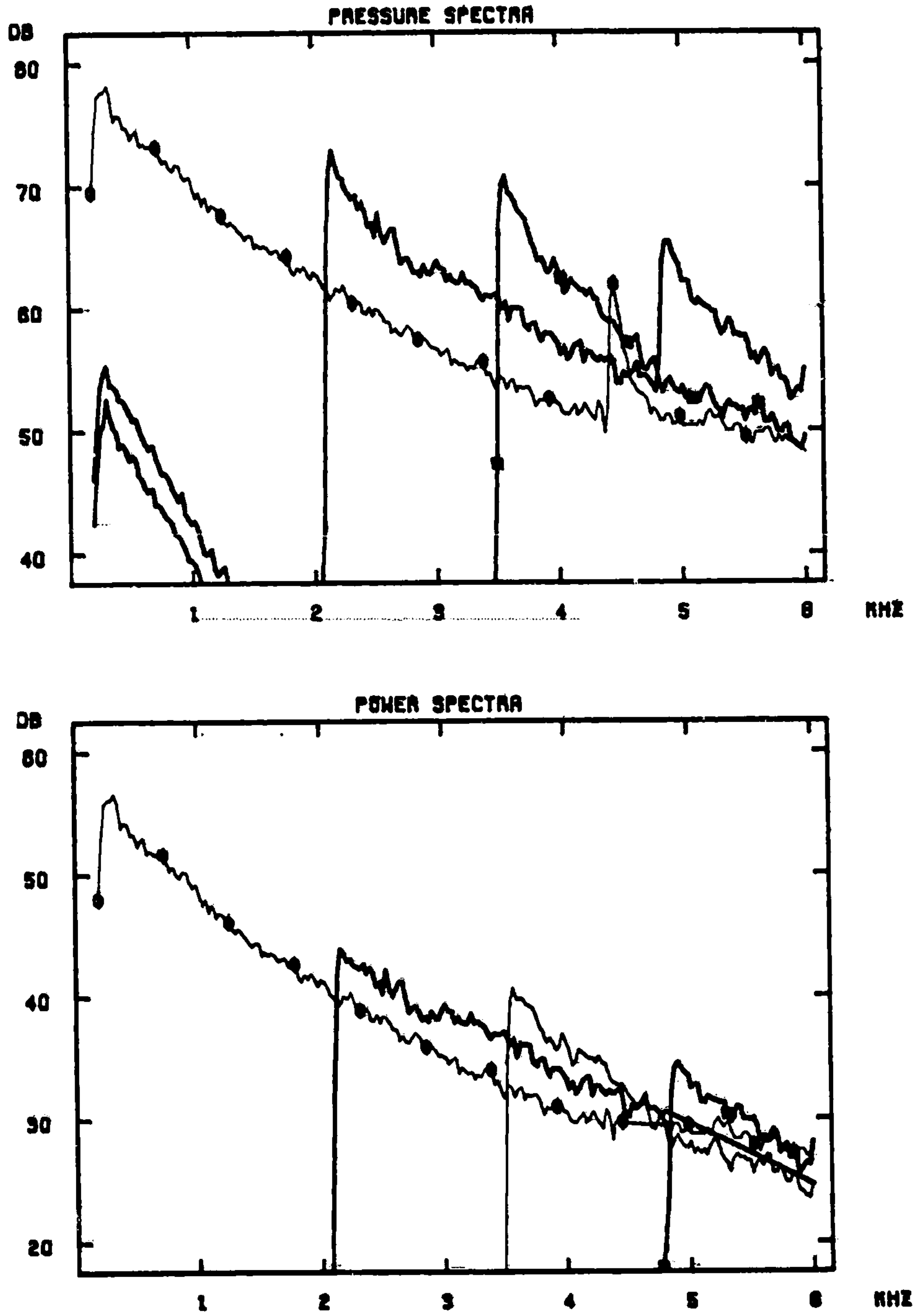

Fig. A3-13. 31.8 mm diameter orifice ($\frac{d}{D}$ = 0.327), M_1 = 0.277, f_r = 0.841.

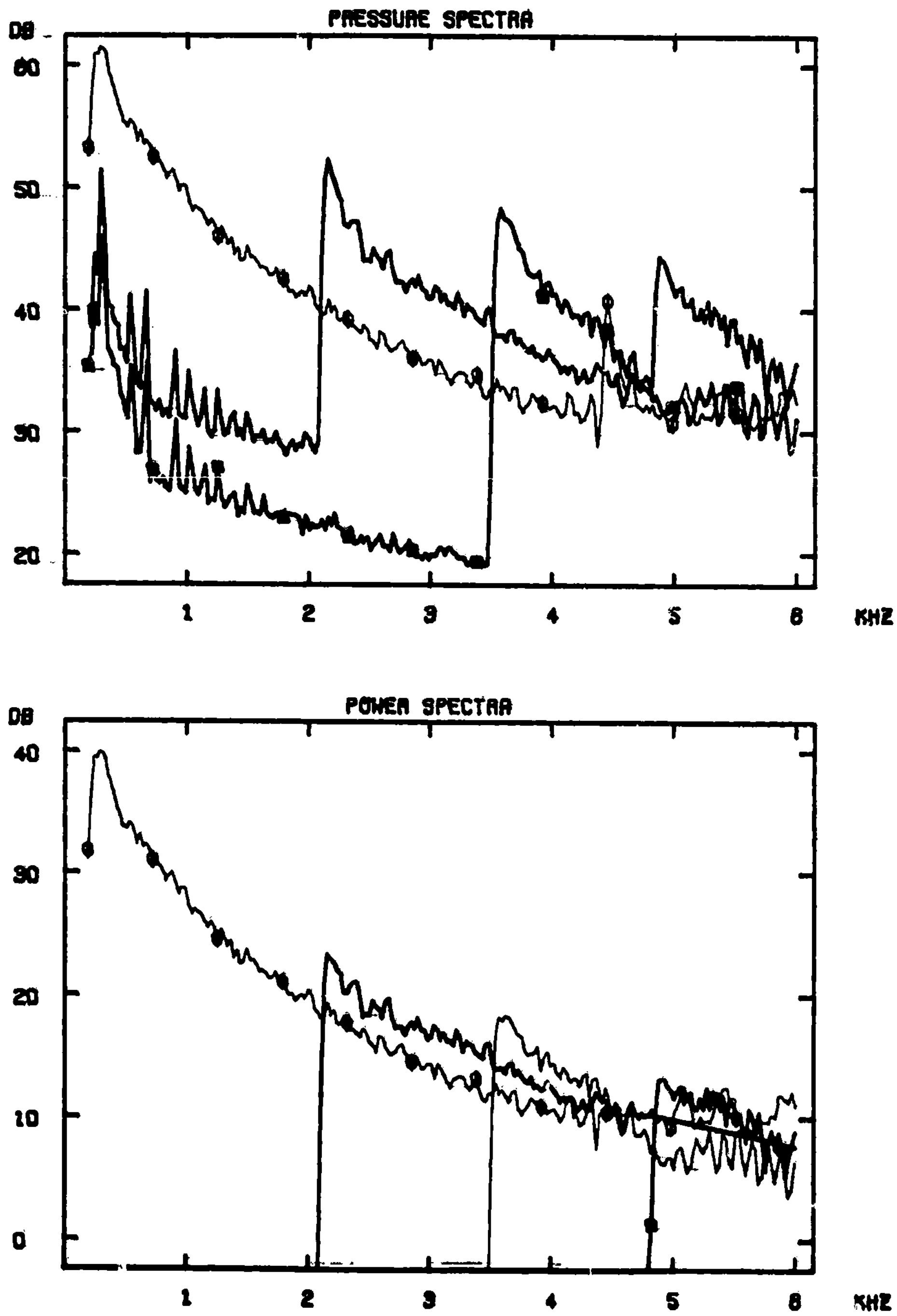

Fig. A3-14. 31.8 mm diameter orifice, $(\frac{d}{D} = 0.327)$, $M_1 = 0.149$, $f_r = 0.455$.

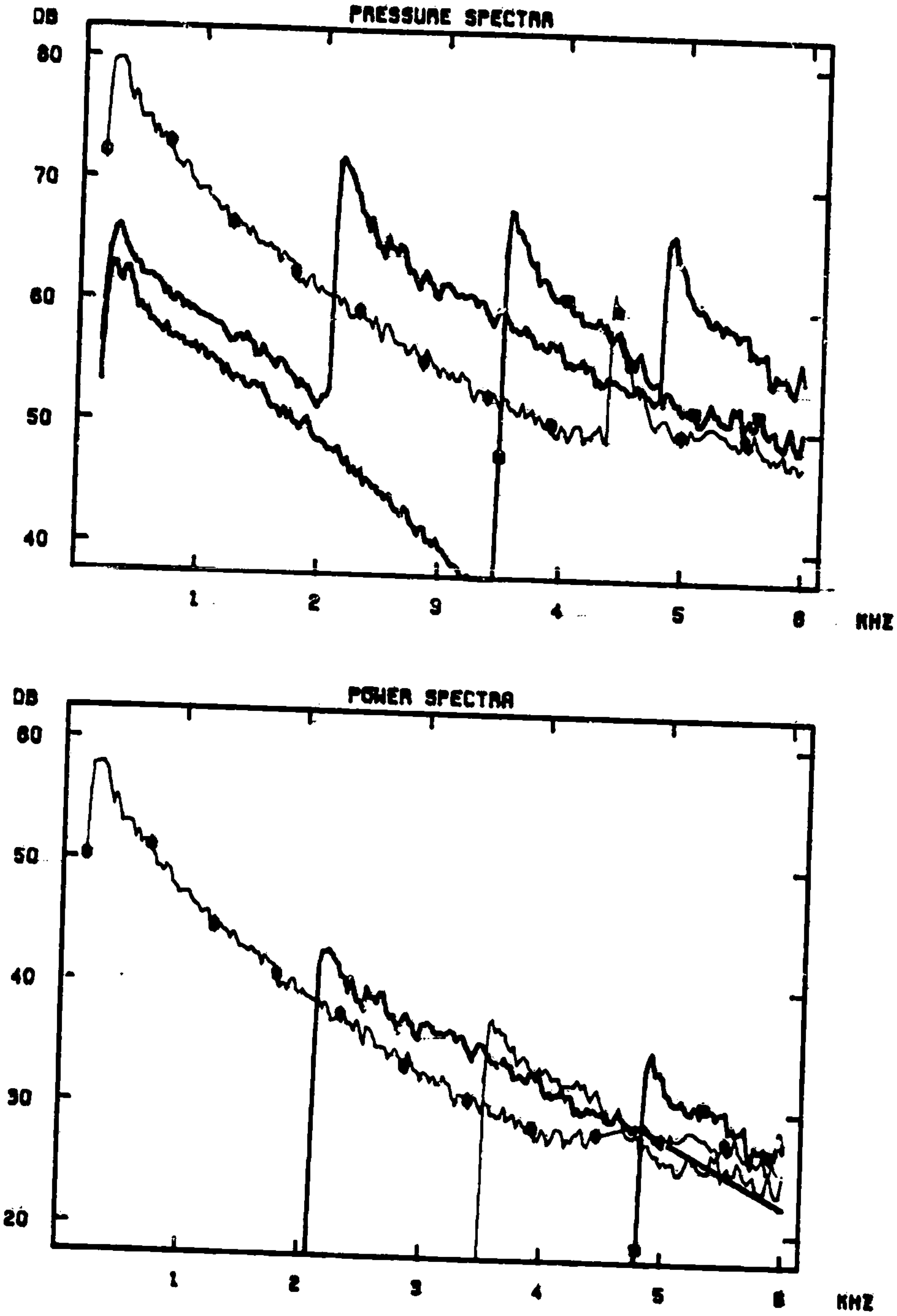

Fig. A3-15. 50.8 mm diameter orifice ($\frac{d}{D}$ = 0.523),
M_i = 0.225, f_r = 0.428.

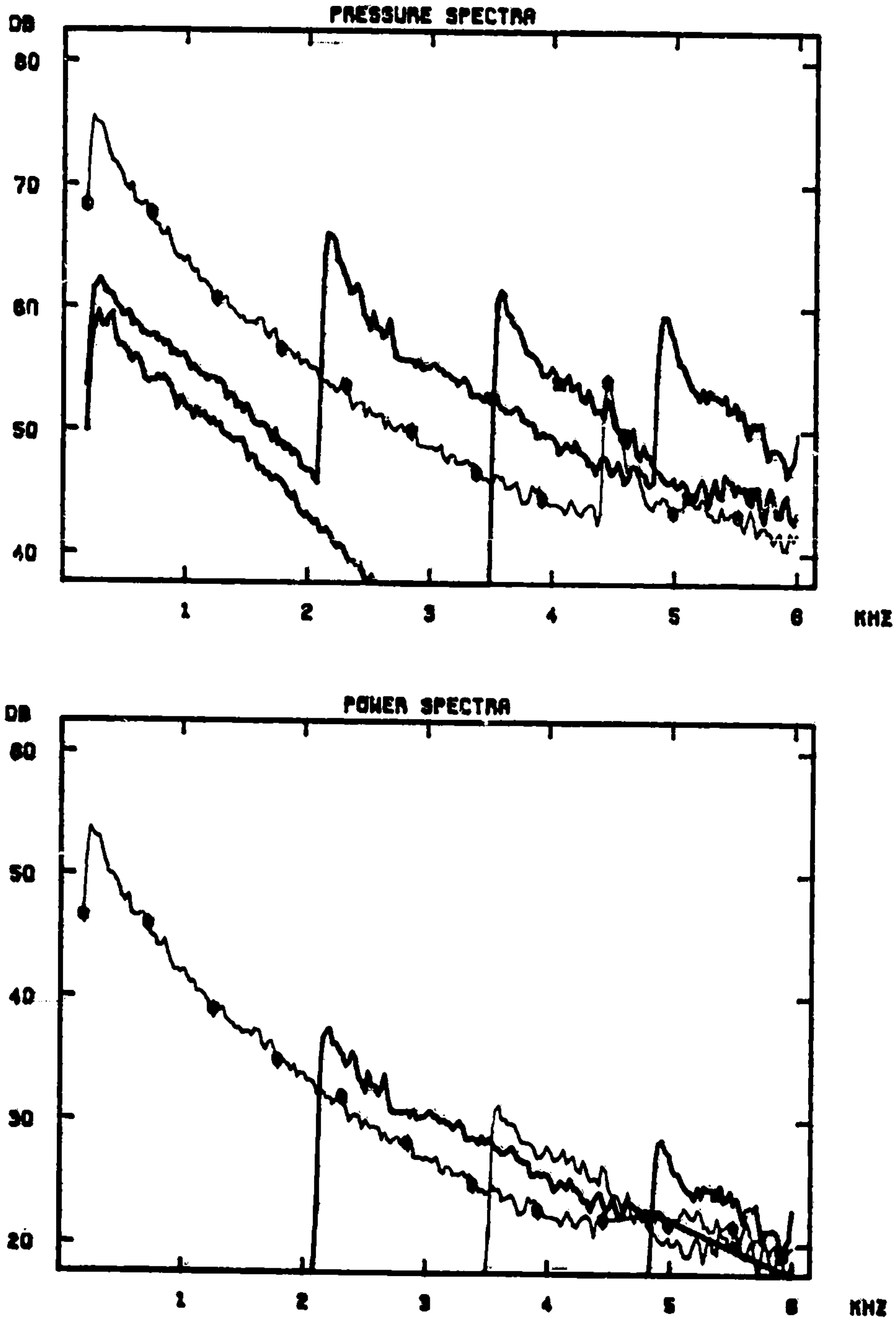

Fig. A3-16. 50.8 mm diameter orifice ($\frac{d}{D}$ = 0.523), M_1 = 0.187, f_r = 0.356.

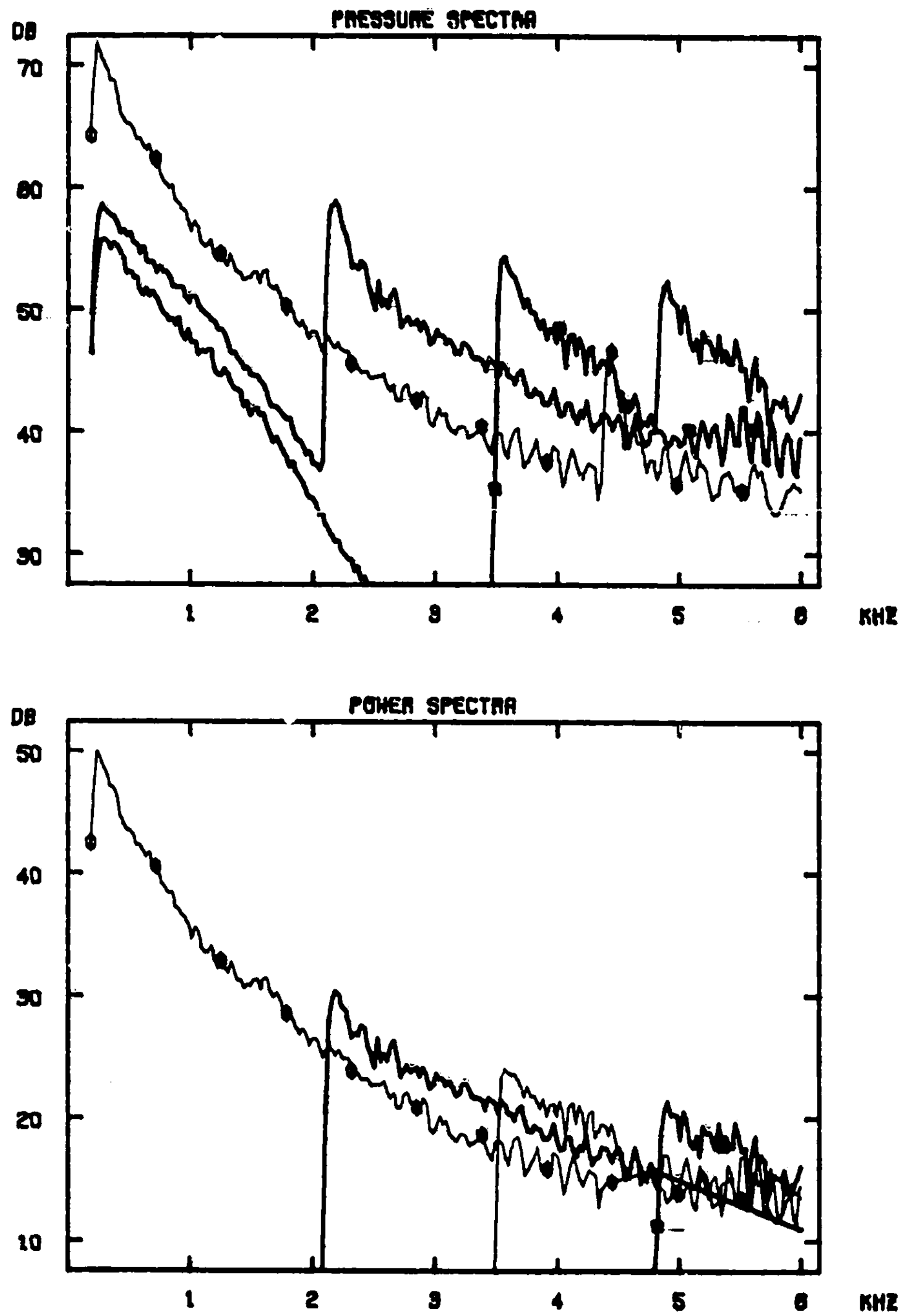

Fig. A3-17. 50.8 mm diameter orifice ($\frac{d}{D}$ = 0.523), M_i = 0.150, f_r = 0.287.

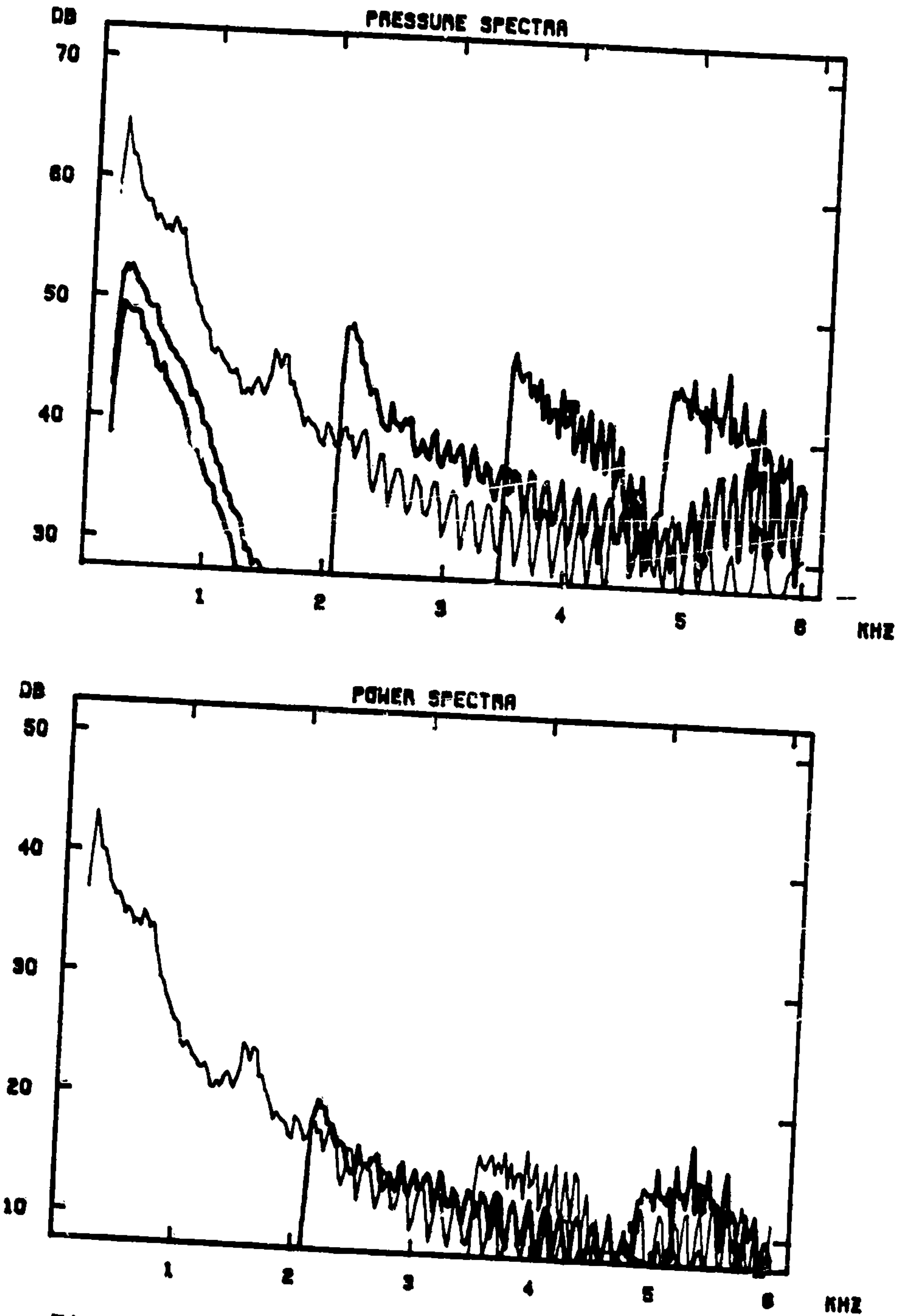

Fig. A3-18. 50.8 mm diameter orifice $(\frac{d}{D} = 0.523)$, $M_1 = 0.101$, $f_r = 0.184$.

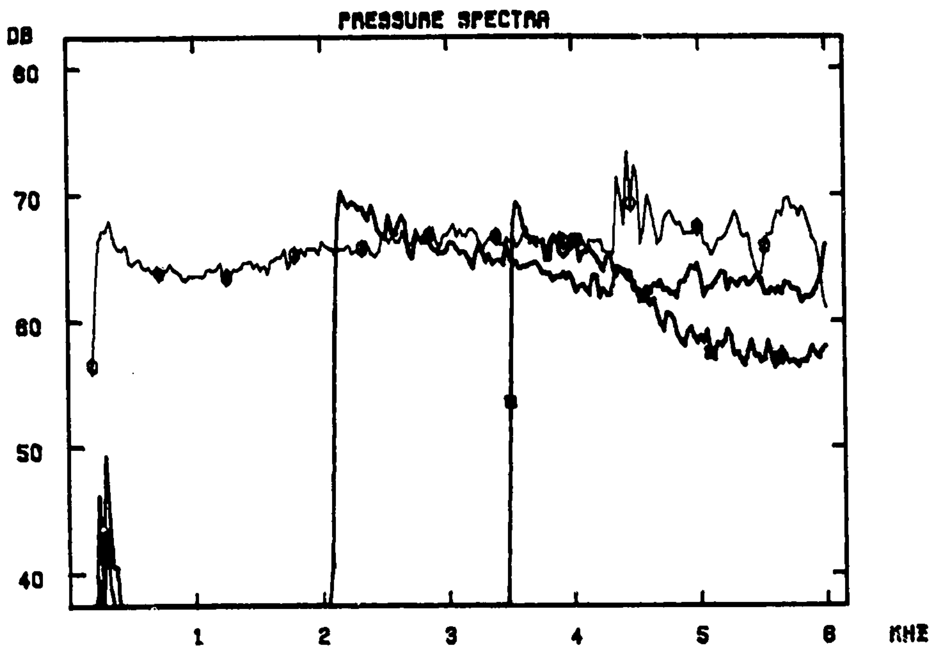

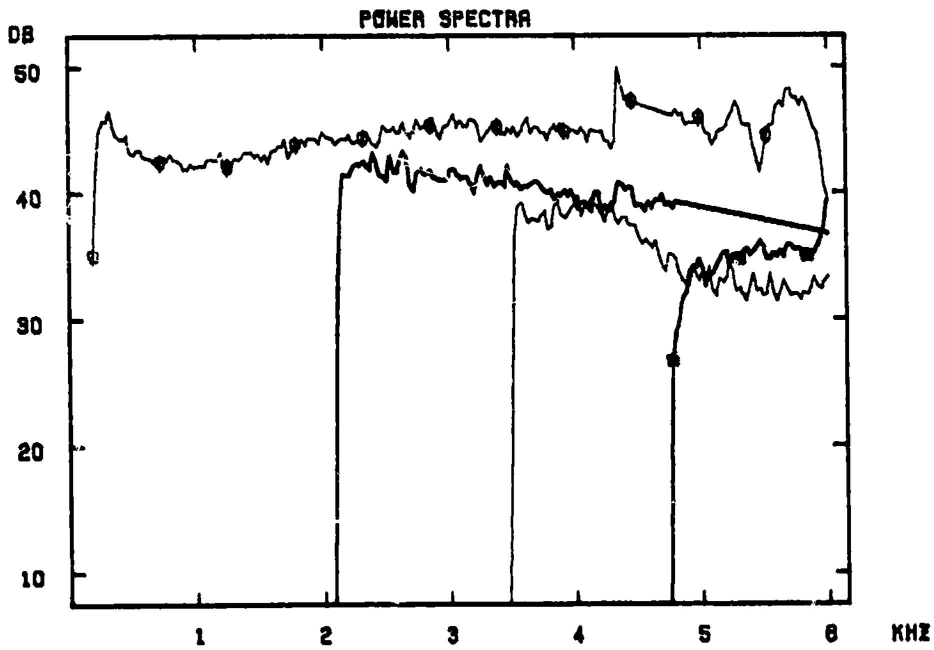

Fig. A3-19. 3.18 mm diameter nozzle ($\frac{d}{D}$ = 0.0327), M_i = 1.00, f_r = 28.0.

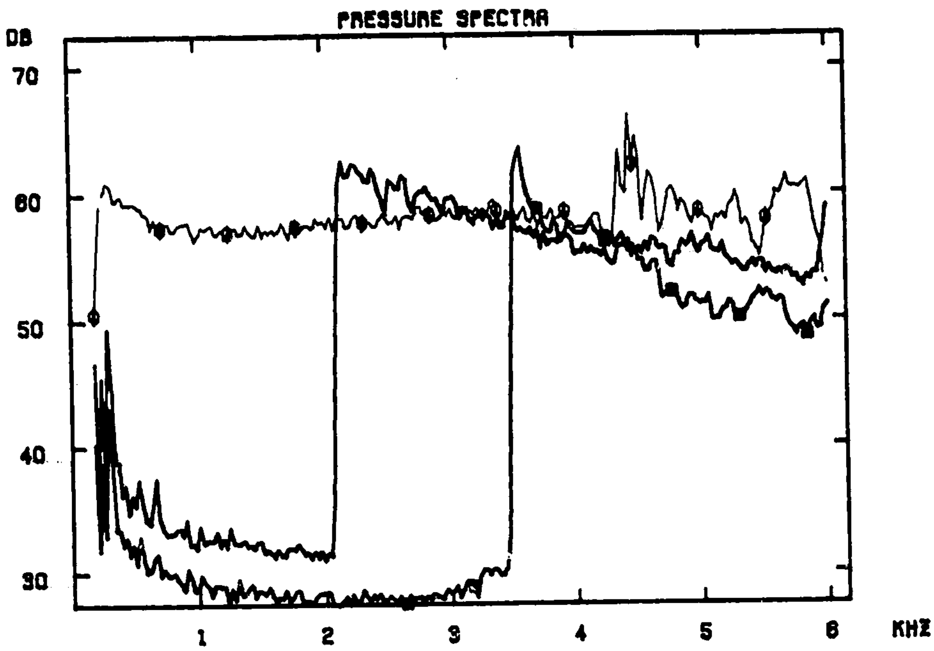

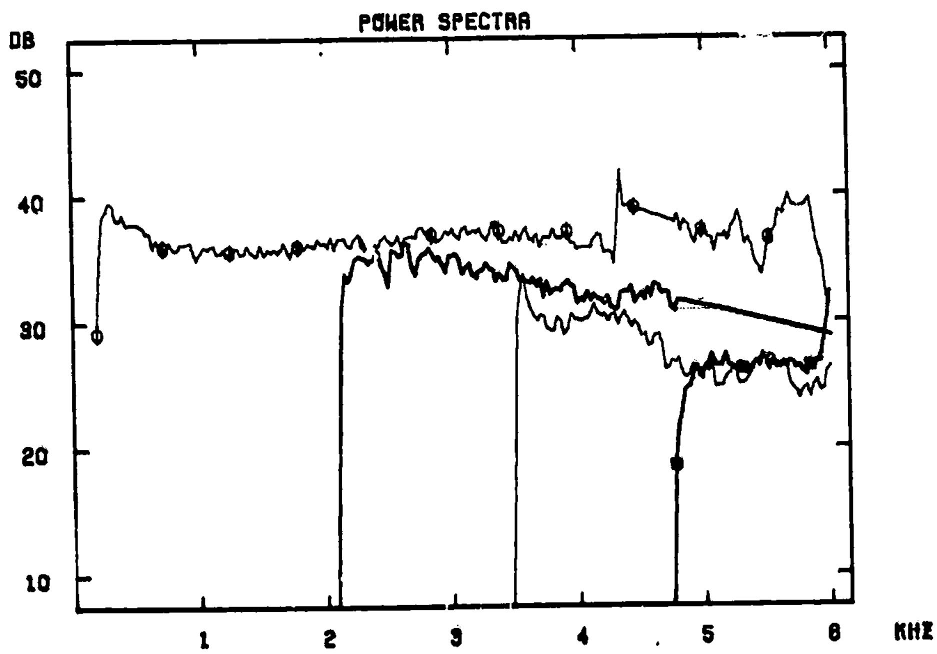

Fig. A3-20. 3.18 mm diameter nozzle ($\frac{d}{D}$ = 0.0327), M_i = 0.750, f_r = 21.8.

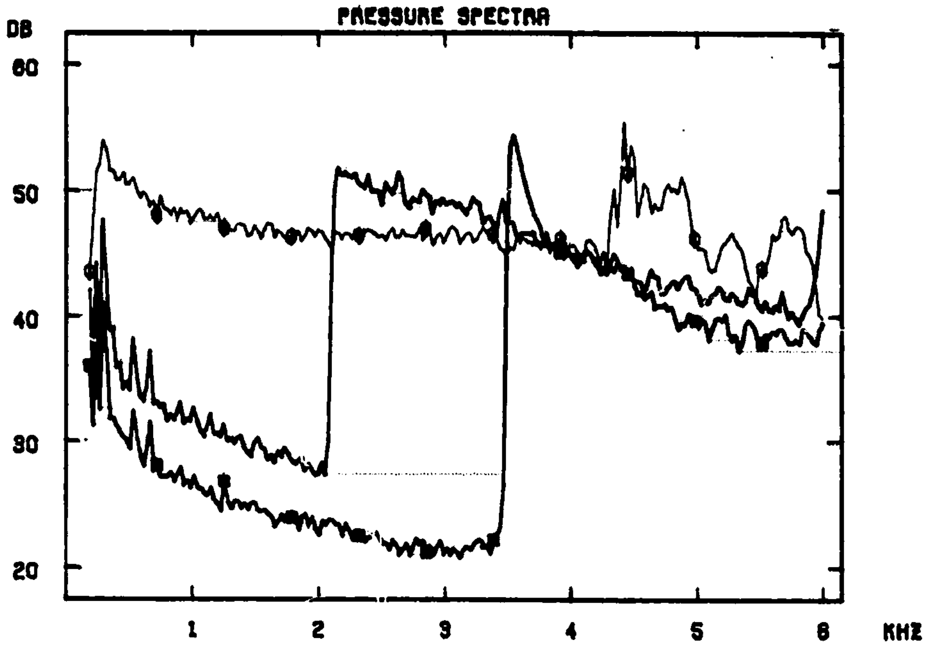

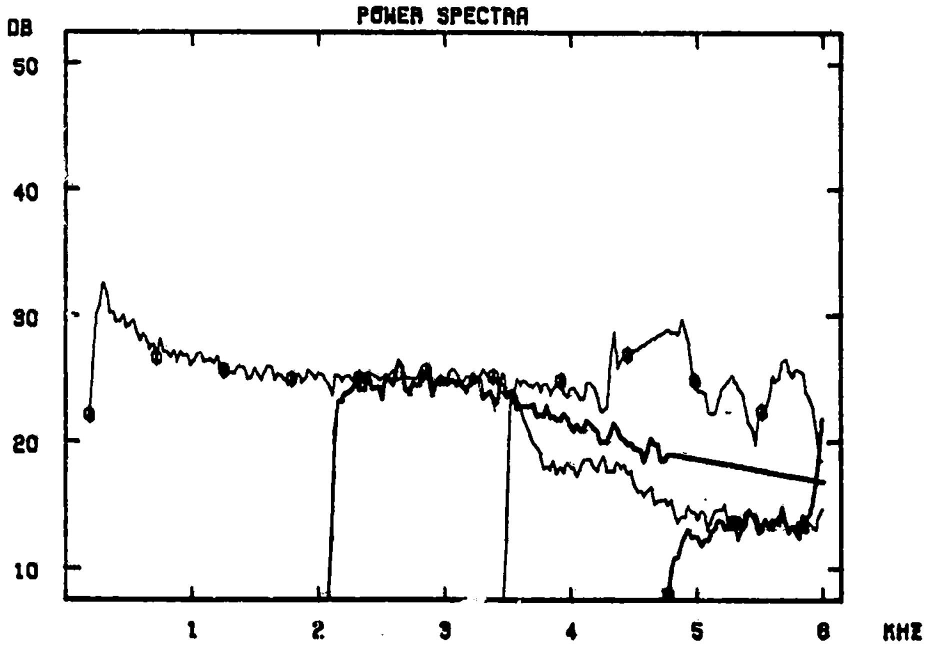

Fig. A3-21. 3.18 mm diameter nozzle ($\frac{d}{D}$ = 0.0327), M_i = 0.500, f_r = 15.0.

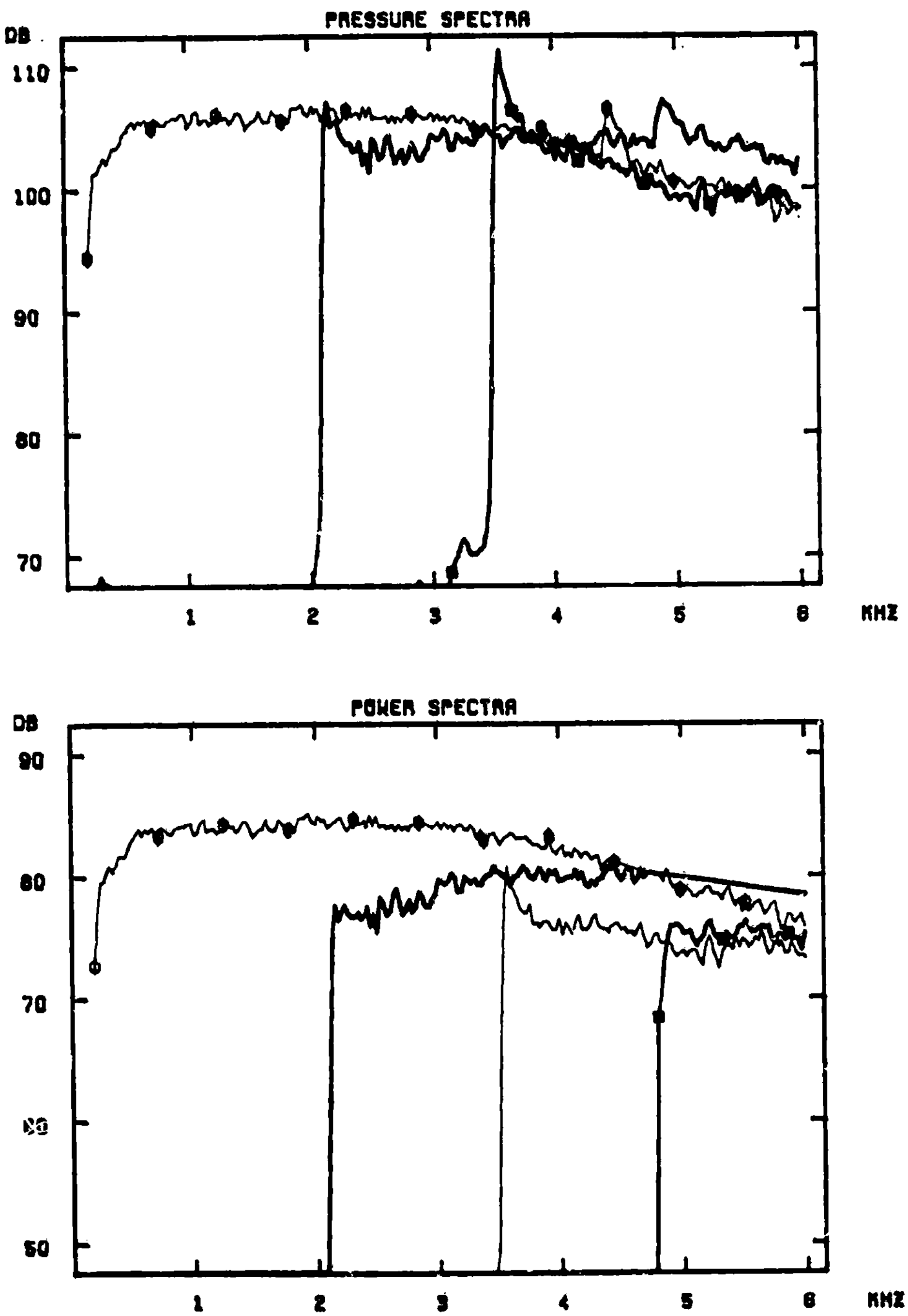

Fig. A3-22. 16.2 mm diameter nozzle ($\frac{d}{D}$ = 0.167), M_i = 1.12, f_r = 5.98, L_t/d = 1.

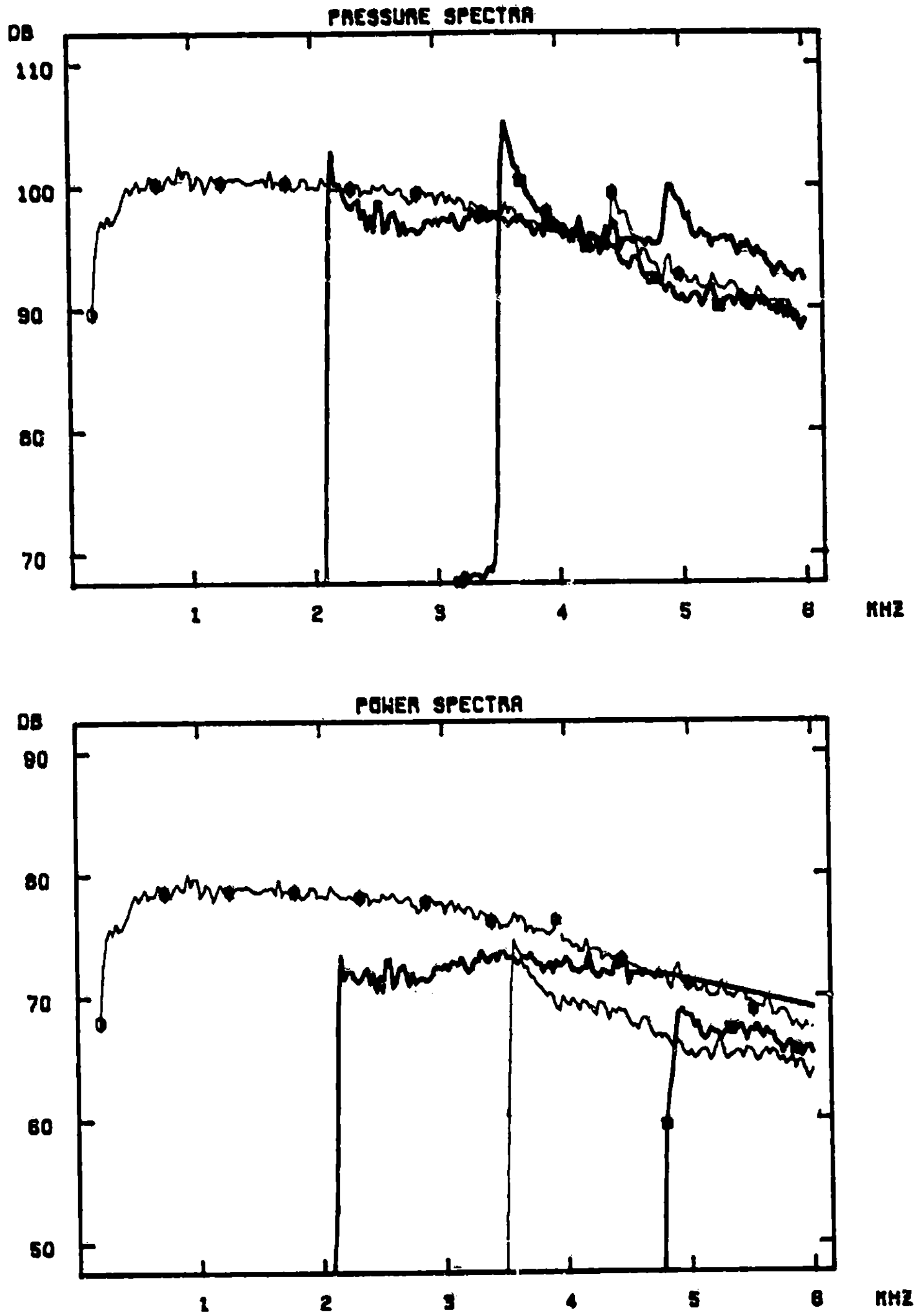

Fig. A3-23. 16.2 mm diameter nozzle ($\frac{d}{D}$ = 0.167), M_i = 0.917, f_r = 5.07, L_t/d = 1.

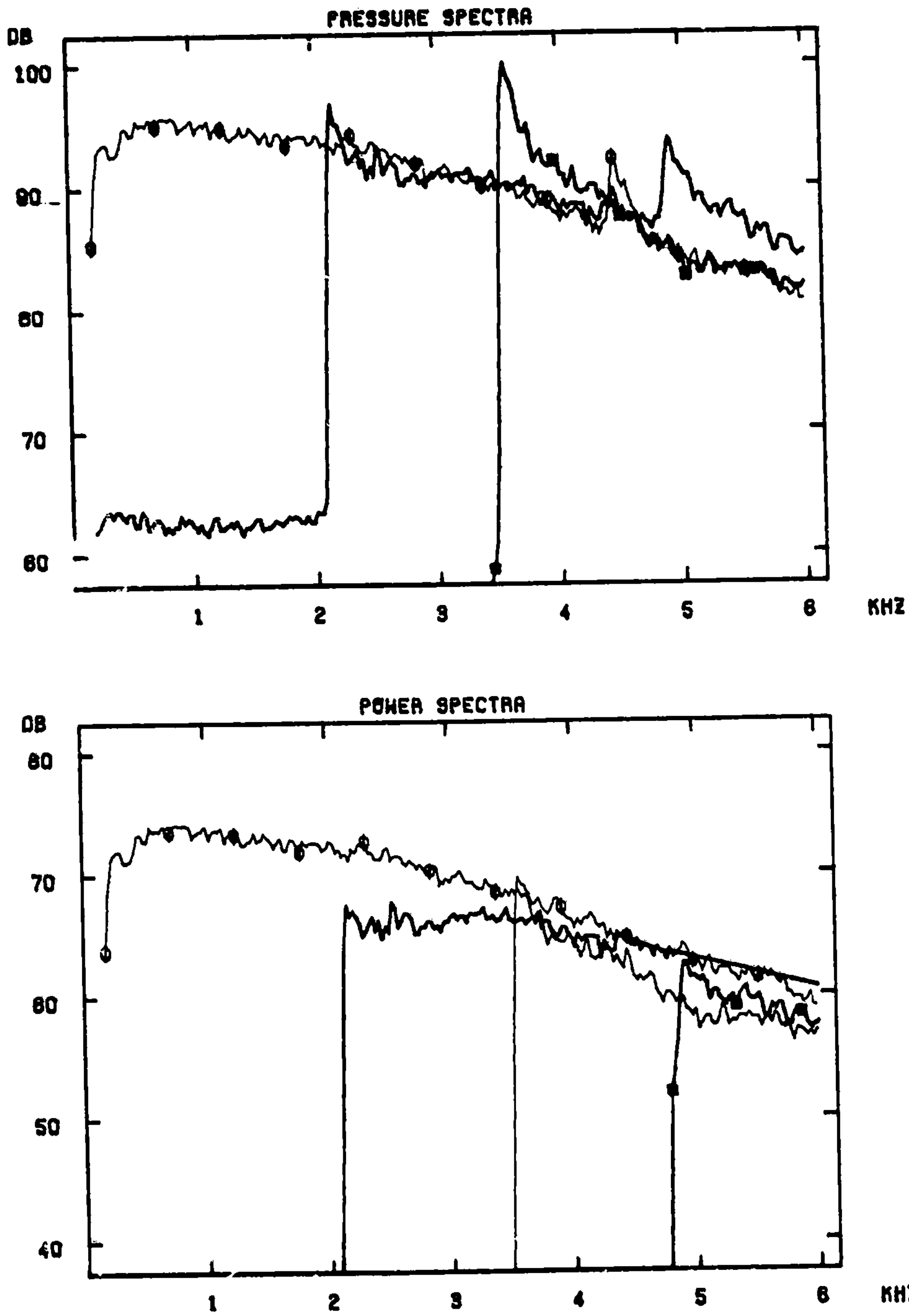

Fig. A3-24. 16.2 mm diameter nozzle ($\frac{d}{D}$ = 0.167), M_i = 0.752, f_r = 4.27, L_t/d = 1.

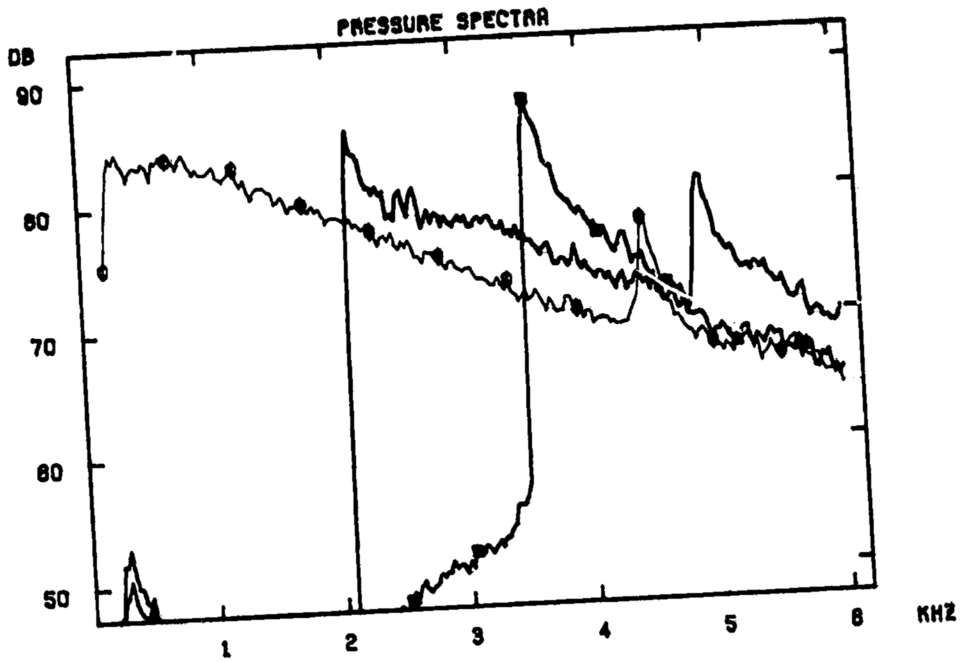

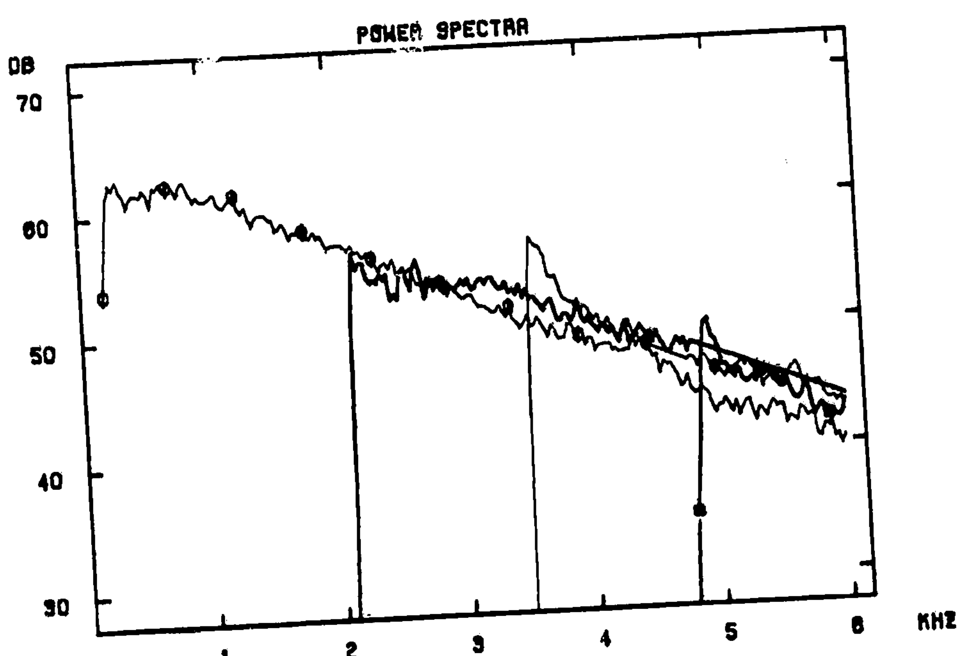

Fig. A3-25. 16.2 mm diameter nozzle ($\frac{d}{D}$ = 0.167), M_i = 0.500, f_r = 2.92, L_t/d = 1.

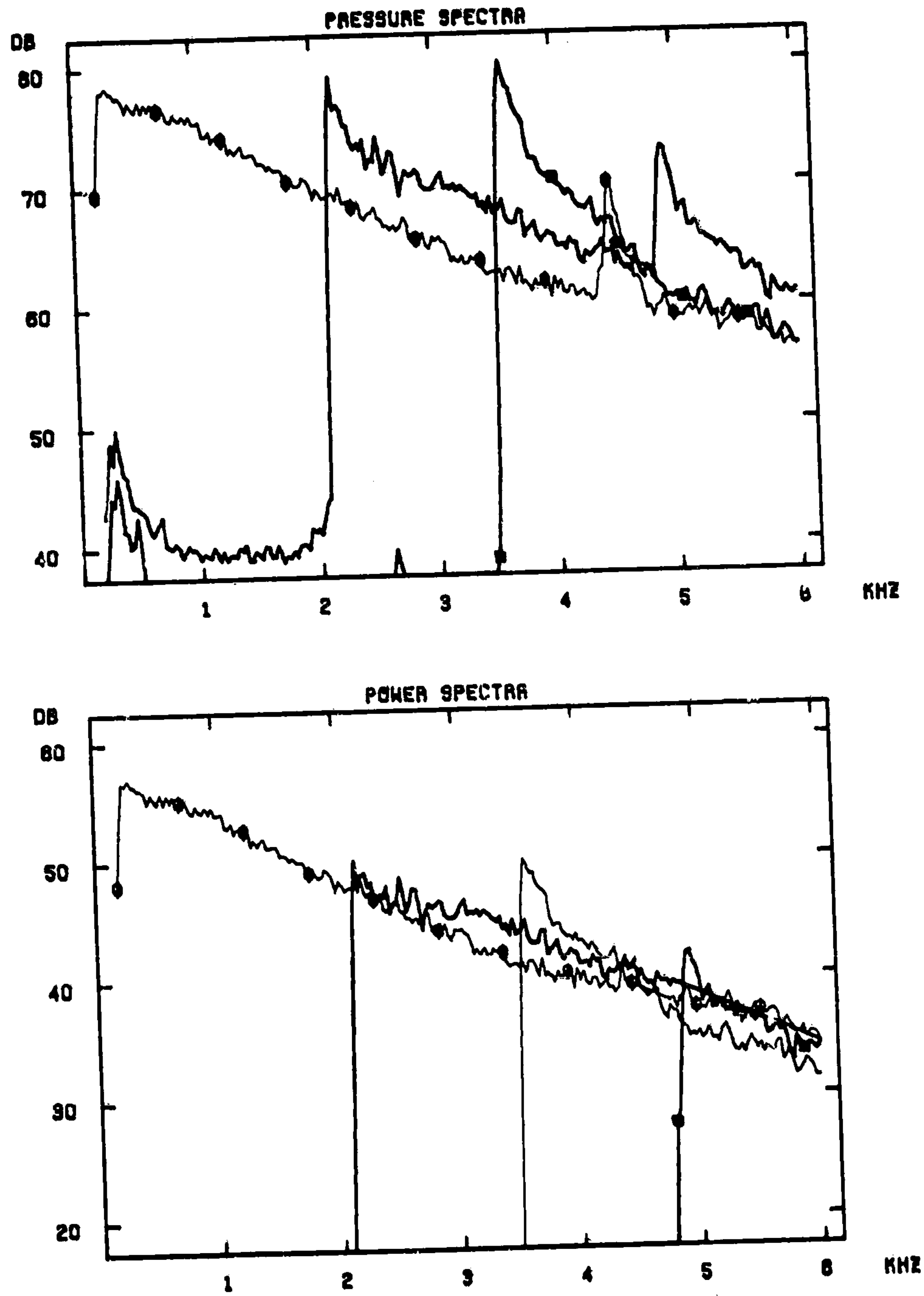

Fig. A3-26. 16.2 mm diameter nozzle $(\frac{d}{D} = 0.167)$, $M_i = 0.394$, $f_r = 2.32$, $L_t/d = 1$.

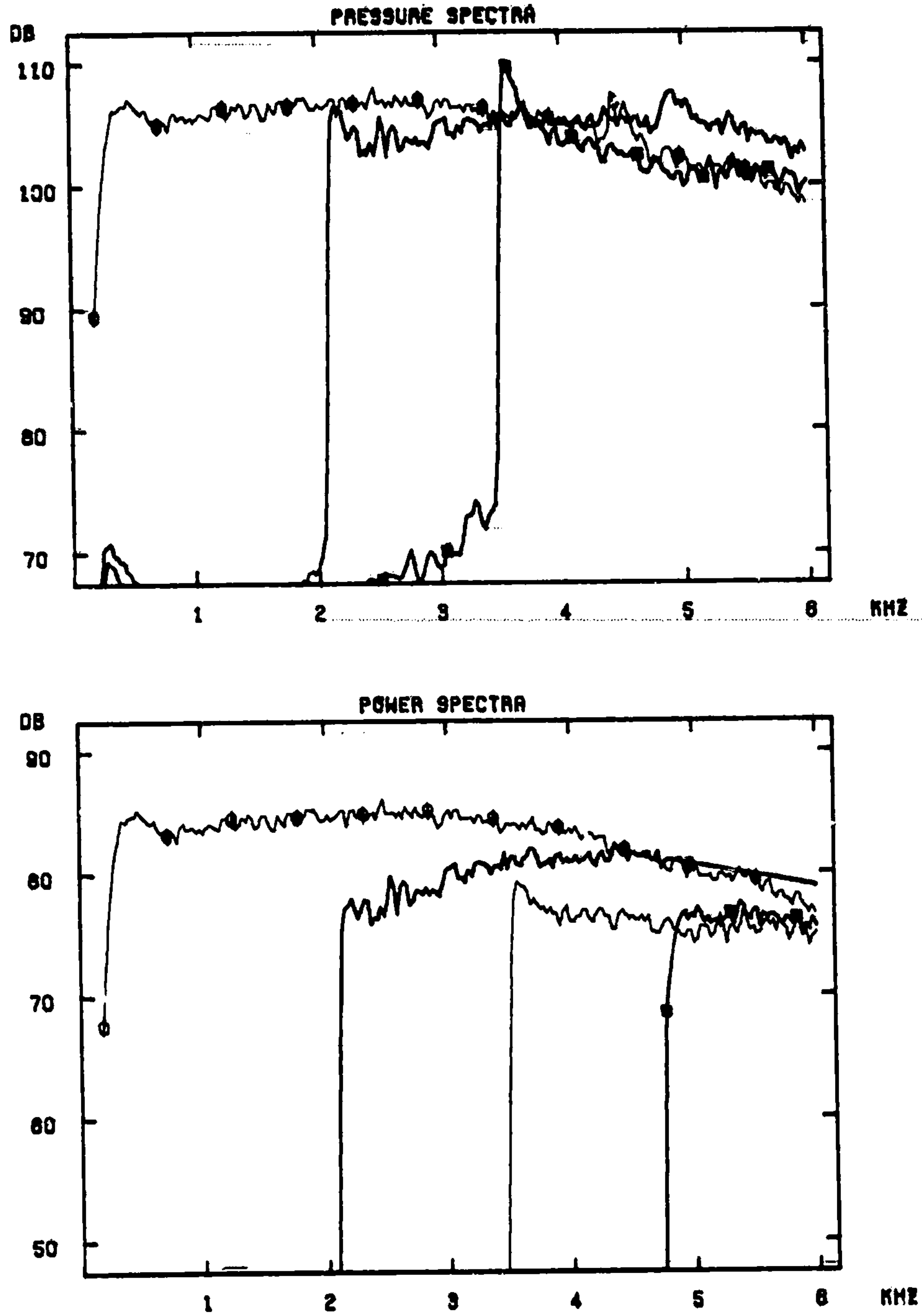

Fig. A3-27. 16.2 mm diameter long nozzle $(\frac{d}{D} = 0.167)$
$M_i = 1.16$, $f_r = 6.19$,
$L_t/d = 8$.

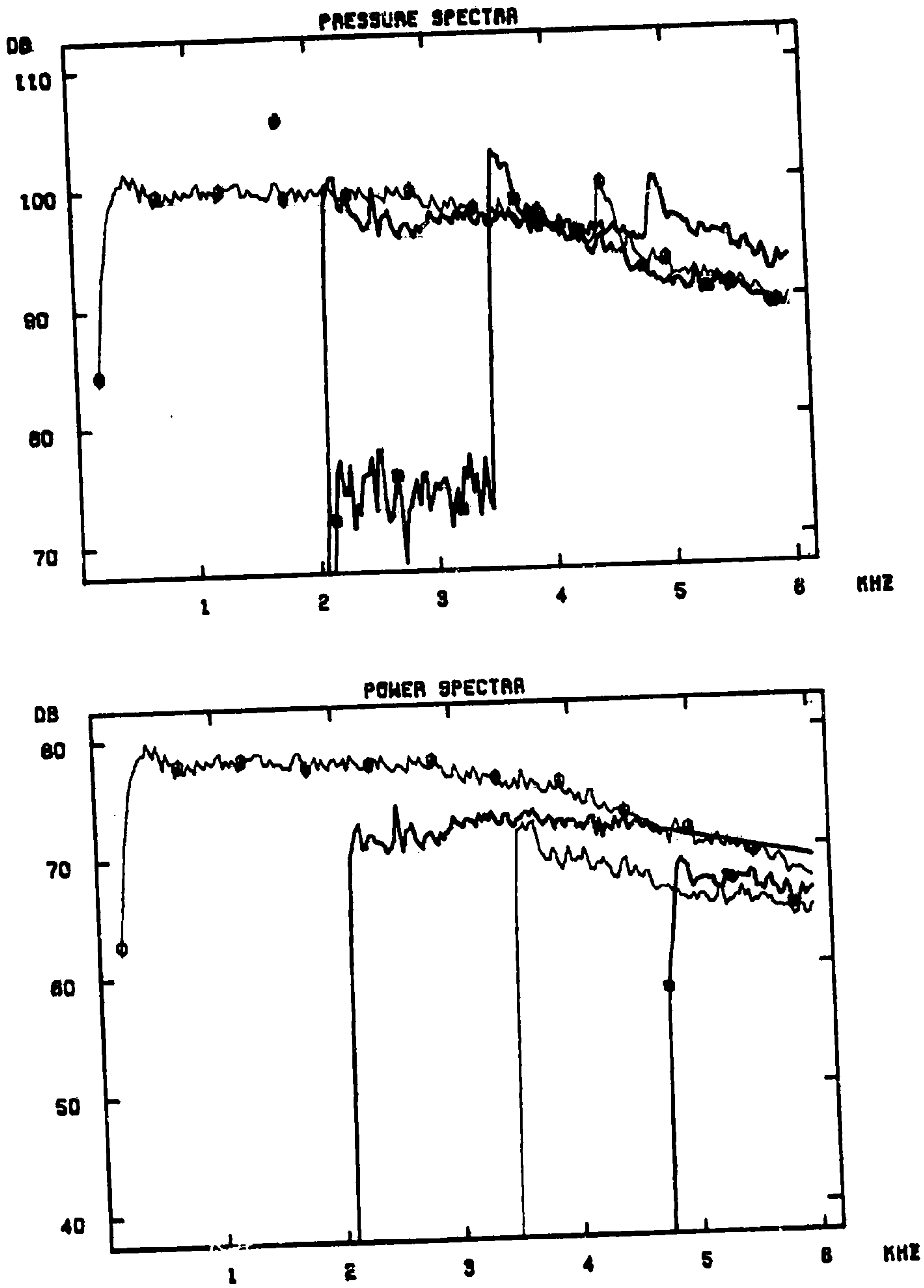

Fig. A3-28. 16.2 mm diameter long nozzle ($\frac{d}{D}$ = 0.167), M_i = 0.926, f_r = 5.12, L_t/d = 8.

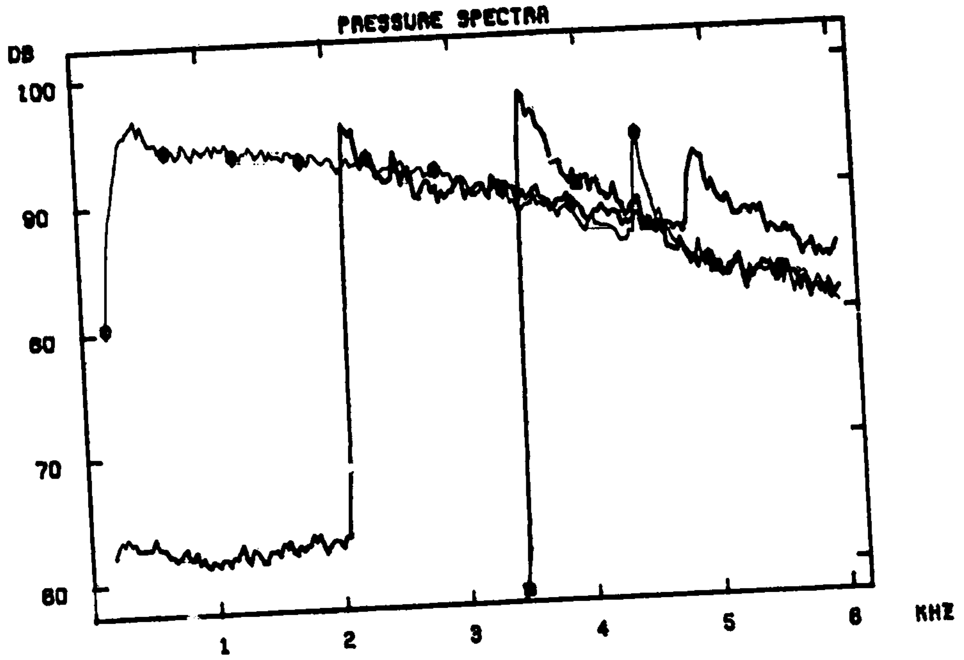

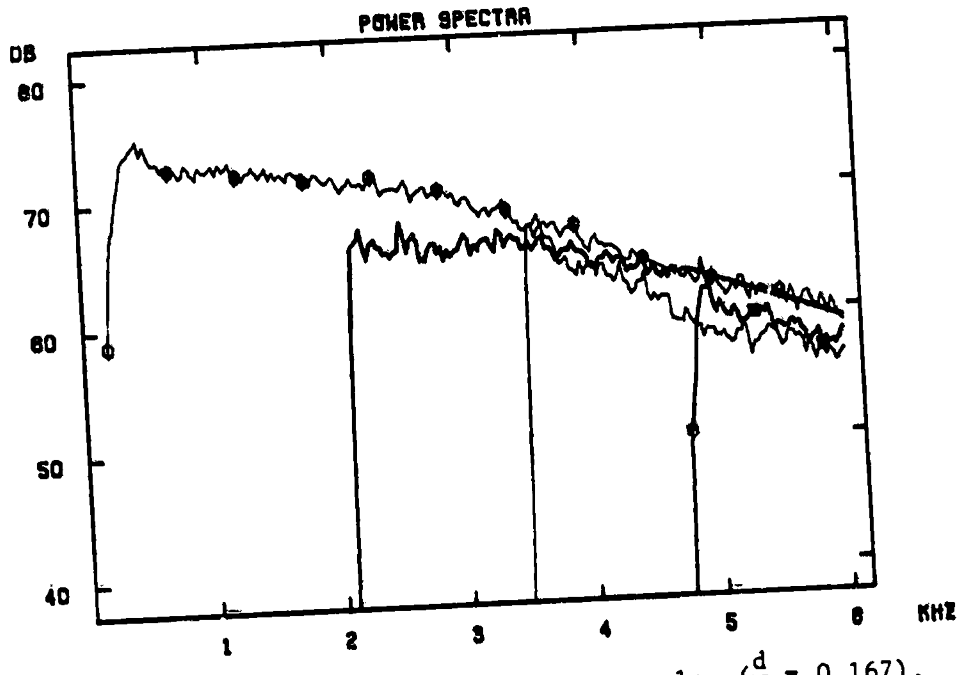

Fig. A3-29. 16.2 mm diameter long nozzle ($\frac{d}{D}$ = 0.167), M_i = 0.926, f_r = 5.12, L_t^i/d = 8.

ORIGINAL PAGE IS
OF POOR QUALITY

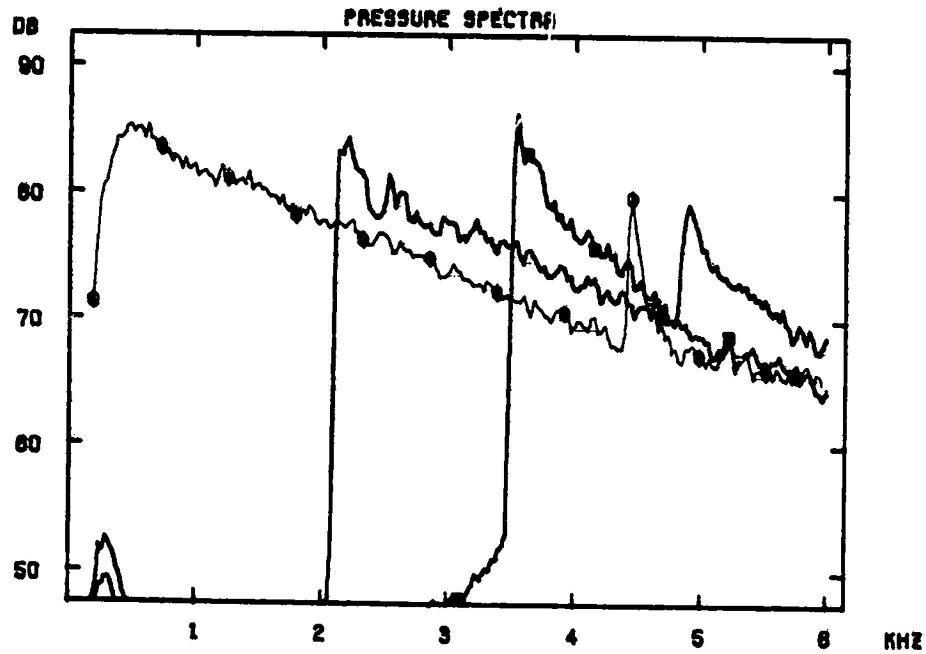

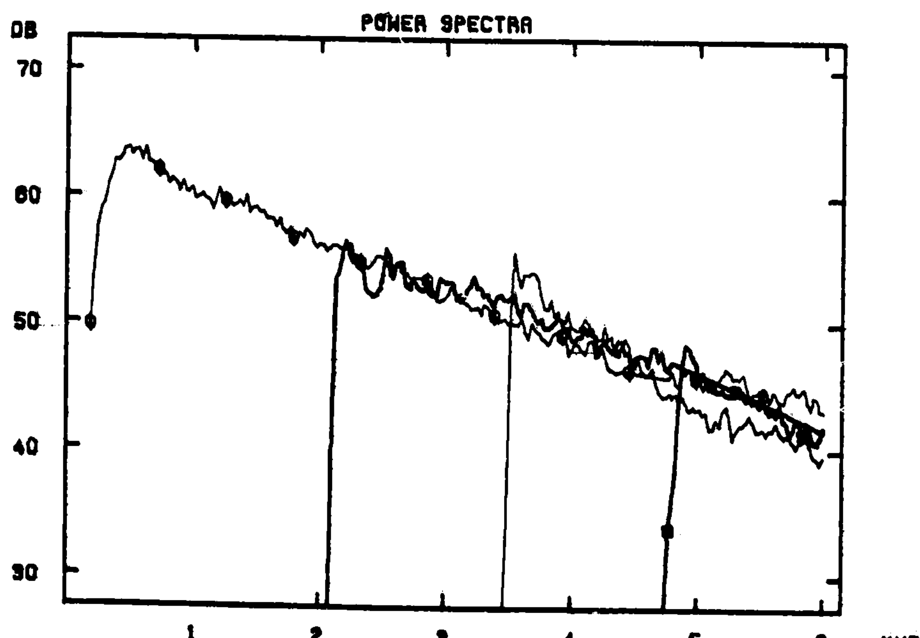

Fig. A3-30. 16.2 mm diameter long nozzle $(\frac{d}{D} = 0.167)$, $M_i = 0.501$, $f_r = 2.93$, $L_t/d = 8$.

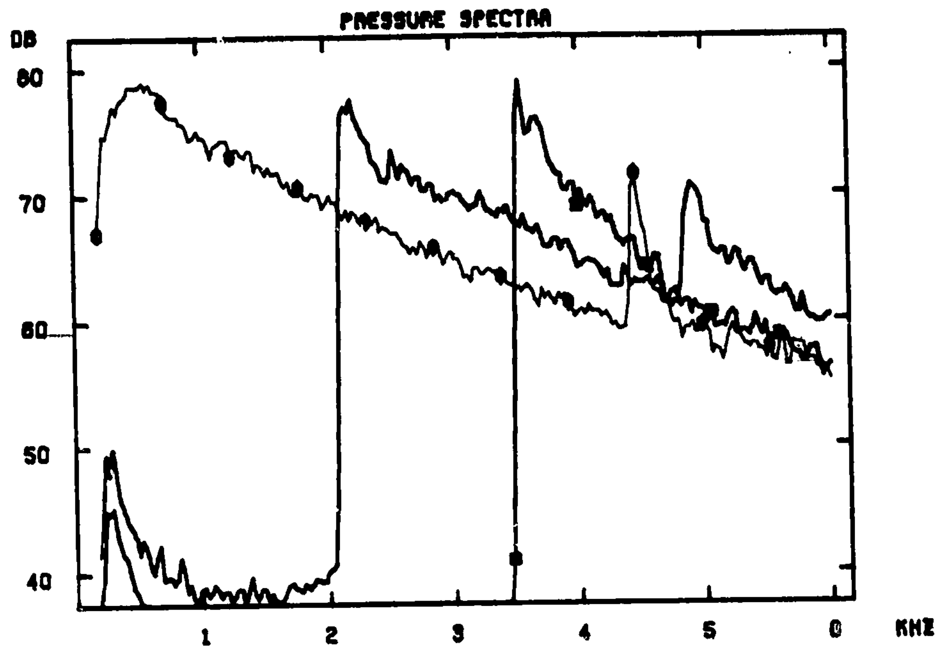

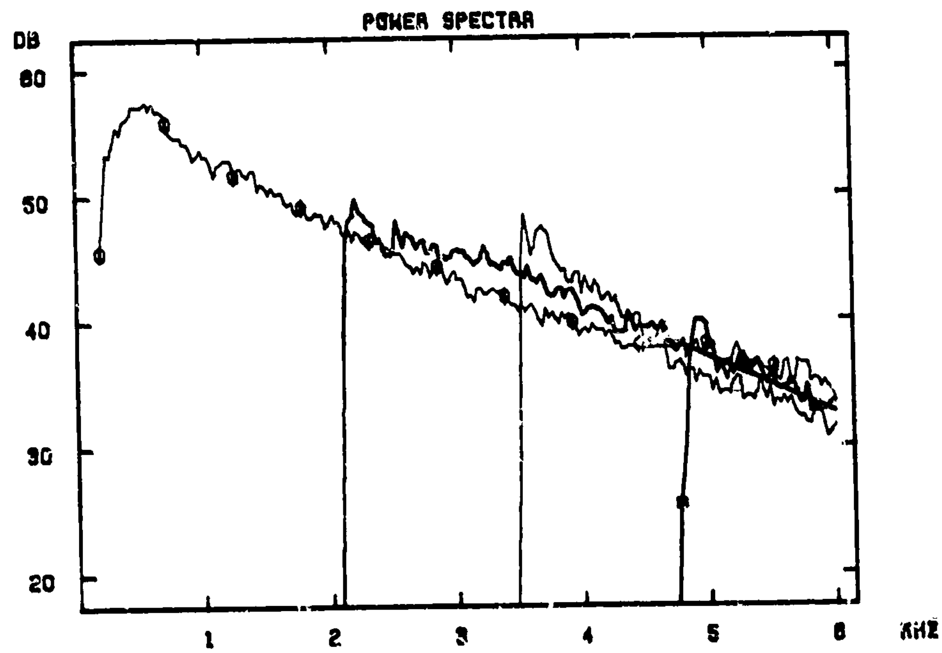

Fig. A3-31. 16.2 mm diameter long nozzle $(\frac{d}{D} = 0.167)$, $M_1 = 0.398$, $f_r = 2.35$, $L_t/d = 8$.

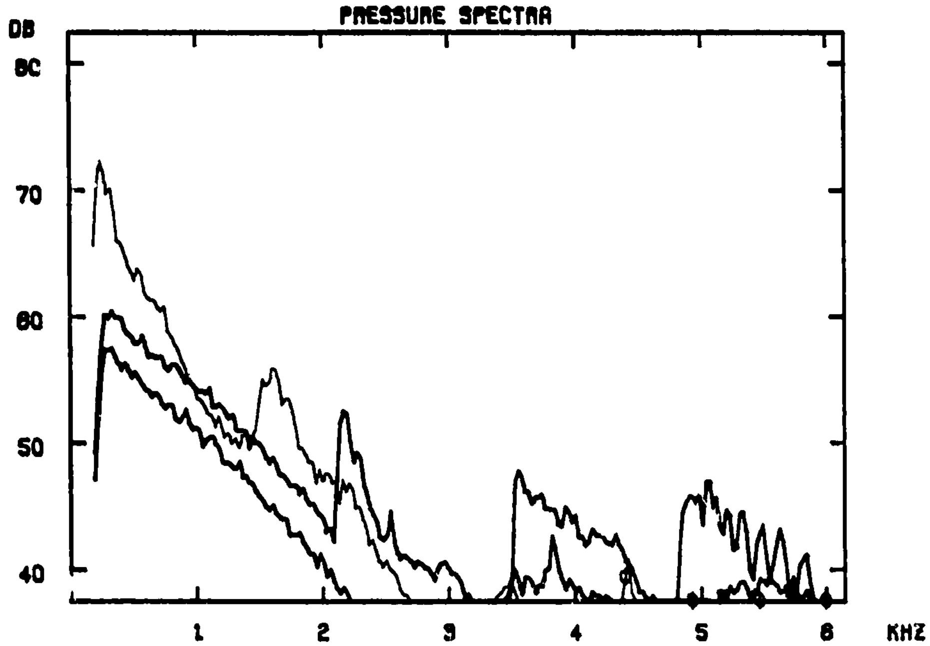

Fig. A3-32. Background noise measured with no restriction in the pipe. $\dot{m}$ = 0.249 lbm/sec.

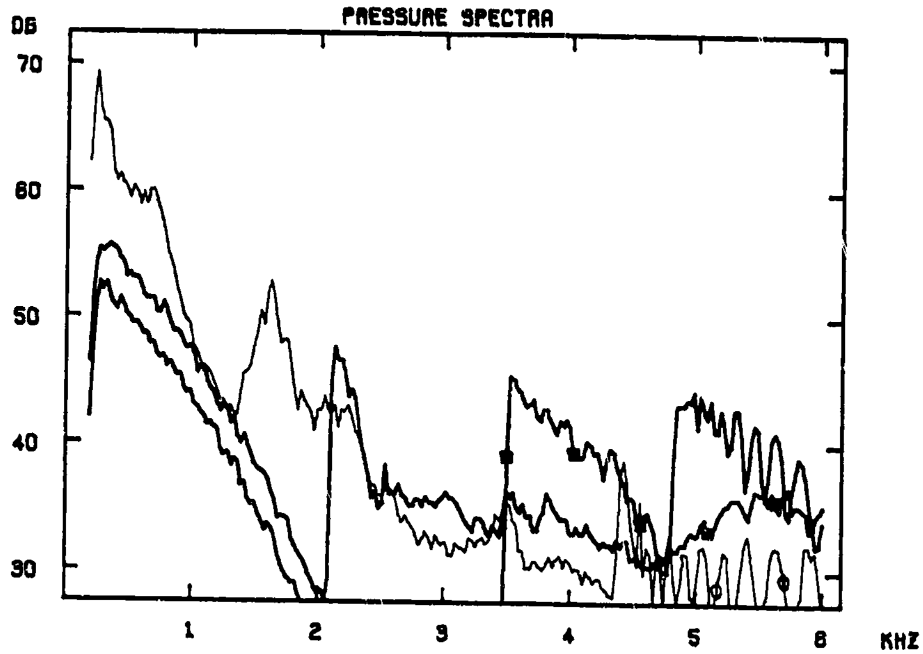

Fig. A3-33. Background noise measured with no restriction in the pipe. $\dot{m}$ = 0.174 lbm/sec.

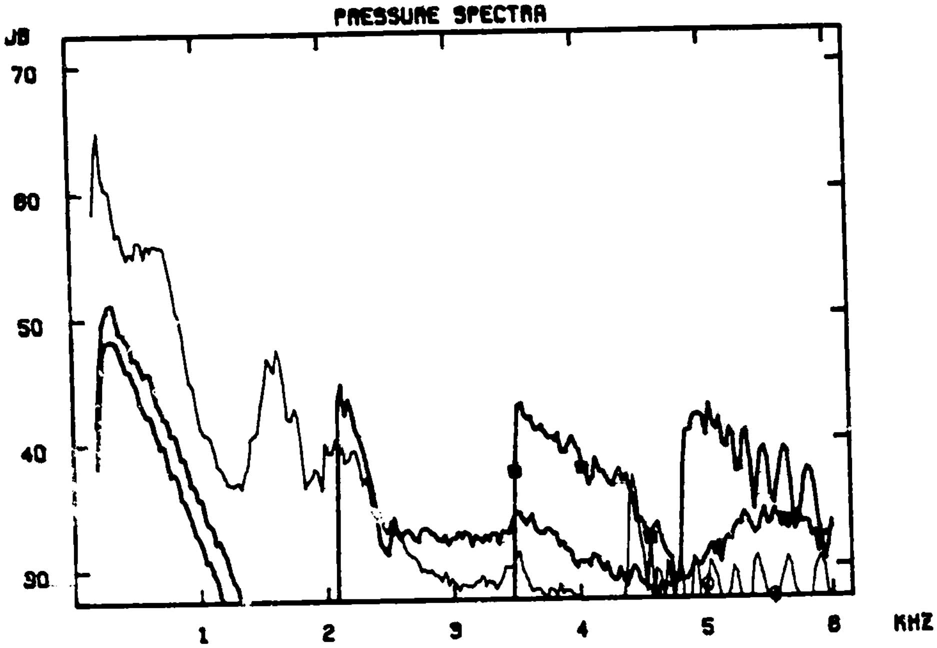

Fig. A3-34. Background noise measured with no restriction in the pipe. $\dot{m}$ = 0.124 lbm/sec.

Appendix A4

TABULATED EXPERIMENTAL RESULTS

Table A4.1

12.7 mm Orifice ($\frac{d}{D}$ = 0.131)

M_i	.499	.752	.918	1.08	1.24
U_i (ft/sec)	554	807	964	1103	1229
$\dot{m}$ (lbm/sec)	.0368	.0615	.0818	.106	.134
$Re = \rho_i U_i d/\mu_i$	1.53×10^5	2.49×10^5	3.19×10^5	3.98×10^5	4.83×10^5
P_o upstream (in. Hg)	35.77	44.32	52.72	63.97	78.57
T_o (°F)	78°	74°	77°	77°	73°
$f_r = U_i D/a_o d$	3.72	5.44	6.48	7.42	8.25
Acoustic Pressure (db)					
Total:	110.9	124.1	130.9	136.8	141.7
200-2100 Hz:	106.0	118.2	124.2	129.4	133.7
(0,0) Mode:	107.9	121.5	128.2	133.9	138.5
(1,0) Mode:	105.6	118.3	125.0	131.3	136.3
(2,0) Mode:	103.2	115.4	121.9	127.6	132.5
(3,0) Mode:	97.1	112.1	119.7	126.7	131.9
Acoustic Efficiency					
Total:	2.53×10^{-6}	1.56×10^{-5}	3.92×10^{-5}	8.89×10^{-5}	1.69×10^{-4}
Plane Wave Assumption:	3.73×10^{-6}	2.18×10^{-5}	5.42×10^{-5}	1.25×10^{-4}	2.39×10^{-4}
200-2100 Hz:	1.20×10^{-6}	5.50×10^{-6}	1.16×10^{-5}	2.25×10^{-5}	3.79×10^{-5}
(0,0) Mode:	1.86×10^{-6}	1.18×10^{-5}	2.94×10^{-5}	6.33×10^{-5}	1.16×10^{-4}
(1,0) Mode:	4.80×10^{-7}	2.76×10^{-6}	7.13×10^{-6}	1.89×10^{-5}	3.87×10^{-5}
(2,0) Mode:	1.63×10^{-7}	7.96×10^{-7}	1.88×10^{-6}	4.31×10^{-6}	8.87×10^{-6}
(3,0) Mode:	2.90×10^{-8}	2.61×10^{-7}	8.05×10^{-7}	$2.35\ 10^{-6}$	$4.95\ 10^{-6}$

Table A4.2

19.0 mm Orifice ($\frac{d}{D}$ = 0.196)

M_i	.393	.492	.755	.918	1.07
U_i (ft/sec)	439	547	814	966	1100
$\dot{m}$ (lbm/sec)	.0645	.0830	.143	.191	.252
$Re = \rho_i U_i d/\mu_i$	1.79×10^5	2.30×10^5	3.82×10^5	4.95×10^5	6.23×10^5
P_o upstream (in. Hg)	33.97	36.32	45.72	54.82	66.77
T_o (°F)	78°	79°	79°	79°	78°
$f_r = U_i D/a_o d$	1.97	2.45	3.65	4.33	4.94
Acoustic Pressure (dB)					
Total:	110.0	117.3	131.5	138.6	144.4
200-2100 Hz:	106.8	113.6	126.7	132.7	137.6
(0,0) Mode:	107.5	114.6	128.9	135.1	141.5
(1,0) Mode:	104.4	111.6	125.3	132.8	138.6
(2,0) Mode:	101.4	109.0	123.2	129.7	135.8
(3,0) Mode:	95.7	104.1	119.2	127.3	133.9
Acoustic Efficiency					
Total:	1.94×10^{-6}	5.06×10^{-6}	3.52×10^{-5}	9.57×10^{-5}	2.02×10^{-4}
Plane Wave Assumption:	2.74×10^{-6}	7.28×10^{-6}	4.92×10^{-5}	1.32×10^{-4}	2.84×10^{-4}
200-2100 Hz:	1.30×10^{-6}	3.09×10^{-6}	1.61×10^{-5}	3.40×10^{-5}	5.88×10^{-5}
(0,0) Mode:	1.53×10^{-6}	3.92×10^{-6}	2.71×10^{-5}	7.17×10^{-5}	1.46×10^{-4}
(1,0) Mode:	3.00×10^{-7}	8.11×10^{-7}	5.74×10^{-6}	1.77×10^{-5}	4.01×10^{-5}
(2,0) Mode:	9.13×10^{-8}	2.68×10^{-7}	1.86×10^{-6}	4.54×10^{-6}	1.11×10^{-5}
(3,0) Mode:	1.80×10^{-8}	6.19×10^{-8}	5.20×10^{-7}	1.76×10^{-6}	4.74×10^{-6}

Table A4.3

31.8 mm Orifice ($\frac{d}{D}$ = 0.327)

M_i	.149	.277	.397	.500	
U_i (ft/sec)	169.4	312	442	553	
$\dot{m}$ (lbm/sec)	.0657	.127	.192	.257	
$Re = \rho_i U_i d/\mu_i$	1.10×10^5	2.16×10^5	3.22×10^5	4.24×10^5	
P_o upstream (in. Hg)	30.88	33.33	36.01	39.23	
T_o (°F)	78°	76°	74°	74°	
$U_r = U_i D/a_o d$	0.455	0.841	1.19	1.49	
Acoustic Pressure (dB)					
Total:	86.9	106.0	117.9	125.5	
200-2100 Hz:	85.9	104.3	115.5	122.8	
(0,0) Mode:	86.0	104.5	115.9	123.3	
(1,0) Mode:	77.2	98.4	111.0	118.9	
(2,0) Mode:	73.8	95.4	108.7	116.6	
(3,0) Mode:	70.3	90.6	104.2	112.9	
Acoustic Efficiency					
Total:	7.65×10^{-8}	8.56×10^{-7}	3.92×10^{-6}	1.05×10^{-5}	
Plane Wave Assumption:	8.72×10^{-8}	1.07×10^{-6}	5.22×10^{-6}	1.43×10^{-5}	
200-2100 Hz:	6.96×10^{-8}	7.24×10^{-7}	3.02×10^{-6}	7.61×10^{-6}	
(0,0) Mode:	7.17×10^{-8}	7.61×10^{-7}	3.30×10^{-6}	8.61×10^{-6}	
(1,0) Mode:	3.43×10^{-9}	6.84×10^{-8}	4.29×10^{-7}	1.31×10^{-6}	
(2,0) Mode:	1.03×10^{-9}	2.13×10^{-8}	1.48×10^{-7}	4.40×10^{-7}	
(3,0) Mode:	3.51×10^{-10}	5.28×10^{-9}	3.89×10^{-8}	1.38×10^{-7}	

Table A4.4*

50.8 mm Orifice ($\frac{d}{D}$ = 0.523)

M_i	.101	.150	.187	.225	
U_i (ft/sec)	109	170	212	254	
$\dot{m}$ (lbm/sec)	.122	.191	.247	.306	
$Re = \rho_i U_i d/\mu_i$	1.24×10^5	1.92×10^5	2.43×10^5	3.06×10^5	
P_o upstream (in. Hg)	33.29	33.38	34.31	35.61	
T_o (°F)	75°	76°	79°	76°	
$f_r = U_i D/a_o d$	0.184	0.287	0 356	0.428	
<u>Acoustic Pressure (dB)</u>					
Total:	87.9	95.9	101.1	106.2	
200-2100 Hz:	87.3	95.4	100.2	105.1	
(0,0) Mode:	87.4	95.4	100.3	105.3	
(1,0) Mode:	74.0	84.0	91.2	97.3	
(2,0) Mode:	73.1	80.1	86.8	92.9	
(3,0) Mode:	72.2	77.9	84.3	90.6	
<u>Acoustic Efficiency</u>					
Total:	1.16×10^{-7}	2.10×10^{-7}	3.21×10^{-7}	5.61×10^{-7}	
Plane Wave Assumption:	1.25×10^{-7}	2.27×10^{-7}	3.63×10^{-7}	6.54×10^{-7}	
200-2100 Hz:	1.11×10^{-7}	2.00×10^{-7}	2.97×10^{-7}	5.07×10^{-7}	
(0,0) Mode:	1.13×10^{-7}	2.03×10^{-7}	3.04×10^{-7}	5.22×10^{-7}	
(1,0) Mode:	1.90×10^{-9}	5.09×10^{-9}	1.32×10^{-8}	2.94×10^{-8}	
(2,0) Mode:	1.12×10^{-9}	1.51×10^{-9}	3.32×10^{-9}	7.31×10^{-9}	
(3,0) Mode:	6.59×10^{-10}	6.45×10^{-10}	1.32×10^{-9}	3.01×10^{-9}	

*For qualifications of the 50.8 mm orifice data see Sections 3.6 and 3.7 of Chapter 3.

Table A4.5

16.2 mm Nozzle: Throat Length-to-Diameter Ratio = 1

($\frac{d}{D}$ = 0.167)

M_i	.394	.500	.752	.917	1.12
U_i (ft/sec)	442	556	813	967	1136
$\dot{m}$ (lbm/sec)	.0741	.0944	.150	.191	.251
$Re = \rho_i U_i d/\mu_i$	1.55×10^5	2.02×10^5	3.26×10^5	4.20×10^5	5.58×10^5
$P_{o\ upstream}$ (in.Hg)	34.30	36.83	45.93	54.93	70.33
T_o (°F)	81°	81°	81°	82°	81°
$f_r = U_i D/a_o d$	2.32	2.92	4.27	5.07	5.98
Acoustic Pressure (dB)					
Total:	111.0	118.6	132.0	138.4	145.2
200-2100 Hz:	107.7	114.9	127.2	132.8	138.2
(0,0) Mode:	108.3	115.8	129.4	135.8	142.1
(1,0) Mode:	104.7	112.4	125.5	132.3	139.6
(2,0) Mode:	103.5	111.1	124.2	129.7	136.6
(3,0) Mode:	97.1	105.3	119.5	126.7	134.9
Acoustic Efficiency					
Total:	2.00×10^{-6}	5.64×10^{-6}	3.70×10^{-5}	8.97×10^{-5}	2.24×10^{-4}
Plane Wave Assumption:	2.90×10^{-6}	8.21×10^{-6}	5.21×10^{-5}	1.24×10^{-4}	3.20×10^{-4}
200-2100 Hz:	1.38×10^{-6}	3.55×10^{-6}	1.75×10^{-5}	3.40×10^{-5}	6.35×10^{-5}
(0,0) Mode:	1.59×10^{-6}	4.39×10^{-6}	2.88×10^{-5}	6.82×10^{-5}	1.58×10^{-4}
(1,0) Mode:	2.77×10^{-7}	8.57×10^{-7}	5.64×10^{-6}	1.57×10^{-5}	4.84×10^{-5}
(2,0) Mode:	1.13×10^{-7}	3.25×10^{-7}	2.08×10^{-6}	4.32×10^{-6}	1.26×10^{-5}
(3,0) Mode:	1.98×10^{-8}	6.64×10^{-8}	5.24×10^{-7}	1.53×10^{-6}	5.79×10^{-6}

Table A4.6

16.2 mm Nozzle: Throat Length-to-Diameter Ratio = 8

$(\frac{d}{D} = 0.167)$

M_i	.398	.501	.762	.926	1.16
U_i	445	555	819	972	1172
$\dot{m}$ (lbm/sec)	.0710	.0897	.143	.183	.253
$Re = \rho_i U_i d/\mu_i$	1.58×10^{5}	2.02×10^{5}	3.33×10^{5}	4.28×10^{5}	5.96×10^{5}
P_o upstream (in. Hg)	34.33	36.77	46.27	55.37	74.77
T_o (°F)	77°	77°	77°	78°	77°
$f_r = U_i D/a_o d$	2.35	2.93	4.32	5.12	6.19
Acoustic Pressure (dB)					
Total:	110.7	118.0	131.5	138.1	146.0
200-2100 Hz:	107.7	114.5	126.8	132.4	138.6
(0,0) Mode:	108.2	115.4	128.9	135.5	142.8
(1,0) Mode:	104.4	111.8	125.2	132.0	140.4
(2,0) Mode:	102.7	110.0	123.3	129.1	137.1
(3,0) Mode:	96.0	104.2	119.0	126.7	135.9
Acoustic Efficiency					
Total:	1.98×10^{-6}	5.31×10^{-6}	3.41×10^{-5}	8.63×10^{-5}	2.50×10^{-4}
Plane Wave Assumption:	2.78×10^{-6}	7.55×10^{-6}	4.76×10^{-5}	1.19×10^{-4}	3.55×10^{-4}
200-2100 Hz:	1.40×10^{-6}	3.41×10^{-6}	1.61×10^{-5}	3.21×10^{-5}	6.59×10^{-5}
(0,0) Mode:	1.60×10^{-6}	4.19×10^{-6}	2.64×10^{-5}	6.52×10^{-5}	1.73×10^{-4}
(1,0) Mode:	2.65×10^{-7}	7.81×10^{-7}	5.32×10^{-6}	1.54×10^{-5}	5.54×10^{-5}
(2,0) Mode:	9.98×10^{-8}	2.79×10^{-7}	1.83×10^{-6}	4.14×10^{-6}	1.41×10^{-5}
(3,0) Mode:	1.68×10^{-8}	5.65×10^{-8}	4.84×10^{-7}	1.62×10^{-6}	6.86×10^{-6}

Table A4.7

3.18 mm Nozzle ($\frac{d}{D}$ = 0.0327)

M_i	.500	.750	1.00		
U_i (ft/sec)	553	807	1037		
$\dot{m}$ (lbm/sec)	.0036	.0054	.0074		
$Re = \rho_i U_i d/\mu_i$	3.80×10^4	5.96×10^4	8.45×10^4		
P_o upstream (in. Hg)	35.21	42.59	54.64		
T_o (°F)	74°	76°	76°		
$f_r = U_i D/a_o d$	15.0	21.8	28.0		
Acoustic Pressure (dB)					
Total:	87.8	98.7	106.4		
200-2100 Hz:	81.4	90.6	97.5		
(0,0) Mode:	85.1	96.0	104.0		
(1,0) Mode:	82.6	93.4	100.6		
(2,0) Mode:	78.6	89.4	96.9		
(3,0) Mode:	73.0	85.9	94.0		
Acoustic Efficiency					
Total:	1.37×10^{-7}	5.23×10^{-7}	1.41×10^{-6}		
Plane Wave Assumption:	1.89×10^{-7}	7.23×10^{-7}	1.90×10^{-6}		
200-2100 Hz:	4.36×10^{-8}	1.13×10^{-7}	2.46×10^{-7}		
(0,0) Mode:	1.02×10^{-7}	3.89×10^{-7}	1.08×10^{-6}		
(1,0) Mode:	2.76×10^{-8}	1.02×10^{-7}	2.40×10^{-7}		
(2,0) Mode:	5.66×10^{-9}	2.38×10^{-8}	6.08×10^{-8}		
(3,0) Mode:	1.38×10^{-9}	7.74×10^{-9}	2.33×10^{-8}		

Appendix A-5

UNCERTAINTY ANALYSIS

The experimental uncertainties for $\dot{m}$, M_i, U_i, acoustic pressure, acoustic power, and acoustic efficiency were determined. The method of Kline and McClintock (1953) was used, since this method is appropriate for single-sample measurements. Using this technique, the uncertainty in a final result R can be obtained from the known values of uncertainty in all the independent measurands δx_i by the expression

$$\delta R = \left\{ \sum_{i=1}^{N} \left(\frac{\partial R}{\partial x_i} \delta x_i \right)^2 \right\}^{1/2}$$

In all calculations to follow, odds of (20:1) were assumed for the δx_i and R.

Mass Flow Rate

The mass flow rate, $\dot{m}$, was determined by use of a Meriam laminar flow meter. The mass flow rate is found by

$$\dot{m} = K \times PCF \times TCF \times \Delta H$$

where

K = calibration constant for flow meter,
PCF = pressure correction factor,
TCF = temperature correction factor,
ΔH = pressure drop across the meter.

Thus the uncertainty can be expressed by

$$\frac{\delta \dot{m}}{\dot{m}} = \left\{ \left(\frac{\delta K}{K}\right)^2 + \left(\frac{\delta PCF}{PCF}\right)^2 + \left(\frac{\delta TCF}{TCF}\right)^2 + \left(\frac{\delta \Delta H}{H}\right)^2 \right\}^{1/2}$$

K is determined by the instrument manufacturer and is estimated to have an uncertainty $\delta K/K = \pm 0.5\%$. PCF is given by

$$PCF = \left(\frac{\Delta H}{13.59} + P_{amb} \right) \Big/ 29.92$$

where P_{amb} is the barometric pressure. The uncertainties in these quantities are estimated to be $\delta \Delta H = \pm 0.01$ in. H_2O, $\delta P_{amb} = \pm 0.02$ in. Hg. Using a typical value of PCF = 1.0, we have $\delta PCF/PCF = 0.07\%$, which can be neglected. TCF is given by $TCF = (530/T_{out})^{1.7}$, where T_{out} is the temperature upstream of the meter. This temperature is measured by a thermocouple and estimated to have an uncertainty of $\pm 2°R$. T_{out} was nominally room temperature. Thus,

$$\frac{\delta TCF}{TCF} = -1.7 \frac{\delta T_{out}}{T_{out}} = 0.64\%$$

ΔH was measured with a slant-tube manometer and varied over the range 0.6 to 4.0 in. H_2O. The uncertainty in the reading was $\pm$ 0.01 in. H_2O. Thus, $\delta \Delta H/\Delta H$ ranged from 1.7% to 0.25%. However, due to small levels of flow unsteadiness, a minimum value of $\delta \Delta H/\Delta H$ = 0.5% was used.

Using these values, we have

$$\frac{\delta \dot{m}}{\dot{m}} = \sqrt{(.005)^2 + (.0064)^2 + (.005)^2} = 0.95\% \quad \text{(high flow rate)}$$

$$\frac{\delta \dot{m}}{\dot{m}} = \sqrt{(.005)^2 + (.0064)^2 + (.017)^2} = 1.9\% \quad \text{(low flow rate)}$$

The values of $\dot{m}$ calculated using the laminar flow meter were compared to values obtained using the pressure drop across the orifices. The results agreed to within these uncertainty bounds when the orifices were in the proper ASME-recommended size range $0.15 \le \frac{d}{D} \le 0.75$.

M_i

The indicated Mach number, M_i, was calculated from the measured pressure ratio (P_{01}/P_i) assuming an isentropic expansion to the minimum pressure just downstream of the orifice. P_{01} is the upstream stagnation pressure and P_i is the pressure at the orifice vena contracta (or at the exit plane of the nozzle). Thus,

$$M_i = \left[\frac{2}{\gamma-1}\left(\left(\frac{P_{01}}{P_i}\right)^{\frac{\gamma-1}{\gamma}} - 1\right)\right]^{1/2}$$

where γ is the ratio of specific heats (1.4 for air). Then,

$$\frac{\delta M_i}{M_i} = \frac{\delta\left(\frac{P_{01}}{P_i}\right)}{\gamma\left(\frac{P_{01}}{P_i}\right)^{1/\gamma} M_i^2}$$

The pressure ratio was calculated from measurements of the upstream stagnation pressure, P_{up}, and the pressure drop across the orifice, ΔP. Then

$$\frac{P_{01}}{P_i} = \frac{P_{amb} + P_{up}}{P_{amb} + P_{up} - \Delta P}$$

Thus

$$\delta\left(\frac{P_{01}}{P_i}\right) = \frac{\Delta P(P_{up} + P_{amb})}{(P_{up} + P_{amv} - \Delta P)^2}\left\{\frac{(\delta P_{up})^2 + (\delta P_{amb})^2}{(P_{up} + P_{amb})^2} + \left(\frac{\delta\Delta P}{P}\right)^2\right\}^{1/2}$$

Then,

$$\frac{\delta M_i}{M_i} = \frac{(\Delta P)(P_{up} + P_{amb})}{\gamma M_i^2\left(\frac{P_{01}}{P_i}\right)^{1/\gamma}(P_{up} + P_{amb} - \Delta P)^2}\left\{\frac{(\delta P_{up})^2 + (\delta P_{amb})^2}{(P_{up} + P_{amb})^2} + \left(\frac{\delta\Delta P}{\Delta P}\right)^2\right\}^{1/2}$$

The uncertainty was calculated for two cases.

a. 31.8 mm orifice, $M_i = 0.149$

P_{amb} = 29.76 ± 0.02 in. Hg

P_{up} = 15.2 ± 0.1 in. H_2O

ΔP = 6.5 ± 0.1 in. H_2O

Evaluating the above expression, we have

$$\frac{\delta M_i}{M_i} = 0.78\%$$

b. 12.7 mm orifice, $M_i = 1.235$

P_{amb} = 29.82 ± 0.02 in. Hg

P_{up} = 48.75 ± 0.2 in. Hg

ΔP = 47.65 ± 0.2 in. Hg

Then

$$\frac{\delta M_i}{M_i} = 0.46\%$$

These are fairly representative cases. Thus the relative uncertainty of M_i was always less than 1%.

$\underline{U_i}$

The indicated velocity is calculated from the perfect gas relation:

$$U_i = \sqrt{\gamma R\, T_i}\, M_i = \frac{\sqrt{\gamma R\, T_o}\, M_i}{\sqrt{1 + \frac{\gamma-1}{2} M_i^2}}$$

Then

$$\frac{\delta U_i}{U_i} = \left\{\left(\frac{1}{2}\frac{\delta T_o}{T_o}\right)^2 + \left(\frac{T_i}{T_o}\frac{\delta M_i}{M_i}\right)^2\right\}^{1/2}$$

T_o was measured using a thermocouple, thus

$$\frac{1}{2}\frac{\delta T_o}{T_o} = 0.0019$$

$\delta M_i/M_i$ appears to be the largest of low values of M_i. Thus, using

$$\frac{T_i}{T_o}\frac{\delta M_i}{M_i} = 0.0078$$

we have

$$\frac{\delta U_i}{U_i} = 0.8\% \quad .$$

Acoustic Pressure

The microphones were calibrated using a B&K pistonphone. The uncertainty in this calibration technique is less than 0.2 dB SPL. Now,

$$\text{SPL (dB)} = 10 \log_{10}\left(\frac{\overline{p^2}}{p_{ref}^2}\right)$$

Thus,

$$\overline{p^2} = (p^2_{ref})\ 10^{\frac{SPL}{10}}$$

and

$$\frac{\delta\overline{p^2}}{\overline{p^2}} = \frac{\ln 10}{10}\ \delta SPL = 4.6\%$$

Thus the uncertainty in the time-averaged mean square acoustic pressure was less than 4.6%.

Acoustic Power

The acoustic power is calculated by an integration over frequency of the expression

$$\mathcal{P} = \frac{\overline{p^2}}{\rho_o a_o}\ (EWF)$$

where EWF is the energy weighting function discussed in Chapter 4. The uncertainty in values of the energy weighting function (due to the slug flow assumption) is less than 2%, and the uncertainty in $\rho_o a_o$ is negligible. Thus we have

$$\frac{\delta\mathcal{P}}{\mathcal{P}} = \left\{\left(\frac{\delta\overline{p^2}}{\overline{p^2}}\right)^2 + \left(\frac{\delta EWF}{EWF}\right)^2\right\}^{1/2}$$

$$\frac{\delta\mathcal{P}}{\mathcal{P}} = \pm 5\%$$

Acoustic Efficiency

The acoustic efficiency, η, is calculated by

$$\eta = \frac{\mathcal{P}}{\frac{1}{2}\dot{m}U_i^2}$$

Thus,

$$\frac{\delta\eta}{\eta} = \left\{\left(\frac{\delta\mathcal{P}}{\mathcal{P}}\right)^2 + \left(\frac{\delta\dot{m}}{\dot{m}}\right)^2 + \left(2\frac{\delta U_i}{U_i}\right)^2\right\}^{1/2}$$

$$\frac{\delta\eta}{\eta} = \left\{(0.050)^2 + (0.019)^2 + (0.016)^2\right\}^{1/2}$$

$$\frac{\delta\eta}{\eta} = 5.6\% \quad .$$

The worst case value was used for $\delta\dot{m}/m$. Thus all values of η presented in this report have an uncertainty of less than 5.6%.

Appendix A6

WALL STATIC PRESSURE PROFILES FOR THE 16.2 mm NOZZLES

This appendix contains wall static pressure profiles for the two 16.2 mm nozzles. The measurements were made using a water manometer which was connected to the wall static pressure taps through a valve manifold. For details of the static pressure taps, see Roberts and Johnston (1974).

The static pressure profiles for the short nozzle (throat length-to-diameter ratio of 1) are shown in Fig. A6-1. The wall static pressures are normalized by the jet exit kinetic energy and plotted vs. a nondimensional axial length, x/(D-d), where x is the distance downstream of the jet exit plane, D is the pipe inside diameter, and d is the nozzle diameter*. The static pressure drops slightly just downstream of the nozzle exit plane, and then rises rapidly as the kinetic energy of the jet is reduced by turbulent mixing. The rapid static pressure rise levels off at approximately x/(D-d) = 5, indicating that the flow has reattached to the pipe wall. The general shape of the static pressure curve is not influenced strongly by jet exit Mach number.

The wall static pressure profiles for the long nozzle (throat length-to-diameter ratio of 8) are shown in Fig. A6-2. The curves for the long nozzle agree closely with those for the short nozzle. This indicates that the overall fluid dynamic characteristics of the two nozzles are very similar.

The diameter of the nozzles was chosen to match that of the vena contracta of the 19.0 mm orifice. Thus we would expect the fluid dynamic characteristics of the two nozzles to be similar to those of the 19.0 mm orifice. To check this, the static pressure profiles for the two 16.2 mm nozzles were compared to those for the 19.0 mm orifice**.

*A similar nondimensional length was used by Roberts and Johnston (1974) in presenting static pressure profiles downstream of orifices.

**Presented by Roberts and Johnston (1974), Fig. 22, p. 41.

The agreement was excellent, confirming that nozzles and orifices exhibit similar fluid dynamic characteristics when the comparison is made using nozzle exit plane and orifice vena contracta conditions.

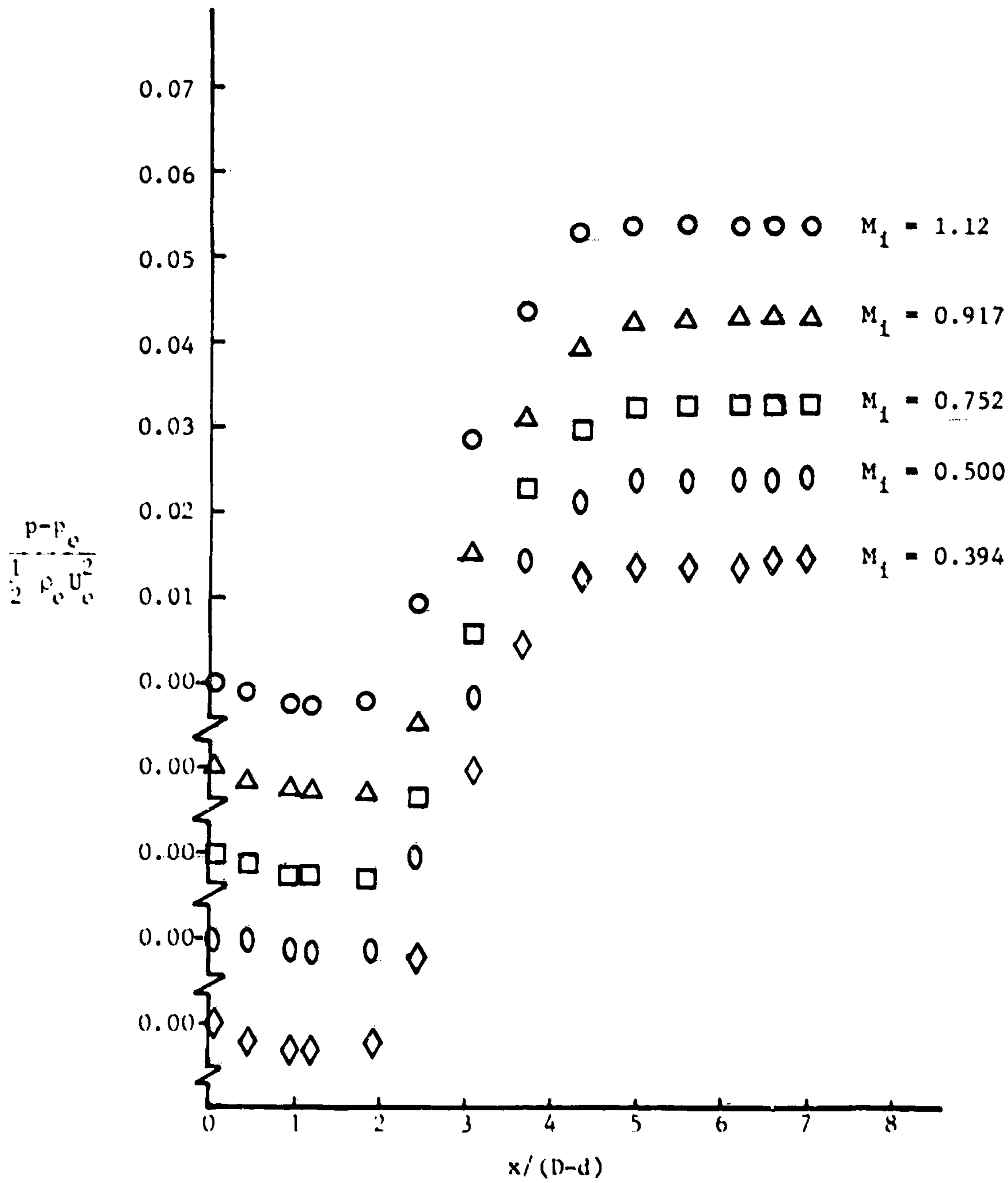

Fig. A6-1. Static pressure profiles for 16.2 mm nozzle (throat length-to-diameter ratio = 1)

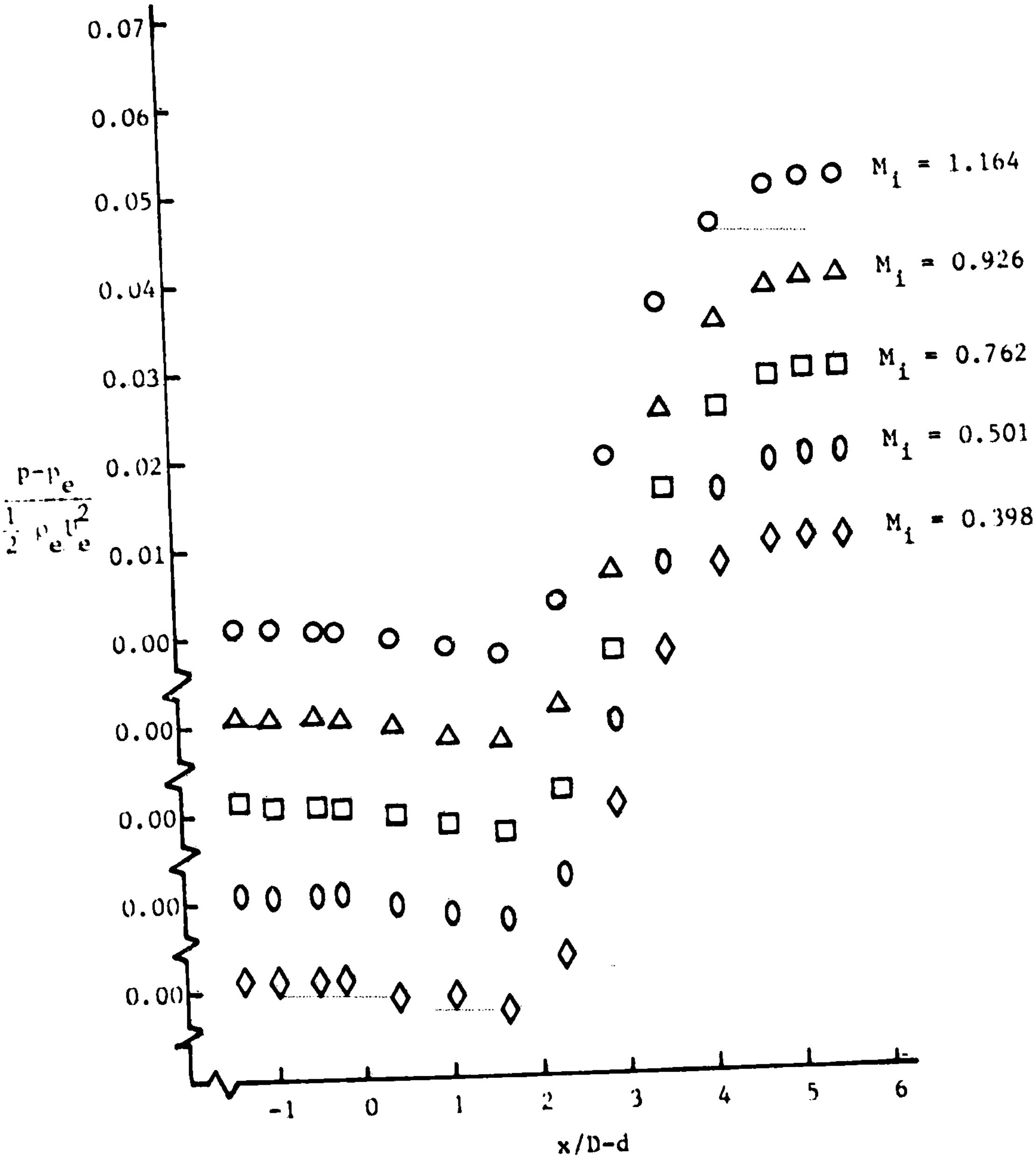

Fig. A6-2. Static pressure profiles for 16.2 mm nozzle (throat length-to-diameter ratio = 8)

APPENDIX A7

CROSS-CORRELATION MEASUREMENTS OF THE HYDRODYNAMIC PRESSURE FLUCTUATIONS

This appendix presents measurements of the relative rms levels of the acoustic and hydrodynamic pressure fluctuations in the frequency range 200-2100 Hz. The measurements were made using the cross-correlation technique discussed in section 3.1. One microphone was mounted at the axial location used for the modal measurements. A second microphone was located 0.25 m farther downstream. The microphones were time-delay cross-correlated. The value of the cross-correlation at a time delay equal to the time it takes for the acoustic wave to travel the distance between the two microphones gives the magnitude of the acoustic pressure, $\overline{p^2_{ac}}$. If the acoustic pressure fluctuations are assumed to be uncorrelated with the hydrodynamic pressure fluctuations, the mean square value of the wall pressure fluctuations is given by $\overline{p^2_{ac}} + \overline{p^2_{hydro}}$. Thus the magnitude of the hydrodynamic pressure fluctuations can be determined by subtracting the mean square acoustic pressure from the total mean square pressure measurement.

The measurements were made using two Hewlett-Packard HP3721A correlators. The microphone outputs were bandpass filtered between 200 and 2100 Hz before being fed to the correlators. The total mean square wall pressure fluctuation was obtained from the autocorrelation at zero time delay. The geometric mean of the values for the two microphones was used to define the total mean square pressure.

The table below gives the values of the acoustic and hydrodynamic pressures in the frequency range 200-2100 Hz. The uncertainty associated with the value of $\overline{p^2_{hydro}}$ is large, especially for cases where $\overline{p^2_{hydro}}$ is much smaller than $\overline{p^2_{ac}}$, since $\overline{p^2_{hydro}}$ is found by taking the difference of two large numbers. However, the measurements show that the level of the hydrodynamic pressure fluctuations was much lower than that of the acoustic pressure fluctuations. Thus the presence of hydrodynamic pressure fluctuations did not influence the acoustic measurements, with the possible exception of the 50.8 mm orifice.

Table A7.1

Relative Levels of the Acoustic
and Hydrodynamic Pressure Fluctuations
in the Frequency Range 200-2100 Hz

Restriction	M_i	SPL_{ac} (dB)	SPL_{hydro}	$SPL_{ac}-SPL_{hydro}$
12.7 mm Orifice	1.21 0.63	127.1 106.0	110.4 80.4	16.7 25.6
19.0 mm Orifice	1.07 0.40	135.4 103.6	119.6 86.9	15.8 16.7
31.8 mm Orifice	0.49 0.37 0.31	119.4 106.6 106.2	93.8 87.4 92.0	26.0 19.2 14.2
50.8 mm Orifice	0.21	102.0	93.8	8.2
16.2 mm Nozzle $L_t/d = 1$	1.17 0.76 0.41	136.2 124.1 106.5	125.7 109.2 89.1	10.5 14.9 17.4
16.2 mm Nozzle $L_t/d = 8$	1.17 0.78 0.40	137.0 125.5 104.3	122.0 112.2 90.4	15.0 13.3 13.9

Appendix A8

DERIVATION OF THE PHYSICAL ENERGY EQUATION AND ACOUSTIC ENERGY FLOW EXPRESSIONS

A8.1. Introduction

This appendix contains details of the derivations of the physical energy equation results. The format generally follows that used in Chapter 4. Section A8.2 contains the derivation of the physical energy equation. Section A8.3 gives details of the evaluation of $\int_s < J^P_{s_z} > ds$. As explained in Chapter 4, the integrated acoustic energy flux, $\int_s < J^P_{s_z} > ds$, can be separated into two parts, $\mathcal{P}^P_a$ and $\mathcal{P}^P_b$. The details of the evaluation of $\mathcal{P}^P_a$ are given in Section 4.3.2 of Chapter 4, and hence are not covered in this appendix. The details of the evaluation of $\mathcal{P}^P_b$ are given in Section A8.4. The evaluation of the source terms in Section 4.3.4 of Chapter 4 is also given sufficient detail that no amplification is needed here.

A8.2. A Detailed Derivation of the Physical Energy Equation

Viscous heat conduction and potential field effects are ignored in the derivation of the physical energy equation. The entropy of the mean flow is also assumed to be constant. Thus the acoustic perturbations are isentropic. With these restrictions, the fluid motion obeys the following set of equations.

Continuity: $$\frac{\partial \rho}{\partial t} + \operatorname{div}(\rho \bar{V}) = 0 \qquad \text{(A8-1a)}$$

Momentum: $$\rho \frac{\partial \bar{V}}{\partial t} + \rho \bar{V} \cdot \nabla \bar{V} + \nabla p = 0 \qquad \text{(A8-1b)}$$

Energy: $$\frac{\partial}{\partial t}\left\{\rho\left(e + \frac{V^2}{2}\right)\right\} + \operatorname{div}\left\{\left[\rho\left(e + \frac{\bar{V}^2}{2}\right) + p\right]\bar{V}\right\} = 0 \qquad \text{(A8-1c)}$$

Eqns. of state: $$p = p(\rho) \quad , \quad e = e(\rho) \qquad \text{(A8-1d)}$$

We first separate the variables into mean and perturbation quantities, i.e., $P = P_o + p'$, etc. Substituting into the above equations, we have (noting that time derivatives of the mean flow quantities are zero)

$$\frac{\partial \rho'}{\partial t} + \mathrm{div}\left[(\rho_o + \rho')(\overline{V}_o + \overline{v}')\right] = 0 \qquad \text{(A8-2a)}$$

$$(\rho_o + \rho')\frac{\partial \overline{v}'}{\partial t} + (\rho_o + \rho')(\overline{V}_o + \overline{v}') \cdot \nabla(\overline{V}_o + \overline{v}') + \nabla(P_o + p') = 0 \qquad \text{(A8-2b)}$$

$$\frac{\partial}{\partial t}\left\{(\rho_o + \rho')\left[e_o + e' + \frac{1}{2}(\overline{V}_o + \overline{v}') \cdot (\overline{V}_o + \overline{v}')\right]\right\}$$
$$+ \mathrm{div}\left\{\left[(\rho_o + \rho')\left(e_o + e' + \frac{1}{2}(\overline{V}_o + \overline{v}') \cdot (\overline{V}_o + \overline{v}')\right) + (P_o + p')\right](\overline{V}_o + \overline{v}')\right\} = 0 \qquad \text{(A8-2c)}$$

The mean flow quantities must independently satisfy these equations. Thus we have

$$\mathrm{div}(\rho_o \overline{V}_o) = 0 \qquad \text{(A8-3a)}$$

$$\rho_o \overline{V}_o \cdot \nabla \overline{V}_o + \nabla P_o = 0 \qquad \text{(A8-3b)}$$

$$\mathrm{div}\left\{\left[\rho_o\left(e_o + \frac{\overline{V}_o^2}{2}\right) + P_o\right]\overline{V}_o\right\} = 0 \qquad \text{(A8-3c)}$$

Subtracting Eqns. (A8-3) from (A8-2), we have

$$\frac{\partial \rho'}{\partial t} + \mathrm{div}(\rho_o \overline{v}' + \rho' \overline{V}_o + \rho' \overline{v}') = 0 \qquad \text{(A8-4a)}$$

$$(\rho_o + \rho')\frac{\partial \overline{v}'}{\partial t} + (\rho_o + \rho')\left(\overline{V}_o \cdot \nabla \overline{v}' + \overline{v}' \cdot \nabla \overline{V}_o + \overline{v}' \cdot \nabla \overline{v}'\right) + \rho' \overline{V}_o \cdot \nabla \overline{V}_o + \nabla p' = 0 \qquad \text{(A8-4b)}$$

$$\frac{\partial}{\partial t}\left\{(\rho_o+\rho')\left(e'+\bar{V}_o\cdot\bar{v}'+\frac{1}{2}\bar{v}'^2\right)+\rho'\left(e_o+\frac{1}{2}\bar{V}_o^2\right)\right\}$$

$$+\operatorname{div}\left\{\left[(\rho_o+\rho')\left(e'+\bar{V}_o\cdot\bar{v}'+\frac{1}{2}\bar{v}'^2\right)+p'\right](\bar{V}_o+\bar{v}')\right.$$

$$\left.+P_o\bar{v}'+\left(e_o+\frac{1}{2}\bar{V}_o^2\right)(\rho_o\bar{v}'+\rho'\bar{V}_o+\rho'\bar{v}')\right\} = 0 \qquad \text{(A8-4c)}$$

At this point the equations are exact. We next multiply Eqn. (A8-4a) by $\bar{v}'$ and add to Eqn. (A8-4b). Neglecting the third-order terms $\bar{v}'\operatorname{div}(\rho'\bar{v}')$ and $\rho'\bar{v}'\cdot\nabla\bar{v}'$, we have

$$\rho_o\frac{\partial\bar{v}'}{\partial t}+\frac{\partial}{\partial t}(\rho'\bar{v}')+\bar{v}'\operatorname{div}(\rho_o\bar{v}'+\rho'\bar{V}_o)+(\rho_o+\rho')(\bar{V}_o\cdot\nabla\bar{v}'+\bar{v}'\cdot\nabla\bar{V}_o)$$

$$+\rho_o\bar{v}'\cdot\nabla\bar{v}'+\rho'\bar{V}_o\cdot\nabla\bar{V}_o+\nabla p' = 0 \qquad \text{(A8-5)}$$

This equation will be used later in simplifying the energy equation.

Now examine the equation of state. To second-order accuracy, we have for isentropic flow

$$\rho e = \rho_o e_o+\left.\frac{\partial(\rho e)}{\partial\rho}\right|_{\rho=\rho_o}\rho'+\frac{1}{2}\left.\frac{\partial^2(\rho e)}{\partial\rho^2}\right|_{\rho=\rho_o}\rho'^2$$

Using the result from thermodynamics, $de = Tds+(p/\rho^2)d\rho$, we have $\left.\frac{\partial e}{\partial\rho}\right|_s = \frac{p}{\rho^2}$. Thus, $\left.\frac{\partial(\rho e)}{\partial\rho}\right|_{\rho=\rho_o} = h_o$ and $\left.\frac{\partial^2(\rho e)}{\partial\rho^2}\right|_s = \left.\frac{\partial h}{\partial\rho}\right|_s$. From the thermodynamic equation $dh = Tds+\frac{1}{\rho}dP$ we have $\left.\frac{\partial h}{\partial P}\right|_s = \frac{1}{\rho}$. Now $\frac{\partial h}{\partial\rho} = \frac{\partial h}{\partial P}\frac{\partial P}{\partial\rho}$, which gives $\left.\frac{\partial^2(\rho e)}{\partial\rho^2}\right|_{\rho=\rho_o} = a_o^2/\rho_o$. Thus we have

$$\rho e = \rho_o e_o+h_o\rho'+\frac{a_o^2}{\rho_o}\frac{\rho'^2}{2} \qquad \text{(A8-6)}$$

accurate to $O(\varepsilon^2)$.

Substituting into Eqn. (A8-4c) and neglecting terms of $O(\varepsilon^3)$, we obtain

$$\frac{\partial}{\partial t}\left\{\xi_s + \rho'\left(h_o + \frac{\bar{V}_o^2}{2}\right) + (\rho_o + \rho')(\bar{V}_o \cdot \bar{v}')\right\}$$

$$+ \operatorname{div}\left\{\bar{J}_s^P + \left(h_o + \frac{\bar{V}_o^2}{2}\right)\left[\rho_o\bar{v}' + \rho'\bar{V}_o + \rho'\bar{v}'\right] + (\bar{V}_o \cdot \bar{v}')\left[(\rho_o + \rho')\bar{V}_o + \rho_o\bar{v}'\right]\right.$$

$$\left. + p'\bar{V}_o\right\} = 0 \qquad \text{(A8-7)}$$

where the acoustic energy density, ξ_s, and the physical energy flux, $\bar{J}_s^P$, are given by

$$\xi_s = \frac{a_o^2}{2\rho_o}\rho'^2 + \frac{\rho_o}{2}\bar{v}'^2 \qquad \text{(A8-8a)}$$

$$\bar{J}_s^P = \xi_s\bar{V}_o + p'\bar{v}' \qquad \text{(A8-8b)}$$

Simplifying, we have

$$\frac{\partial \xi_s}{\partial t} + \operatorname{div}\bar{J}_s^P + \left(h_o + \frac{\bar{V}_o^2}{2}\right)\left[\frac{\partial \rho'}{\partial t} + \operatorname{div}(\rho_o\bar{v}' + \rho'\bar{V}_o + \rho'\bar{v}')\right]$$

$$+ \bar{V}_o \cdot \left[\rho_o\frac{\partial \bar{v}'}{\partial t} + \frac{\partial}{\partial t}(\rho'\bar{v}') + \nabla p'\right] + \nabla\left(h_o + \frac{\bar{V}_o^2}{2}\right) \cdot (\rho_o\bar{v}' + \rho'\bar{v}_o + \rho'\bar{v}')$$

$$+ \operatorname{div}\left[(\rho_o + \rho')(\bar{V}_o \cdot \bar{v}')(\bar{V}_o + \bar{v}')\right] + p' \operatorname{div}\bar{V}_o = 0 \qquad \text{(A8-9)}$$

First note that the third term in Eqn. (A8-9) is equal to zero by virtue of the continuity equation. Also, by examination of the mean flow energy equation (Eqn. (A8-3c)), it can be seen that

$$\nabla\left(h_o + \frac{\bar{V}_o^2}{2}\right) \cdot \bar{V}_o = 0 \ .$$

Then, using

$$\operatorname{div}\left[(\rho_o + \rho')(\bar{V}_o \cdot \bar{v}')(\bar{V}_o + \bar{v}')\right] = \bar{V}_o \cdot \left[\bar{v}' \operatorname{div}(\rho_o\bar{v}' + \rho'\bar{V}_o)\right.$$

$$\left. + (\rho_o + \rho')\nabla(\bar{V}_o \cdot \bar{v}')\right] + \rho_o\bar{v}' \cdot \nabla(\bar{V}_o \cdot \bar{v}') \quad ,$$

Equation (A8-9) can be rewritten as

$$\frac{\partial \mathcal{E}_s}{\partial t} + \text{div}\ \overline{J}_s^P + \overline{V}_o \cdot \left[\rho_o \frac{\partial \overline{v}'}{\partial t} + \frac{\partial}{\partial t}(\rho'\overline{v}') + \overline{v}'\ \text{div}(\rho_o \overline{v}' + \rho'\overline{V}_o) + (\rho_o + \rho')\nabla(\overline{V}_o \cdot \overline{v}') + \nabla p' \right] + \overline{v}' \cdot \left[\rho_o \nabla(\overline{V}_o \cdot \overline{v}') + (\rho_o + \rho')\ \nabla\left(h_o + \frac{\overline{V}_o^2}{2}\right)\right] + p'\ \text{div}\ \overline{V}_o = 0 \qquad \text{(A8-10)}$$

Next, noting that

$$\nabla(\overline{V}_o \cdot \overline{v}') = \overline{V}_o \cdot \nabla\overline{v}' + \overline{v}' \cdot \nabla\overline{V}_o + \overline{V}_o \times (\nabla \times \overline{v}') + \overline{v}' \times (\nabla \times \overline{V}_o) \quad ,$$

Equation (A8-5) can be used to simplify the third term in Eqn. (A8-10), giving

$$\frac{\partial \mathcal{E}_s}{\partial t} + \text{div}\ \overline{J}_s^P + \overline{V}_o \cdot \left[(\rho_o + \rho')\ \overline{v} \times (\nabla \times \overline{V}_o) - \rho_o \overline{v}' \cdot \nabla\overline{v}' - \rho'\overline{V}_o \cdot \nabla\overline{V}_o \right] + \overline{v}' \left[\rho_o \nabla(\overline{V}_o \cdot \overline{v}') + (\rho_o + \rho')\ \nabla\left(h_o + \frac{\overline{V}_o^2}{2}\right)\right] + p'\ \text{div}\ \overline{V}_o = 0 \qquad \text{(A8-11)}$$

Now we have

$$\overline{V}_o \cdot \overline{v}' \times (\nabla \times \overline{V}_o) + \nabla\left(h_o + \frac{\overline{V}_o^2}{2}\right) \cdot \overline{v}' = \left(\nabla h_o - \frac{1}{\rho_o} \nabla P_o\right) \cdot \overline{v}'$$

after using Eqn. (A8-3b) to eliminate $\overline{V}_o \cdot \nabla\overline{V}_o$. But for isentropic flow, $\nabla h = \frac{1}{\rho} \nabla P$. Thus Eqn. (A8-11) can be written as

$$\frac{\partial \mathcal{E}_s}{\partial t} + \text{div}\ \overline{J}_s^P + \frac{\rho'}{\rho_o} \nabla P_o \cdot \overline{V}_o + p'\ \text{div}\ \overline{V}_o - \rho_o \overline{V}_o \cdot (\overline{v}' \cdot \nabla\overline{v}') + \rho_o \overline{v}' \cdot \nabla(\overline{V}_o \cdot \overline{v}') = 0$$

Furthermore, it can be shown that

$$\overline{v}' \cdot \nabla(\overline{V}_o \cdot \overline{v}') = \overline{V}_o \cdot (\overline{v}' \cdot \nabla\overline{v}') + \overline{v}' \cdot (\overline{v}' \cdot \nabla\overline{V}_o)$$

Thus we have

$$\frac{\partial \xi_s}{\partial t} + \text{div}\,\overline{J}_s^P = -\frac{\rho'}{\rho_o}\nabla P_o \cdot \overline{V}_o - p'\,\text{div}\,\overline{V}_o - \rho_o \overline{v}' \cdot \nabla\overline{V}_o \cdot \overline{v}' \qquad \text{(A8-12)}$$

Now, Eqn. (A8-12) is accurate to $O(\varepsilon^2)$. Thus we need ρ' and p' to $O(\varepsilon^2)$ accuracy. For constant entropy, we have

$$p' = \left.\frac{\partial P}{\partial \rho}\right|_o \rho' + \left.\frac{\partial^2 P}{\partial \rho^2}\right|_o \rho'^2$$

Substituting $p' = \varepsilon P_1 + \varepsilon^2 P_2$ and $\rho' = \varepsilon \rho_1 + \varepsilon^2 \rho_2$, and using $\frac{\partial P}{\partial \rho} = a_o^2$, we obtain

$$P_1 = a_o^2 \rho_1 \qquad \text{(8-13a)}$$

$$P_2 = a_o^2 \rho_2 + \frac{1}{2}\frac{\partial a_o^2}{\partial \rho}\rho_1^2 \qquad \text{(8-13b)}$$

Next, note that, for constant entropy, $\nabla P_o = a_o^2 \nabla \rho_o$. Thus, Eqn. (A8-3a) can be written as

$$\rho_o\,\text{div}\,\overline{V}_o + \frac{1}{a_o^2}\nabla P_o \cdot \overline{V}_o = 0$$

Using this result in combination with Eqns. (A8-13), we obtain

$$\frac{\partial \xi_s}{\partial t} + \text{div}\,\overline{J}_s^P = -a_o \frac{\partial a_o}{\partial \rho}\rho'^2\,\text{div}\,\overline{V}_o - \overline{v}' \cdot \nabla\overline{V}_o \cdot \overline{v}'$$

accurate to $O(\varepsilon^2)$. Equivalently, this can be written as

$$\frac{\partial \xi_s}{\partial t} + \text{div}\,\overline{J}_s^P = -\frac{(\Gamma-1)}{\rho_o a_o^2}\,p'^2\,\text{div}\,\overline{V}_o - \overline{v}' \cdot \nabla\overline{V}_o \cdot \overline{v}' \qquad \text{(A8-14)}$$

where $\Gamma = \left.\frac{1}{a}\frac{\partial(\rho a)}{\partial \rho}\right|_o$. Eqn. (A8-14) is referred to as the physical energy equation in Chapter 4.

A8.3. Evaluation of $\int_s < J^P_{s_z} > ds$

We have

$$< J^P_{s_z} > \;=\; < \frac{p'^2}{2\rho_o a_o^2} + \frac{\rho_o}{2}\left(u_r'^2 + u_\theta'^2 + u_z'^2\right) > U_o + < p'u_z' > \qquad \text{(A8-15)}$$

where the perturbation quantities are given by

$$p' = \sum_{m,n} \mathrm{Re}\left[P_{mn}(r,\theta)\, e^{i(\omega t - k_{z_{mn}} z)}\right]$$

$$u_r' = \sum_{m,n} \mathrm{Re}\left[V_{r_{mn}}(r,\theta)\, e^{i(\omega t - k_{z_{mn}} z)}\right], \qquad \text{etc.}$$

Substituting these expressions into the above equation, we obtain

$$< J^P_{s_z} > = \frac{1}{2}\,\mathrm{Re}\left\{\sum_{m,n}\sum_{b,c}\left[\left(\frac{P_{mn}P^*_{bc}}{2\rho_o a_o^2} + \frac{\rho_o}{2} V_{r_{mn}} V^*_{r_{bc}} + \frac{\rho_o}{2} V_{\theta_{mn}} V^*_{\theta_{bc}} + \frac{\rho_o}{2} V_{z_{mn}} V^*_{z_{bc}}\right) U_o + P_{mn} V^*_{z_{bc}}\right] e^{i(k_{z_{bc}} - k_{z_{mn}})z}\right\} \qquad \text{(A8-16)}$$

The functions $V_{r_{mn}}$, $V_{\theta_{mn}}$, and $V_{z_{mn}}$ are given by

$$V_{r_{mn}} = \frac{i\,\frac{\partial P_{mn}}{\partial r}}{\rho_o(\omega - k_{z_{mn}} U_o)} \qquad \text{(A8-17a)}$$

$$V_{\theta_{mn}} = \frac{i\,\frac{\partial P_{mn}}{r\partial\theta}}{\rho_o(\omega - k_{z_{mn}} U_o)} \qquad \text{(A8-17b)}$$

$$V_{z_{mn}} = \frac{k_{z_{mn}} P_{mn}}{\rho_o(\omega - k_{z_{mn}} U_o)} - \frac{\frac{\partial P_{mn}}{\partial r}\,\frac{dU_o}{dr}}{\rho_o(\omega - k_{z_{mn}} U_o)^2} \qquad \text{(A8-17c)}$$

where

$$P_{mn}(r,\theta) = C_{mn} \cos(m\theta + \phi_{mn})\, R_{mn}(r) \qquad \text{(A8-17d)}$$

The coefficient C_{mn} is considered to be real, and ϕ_{mn} is related to the angle of the nodal diameter. Since we are considering only cuton modes, $R_{mn}(r)$ is a real function and $k_{z_{mn}}$ is real. Examining the first term in Eqn. (A8-16), we have

$$\frac{1}{2}\,\mathrm{Re}\left\{\frac{p_{mn}p^*_{bc}}{2\rho_o a_o^2}\, e^{i(k_{z_{bc}}-k_{z_{mn}})z}\right\} = \frac{C_{mn}C_{bc}}{4\rho_o a_o^2}\cos(m\theta+\phi_{mn})\cos(b\theta+\phi_{bc})$$

$$\cdot\, R_{mn}R_{bc}\cos(k_{z_{bc}}-k_{z_{mn}})z$$

Integrating across the duct cross section, we obtain

$$\int_0^{2\pi}\int_0^{r_o}\frac{1}{2}\,\mathrm{Re}\left\{\frac{p_{mn}p^*_{bc}}{2\rho_o a_o^2}\, e^{i(k_{z_{bc}}-k_{z_{mn}})z}\right\} U_o\, r\,dr\,d\theta = 0\ , \qquad m \neq b\ ;$$

$$= \frac{\pi C_{mn}C_{mc}\cos(\phi_{mc}-\phi_{mn})}{2\rho_o(1+\epsilon_m)}\int_0^{r_o} R_{mn}R_{mc}\frac{U_o}{a_o}\, r\,dr\,\cos(k_{z_{mc}}-k_{z_{mn}})z\ ,$$

$$m = b\ ,$$

where $\epsilon_m = 0$, $m = 0$; $= 1$, $m = 1,2,3,\ldots$.

The integrals of the other terms in Eqn. (A8-16) are given by similar expressions. Thus, the integrated acoustic energy flux can be written as

$$\int_S \mathbf{I}^P_{s_z}\cdot d\mathbf{s} = \sum_{m,n}\sum_{c}\frac{\pi C_{mn}C_{mc}\cos(\phi_{mc}-\phi_{mn})}{\rho_o(1+\epsilon_m)}\int_0^{r_o}\left\{\left[\frac{R_{mn}R_{mc}}{a_o^2}\right.\right.$$

$$+\frac{\frac{dR_{mn}}{dr}\frac{dR_{mc}}{dr}}{(\omega-k_{z_{mn}}U_o)(\omega-k_{z_{mc}}U_o)}+\frac{m^2R_{mn}R_{mc}}{r^2(\omega-k_{z_{mn}}U_o)(\omega-k_{z_{mc}}U_o)}$$

$$\left.+\left(\frac{k_{z_{mn}}R_{mn}}{(\omega-k_{z_{mn}}U_o)}-\frac{\frac{dR_{mn}}{dr}\frac{dU_o}{dr}}{(\omega-k_{z_{mn}}U_o)^2}\right)\left(\frac{k_{z_{mc}}R_{mc}}{(\omega-k_{z_{mc}}U_o)}-\frac{\frac{dR_{mn}}{dr}\frac{dU_o}{dr}}{(\omega-k_{z_{mc}}U_o)^2}\right)\right]\frac{U_o}{2}$$

$$\left.+\frac{k_{z_{mc}}R_{mn}R_{mc}}{(\omega-k_{z_{mc}}U_o)}-\frac{R_{mn}\frac{dR_{mc}}{dr}\frac{dU_o}{dr}}{(\omega-k_{z_{mc}}U_o)^2}\right\} r\,dr\,\cos(k_{z_{mc}}-k_{z_{mn}})z\ .$$

Simplifying this expression and nondimensionalizing, we obtain the final result.

$$\int_S \langle J_{s_z}^p \rangle \, ds = \frac{\pi r_o^2}{\rho_o a_o} \sum_{m,n} \sum_{e} \frac{C_{mn} C_{me} \cos(\phi_{me} - \phi_{mn})}{2(1+\epsilon_m)} \int_o^1 \left\{ \frac{M}{2} \left[R_{mn} R_{me} \right.\right.$$

$$+ \frac{\frac{dR_{mn}}{d\bar{r}} \frac{dR_{me}}{d\bar{r}}}{\gamma^2 K_{mn} K_{me}} + \frac{m^2 R_{mn} R_{me}}{\gamma^2 \bar{r}^2 K_{mn} K_{me}} + \frac{\bar{k}_{mn} \bar{k}_{me} R_{mn} R_{me}}{K_{mn} K_{me}} + \frac{\frac{dR_{mn}}{d\bar{r}} \frac{dR_{me}}{d\bar{r}} \left(\frac{dM}{d\bar{r}}\right)^2}{\gamma^4 K_{mn}^2 K_{me}^2}$$

$$\left. - \frac{\bar{k}_{mn} R_{mn} \frac{dR_{me}}{d\bar{r}} \frac{dM}{d\bar{r}}}{\gamma^2 K_{mn} K_{me}^2} - \frac{\bar{k}_{me} R_{me} \frac{dR_{mn}}{d\bar{r}} \frac{dM}{d\bar{r}}}{\gamma^2 K_{me} K_{mn}^2} \right] + \frac{\bar{k}_{me} R_{mn} R_{me}}{K_{me}} - \left. \frac{R_{mn} \frac{dR_{me}}{d\bar{r}} \frac{dM}{d\bar{r}}}{\gamma^2 K_{me}^2} \right\}$$

$$\cdot \, 2\bar{r} d\bar{r} \cos(\bar{k}_{me} - k_{mn}) \bar{z} \quad . \qquad \text{(A8-18)}$$

The nondimensional variables are defined as

$$\bar{r} = \frac{r}{r_o} \;, \quad \bar{k}_{mn} = \frac{k_{z_{mn}} a_o}{\omega} \;, \quad M = \frac{U_o}{a_o} \;, \quad K_{mn} = (1 - \bar{k}_{mn} M) \;,$$

$$\gamma = \frac{\omega r_o}{a_o} \;, \text{ and } \bar{z} = \frac{\omega z}{a_o} \;.$$

A8.4. Evaluation of $\mathcal{P}_b^p$

The cross mode energy flow, $\mathcal{P}_b^p$, is the sum of the terms in $\int_s \langle J_{s_z}^p \rangle ds$ for which $n \neq e$. Noting that the summations over n and e both have the same upper bound, we can combine terms to obtain

$$\mathcal{P}_b^p = \frac{\pi r_o^2}{\rho_o a_o} \sum_{m,n} \sum_{e>n} \frac{C_{mn} C_{me} \cos(\phi_{me} - \phi_{mn})}{2(1+\varepsilon_m)} \int_0^1 \left\{ M \left[R_{mn} R_{me} \right.\right.$$

$$+ \frac{\frac{dR_{mn}}{d\bar{r}} \frac{dR_{me}}{d\bar{r}}}{\gamma^2 K_{mn} K_{me}} + \frac{m^2 R_{mn} R_{me}}{\gamma^2 \bar{r}^2 K_{mn} K_{me}} + \frac{\bar{k}_{mn} \bar{k}_{me} R_{mn} R_{me}}{K_{mn} K_{me}} + \frac{\frac{dR_{mn}}{d\bar{r}} \frac{dR_{me}}{d\bar{r}}}{\gamma^4 K_{mn}^2 K_{me}^2} \left(\frac{dM}{d\bar{r}}\right)^2$$

$$\left. - \frac{\frac{dM}{d\bar{r}}}{\gamma^2 K_{mn} K_{me}} \left(\frac{\bar{k}_{mn} R_{mn} \frac{dR_{me}}{d\bar{r}}}{K_{me}} + \frac{\bar{k}_{me} R_{me} \frac{dR_{mn}}{d\bar{r}}}{K_{mn}} \right) \right] + \left(\frac{\bar{k}_{mn}}{K_{mn}} + \frac{\bar{k}_{me}}{K_{me}} \right) R_{mn} R_{me}$$

$$\left. - \frac{\frac{dM}{d\bar{r}}}{\gamma^2} \left(\frac{R_{mn} \frac{dR_{me}}{d\bar{r}}}{K_{me}^2} + \frac{R_{me} \frac{dR_{mn}}{d\bar{r}}}{K_{mn}^2} \right) \right\} 2\bar{r} d\bar{r} \cos(\bar{k}_{me} - \bar{k}_{mn}) \bar{z} \qquad \text{(A8-19)}$$

Equation (A8-19) can be simplified by integrating the term

$$\int_0^1 \frac{M \left(\frac{dR_{mn}}{d\bar{r}}\right) \left(\frac{dR_{me}}{d\bar{r}}\right)}{\gamma^2 K_{mn} K_{me}} 2\bar{r} d\bar{r}$$

by parts. First, we have

$$\frac{1}{\gamma^2} \int_0^1 \left(\frac{\bar{r} M \frac{dR_{mn}}{d\bar{r}}}{K_{mn} K_{me}} \right) \frac{dR_{me}}{d\bar{r}} d\bar{r} = -\frac{1}{\gamma^2} \int_0^1 R_{me} \frac{d}{d\bar{r}} \left| \frac{\bar{r} M \frac{dR_{mn}}{d\bar{r}}}{K_{mn} K_{me}} \right| d\bar{r}$$

since the contributions of the end points vanish by virtue of the boundary conditions. Similarly, we have

$$\frac{1}{\gamma^2} \int_0^1 \left(\frac{\bar{r} M \frac{dR_{me}}{d\bar{r}}}{K_{mn} K_{me}} \right) \frac{dR_{mn}}{d\bar{r}} d\bar{r} = -\frac{1}{\gamma^2} \int_0^1 R_{mn} \frac{d}{d\bar{r}} \left| \frac{\bar{r} M \frac{dR_{me}}{d\bar{r}}}{K_{mn} K_{me}} \right| d\bar{r}$$

Adding these together, we obtain

$$\int_0^1 \frac{M \frac{dR_{mn}}{d\bar{r}} \frac{dR_{mc}}{d\bar{r}}}{\gamma^2 K_{mn} K_{mc}} 2\bar{r}d\bar{r} = -\frac{1}{\gamma^2}\int_0^1 \left[R_{mc} \frac{d}{d\bar{r}}\left(\frac{\bar{r} M \frac{dR_{mn}}{d\bar{r}}}{K_{mn}K_{mc}} \right) + R_{mn} \frac{d}{d\bar{r}}\left(\frac{\bar{r} M \frac{dR_{mc}}{d\bar{r}}}{K_{mn}K_{mc}} \right)\right] d\bar{r} \quad \text{(A8-20)}$$

Now we have

$$\frac{d}{d\bar{r}}\left[\frac{\bar{r}\frac{dR_{mn}}{d\bar{r}} M}{K_{mn}K_{mc}}\right] = \frac{d}{d\bar{r}}\left[\frac{\bar{r}\frac{dR_{mn}}{d\bar{r}}}{K_{mn}^2}\right]\frac{K_{mn}}{K_{mc}} M + \frac{\bar{r}\frac{dR_{mn}}{d\bar{r}}}{K_{mn}^2}\frac{d}{d\bar{r}}\left(\frac{K_{mn}}{K_{mc}} M\right)$$

Using the differential equation for R_{mn} (Eqn. (2-3)) to replace the derivative in the first term on the right-hand side, we obtain

$$\frac{d}{d\bar{r}}\left[\frac{\bar{r}\frac{dR_{mn}}{d\bar{r}} M}{K_{mn}K_{mc}}\right] = \gamma^2 \bar{r} M\left[-\frac{R_{mn}K_{mn}}{K_{mc}} + \frac{m^2 R_{mn}}{\gamma^2\bar{r}^2 K_{mn}K_{mc}} + \frac{\bar{k}_{mn}^2 R_{mn}}{K_{mn}K_{mc}}\right] + \frac{\bar{r}\frac{dR_{mn}}{d\bar{r}}\frac{dM}{d\bar{r}}}{K_{mn}K_{mc}}\left(1 - \frac{\bar{k}_{mn}M}{K_{mn}} + \frac{\bar{k}_{mc}M}{K_{mc}}\right) \quad \text{(A8-21a)}$$

Similarly, we have

$$\frac{d}{d\bar{r}}\left[\frac{\bar{r}\frac{dR_{mc}}{d\bar{r}} M}{K_{mn}K_{mc}}\right] = \gamma^2 \bar{r} M\left[-\frac{R_{mc}K_{mc}}{K_{mn}} + \frac{m^2 R_{mc}}{\gamma^2\bar{r}^2 K_{mn}K_{mc}} + \frac{\bar{k}_{mc}^2 R_{mc}}{K_{mn}K_{mc}}\right] + \frac{\bar{r}\frac{dR_{mc}}{d\bar{r}}\frac{dM}{d\bar{r}}}{K_{mn}K_{mc}}\left(1 - \frac{\bar{k}_{mc}M}{K_{mc}} + \frac{\bar{k}_{mn}M}{K_{mn}}\right) \quad \text{(A8-21b)}$$

Substituting Eqn.s (A8-21) into Eqn. (A8-20), we obtain

$$\int_o^1 \frac{M \frac{dR_{mn}}{d\bar{r}} \frac{dR_{mc}}{d\bar{r}}}{\gamma^2 K_{mn} K_{mc}} 2\bar{r}d\bar{r} = \int_o^1 \Bigg\{ \frac{M}{2}\left[\frac{K_{mc}}{K_{mn}} + \frac{K_{mn}}{K_{mc}} - \frac{(\bar{k}_{mc}^2 + \bar{k}_{mn}^2)}{K_{mc}K_{mn}}\right] R_{mn}R_{mc}$$

$$- M \frac{m^2}{\gamma^2 \bar{r}^2} \frac{R_{mn}R_{mc}}{K_{mn}K_{mc}} - \frac{\frac{dM}{d\bar{r}}}{2\gamma^2 K_{mn}K_{mc}} \left[R_{mc} \frac{dR_{mn}}{d\bar{r}} \left(1 - \frac{\bar{k}_{mn}M}{K_{mn}} + \frac{\bar{k}_{mc}M}{K_{mc}}\right)\right.$$

$$\left. + R_{mn} \frac{dR_{mc}}{d\bar{r}} \left(1 - \frac{\bar{k}_{mc}M}{K_{mc}} + \frac{\bar{k}_{mn}M}{K_{mn}}\right)\right] \Bigg\} 2\bar{r}d\bar{r} \qquad \text{(A8-22)}$$

Substituting Eqn. (A8-22) into Eqn. (A8-19), we obtain, after simplification,

$$\mathcal{P}_b^p = \frac{\pi r_o^2}{\rho_o a_o} \sum_{m,n} \sum_{c\neq n} \frac{C_{mn}C_{mc} \cos(\phi_{mc} - \phi_{mn})}{2(1+\epsilon_m)} \int_o^1 \Bigg\{ \left[\frac{M}{2}\left(\frac{(K_{mn} + K_{mc})^2 - (\bar{k}_{mn} - \bar{k}_{mc})^2}{K_{mn}K_{mc}}\right)\right.$$

$$\left. + \frac{\bar{k}_{mn}}{K_{mn}} + \frac{\bar{k}_{mc}}{K_{mc}} \right] R_{mn}R_{mc} - \left[\frac{(1 - 2\bar{k}_{mn}M + \bar{k}_{mn}\bar{k}_{mc}M^2)}{2K_{mc}^2} + \frac{1}{K_{mc}}\right]$$

$$\cdot \frac{R_{mc} \frac{dR_{mn}}{d\bar{r}} \frac{dM}{d\bar{r}}}{\gamma^2 K_{mn}^2}$$

$$- \left[\frac{(1 - 2\bar{k}_{mc}M + \bar{k}_{mn}\bar{k}_{mc}M^2)}{2K_{mn}^2} + \frac{1}{K_{mn}}\right] \frac{R_{mn} \frac{dR_{mc}}{d\bar{r}} \frac{dM}{d\bar{r}}}{\gamma^2 K_{mc}^2}$$

$$+ \frac{M \frac{dR_{mn}}{d\bar{r}} \frac{dR_{mc}}{d\bar{r}} \left(\frac{dM}{d\bar{r}}\right)^2}{\gamma^4 K_{mn}^2 K_{mc}^2} \Bigg\} 2\bar{r}d\bar{r} \cos(\bar{k}_{mc} - \bar{k}_{mn})\ z \qquad \text{(A8-23)}$$

Appendix A9

DERIVATION OF ACOUSTIC ENERGY EXPRESSIONS BASED ON THE WORK OF BLOCKHINTSEV AND MÖHRING

A9.1 Results Based on the Work of Blockhintsev

The Blockhintsev energy flux can be expressed as

$$\overline{J}_s^B = p'\overline{v}' + \rho_o(\overline{V}_o \cdot \overline{v}')\, v' + \frac{p'^2}{\rho_o a_o^2}\,\overline{V}_o + \frac{p'}{a_o^2}\,(\overline{V}_o \cdot \overline{v}')\,\overline{V}_o$$

For our particular case $\overline{V}_o = U_o \overline{e}_z$, and we are only interested in the axial or z component of the acoustic energy flux. Thus the time averaged energy flux is given by

$$\langle J_{s_z}^B \rangle = \langle p' u_z' \rangle (1 + M^2) + M\left(\rho_o a_o \langle u_z'^2 \rangle + \frac{\langle p'^2 \rangle}{\rho_o a_o}\right) \qquad \text{(A9-1)}$$

Using the expressions

$$p' = \sum_{m,n} \mathrm{Re}\left[P_{mn}(r,\theta)\, e^{i(\omega t - k_{z_{mn}} z)}\right]$$

and

$$u_z' = \sum_{m,n} \mathrm{Re}\left[V_{z_{mn}}(r,\theta)\, e^{i(\omega t - k_{z_{mn}} z)}\right]$$

and time averaging, we obtain

$$\langle J_{s_z}^B \rangle = \frac{1}{2}\sum_{m,n}\sum_{b,c} \mathrm{Re}\left\{\left[P_{mn} V_{z_{bc}}^* (1 + M^2) + M\left(\rho_o a_o V_{z_{mn}} V_{z_{bc}}^* + \frac{P_{mn} P_{bc}^*}{\rho_o a_o}\right)\right] e^{i(k_{z_{bc}} - k_{z_{mn}}) z}\right\} \qquad \text{(A9-2)}$$

We have

$$V_{z_{mn}} = \frac{k_{z_{mn}} P_{mn}}{\rho_o(\omega - k_{z_{mn}} U_o)} - \frac{\frac{\partial P_{mn}}{\partial r}\frac{dU_o}{dr}}{\rho_o(\omega - k_{z_{mn}} U_o)^2}$$

where

$$p_{mn} = C_{mn} \cos(m\theta+\phi_{mn}) R_{mn}(r)$$

The coefficient C_{mn} is considered to be real and ϕ_{mn} gives the location of the modal diameter. Since we are only considering cut on modes, R_{mn} and $k_{z_{mn}}$ are real. Substituting the above expressions into the first term of equation (A9-2) and integrating across the duct cross section we have

$$\int_0^{2\pi}\int_0^{r_o} \frac{1}{2} \mathrm{Re}\left[p_{mn} V^*_{z_{bc}} (1+M^2)\, e^{i(k_{z_{bc}}-k_{z_{mn}})z}\right] r\,dr\,d\theta = 0 \;, \quad m \neq b \;,$$

$$= \frac{\pi C_{mn} C_{mc} \cos(\phi_{mn}-\phi_{mc})}{(1+\varepsilon_m)} \int_0^{r_o} R_{mn}\left[\frac{k_{z_{mc}} R_{mc}}{\rho_o(\omega-k_{z_{mc}}U_o)} - \frac{\frac{dR_{mc}}{dr}\frac{dV_o}{dr}}{\rho_o(\omega-k_{z_{mc}}U_o)^2}\right](1+M^2)\,r\,dr$$

$$\cdot \cos(k_{z_{mc}}-k_{z_{mn}})z \;, \quad m = b \;,$$

where $\varepsilon_m = 0$, $m = 0$; $= 1$, $m = 1,2,3,\ldots$. The integrals of the other terms in Eqn. (A9-2) are given by similar expressions. Evaluating these terms and summing, we have

$$\int_s \langle J^B_{s_z}\rangle ds = \sum_{m,n}\sum_c \frac{\pi C_{mn}C_{mc}\cos(\phi_{mn}-\phi_{mc})}{2(1+\varepsilon_m)} \int_0^{r_o} \Bigg\{ R_{mn}\left[\frac{k_{z_{mc}}R_{mc}}{\rho_o(\omega-k_{z_{mc}}U_o)} - \right.$$

$$\left.\frac{\frac{dR_{mc}}{dr}\frac{dU_o}{dr}}{\rho_o(\omega-k_{z_{mc}}U_o)^2}\right](1+M^2) + M\rho_o a_o\left[\frac{k_{z_{mn}}R_{mn}}{\rho_o(\omega-k_{z_{mn}}U_o)} - \frac{\frac{dR_{mn}}{dr}\frac{dV_o}{dr}}{\rho_o(\omega-k_{z_{mn}}U_o)^2}\right] \times$$

$$\left[\frac{k_{z_{mc}}R_{mc}}{\rho_o(\omega-k_{z_{mc}}U_o)} - \frac{\frac{dR_{mc}}{dr}\frac{dU_o}{dr}}{\rho_o(\omega-k_{z_{mc}}U_o)^2}\right] + \frac{M}{\rho_o a_o}R_{mn}R_{mc}\Bigg\} 2rdr \cos(k_{z_{mc}}-k_{z_{mn}})z$$

Nondimensionalizing we obtain

$$\int_s \langle J^B_{s_z}\rangle ds = \frac{\pi r_o^2}{\rho_o a_o}\sum_{m,n}\sum_c \frac{C_{mn}C_{mc}\cos(\phi_{mn}-\phi_{mc})}{2(1+\varepsilon_m)}$$

$$\int_0^1 \Bigg\{ R_{mn}\left[\frac{\bar{k}_{mc}R_{mc}}{K_{mc}} - \frac{\frac{dR_{mc}}{d\bar{r}}\frac{dM}{d\bar{r}}}{\gamma^2 K^2_{mc}}\right](1+M^2) + M\left(\frac{\bar{k}_{mn}R_{mn}}{K_{mn}} - \frac{\frac{dR_{mn}}{d\bar{r}}\frac{dM}{d\bar{r}}}{\gamma^2 K^2_{mn}}\right) \times$$

$$\left(\frac{\bar{k}_{mc}R_{mc}}{K_{mc}} - \frac{\frac{dR_{mc}}{d\bar{r}}\frac{dM}{d\bar{r}}}{\gamma^2 K^2_{mc}}\right) + MR_{mn}R_{mc}\Bigg\} 2\bar{r}d\bar{r} \cos(\bar{k}_{mc}-\bar{k}_{mn})\bar{z}$$

(A9-3)

where the nondimensional variables are defined by

$$\bar{r} = \frac{r}{r_o}\ ,\ \bar{K}_{mn} = \frac{k_{z_{mn}}a_o}{\omega}\ ,\ M = \frac{U_o}{a_o}\ ,\ K_{mn} = (1-\bar{K}_{mn}M)\ ,\ \gamma = \frac{\omega r_o}{a_o}\ \text{and}\ \bar{z} = \frac{\omega z}{a_o}\ .$$

The integrated energy flux can be separated into two parts, $\mathbb{P}_a^B$ and $\mathbb{P}_b^B$, where $\mathbb{P}_a^B$ is independent of $\bar{z}$ and $\mathbb{P}_b^B$ has a cosine dependence on $\bar{z}$. Thus

$$\int_s \langle J_{s_z}^B \rangle ds = \mathbb{P}_a^B + \mathbb{P}_b^B \tag{A9-4}$$

Further manipulations of $\mathbb{P}_a^B$ and $\mathbb{P}_b^B$ will be performed separately. We then have

$$\mathbb{P}_a^B = \frac{\pi r_o^2}{\rho_o a_o} \sum_{m,n} \overline{p_{mn}^2} \int_o^1 \left\{ R_{mn} \left(\frac{\bar{k}_{mn} R_{mn}}{K_{mn}} - \frac{\frac{dR_{mn}}{d\bar{r}} \frac{dM}{d\bar{r}}}{\gamma^2 K_{mn}^2} \right) (1+M^2) + \right.$$

$$\left. M \left(\frac{\bar{k}_{mn} R_{mn}}{K_{mn}} - \frac{\frac{dR_{mn}}{d\bar{r}} \frac{dM}{d\bar{r}}}{\gamma^2 K_{mn}^2} \right)^2 + MR_{mn}^2 \right\} 2\bar{r}d\bar{r}$$

where

$$\overline{p_{mn}^2} = \frac{C_{mn}^2}{2(1+\varepsilon_m)}$$

Collecting coefficients of R_{mn}, $\frac{dR_{mn}}{d\bar{r}}$ and $\left(\frac{dR_{mn}}{d\bar{r}}\right)^2$ we obtain the final result for $\mathbb{P}_a^B$

$$\mathbb{P}_a^B = \frac{\pi r_o^2}{\rho_o a_o} \sum_{m,n} \overline{p_{mn}^2} \int_o^1 \left\{ \left[\frac{M}{K_{mn}} + \frac{\bar{k}_{mn}}{K_{mn}^2} \right] R_{mn}^2 - \right.$$

$$\left. [1+M^2(K_{mn}^2-\bar{k}_{mn}^2)] \frac{R_{mn} \frac{dR_{mn}}{d\bar{r}} \frac{dM}{d\bar{r}}}{\gamma^2 K_{mn}^4} + \frac{\left(\frac{dR_{mn}}{d\bar{r}}\right)^2 \left(\frac{dM}{d\bar{r}}\right)^2 M}{\gamma^4 K_{mn}^4} \right\} 2\bar{r}d\bar{r} \tag{A9-5}$$

Now examine $\mathbb{P}_{a}^{B}$, the part of the integrated energy flux which is not independent of $\bar{z}$. We have

$$\mathbb{P}_b^B = \frac{\pi r_o^2}{\rho_o a_o} \sum_{m,n} \sum_{c\neq n} \frac{C_{mn} C_{mc} \cos(\phi_{mn}-\phi_{mc})}{2(1+\varepsilon_m)} \int_0^1 \left\{ R_{mn} \left[\frac{\bar{k}_{mc} R_{mc}}{K_{mc}} - \frac{\frac{dR_{mc}}{d\bar{r}} \frac{dM}{d\bar{r}}}{\gamma^2 K_{mc}^2} \right] (1+M^2) \right.$$

$$\left. + M \left(\frac{\bar{k}_{mn} R_{mn}}{K_{mn}} - \frac{\frac{dR_{mn}}{d\bar{r}} \frac{dM}{d\bar{r}}}{\gamma^2 K_{mn}^2} \right) \left(\frac{\bar{k}_{mc} R_{mc}}{K_{mc}} - \frac{\frac{dR_{mc}}{d\bar{r}} \frac{dM}{d\bar{r}}}{\gamma^2 K_{mc}^2} \right) + M R_{mn} R_{mc} \right\} 2\bar{r}d\bar{r} \cos(\bar{k}_{mc}-\bar{k}_{mn})\bar{z}$$

Collecting terms we obtain

$$\mathbb{P}_b^B = \frac{\pi r_o^2}{\rho_o a_o} \sum_{m,n} \sum_{c\neq n} \frac{C_{mn} C_{mc} \cos(\phi_{mn}-\phi_{mc})}{2(1+\varepsilon_m)} \int_0^1 \left\{ [M+\bar{k}_{mc}-\bar{k}_{mn} M^2] \frac{R_{mn} R_{mc}}{K_{mn} K_{mc}} \right.$$

$$- \frac{\frac{dM}{d\bar{r}}}{\gamma^2 K_{mc}^2 K_{mn}^2} \left[R_{mn} \frac{dR_{mc}}{d\bar{r}} (1-\bar{k}_{mn} M + M^2 K_{mn}^2) + R_{mc} \frac{dR_{mn}}{d\bar{r}} \bar{k}_{mc} K_{mc} M \right] +$$

$$\left. \frac{\frac{dR_{mc}}{d\bar{r}} \frac{dR_{mn}}{d\bar{r}} \left(\frac{dM}{d\bar{r}}\right)^2 M}{\gamma^4 K_{mc}^2 K_{mn}^2} \right\} 2\bar{r}d\bar{r} \cos(\bar{k}_{mc}-\bar{k}_{mn})\bar{z}$$

Noting that the summations over n and c have the same upper bound we can combine terms to obtain the final result for $\mathbb{P}_b^B$,

$$\mathbb{P}_b^B = \frac{\pi r_o^2}{\rho_o a_o} \sum_{m,n} \sum_{c<n} \frac{C_{mn} C_{mc} \cos(\phi_{mn}-\phi_{mc})}{2(1+\varepsilon_m)} \int_0^1 \left\{ \left[\frac{2M+(\bar{k}_{mn}+\bar{k}_{mc})(1-M^2)}{K_{mc} K_{mn}} \right] R_{mn} R_{mc} \right.$$

$$- \frac{\frac{dM}{d\bar{r}}}{\gamma^2 K_{mn}^2 K_{mc}^2} \left[R_{mn} \frac{dR_{mc}}{d\bar{r}} [1+M^2(K_{mn}^2-\bar{k}_{mn}^2)] + R_{mc} \frac{dR_{mn}}{d\bar{r}} [1+M^2(K_{mc}^2-\bar{k}_{mc}^2)] \right]$$

$$+ 2 \frac{\frac{dR_{mc}}{d\bar{r}} \frac{dR_{mn}}{d\bar{r}} \left(\frac{dM}{d\bar{r}}\right)^2 M}{\gamma^4 K_{mn}^2 K_{mc}^2} \Bigg\} 2\bar{r}d\bar{r} \cos(\bar{k}_{mc}-\bar{k}_{mn})\bar{z} \tag{A9-6}$$

A9.2. Results Based on the Work of Möhring

Möhring (1971) presents an acoustic energy flux expression for the case of a two dimensional duct containing a sheared mean flow. The acoustic pressure for a two dimensional duct is given by -

$$P'(y,z,t) = \sum_n C_n P_n(y)\, e^{i(\omega t - k_{z_n} z)} \tag{A9-7}$$

The acoustic energy flow of Möhring can be expressed as

$$\mathbb{P}^M_{2-D} = \sum_n \sum_c \frac{C_n C_c \omega}{4\rho_o} \int_o^{y_o} \Bigg\{ \left[\frac{2\omega U_o}{a_o^2} + (k_{z_n}+k_{z_c}) \left(1 - \frac{U_o^2}{a_o^2}\right) \right] \frac{P_n P_c}{(\omega-k_{z_n}U_o)(\omega-k_{z_c}U_o)}$$

$$- \frac{\omega \frac{dU_o}{dy} \left(P_n \frac{dP_c}{dy} + P_c \frac{dP_n}{dy} \right)}{(\omega-k_{z_n}U_o)^2 (\omega-k_{z_c}U_o)^2} \Bigg\} dy \cos(k_{z_c}-k_{z_n})z \tag{A9-8}$$

Introducing the nondimensional variables

$$\bar{y} = \frac{y}{y_o}, \quad \bar{k}_n = \frac{k_{z_n} a_o}{\omega}, \quad M = \frac{U_o}{a_o}, \quad K_n = (1-\bar{k}_n M), \quad \gamma = \frac{\omega y_o}{a_o} \quad \text{and} \quad \bar{z} = \frac{\omega z}{a_o}$$

we obtain

$$\mathbb{P}^{M}_{2-D} = \frac{y_o}{\rho_o a_o} \sum_n \sum_c \frac{C_n C_c}{4} \int_0^1 \left\{ \left[\frac{2M + (k_n + \bar{k}_c)(1-M^2)}{K_n K_c} \right] P_n P_c \right.$$

$$\left. - \frac{\frac{dM}{d\bar{y}}}{\gamma^2} \frac{\left(P_n \frac{dP_c}{d\bar{y}} + P_c \frac{dP_n}{d\bar{y}} \right)}{K_n^2 K_c^2} \right\} d\bar{y} \cos(\bar{k}_c - \bar{k}_n)\bar{z} \quad \text{(A9-9)}$$

We wish to find the equivalent of equation (A9-9) for the case of a circular duct. For a circular duct, the coordinate $\bar{r}$ replaces $\bar{y}$ and the area is given by πr_o^2 rather than y_o. The modes have a double index (m,n) and the differential element of volume is $\bar{r}d\theta d\bar{r}$ instead of $d\bar{y}$. The integration over θ introduces the factor $\frac{2 \cos(\phi_{mc} - \phi_{mn})}{(1+\varepsilon_m)}$. Thus the equivalent of equation (A9-9) for the circular duct case is

$$\mathbb{P}^{M} = \frac{\pi r_o^2}{\rho_o a_o} \sum_{m,n} \sum_c \frac{C_{mn} C_{mc} \cos(\phi_{mc} - \phi_{mn})}{4(1+\varepsilon_m)}$$

$$\int_0^1 \left\{ \left[2M + (\bar{k}_{mn} + \bar{k}_{mc})(1-M^2) \right] \frac{R_{mn} R_{mc}}{K_{mn} K_{mc}} - \right.$$

$$\left. \frac{\frac{dM}{d\bar{r}}}{\gamma^2} \frac{\left(R_{mn} \frac{dR_{mc}}{d\bar{r}} + R_{mc} \frac{dR_{mn}}{d\bar{r}} \right)}{K_{mc}^2 K_{mn}^2} \right\} 2\bar{r}d\bar{r} \cos(\bar{k}_{mc} - \bar{k}_{mn})\bar{z} \quad \text{(A9-10)}$$

The integrated power flux can be separated into two parts, $\mathbb{P}_a^M$ and $\mathbb{P}_b^M$, where $\mathbb{P}_a^M$ is independent of $\bar{z}$ and $\mathbb{P}_b^M$ has a cosine dependence on $\bar{z}$. Thus we have

$$\mathbb{P}_a^M = \frac{\pi r_o^2}{\rho_o a_o} \sum_{m,n} \frac{C_{mn}^2}{2(1+\varepsilon_m)} \int_o^1 \left\{ \left[M + \bar{k}_{mn}(1-M^2)\right] \frac{R_{mn}^2}{K_{mn}^2} - \frac{\frac{dM}{d\bar{r}} R_{mn} \frac{dR_{mn}}{d\bar{r}}}{\gamma^2 K_{mn}^4} \right\} 2rdr$$

Thus $\mathbb{P}_a^M$ can be expressed as

$$\mathbb{P}_a^M = \frac{\pi r_o^2}{\rho_o a_o} \sum_{m,n} \overline{P_{mn}^2} \int_o^1 \left\{ \left[\frac{M}{K_{mn}} + \frac{\bar{k}_{mn}}{K_{mn}^2}\right] R_{mn}^2 - \frac{R_{mn} \frac{dR_{mn}}{d\bar{r}} \frac{dM}{d\bar{r}}}{\gamma^2 K_{mn}^4} \right\} 2\bar{r}d\bar{r} \tag{A9-11}$$

Collecting the terms of $\mathbb{P}^M$ which have a cosine dependence on $\bar{z}$ we have

$$\mathbb{P}_b^M = \frac{\pi r_o^2}{\rho_o a_o} \sum_{m,n} \sum_{c \neq n} \frac{C_{mn} C_{mc} \cos(\phi_{mc} - \phi_{mn})}{4(1+\varepsilon_m)}$$

$$\int_o^1 \left\{ \left[2M + (\bar{k}_{mn} + \bar{k}_{mc})(1-M^2)\right] \frac{R_{mn} R_{mc}}{K_{mn} K_{mc}} - \right.$$

$$\left. \frac{dM}{d\bar{r}} \frac{\left(R_{mn} \frac{dR_{mc}}{d\bar{r}} + R_{mc} \frac{dR_{mn}}{d\bar{r}}\right)}{\gamma^2 K_{mc}^2 K_{mn}^2} \right\} 2\bar{r}d\bar{r} \cos(\bar{k}_{mc} - \bar{k}_{mn})\bar{z}$$

Noting that the summations over n and c have the same upper bound $\mathbb{P}_b^M$ can be written in final form as

$$\mathbb{P}_b^M = \frac{\pi r_o^2}{\rho_o a_o} \sum_{m,n} \sum_{c<n} \frac{C_{mn} C_{mc} \cos(\phi_{mc} - \phi_{mn})}{2(1+\varepsilon_m)}$$

$$\int_o^1 \left\{ \left[2M + (\bar{k}_{mn} + \bar{k}_{mc})(1-M^2) \right] \frac{R_{mn} R_{mc}}{K_{mn} K_{mc}} - \right.$$

$$\left. \frac{dM}{d\bar{r}} \frac{\left(R_{mn} \frac{dR_{mc}}{d\bar{r}} + R_{mc} \frac{dR_{mn}}{d\bar{r}} \right)}{\gamma^2 K_{mn}^2 K_{mc}^2} \right\} 2\bar{r} d\bar{r} \cos(\bar{k}_{mc} - \bar{k}_{mn}) \bar{z} \qquad \text{(A9-12)}$$

Appendix A10

COMPUTER PROGRAMS FOR THE ENERGY-WEIGHTING FUNCTION ANALYSIS

The computer programs in this appendix are FORTRAN programs which were written for the IBM 370/168 computer. The program MODE was compiled on a FORTRAN-H compiler. The program INTGRTE was used with the WATFIV compiler.

A10.1. Program MODE

The computer program MODE calculates the radial mode shape functions $R_{mn}(\bar{r})$ and normalized axial wavenumbers $\bar{k}_{mn}$ of propagating acoustic modes for a given mean flow profile $M(\bar{r})$. The program also calculates the physical, Möhring, and Blockhintsev energy weighting functions.

The mean flow profile shape is calculated by the subroutine FLOPRO. The listing following this d.scussion contains the equation for a one-seventh power profile. To obtain results for other profile shapes, the subroutine FLOPRO would have to be modified accordingly.

The necessary input data consis of a first line which tells the pro- ram how many cases are to be calculated, and an additional line for each case to set the proper input parameters.

The first line of data contains the chosen value of NUMRUN, which tells the computer how many modes are to be calculated. NUMRUN is an integer which can rang from 1 to 99 and is read using FORMAT statement 1 in the program.

Each succeeding line of data gives the input parameters for a particular mode. The data are read using FORMAT statement 1 in the program. The following list explains each input parameter.

a) NN is an integer which is less than or equal to 10 and controls the number of intervals which the duct radius is divided into. The actual number of intervals is given by 2^{NN}.

b) M is an integer which can range from 0 to 9 and gives the circumferential mode number. For example, to calculate the (2,0) mode, M would be set equal to 2.

c) NMODE is an integer which can range from 0 to 9 and gives the desired radial mode number. However, NMODE is only used in the output subroutine and does not control which radial mode number is actually found. The program converges on the radial mode number whose eigenvalue is closest to the estimated eigenvalue, K (see below). The output can easily be checked to see that the correct radial mode number has been found by applying the following rule. The (m,n) mode eigenfunction has n zeros in the interval $0 < \bar{r} < 1$. Note that the origin is excluded in applying this rule.

d) C is a REAL*8 number which gives the value of the reduced frequency, γ.

e) K is a REAL*8 number which is the estimated value of the normalized axial wavenumber, $\bar{k}_{mn}$. The accuracy of the estimate strongly affects the number of interations the program performs to obtain the solution. The program will find the radial mode whose normalized axial wavenumber is closest to K. Thus the choice of K also affects the radial mode number of the solution. However, under most circumstances the value of $\bar{k}_{mn}$ can be estimated accurately enough to produce convergence to the desired mode.

f) LB is a REAL*8 number which defines the lower bound of the range searched for eigenvalues $\bar{k}^2_{mn}$. The values of LB and UB should be chosen such that not more than two eigenvalues lie in the specified range. If more than two eigenvalues are found, the program is terminated after printing a nonzero value of IERR. If no eigenvalues are found in the specified range at any iteration step, the program prints "NO EIGENVALUE FOUND FOR ESTIMATE K = ____ " and terminates.

g) UB is a REAL*8 number which defines the upper bound of the range searched for eigenvalues $\bar{k}^2_{mn}$. Guidelines for selecting values of UB were discussed above.

h) W is a REAL*8 number which is chosen to accelerate convergence of K. If W is set too high, convergence will be slow, with successive iterations overshooting the correct value in an oscillatory fashion. If W is set too low, it may take many iterations to obtain the solution. As a general guideline, for modes close to cutoff low values of W such as 0.25 to 0.50 should be chosen, while for modes far above cutoff values from 0.8 to 1.0 give rapid convergence.

A sample output of the computer program is shown following the listing. The value of the eigenvalue K^2 found in each iteration is printed out. The message "IERR = 0" denotes a normal return from the subroutine TSTURM. After the value of K^2 has converged, the normalized axial wavenumber is printed out. The integrals in the energy weighting functions are then calculated using a Romberg integration scheme (see Hornbeck (1975)). The Romberg integration scheme is terminated when the value of the integral has converged to 0.5% uncertainty or all the data points have been used, whichever comes first. The value of the integral, the uncertainty, and the number of integration steps are then printed out. The maximum number of steps is (NN+1). The definitions of the integrals listed are given below.

$$\mathrm{INT}(1) = \int_0^1 \frac{M\, R_{mn}^2}{K_{mn}}\, 2\bar{r}d\bar{r}$$

$$\mathrm{INT}(2) = \int_0^1 \frac{\bar{k}_{mn}\, R_{mn}^2}{K_{mn}^2}\, 2\bar{r}d\bar{r}$$

$$\mathrm{INT}(3) = -\int_0^1 \frac{R_{mn}\,\dfrac{dR_{mn}}{d\bar{r}}\,\dfrac{dM}{d\bar{r}}}{\gamma^2\, K_{mn}^4}\, 2\bar{r}d\bar{r}$$

$$\mathrm{INT}(4) = -\int_0^1 \frac{R_{mn}\,\dfrac{dR_{mn}}{d\bar{r}}\,\dfrac{dM}{d\bar{r}}}{\gamma^2\, K_{mn}^4}\, M^2(K_{mn}^2 - \bar{k}_{mn}^2)\; 2\bar{r}d\bar{r}$$

$$\mathrm{INT}(5) = \int_0^1 \frac{M\left(\dfrac{dR_{mn}}{d\bar{r}}\,\dfrac{dM}{d\bar{r}}\right)^2}{\gamma^4\, K_{mn}^4}\, 2\bar{r}d\bar{r}$$

$$\mathrm{PINT}(1) = \int_0^1 M R_{mn}^2\, 2\bar{r}d\bar{r}$$

$$\mathrm{PINT}(2) = \int_0^1 \frac{\bar{k}_{mn}\, R_{mn}^2}{K_{mn}}\, 2\bar{r}d\bar{r}$$

$$\text{PINT}(3) = -\int_{o}^{1} \left(\frac{1}{K_{mn}} + \frac{1}{2}\right) \frac{R_{mn} \frac{dR_{mn}}{d\bar{r}} \frac{dM}{d\bar{r}}}{\gamma^2 K_{mn}^2} 2\bar{r}d\bar{r}$$

$$\text{PINT}(4) = \int_{o}^{1} \frac{M\left(\frac{dR_{mn}}{d\bar{r}} \frac{dM}{d\bar{r}}\right)^2}{2\gamma^4 K_{mn}^4} 2\bar{r}d\bar{r}$$

The values of the Blockhintsev, Möhring, and physical energy-weighting functions are printed out after evaluation of the integrals.

The subroutine OUTPUT is then used to print out the values of the eigenfunction R_{mn} and the integrands of the above integrals (excluding the factor $2\bar{r}$) at 33 points across the duct radius. The Products, Möhring Shear, and Blockhintsev Additional categories of the Möhring/Blockhintsev flux terms refer to the integrands of (INT(1)+INT(2)), INT(3), and (INT(4)+INT(5)), respectively. The Products and Shear categories of the physical flux terms refer to (PINT(1)+PINT(2)) and (PINT(3)+PINT(4)), respectively. Since the listing of the eigenfunctions and integrands is controlled by a separate subroutine, more detailed output can be obtained easily by simply modifying the subroutine OUTPUT.

A listing of the program MODE and a sample of the output follows.

Listing of Program MODE

```
 REAL*8  W,K,KNEW,G,LB,UB,K2NEW,EPS1,SUM,FM,FB,FP
 REAL*8 R(1025),B(1025),AE(1025),AD(1025),D(1025),E(1025),E2(1025),
$K2(2),Z(1025,2),RV1(1025),RV2(1025),RV3(1025),RV4(1025),RV5(1025),
$RV6(1025),KM(2049),MACH(2049),T(8),T1(11),T2(11),INT(9),DELINT(9),
$PERINT(9),FI1(1025),FI2(1025),FI3(1025),FI4(1025),FI5(1025),
$PFI1(1025),PFI2(1025),PFI3(1025)
 REAL*8 DSQRT,DABS
 COMMON MACH,R,B,AE,AD,FI4,FI5,PFI1,PFI2,PFI3,K
 EQUIVALENCE (B(1),FI1(1)),(AE(1),FI2(1)),(AD(1),FI3(1))
 DIMENSION NSTEP(9)
 READ(5,1) NUMRUN
 DO 1000 III=1,NUMRUN

 **** N=2**NN IS THE NUMBER OF INTERVALS.
 **** M IS THE CIRCUMFERENTIAL MODE NUMBER.
**** NMODE IS THE DESIRED RADIAL MODE NUMBER.
 **** G IS THE REDUCED FREQUENCY GAMMA.
**** K IS THE ESTIMATED NORMALIZED WAVE NUMBER.
 **** LB AND UB DEFINE THE RANGE SEARCHED FOR
 **** EIGENVALUES K2.
**** W IS CHOSEN TO ACCELERATE CONVERGENCE OF K.

  READ(5,1) NN,M,NMODE,G,K,LB,UB,W
1 FORMAT(3I2,5D12.5)
  N=2**NN
  N1=N+1
  N2=2*N+1
  N3=N/32
  N11=N-1
  NITER = 0
  WRITE(6,2) M,NMODE,G,N,LB,UB,W
2 FORMAT(////' (',I1,',',I1,') MODE',4X,'GAMMA=',D11.4,4X,I3,' INTER
 $VALS'/' LB=',D11.4,4X,'UB=',D11.4,4X,'W=',D11.4/)

  **** GENERATE MACH NUMBER PROFILE ARRAY.

  CALL FLOPRO(N2,N)

  **** GENERATE KM ARRAY USING ESTIMATED VALUE OF K.

90 DO 20 I=1,N2
20 KM(I)=1.D0-K*MACH(I)

   **** GENERATE ARRAYS FOR A*R=K2*B*R.
   **** A IS TRIDIAGONAL,  AD(I) ARE DIAGONAL ELEMENTS,
   **** AE(I) ARE SUBDIAGONAL ELEMENTS.  B IS DIAGONAL,
   **** B(I) ARE THE SQUARE ROOTS OF THE DIAGONAL ELEMENTS.

   IF(M.EQ.0) GO TO 29
   N12=N
   DO 30 I=1,N11
30 B(I)=G*DSQRT(1.D0*I/N)/(KM(2*I+1)*N)
   B(N)=G*DSQRT((N-.5D0)/(2.D0*N))/(KM(2*N)*N)
   AE(1)=0.D0
   DO 40 I=2,N
40 AE(I)=(I-.5D0)/(KM(2*I)**2.D0*N)
   AD(1)=G*G/(N**3)-M*M/(KM(3)**2*N)-1.D0/(KM(2)*
  $*2*2.D0*N)-AE(2)
```

```
      DO 50 I=2,N11
   50 AD(I)=G*G*I/(N**3)-M*M/(KM(2*I+1)**2*I*N)-AE(I)-AE(I+1)
      AD(N)=AE(N)/(2.D0*N*N)*(G*G*KM(N2)**2-M*M-2.D0*N*N)
      GO TO 59
   29 N12=N1
      B(1)=G/(KM(2)*(2.D0*N)**1.5D0)
      DO 31 I=2,N
   31 B(I)=G*DSQRT((I-1.D0)/N)/(KM(2*I-1)*N)
      B(N1)=G*DSQRT((N-.5D0)/(2.D0*N))/(KM(2*N)*N)
      AE(1)=0.D0
      DO 41 I=2,N1
   41 AE(I)=(I-1.5D0)/(KM(2*I-2)**2.D0*N)
      AD(1)=AE(2)/(4.D0*N*N)*(G*G*KM(1)**2.D0-4.D0*N*N)
      DO 51 I=2,N
   51 AD(I)=G*G*(I-1.D0)/(N**3)-AE(I)-AE(I+1)
      AD(N1)=AE(N1)/(2.D0*N*N)*(G*G*KM(N2)**2-2.D0*N*N)

      **** PERFORM CHOLESKI DECOMPOSITION.  GENERATE (C-K2*I)*Z=0,
      **** WHERE Z(I)=B(I)*R(I)

   59 E(1)=0.D0
      DO 60 I=2,N12
   60 E(I)=AE(I)/(B(I)*B(I-1))
      DO 70 I=1,N12
      D(I)=AD(I)/(B(I)*B(I))
   70 E2(I)=E(I)*E(I)

      **** USE SUBROUTINE TSTURM TO FIND EIGENVALUES K2 IN (LB,UB) AND
      **** THEIR ASSOCIATED EIGENVECTORS Z.

      EPS1= -1.D0
      CALL TSTURM(1025,N12,EPS1,D,E,E2,LB,UB,2,NEIGEN,K2,Z,IERR,RV1,RV2,
     $RV3,RV4,RV5,RV6)
      IF(NEIGEN.GT.0) GO TO 71
  900 WRITE(6,12) K
   12 FORMAT(' NO EIGENVALUE FOUND FOR ESTIMATE K=',D13.5)
      GO TO 1000
   71 WRITE(6,3) IERR,(K2(J),J=1,NEIGEN)
    3 FORMAT(' IERR=',I3,5X,'K2=',D12.4,3X,D12.4)
      IF(IERR.NE.0) GO TO 1000

      **** IF MORE THAN ONE EIGENVALUE FOUND, CHOOSE THE ONE CLOSEST
      **** TO THE ESTIMATED K AND CHECK CONVERGENCE. IF K HAS NOT
      **** CONVERGED, ITERATE USING NEW VALUE OF K.

      NITER = NITER + 1
      K2NEW=K2(1)
      II=1
      DO 80 I=1,NEIGEN
      IF(DABS(K2(I)-K*K).GE.DABS(K2NEW-K*K)) GO TO 80
      K2NEW = K2(I)
      II=I
   80 CONTINUE
      IF(DABS(K2NEW-K*K).LE.1.D-4*K*K) GO TO 100
      KNEW=DSQRT(K2NEW)
      IF(K.LT.0.D0) KNEW=-KNEW
      K=K+W*(KNEW-K)
      IF (NITER.GE.8) GO TO 1000
      GO TO 90

      **** IF K HAS CONVERGED, GENERATE R FROM Z.

  100 KNEW=DSQRT(K2NEW)
      IF(K.LT.0.D0) KNEW= -KNEW
      K=KNEW
      IF(M.EQ.0) GO TO 101
      R(1)=0.D0
```

```
      DO 110 I=2,N1
110   R(I)=Z(I-1,II)*B(N)/(B(I-1)*Z(N,II))
      GO TO 102
101   DO 111 I=1,N1
111   R(I)=Z(I,II)*B(N1)/(B(I)*Z(N1,II))
102   WRITE(6,4) K
    4 FORMAT(/' ',4X,'K=',D12.4)
      WRITE(6,5)
    5 FORMAT('     ')

      **** INTEGRATE EIGHT INTEGRALS USING ROMBERG INTEGRATION.
      **** FI1(I),FI2(I),FI3(I),FI4(I) AND FI5(I) ARE VALUES
      **** OF THE INTEGRANDS EXCLUDING THE (2*RAD) TERM.
      **** T(JJ) ARE INITIAL ESTIMATES IN THE INTEGRATION SCHEME.

      DO 120 I=1,N1
      FI1(I)=0.D0
      FI2(I)=0.D0
      FI3(I)=0.D0
      FI4(I)=0.D0
      FI5(I)=0.D0
      PFI1(I)=0.D0
      PFI2(I)=0.D0
120   PFI3(I)=0.D0
      FI1(1)=MACH(1)*R(1)*R(1)/KM(1)
      FI1(N1)=MACH(N2)*R(N1)*R(N1)/KM(N2)
      FI2(1)=K*R(1)*R(1)/KM(1)**2.D0
      FI2(N1)=K*R(N1)*R(N1)/KM(N2)**2.D0
      PFI1(1)=MACH(1)*R(1)*R(1)
      PFI1(N1)=MACH(N2)*R(N1)*R(N1)
      PFI2(1)=K*R(1)*R(1)/KM(1)
      PFI2(N1)=K*R(N1)*R(N1)/KM(N2)

      **** FI3,FI4,FI5 AND PFI3 ARE IDENTICALLY ZERO AT THE END
      **** POINTS BY VIRTUE OF THE BOUNDARY CONDITIONS.
      T(1)=FI1(N1)
      T(2)=FI2(N1)
      T(3)=0.D0
      T(4)=0.D0
      T(5)=0.D0
      T(6)=PFI1(N1)
      T(7)=PFI2(N1)
      T(8)=0.D0
      DO 130 JJ=1,8
      T2(1)=T(JJ)
      N4=1
180   DO 140 I=1,N4
140   T1(I)=T2(I)
      N4=N4+1
      N5=2**(N4-1)
      N6=N/N5
      N7=2*N6
      SUM=0.D0
      GO TO (131,132,133,134,135,136,137,138),JJ
131   DO 141 I=1,N5,2
      FI1(I*N6+1)=MACH(I*N7+1)*R(I*N6+1)*R(I*N6+1)/KM(I*N7+1)
141   SUM=SUM+I*FI1(I*N6+1)
      GO TO 150
132   DO 142 I=1,N5,2
      FI2(I*N6+1)=K*(DABS(R(I*N6+1)/KM(I*N7+1)))**2.D0
142   SUM=SUM+I*FI2(I*N6+1)
      GO TO 150
133   DO 143 I=1,N5,2
      FI3(I*N6+1)=-R(I*N6+1)*.5D0*N*N*(R(I*N6+2)-R(I*N6))*
     $(MACH(I*N7+2)-MACH(I*N7))/(G*G*KM(I*N7+1)**4.D0)
143   SUM=SUM+I*FI3(I*N6+1)
      GO TO 150
```

```
134 DO 144 I=1,N5,2
    FI4(I*N6+1)=-R(I*N6+1)*.5D0*N*N*(R(I*N6+2)-R(I*N6))*
   $(MACH(I*N7+2)-MACH(I*N7))/(G*G*KM(I*N7+1)**4.D0)*MACH(I*N7+1)*
   $MACH(I*N7+1)*(KM(I*N7+1)**2.D0-K*K)
144 SUM=SUM+I*FI4(I*N6+1)
    GO TO 150
135 DO 145 I=1,N5,2
    FI5(I*N6+1)=MACH(I*N7+1)*.25D0*N*N*N*N*(DABS((MACH(I*N7+2)-
   $MACH(I*N7))*(R(I*N6+2)-R(I*N6))))**2.D0/(G*KM(I*N7+1))**4.D0
145 SUM=SUM+I*FI5(I*N6+1)
    GO TO 150
136 DO 146 I=1,N5,2
    PFI1(I*N6+1)=MACH(I*N7+1)*R(I*N6+1)*R(I*N6+1)
146 SUM=SUM+I*PFI1(I*N6+1)
    GO TO 150
137 DO 147 I=1,N5,2
    PFI2(I*N6+1)=K*R(I*N6+1)*R(I*N6+1)/KM(I*N7+1)
147 SUM=SUM+I*PFI2(I*N6+1)
    GO TO 150
138 DO 148 I=1,N5,2
    PFI3(I*N6+1)=-R(I*N6+1)*.5D0*N*N*(R(I*N6+2)-R(I*N6),*
   $(MACH(I*N7+2)-MACH(I*N7))/(G*KM(I*N7+1))**2*
   $(1.D0/KM(I*N7+1)+0.5D0)
148 SUM=SUM+I*PFI3(I*N6+1)

    **** THE CONSTANT PART OF (2*RAD), (2.D0/N5), OMITTED FROM
    **** SUM IS INCLUDED IN THE EXPRESSION FOR T2(1).

150 T2(1)=T1(1)/2.D0+SUM*2.D0/N5**2
    DO 160 I=2,N4
160 T2(I)=(4.D0**(I-1.D0)*T2(I-1)-T1(I-1))/(4.D0**(I-1.D0)-1.D0)
    IF (N4.LT.6) GO TO 180
    INT(JJ)=T2(N4)
    DELINT(JJ)=DABS(INT(JJ)-T1(N4-1))
    IF(DELINT(JJ).LE.5.D-3*DABS(INT(JJ))) GO TO 170
    IF(N4.LT.NN+1) GO TO 180
170 PERCNT(JJ)=0.0
    IF(N4.GT.2) PERCNT(JJ)=100.*DELINT(JJ)/DABS(INT(JJ))
    NSTEP(JJ)=N4
130 CONTINUE
    INT(9)=INT(5)/2.D0
    PERCNT(9)=PERCNT(5)
    NSTEP(9)=NSTEP(5)
    DO 175 JJ=1,4
    J1=JJ+5
    WRITE(6,9) JJ,INT(JJ),PERCNT(JJ),NSTEP(JJ),JJ,INT(J1),PERCNT(J1),
   $NSTEP(J1)
  9 FORMAT(' INT(',I1,')=',D12.4,F5.1,' %UNCER'
   $,X,I2,' STEPS.',10X,'  PINT(',I1,')=',D12.4,F5.1,' %UNCER',X,
   $I2,' STEPS.')
175 CONTINUE
    JJ=5
    WRITE(6,6) JJ,INT(JJ),PERCNT(JJ),NSTEP(JJ)
  6 FORMAT(' INT(',I1,')=',D12.4,F5.1,' %UNCER'
   $,X,I2,' STEPS.')
    FM=INT(1)+INT(2)+INT(3)
    FMPRCT=(INT(1)*PERCNT(1)+INT(2)*PERCNT(2)+INT(3)*PERCNT(3))/FM
    FB=INT(1)+INT(2)+INT(3)+INT(4)+INT(5)
    FBPRCT=(INT(1)*PERCNT(1)+INT(2)*PERCNT(2)+INT(3)*PERCNT(3)+INT(4)*
   $PERCNT(4)+INT(5)*PERCNT(5))/FB
    FP=INT(6)+INT(7)+INT(8)+INT(9)
    FPPRCT=(INT(6)*PERCNT(6)+INT(7)*PERCNT(7)+INT(8)*PERCNT(8)
   $+INT(9)*PERCNT(9))/FP
```

```
      WRITE(6,8) FB,FBPRCT,FM,FMPRCT,FP,FPPRCT
    8 FORMAT(/' BLOCKHINTSEV ENERGY WEIGHTING FUNCTION =',D12.4,
     $5X,F5.1,' % UNCERTAINTY'/'   MOHRING ENERGY WEIGHTING FUNCT',
     $'ION    =',D12.4,5X,F5.1,' % UNCERTAINTY'/,'  PHYSICAL ENERGY',
     $' WEIGHTING FUNCTION     =',D12.4,5X,F5.1,' % UNCERTAINTY',/)
      CALL OUTPUT(N1,N3)
 1000 CONTINUE
      WRITE(6,10)
   10 FORMAT(///'    ')
      STOP
      END
****************** START OF TSTURM *****************
                         4/2/73

      ------------------------------------------------------------------

      SUBROUTINE TSTURM(NM,N,EPS1,D,E,E2,LB,UB,MM,M,W,Z,
     X                  IERR,RV1,RV2,RV3,RV4,RV5,RV6)

      INTEGER I,J,K,M,N,P,Q,R,S,II,IP,JJ,MM,M1,M2,NM,ITS,
     X        IERR,GROUP,ISTURM
      REAL*8 D(N),E(N),E2(N),W(MM),Z(NM,MM),
     X       RV1(N),RV2(N),RV3(N),RV4(N),RV5(N),RV6(N)
      REAL*8 U,V,LB,T1,T2,UB,UK,XU,X0,X1,EPS1,EPS2,EPS3,EPS4,
     X       NORM,MACHEP
      REAL*8 DSQRT,DABS,DMAX1,DMIN1,DFLOAT

      THIS SUBROUTINE IS A TRANSLATION OF THE ALGOL PROCEDURE TRISTURM
      BY PETERS AND WILKINSON.
      HANDBOOK FOR AUTO. COMP., VOL.II-LINEAR ALGEBRA, 418-439(1971).

      THIS SUBROUTINE FINDS THOSE EIGENVALUES OF A TRIDIAGONAL
      SYMMETRIC MATRIX WHICH LIE IN A SPECIFIED INTERVAL AND THEIR
      ASSOCIATED EIGENVECTORS, USING BISECTION AND INVERSE ITERATION.

      ON INPUT:

         NM MUST BE SET TO THE ROW DIMENSION OF TWO-DIMENSIONAL
           ARRAY PARAMETERS AS DECLARED IN THE CALLING PROGRAM
           DIMENSION STATEMENT;

         N IS THE ORDER OF THE MATRIX;

         EPS1 IS AN ABSOLUTE ERROR TOLERANCE FOR THE COMPUTED
           EIGENVALUES.  IT SHOULD BE CHOSEN COMMENSURATE WITH
           RELATIVE PERTURBATIONS IN THE MATRIX ELEMENTS OF THE
           ORDER OF THE RELATIVE MACHINE PRECISION.  IF THE
           INPUT EPS1 IS NON-POSITIVE, IT IS RESET FOR EACH
           SUBMATRIX TO A DEFAULT VALUE, NAMELY, MINUS THE
           PRODUCT OF THE RELATIVE MACHINE PRECISION AND THE
           1-NORM OF THE SUBMATRIX;

         D CONTAINS THE DIAGONAL ELEMENTS OF THE INPUT MATRIX;

         E CONTAINS THE SUBDIAGONAL ELEMENTS OF THE INPUT MATRIX
           IN ITS LAST N-1 POSITIONS.  E(1) IS ARBITRARY;

         E2 CONTAINS THE SQUARES OF THE CORRESPONDING ELEMENTS OF E.
           E2(1) IS ARBITRARY;

         LB AND UB DEFINE THE INTERVAL TO BE SEARCHED FOR EIGENVALUES.
           IF LB IS NOT LESS THAN UB, NO EIGENVALUES WILL BE FOUND;

         MM SHOULD BE SET TO AN UPPER BOUND FOR THE NUMBER OF
           EIGENVALUES IN THE INTERVAL.  WARNING: IF MORE THAN
           MM EIGENVALUES ARE DETERMINED TO LIE IN THE INTERVAL,
           AN ERROR RETURN IS MADE WITH NO VALUES OR VECTORS FOUND.
```

```
      ON OUTPUT:

         EPS1 IS UNALTERED UNLESS IT HAS BEEN RESET TO ITS
           (LAST) DEFAULT VALUE;

         D AND E ARE UNALTERED;

         ELEMENTS OF E2, CORRESPONDING TO ELEMENTS OF E REGARDED
           AS NEGLIGIBLE, HAVE BEEN REPLACED BY ZERO CAUSING THE
           MATRIX TO SPLIT INTO A DIRECT SUM OF SUBMATRICES.
           E2(1) IS ALSO SET TO ZERO;

         M IS THE NUMBER OF EIGENVALUES DETERMINED TO LIE IN (LB,UB);

         W CONTAINS THE M EIGENVALUES IN ASCENDING ORDER IF THE MATRIX
           DOES NOT SPLIT.  IF THE MATRIX SPLITS, THE EIGENVALUES ARE
           IN ASCENDING ORDER FOR EACH SUBMATRIX.  IF A VECTOR ERROR
           EXIT IS MADE, W CONTAINS THOSE VALUES ALREADY FOUND;

         Z CONTAINS THE ASSOCIATED SET OF ORTHONORMAL EIGENVECTORS.
           IF AN ERROR EXIT IS MADE, Z CONTAINS THOSE VECTORS
           ALREADY FOUND;

         IERR IS SET TO
           ZERO       FOR NORMAL RETURN,
           3*N+1      IF M EXCEEDS MM;
           4*N+R      IF THE EIGENVECTOR CORRESPONDING TO THE R-TH
                      EIGENVALUE FAILS TO CONVERGE IN 5 ITERATIONS;

         RV1, RV2, RV3, RV4, RV5, AND RV6 ARE TEMPORARY STORAGE ARRAYS.

      THE ALGOL PROCEDURE STURMCNT CONTAINED IN TRISTURM
      APPEARS IN TSTURM IN-LINE.

      NOTE THAT SUBROUTINE TQL2 OR IMTQL2 IS GENERALLY FASTER THAN
      TSTURM, IF MORE THAN N/4 EIGENVALUES AND VECTORS ARE TO BE FOUND.

      QUESTIONS AND COMMENTS SHOULD BE DIRECTED TO B. S. GARBOW,
      APPLIED MATHEMATICS DIVISION, ARGONNE NATIONAL LABORATORY

      ------------------------------------------------------------------

      :::::::::: MACHEP IS A MACHINE DEPENDENT PARAMETER SPECIFYING
                 THE RELATIVE PRECISION OF FLOATING POINT ARITHMETIC.
                 MACHEP = 16.0D0**(-13) FOR LONG FORM ARITHMETIC
                 ON S360 ::::::::::
      DATA MACHEP/Z3410000000000000/

      IERR = 0
      T1 = LB
      T2 = UB
      :::::::::: LOOK FOR SMALL SUB-DIAGONAL ENTRIES ::::::::::
      DO 40 I = 1, N
         IF (I .EQ. 1) GO TO 20
         IF (DABS(E(I)) .GT. MACHEP * (DABS(D(I)) + DABS(D(I-1))))
     X      GO TO 40
   20    E2(I) = 0.0D0
   40 CONTINUE
      :::::::::: DETERMINE THE NUMBER OF EIGENVALUES
                 IN THE INTERVAL ::::::::::
      P = 1
      Q = N
      X1 = UB
      ISTURM = 1
      GO TO 320
   60 M = S
      X1 = LB
      ISTURM = 2
      GO TO 320
   80 M = M - S
      IF (M .GT. MM) GO TO 980
```

```
      Q = 0
      R = 0
C     :::::::::: ESTABLISH AND PROCESS NEXT SUBMATRIX, REFINING
C                INTERVAL BY THE GERSCHGORIN BOUNDS ::::::::::
  100 IF (R .EQ. M) GO TO 1001

      P = Q + 1
      XU = D(P)
      X0 = D(P)
      U = 0.0D0

      DO 120 Q = P, N
         X1 = U
         U = 0.0D0
         V = 0.0D0
         IF (Q .EQ. N) GO TO 110
         U = DABS(E(Q+1))
         V = E2(Q+1)
  110    XU = DMIN1(D(Q)-(X1+U),XU)
         X0 = DMAX1(D(Q)+(X1+U),X0)
         IF (V .EQ. 0.0D0) GO TO 140
  120 CONTINUE

  140 X1 = DMAX1(DABS(XU),DABS(X0)) * MACHEP
      IF (EPS1 .LE. 0.0D0) EPS1 = -X1
      IF (P .NE. Q) GO TO 180
C     :::::::::: CHECK FOR ISOLATED ROOT WITHIN INTERVAL ::::::::::
      IF (T1 .GT. D(P) .OR. D(P) .GE. T2) GO TO 940
      R = R + 1

      DO 160 I = 1, N
  160 Z(I,R) = 0.0D0

      W(R) = D(P)
      Z(P,R) = 1.0D0
      GO TO 940
  180 X1 = X1 * DFLOAT(Q-P+1)
      LB = DMAX1(T1,XU-X1)
      UB = DMIN1(T2,X0+X1)
      X1 = LB
      ISTURM = 3
      GO TO 320
  200 M1 = S + 1
      X1 = UB
      ISTURM = 4
      GO TO 320
  220 M2 = S
      IF (M1 .GT. M2) GO TO 940
C     :::::::::: FIND ROOTS BY BISECTION ::::::::::
      X0 = UB
      ISTURM = 5

      DO 240 I = M1, M2
         RV5(I) = UB
         RV4(I) = LB
  240 CONTINUE
C     :::::::::: LOOP FOR K-TH EIGENVALUE
C                FOR K=M2 STEP -1 UNTIL M1 DO --
C                (-DO- NOT USED TO LEGALIZE COMPUTED-GO-TO) ::::::::::
      K = M2
  250    XU = LB
C     :::::::::: FOR I=K STEP -1 UNTIL M1 DO -- ::::::::::
         DO 260 II = M1, K
            I = M1 + K - II
            IF (XU .GE. RV4(I)) GO TO 260
            XU = RV4(I)
            GO TO 280
  260    CONTINUE

  280    IF (X0 .GT. RV5(K)) X0 = RV5(K)
C     :::::::::: NEXT BISECTION STEP ::::::::::
  300    X1 = (XU + X0) * 0.5D0
         IF ((X0 - XU) .LE. (2.0D0 * MACHEP *
     X      (DABS(XU) + DABS(X0)) + DABS(EPS1))) GO TO 420
```

```
      :::::::::: IN-LINE PROCEDURE FOR STURM SEQUENCE ::::::::::
  320 S = P - 1
      U = 1.0D0

      DO 340 I = P, Q
         IF (U .NE. 0.0D0) GO TO 325
         V = DABS(E(I)) / MACHEP
         GO TO 330
  325    V = E2(I) / U
  330    U = D(I) - X1 - V
         IF (U .LT. 0.0D0) S = S + 1
  340 CONTINUE

      GO TO (60,80,200,220,360), ISTURM
      :::::::::: REFINE INTERVALS ::::::::::
  360 IF (S .GE. K) GO TO 400
      XU = X1
      IF (S .GE. M1) GO TO 380
      RV4(M1) = X1
      GO TO 300
  380 RV4(S+1) = X1
      IF (RV5(S) .GT. X1) RV5(S) = X1
      GO TO 300
  400 X0 = X1
      GO TO 300
      :::::::::: K-TH EIGENVALUE FOUND ::::::::::
  420 RV5(K) = X1
      K = K - 1
      IF (K .GE. M1) GO TO 250
      :::::::::: FIND VECTORS BY INVERSE ITERATION ::::::::::
      NORM = DABS(D(P))
      IP = P + 1

      DO 500 I = IP, Q
  500 NORM = NORM + DABS(D(I)) + DABS(E(I))
      :::::::::: EPS2 IS THE CRITERION FOR GROUPING,
                 EPS3 REPLACES ZERO PIVOTS AND EQUAL
                 ROOTS ARE MODIFIED BY EPS3,
                 EPS4 IS TAKEN VERY SMALL TO AVOID OVERFLOW ::::::::::
      EPS2 = 1.0D-3 * NORM
      EPS3 = MACHEP * NORM
      UK = DFLOAT(Q-P+1)
      EPS4 = UK * EPS3
      UK = EPS4 / DSQRT(UK)
      GROUP = 0
      S = P

      DO 920 K = M1, M2
         R = R + 1
         ITS = 1
         W(R) = RV5(K)
         X1 = RV5(K)
      :::::::::: LOOK FOR CLOSE OR COINCIDENT ROOTS ::::::::::
         IF (K .EQ. M1) GO TO 520
         IF (X1 - X0 .GE. EPS2) GROUP = -1
         GROUP = GROUP + 1
         IF (X1 .LE. X0) X1 = X0 + EPS3
      :::::::::: ELIMINATION WITH INTERCHANGES AND
                 INITIALIZATION OF VECTOR ::::::::::
  520    V = 0.0D0

         DO 580 I = P, Q
            RV6(I) = UK
            IF (I .EQ. P) GO TO 560
            IF (DABS(E(I)) .LT. DABS(U)) GO TO 540
            XU = U / E(I)
            RV4(I) = XU
            RV1(I-1) = E(I)
            RV2(I-1) = D(I) - X1
```

```
         RV3(I-1) = 0.0D0
         IF (I .NE. Q) RV3(I-1) = E(I+1)
         U = V - XU * RV2(I-1)
         V = -XU * RV3(I-1)
         GO TO 580
  540    XU = E(I) / U
         RV4(I) = XU
         RV1(I-1) = U
         RV2(I-1) = V
         RV3(I-1) = 0.0D0
  560    U = D(I) - X1 - XU * V
         IF (I .NE. Q) V = E(I+1)
  580 CONTINUE

      IF (U .EQ. 0.0D0) U = EPS3
      RV1(Q) = U
      RV2(Q) = 0.0D0
      RV3(Q) = 0.0D0
C     :::::::::: BACK SUBSTITUTION
C                FOR I=Q STEP -1 UNTIL P DO -- ::::::::::
  600 DO 620 II = P, Q
         I = P + Q - II
         RV6(I) = (RV6(I) - U * RV2(I) - V * RV3(I)) / RV1(I)

         V = U
         U = RV6(I)
  620 CONTINUE
C     :::::::::: ORTHOGONALIZE WITH RESPECT TO PREVIOUS
C                MEMBERS OF GROUP ::::::::::
      IF (GROUP .EQ. 0) GO TO 700

      DO 680 JJ = 1, GROUP
         J = R - GROUP - 1 + JJ
         XU = 0.0D0

         DO 640 I = P, Q
  640    XU = XU + RV6(I) * Z(I,J)

         DO 660 I = P, Q
  660    RV6(I) = RV6(I) - XU * Z(I,J)

  680 CONTINUE

  700 NORM = 0.0D0

      DO 720 I = P, Q
  720 NORM = NORM + DABS(RV6(I))

      IF (NORM .GE. 1.0D0) GO TO 840
C     :::::::::: FORWARD SUBSTITUTION ::::::::::
      IF (ITS .EQ. 5) GO TO 960
      IF (NORM .NE. 0.0D0) GO TO 740
      RV6(S) = EPS4
      S = S + 1
      IF (S .GT. Q) S = P
      GO TO 780
  740 XU = EPS4 / NORM

      DO 760 I = P, Q
  760 RV6(I) = RV6(I) * XU
C     :::::::::: ELIMINATION OPERATIONS ON NEXT VECTOR
C                ITERATE ::::::::::
  780 DO 820 I = IP, Q
         U = RV6(I)
C     :::::::::: IF RV1(I-1) .EQ. E(I), A ROW INTERCHANGE
C                WAS PERFORMED EARLIER IN THE
C                TRIANGULARIZATION PROCESS ::::::::::
         IF (RV1(I-1) .NE. E(I)) GO TO 800
         U = RV6(I-1)
```

```
         RV6(I-1) = RV6(I)
800      RV6(I) = U - RV4(I) * RV6(I-1)
820   CONTINUE

      ITS = ITS + 1
      GO TO 600
C  :::::::::: NORMALIZE SO THAT SUM OF SQUARES IS
C             1 AND EXPAND TO FULL ORDER ::::::::::
840   U = 0.0D0

      DO 860 I = P, Q
860   U = U + RV6(I)**2

      XU = 1.0D0 / DSQRT(U)

      DO 880 I = 1, N
880   Z(I,R) = 0.0D0

      DO 900 I = P, Q
900   Z(I,R) = RV6(I) * XU

      X0 = X1
920 CONTINUE

940 IF (Q .LT. N) GO TO 100
    GO TO 1001
C   :::::::::: SET ERROR -- NON-CONVERGED EIGENVECTOR ::::::::::
960 IERR = 4 * N + R
    GO TO 1001
C   :::::::::: SET ERROR -- UNDERESTIMATE OF NUMBER OF
C              EIGENVALUES IN INTERVAL ::::::::::
980 IERR = 3 * N + 1
1001 LB = T1
    UB = T2
    RETURN

C   :::::::::: LAST CARD OF TSTURM ::::::::::
    END
C********************** END OF TSTURM *****************
      SUBROUTINE FLOPRO(N2,N)
      REAL*8 MACH(2049)
      COMMON MACH
      WRITE(6,2)
    2 FORMAT(' ONE-SEVENTH POWER PROFILE, MAXIMUM M=0.3'/)
      DO 1 I=1,N2
    1 MACH(I)=0.3D0*(1.D0-(I-1.D0)/(2*N))**(1.D0/7.D0)
      RETURN
      END
      SUBROUTINE OUTPUT(N1,N3)
      REAL*8 MACH(2049),R(1025),FI1(1025),FI2(1025),FI3(1025),FI4(1025),
     $FI5(1025),PFI1(1025),PFI2(1025),PFI3(1025)
      REAL*8 F1,F2,F3,F4,F5,K
      COMMON MACH,R,FI1,FI2,FI3,FI4,FI5,PFI1,PFI2,PFI3,K
      WRITE(6,9)
    9 FORMAT(' RADIUS',6X,'EIGENVECTOR',9X,'MOHRING/BLOCKHINTSEV FLUX'
     $,' TERMS            PHYSICAL FLUX TERMS',/,29X,'PRODUCTS     M',
     $'OHRING SHEAR  BLOCKH.ADD.',6X,'PRODUCTS         SHEAR')
      L=-1
      DO 190 I=1,N1,N3
      L=L+1
      RAD=L/32.0
      F1=FI1(I)+FI2(I)
      F2=FI3(I)
      F3=FI4(I)+FI5(I)
      F4=PFI1(I)+PFI2(I)
      F5=PFI3(I)+FI5(I)/2.D0
  190 WRITE(6,11) RAD,R(I),F1,F2,F3,F4,F5
   11 FORMAT(' ',F7.5,3X,D12.4,3X,D12.4,3X,D12.4,3X,D12.4,3X,
     $D12.4,3X,D12.4)
      RETURN
      END
```

Sample Output of Program MODE

```
(0,0) MODE     GAMMA= 0.5000D+01     512 INTERVALS
LB= 0.7200D+00     UB= 0.8100D+00     W= 0.8000D+00

LAMINAR FLOW PROFILE, MAXIMUM M=0.3

IERR=  0     K2=  0.7629D+00
IERR=  0     K2=  0.7629D+00

    K= -0.8734D+00

INT(1)=  0.9768D-01  0.0 %UNCER  6 STEPS.     PINT(1)=  0.8243D-01  0.0 %UNCER  6 STEPS.
INT(2)=  0.7624D+00  0.0 %UNCER  6 STEPS.     PINT(2)=  0.6736D+00  0.0 %UNCER  6 STEPS.
INT(3)=  0.1274D-01  0.0 %UNCER  6 STEPS.     PINT(3)=  0.1596D-01  0.0 %UNCER  6 STEPS.
INT(4)= -0.2438D-04  0.0 %UNCER  6 STEPS.     PINT(4)=  0.1219D-04  0.0 %UNCER  6 STEPS.
INT(5)=  0.2438D-04  0.0 %UNCER  6 STEPS.

BLOCKHINTSEV ENERGY WEIGHTING FUNCTION =  0.8728D+00     0.0 % UNCERTAINTY
  MOHRING ENERGY WEIGHTING FUNCTION    =  0.8728D+00     0.0 % UNCERTAINTY
 PHYSICAL ENERGY WEIGHTING FUNCTION    =  0.7720D+00    -0.0 % UNCERTAINTY
```

RADIUS	EIGENVECTOR	MOHRING/BLOCKHINTSEV FLUX TERMS			PHYSICAL FLUX TERMS	
		PRODUCTS	MOHRING SHEAR	BLOCKH. ADD.	PRODUCTS	SHEAR
0.0	0.5118D+00	0.5266D+00	0.0	0.0	0.3886D+00	0.0
0.03125	0.5125D+00	0.5276D+00	0.5649D-04	-0.1105D-05	0.3895D+00	0.5710D-04
0.06250	0.5145D+00	0.5305D+00	0.2260D-03	-0.4358D-05	0.3920D+00	0.2287D-03
0.09375	0.5179D+00	0.5353D+00	0.5087D-03	-0.9581D-05	0.3963D+00	0.5160D-03
0.12500	0.5227D+00	0.5422D+00	0.9048D-03	-0.1648D-04	0.4023D+00	0.9206D-03
0.15625	0.5289D+00	0.5509D+00	0.1414D-02	-0.2465D-04	0.4101D+00	0.1445D-02
0.18750	0.5364D+00	0.5616D+00	0.2036D-02	-0.3361D-04	0.4196D+00	0.2091D-02
0.21875	0.5453D+00	0.5743D+00	0.2771D-02	-0.4279D-04	0.4310D+00	0.2861D-02
0.25000	0.5556D+00	0.5889D+00	0.3615D-02	-0.5158D-04	0.4442D+00	0.3758D-02
0.28125	0.5673D+00	0.6055D+00	0.4566D-02	-0.5934D-04	0.4594D+00	0.4782D-02
0.31250	0.5803D+00	0.6239D+00	0.5619D-02	-0.6544D-04	0.4764D+00	0.5933D-02
0.34375	0.5947D+00	0.6441D+00	0.6767D-02	-0.6931D-04	0.4953D+00	0.7210D-02
0.37500	0.6104D+00	0.6661D+00	0.7999D-02	-0.7047D-04	0.5161D+00	0.8606D-02
0.40625	0.6275D+00	0.6897D+00	0.9301D-02	-0.6856D-04	0.5388D+00	0.1011D-01
0.43750	0.6458D+00	0.7148D+00	0.1066D-01	-0.6341D-04	0.5634D+00	0.1172D-01
0.46875	0.6654D+00	0.7412D+00	0.1205D-01	-0.5508D-04	0.5897D+00	0.1341D-01
0.50000	0.6861D+00	0.7686D+00	0.1344D-01	-0.4384D-04	0.6176D+00	0.1515D-01
0.53125	0.7078D+00	0.7967D+00	0.1480D-01	-0.3024D-04	0.6469D+00	0.1692D-01
0.56250	0.7306D+00	0.8252D+00	0.1610D-01	-0.1507D-04	0.6774D+00	0.1867D-01
0.59375	0.7541D+00	0.8535D+00	0.1729D-01	0.6521D-06	0.7087D+00	0.2035D-01
0.62500	0.7783D+00	0.8811D+00	0.1833D-01	0.1579D-04	0.7404D+00	0.2190D-01
0.65625	0.8030D+00	0.9074D+00	0.1915D-01	0.2911D-04	0.7720D+00	0.2325D-01
0.68750	0.8278D+00	0.9317D+00	0.1970D-01	0.3950D-04	0.8029D+00	0.2432D-01
0.71875	0.8526D+00	0.9532D+00	0.1993D-01	0.4602D-04	0.8324D+00	0.2503D-01
0.75000	0.8770D+00	0.9710D+00	0.1977D-01	0.4812D-04	0.8597D+00	0.2527D-01
0.78125	0.9006D+00	0.9842D+00	0.1916D-01	0.4574D-04	0.8837D+00	0.2495D-01
0.81250	0.9229D+00	0.9919D+00	0.1806D-01	0.3944D-04	0.9036D+00	0.2396D-01
0.84375	0.9436D+00	0.9931D+00	0.1642D-01	0.3037D-04	0.9181D+00	0.2220D-01
0.87500	0.9620D+00	0.9868D+00	0.1421D-01	0.2020D-04	0.9262D+00	0.1960D-01
0.90625	0.9775D+00	0.9723D+00	0.1144D-01	0.1084D-04	0.9268D+00	0.1610D-01
0.93750	0.9895D+00	0.9489D+00	0.8105D-02	0.4011D-05	0.9168D+00	0.1165D-01
0.96875	0.9972D+00	0.9160D+00	0.4267D-02	0.6148D-06	0.9012D+00	0.6263D-02
1.00000	0.1000D+01	0.8734D+00	0.0	0.0	0.8734D+00	0.0

A10.2. Program INTGRTE

The computer program INTGRTE was used to verify the orthogonality properties derived from the results of Möhring and from the physical energy equation (the integrals in Eqns. (4-30) and (4-34b)). The Blockhintsev cross-mode energy-weighting function (i.e., the integral in Eqn. (4-33b)) was also calculated.

The program uses a Romberg integration scheme similar to that employed in MODE. To facilitate the calculation, each orthogonality property was broken up into several integrals. After evaluation of the individual integrals, the results were then summed.

The Möhring orthogonality expression is broken up into the following integrals.

$$\mathrm{INT}(1) = \int_0^1 \frac{2MR_{mn}R_{me}}{K_{mn}K_{me}}\, 2rdr$$

$$\mathrm{INT}(2) = \int_0^1 \frac{(k_{mn} + k_{me})(1 - M^2)\; R_{mn}R_{me}}{K_{mn}K_{me}}\, 2rdr$$

$$\mathrm{INT}(3) = -\int_0^1 \frac{\frac{dM}{dr} R_{mn} \frac{dR_{me}}{dr}}{\gamma^2 K_{mn}^2 K_{me}^2}\, 2rdr$$

$$\mathrm{INT}(4) = -\int_0^1 \frac{\frac{dM}{dr} R_{me} \frac{dR_{mn}}{dr}}{\gamma^2 K_{mn}^2 K_{me}^2}\, 2rdr$$

The Blockhintsev cross-mode energy-weighting function is broken up into the following integrals.

$$\mathrm{INT}(1) = \int_0^1 \frac{2MR_{mn}R_{me}}{K_{mn}K_{me}}\, 2rdr$$

$$\mathrm{INT}(2) = \int_0^1 \frac{(k_{mn} + k_{me})(1 - M^2)\; R_{mn}R_{me}}{K_{mn}K_{me}}\, 2rdr$$

$$\mathrm{INT}(3) = -\int_0^1 \frac{\frac{dM}{dr} R_{mn} \frac{dR_{me}}{dr}}{\gamma^2 K_{mn}^2 K_{me}^2} \left[1 + M^2 \left(K_{mn}^2 - k_{mn}^2\right) \right] 2rdr$$

$$\mathrm{INT}(4) = -\int_0^1 \frac{\frac{dM}{d\bar{r}} R_{mc} \frac{dR_{mn}}{d\bar{r}}}{\gamma^2 K_{mn}^2 K_{mc}^2} \left[1 + M^2\left(K_{mc}^2 - \bar{k}_{mc}^2\right)\right] 2\bar{r}d\bar{r}$$

$$\mathrm{INT}(5) = \int_0^1 \frac{2M\left(\frac{dM}{d\bar{r}}\right)^2 \frac{dR_{mn}}{d\bar{r}} \frac{dR_{mc}}{d\bar{r}}}{\gamma^4 K_{mn}^2 K_{mc}^2} 2\bar{r}d\bar{r}$$

The orthogonality expression derived from the physical energy equation was broken up into the following integrals.

$$\mathrm{INT}(1) = \int_0^1 \frac{M[(K_{mn} + K_{mc})^2 - (\bar{k}_{mn} - \bar{k}_{mc})^2]}{2K_{mn}K_{mc}} 2\bar{r}d\bar{r}$$

$$\mathrm{INT}(2) = \int_0^1 \left(\frac{\bar{k}_{mn}}{K_{mn}} + \frac{\bar{k}_{mc}}{K_{mc}}\right) R_{mn}R_{mc}\ 2\bar{r}d\bar{r}$$

$$\mathrm{INT}(3) = \int_1^1 \left(\frac{\bar{k}_{mc}}{(\bar{k}_{mn} - \bar{k}_{mc})} - \frac{(1 - 2\bar{k}_{mc}M + \bar{k}_{mc}\bar{k}_{mn}M^2)}{2K_{mn}^2}\right) \frac{R_{mn} \frac{dR_{mc}}{d\bar{r}} \frac{dM}{d\bar{r}}}{\gamma^2 K_{mc}^2} 2\bar{r}d\bar{r}$$

$$\mathrm{INT}(4) = \int_0^1 \left(\frac{\bar{k}_{mn}}{(\bar{k}_{mc} - \bar{k}_{mn})} - \frac{(1 - 2\bar{k}_{mn}M + \bar{k}_{mn}\bar{k}_{mc}M^2)}{2K_{mc}^2}\right) \frac{R_{mc} \frac{dR_{mn}}{d\bar{r}} \frac{dM}{d\bar{r}}}{\gamma^2 K_{mn}^2} 2\bar{r}d\bar{r}$$

The input data to the program INTGRTE consists of one line, which sets the overall parameters for the program, followed by the two sets of eigenvalues and eigenfunctions. Before using INTGRTE, the eigenvalues and eigenfunctions must be calculated using MODE. The subroutine OUTPUT of MODE must be modified to list out the eigenvalue and eigenfunction in formats compatible with FORMAT statements 1 and 2 in INTGRTE.

The input parameters in the first line of data are explained in the following list.

a) NN is an integer which is less than or equal to 10. It should be set to the same value as used in MODE when calculating the eigenfunctions.

b) MMODE1 is an integer which can range from 0 to 9 and gives the circumferential mode number of the first eigenfunction.

c) NMODE1 is an integer which can range from 0 to 9 and gives the radial mode number of the first eigenfunction.

d) MMODE2 is an integer which can range from 0 to 9 and gives the circumferential mode number of the second eigenfunction.

e) NMODE2 is an integer which can range from 0 to 9 and gives the radial mode number of the second eigenfunction.

f) G is a REAL*8 number which gives the value of the reduced frequency, γ.

Sample output from INTGRTE is shown following the program listing. The results from the Möhring, Blockhintsev and Physical energy flux are each listed separately. The values of the integrals are first printed out. Below this, the values of the eigenfunctions and the integrands (excluding the factor $2\bar{r}$) across the duct radius are listed in column form.

A listing of the program INTGRTE and sample output follows.

Listing of Program INTGRTE

```
      REAL *8 K1,K2,G,SUM,INTSUM
      REAL*8 R1(1025),R2(1025),KM1(2049),KM2(2049),MACH(2049),
     $CF1(1025),CF2(1025),CF3(1025),CF4(1025),T(5),T1(11),T2(11),
     $INT(5),PERCNT(5),DELINT(5),CF5(1025)
      REAL*8 DABS
      COMMON MACH,R1,R2,CF1,CF2,CF3,CF4,CF5

      READ(5,3)NN,MMODE1,NMODE1,MMODE2,NMODE2,G
    3 FORMAT(I2,I4,3I1,D23.16)
      READ(5,1)K1
    1 FORMAT(D23.16)
      N=2**NN
      N1=N+1
      N2=2*N+1
      N3=2*N
      N8=N/32
      READ(5,2) (R1(I), I=1,N1)
    2 FORMAT(3D23.16)
      READ(5,1)K2
      READ(5,2) (R2(I), I=1,N1)

      DO 10 I=1,N2
   10 MACH(I) = 0.3D0*(1.D0-((I-1.D0)/N3)**2)
      DO 20 I=1,N2
      KM1(I)=1.D0 - K1*MACH(I)
   20 KM2(I) = 1.D0 - K2*MACH(I)

      I9=1
   22 WRITE(6,23)MMODE1,NMODE1,MMODE2,NMODE2,G,N,K1,K2
   23 FORMAT('1',15X,'CROSS MODE INTEGRATION',//,'    (',I1,',',I1,')',
     $' AND (',I1,',',I1,') MODES',5X,'GAMMA= ',D11.4,4X,I3,' INTERVALS',
     $/,'    K1=',D15.6,5X,'K2=',D15.6,/)
      WRITE(6,24)
   24 FORMAT('    LAMINAR FLOW PROFILE, MMAX=0.3',/)

      GO TO (101,301,201),I9

C     PERFORM INTEGRATIONS USING ROMBERG SCHEME. CF1(I),CF2(I),CF3(I)
C     CF4(I) AND CF5(I) ARE VALUES OF THE INTEGRANDS EXCLUDING THE
C     (2*RAD) TERM. T(JJ) ARE INITIAL ESTIMATES IN THE INTEGRATION SCHEME.

C     MOHRING FLUX TERMS

  101 WRITE(6,26)
   26 FORMAT('    MOHRING FLUX TERMS.',//)

      DO 30 I=1,N1
      CF1(I)=0.D0
      CF2(I)=0.D0
      CF3(I)=0.D0
   30 CF4(I)=0.D0

      CF1(1) = 2.D0*MACH(1)*R1(1)*R2(1)/(KM1(1)*KM2(1))
      CF1(N1) = 2.D0*MACH(N2)*R1(N1)*R2(N1)/(KM1(N2)*KM2(N2))
      CF2(1) = (K1+K2)*(1.D0-MACH(1)**2)*R1(1)*R2(1)/(KM1(1)*KM2(1))
      CF2(N1) = (K1+K2)*(1.D0-MACH(N2)**2)*R1(N1)*R2(N1)/(KM1(N2)
     $*KM2(N2))
C     CF3 AND CF4 ARE IDENTICALLY ZERO AT THE END POINTS BY
C     VIRTUE OF THE BOUNDARY CONDITIONS.
```

```
      T(1) = CF1(N1)
      T(2) = CF2(N1)
      T(3) = 0.D0
      T(4) = 0.D0
      DO 130 JJ =1,4
      T2(1) = T(JJ)
      N4 = 1
180   DO 140 I=1,N4
140   T1(I) = T2(I)
      N4 = N4+ 1
      N5 = 2**(N4-1)
      N6 = N/N5
      N7 = 2*N6
      SUM = 0.D0
      GO TO (131,132,133,134),JJ
131   DO 141 I=1,N5,2
      CF1(I*N6+1) = 2.D0*MACH(I*N7+1)*R1(I*N6+1)*R2(I*N6+1)/(KM1
     $(I*N7+1)*KM2(I*N7+1))
141   SUM=SUM + I*CF1(I*N6 + 1)
      GO TO 150

132   DO 142 I=1,N5,2
      CF2(I*N6+1) = (K1+K2)*(1.D0-MACH(I*N7+1)**2)*R1(I*N6+1)*
     $R2(I*N6+1)/(KM1(I*N7+1)*KM2(I*N7+1))
142   SUM = SUM+I*CF2(I*N6 + 1)
      GO TO 150
133   DO 143 I=1,N5,2
      CF3(I*N6+1) = -0.5D0*N*N*(MACH(I*N7+2)- MACH(I*N7))*
     $R1(I*N6+1)*(R2(I*N6+2)-R2(I*N6))/(G*KM1(I*N7+1)*
     $KM2(I*N7+1))**2
143   SUM = SUM + I*CF3(I*N6+1)
      GO TO 150
134   DO 144 I=1,N5,2
      CF4(I*N6+1) = -0.5D0*N*N*(MACH(I*N7+2)- MACH(I*N7))*
     $R2(I*N6+1)*(R1(I*N6+2)-R1(I*N6))/(G*KM1(I*N7+1)*
     $KM2(I*N7+1))**2
144   SUM=SUM+I*CF4(I*N6+1)
      **** THE CONSTANT PART OF (2*RAD), (2.D0/N5), OMITTED FROM
      **** SUM IS INCLUDED IN THE EXPRESSION FOR T2(1).

150   T2(1)=T1(1)/2.D0+SUM*2.D0/N5**2
      DO 160 I=2,N4
160   T2(I)=(4.D0**(I-1.D0)*T2(I-1)-T1(I-1))/(4.D0**(I-1.D0)-1.D0)
      IF(N4.LT.6) GO TO 180
      INT(JJ)=T2(N4)
      DELINT(JJ)=DABS(INT(JJ)-T1(N4-1))
      IF(DELINT(JJ).LE.5.D-4*DABS(INT(JJ))) GO TO 170
      IF(N4.LT.NN+1) GO TO 180
170   PERCNT(JJ)=0.0
      IF(N4.GT.2) PERCNT(JJ)=100.*DELINT(JJ)/DABS(INT(JJ))
      WRITE(6,6) JJ,INT(JJ),PERCNT(JJ),N4
    6 FORMAT(' INT(',I1,') =',D12.4,6X,F5.2,' PER CENT'
     $,' UNCERTAINTY',6X,I2,' ROMBERG INTEGRATION STEPS')
130   CONTINUE
      INTSUM=0.D0
      DO 185 I=1,4
185   INTSUM=INTSUM+INT(I)
      WRITE(6,188) INTSUM
188   FORMAT(' INT SUM=',D13.5,//)
      CALL OUTPUT(N1,N8,I9)
      I9=I9+1
      WRITE(6,189)
189   FORMAT(////////)
      GO TO 22

      BLOCKHINTSEV FLUX TERMS

301   WRITE(6,326)
326   FORMAT('    BLOCKHINTSEV FLUX TERMS.',//)
```

ORIGINAL PAGE IS
OF POOR QUALITY

```
      DO 329 I=1,N1
      CF1(I)=0.D0
      CF2(I)=0.D0
      CF3(I)=0.D0
      CF4(I)=0.D0
  329 CF5(I)=0.D0

      CF1(1) = 2.D0*MACH(1)*R1(1)*R2(1)/(KM1(1)*KM2(1))
      CF1(N1) = 2.D0*MACH(N2)*R1(N1)*R2(N1)/(KM1(N2)*KM2(N2))
      CF2(1) = (K1+K2)*(1.D0-MACH(1)**2)*R1(1)*R2(1)/(KM1(1)*KM2(1))
      CF2(N1) = (K1+K2)*(1.D0-MACH(N2)**2)*R1(N1)*R2(N1)/(KM1(N2)
     $*KM2(N2))
C    CF3,CF4 AND CF5 ARE IDENTICALLY ZERO AT THE END POINTS BY
C    VIRTUE OF THE BOUNDARY CONDITIONS.
      T(1) = CF1(N1)
      T(2) = CF2(N1)
      T(3) = 0.D0
      T(4) = 0.D0
      T(5)=0.D0
      DO 330 JJ =1,5
      T2(1) = T(JJ)
      N4 = 1
  380 DO 340 I=1,N4
  340 T1(I) = T2(I)
      N4 = N4+ 1
      N5 = 2**(N4-1)
      N6 = N/N5
      N7 = 2*N6
      SUM = 0.D0
      GO TO (331,332,333,334,335),JJ

  331 DO 341 I=1,N5,2
      CF1(I*N6+1) = 2.D0*MACH(I*N7+1)*R1(I*N6+1)*R2(I*N6+1)/(KM1
     $(I*N7+1)*KM2(I*N7+1))
  341 SUM=SUM + I*CF1(I*N6 + 1)
      GO TO 350
  332 DO 342 I=1,N5,2
      CF2(I*N6+1) = (K1+K2)*(1.D0-MACH(I*N7+1)**2)*R1(I*N6+1)*
     $R2(I*N6+1)/(KM1(I*N7+1)*KM2(I*N7+1))
  342 SUM = SUM+I*CF2(I*N6 + 1)
      GO TO 350
  333 DO 343 I=1,N5,2
      CF3(I*N6+1) = -0.5D0*N*N*(MACH(I*N7+2)- MACH(I*N7))*
     $R1(I*N6+1)*(R2(I*N6+2)-R2(I*N6))/(G*KM1(I*N7+1)*
     $KM2(I*N7+1))**2*(1.D0+(MACH(I*N7+1)**2)*(KM1(I*N7+1)**2-K1*K1))
  343 SUM = SUM + I*CF3(I*N6+1)
      GO TO 350
  334 DO 344 I=1,N5,2
      CF4(I*N6+1) = -0.5D0*N*N*(MACH(I*N7+2)- MACH(I*N7))*
     $R2(I*N6+1)*(R1(I*N6+2)-R1(I*N6))/(G*KM1(I*N7+1)*
     $KM2(I*N7+1))**2*(1.D0+(MACH(I*N7+1)**2)*(KM2(I*N7+1)**2-K2*K2))
  344 SUM=SUM+I*CF4(I*N6+1)
      GO TO 350
  335 DO 345 I=1,N5,2
      CF5(I*N6+1)=MACH(I*N7+1)*0.5D0*N*N*N*N*DABS(MACH(I*N7+2)-MACH
     $(I*N7))**2*(R1(I*N6+2)-R1(I*N6))*(R2(I*N6+2)-R2(I*N6))/
     $(G*G*KM1(I*N7+1)*KM2(I*N7+1))**2
  345 SUM=SUM+I*CF5(I*N6+1)
C     **** THE CONSTANT PART OF (2*RAD), (2.D0/N5), OMITTED FROM
C     **** SUM IS INCLUDED IN THE EXPRESSION FOR T2(1)

  350 T2(1)=T1(1)/2.D0+SUM*2.D0/N5**2
      DO 360 I=2,N4
  360 T2(I)=(4.D0**(I-1.D0)*T2(I-1)-T1(I-1))/(4.D0**(I-1.D0)-1.D0)
      IF(N4.LT.6) GO TO 380
      INT(JJ)=T2(N4)
      DELINT(JJ)=DABS(INT(JJ)-T1(N4-1))
      IF(DELINT(JJ).LE.5.D-4*DABS(INT(JJ))) GO TO 370
      IF(N4.LT.NN+1) GO TO 380
```

```
370 PERCNT(JJ)=0.0
    IF(N4.GT.2) PERCNT(JJ)=100.*DELINT(JJ)/DABS(INT(JJ))
    WRITE(6,306) JJ,INT(JJ),PERCNT(JJ),N4
306 FORMAT(' INT(',I1,') =',D12.4,6X,F5.2,' PER CENT'
   $,' UNCERTAINTY',6X,I2,' ROMBERG INTEGRATION STEPS')
330 CONTINUE
    INTSUM=0.D0
    DO 385 I=1,5
385 INTSUM=INTSUM+INT(I)
    WRITE(6,388) INTSUM
388 FORMAT(' INT SUM=',D13.5,//)

    CALL OUTPUT(N1,N8,I9)
    I9=I9+1
    WRITE(6,389)
389 FORMAT(/////////)
    GO TO 22

 PHYSICAL FLUX TERMS

201 WRITE(6,226)
226 FORMAT('    PHYSICAL FLUX TERMS.',//)

    DO 229 I=1,N1
    CF1(I)=0.D0
    CF2(I)=0.D0
    CF3(I)=0.D0
229 CF4(I)=0.D0

    CF1(1) = MACH(1)*((KM1(1)+KM2(1))**2-(DABS(K1-K2))
   $**2)*R1(1)*R2(1)/(2.D0*KM1(1)*KM2(1) )
    CF1(N1) = MACH(N2)*((KM1(N2)+KM2(N2))**2-(DABS(K1-K2))**2)*
   $R1(N1)*R2(N1)/(2.D0*KM1(N2)*KM2(N2)  )
    CF2(1) = (K1/KM1(1) + K2/KM2(1))*R1(1)*R2(1)
    CF2(N1) = (K1/KM1(N2) + K2/KM2(N2))*R1(N1)*R2(N1)
  CF3 AND CF4 ARE IDENTICALLY ZERO AT THE END POINTS BY
  VIRTUE OF THE BOUNDARY CONDITIONS.
    T(1) = CF1(N1)
    T(2) = CF2(N1)
    T(3) = 0.D0
    T(4) = 0.D0
    DO 230 JJ =1,4

     T2(1) = T(JJ)
     N4 = 1
 280 DO 240 I=1,N4
 240 T1(I) = T2(I)
     N4 = N4+ 1
     N5 = 2**(N4-1)
     N6 = N/N5
     N7 = 2*N6
     SUM = 0.D0
     GO TO (231,232,233,234),JJ
 231 DO 241 I=1,N5,2
     CF1(I*N6+1) = MACH(I*N7+1)*((KM1(I*N7+1)+KM2(I*N7+1))**2
    $-(DABS(K1-K2))**2)*R1(I*N6+1)*R2(I*N6+1)/(2.D0*KM1(I*N7+1)
    $*KM2(I*N7+1))
 241 SUM=SUM + I*CF1(I*N6 + 1)
     GO TO 250
 232 DO 242 I=1,N5,2
     CF2(I*N6+1) = (K1/KM1(I*N7+1) + K2/KM2(I*N7+1))*R1(I*N6+1)
    $*R2(I*N6+1)
 242 SUM = SUM+I*CF2(I*N6 + 1)
     GO TO 250
 233 DO 243 I=1,N5,2
     CF3(I*N6+1) = (K2/(K1-K2)-(1.D0-2.D0*K2*MACH(I*N7+1) +
    $K1*K2*MACH(I*N7+1)**2)/(2.D0*KM1(I*N7+1)**2))*R1(I*N6+1)
    $*(R2(I*N6+2)-R2(I*N6))*(MACH(I*N7+2)-MACH(I*N7))*0.5D0*N*N
    $/(G*KM2(I*N7+1))**2
 243 SUM = SUM + I*CF3(I*N6+1)
     GO TO 250
```

```
234 DO 244 I=1,N5,2
    CF4(I*N6+1) = (K1/(K2-K1)-(1.D0-2.D0*K1*MACH(I*N7+1) +
   $K2*K1*MACH(I*N7+1)**2)/(2.D0*KM2(I*N7+1)**2))*R2(I*N6+1)
   $*(R1(I*N6+2)-R1(I*N6))*(MACH(I*N7+2)-MACH(I*N7))*0.5D0*N*N
   $/(G*KM1(I*N7+1))**2
244 SUM=SUM+I*CF4(I*N6+1)
    **** THE CONSTANT PART OF (2*RAD), (2.D0/N5), OMITTED FROM
    **** SUM IS INCLUDED IN THE EXPRESSION FOR T2(1).

250 T2(1)=T1(1)/2.D0+SUM*2.D0/N5**2
    DO 260 I=2,N4
260 T2(I)=(4.D0**(I-1.D0)*T2(I-1)-T1(I-1))/(4.D0**(I-1.D0)-1.D0)
    IF(N4.LT.6) GO TO 280
    INT(JJ)=T2(N4)
    DELINT(JJ)=DABS(INT(JJ)-T1(N4-1))
    IF(DELINT(JJ).LE.5.D-4*DABS(INT(JJ))) GO TO 270
    IF(N4.LT.NN+1) GO TO 280
270 PERCNT(JJ)=0.0
    IF(N4.GT.2) PERCNT(JJ)=100.*DELINT(JJ)/DABS(INT(JJ))
    WRITE(6,206) JJ,INT(JJ),PERCNT(JJ),N4
206 FORMAT(' INT(',I1,') =',D12.4,6X,F5.2,' PER CENT'
   $,' UNCERTAINTY',6X,I2,' ROMBERG INTEGRATION STEPS')
230 CONTINUE
    INTSUM=0.D0
    DO 285 I=1,4
285 INTSUM=INTSUM+INT(I)
    WRITE(6,288) INTSUM
288 FORMAT(' INT SUM=',D13.5,//)
    CALL OUTPUT(N1,N8,I9)
    WRITE(6,289)
289 FORMAT(//////////)
    STOP
    END
    SUBROUTINE OUTPUT(N1,N3,I9)
    REAL*8 MACH(2049),R1(1025),R2(1025),CF1(1025),CF2(1025),
   $CF3(1025),CF4(1025),CF5(1025)
    COMMON MACH,R1,R2,CF1,CF2,CF3,CF4,CF5
    WRITE(6,9)
  9 FORMAT(' RADIUS',12X,'EIGENVECTORS',13X,'CF1',12X,'CF2',12X,'CF3',
   $12X,'CF4',12X,'CF5'/)
    L=-1
    DO 30 I=1,N1,N3
    L=L+1
    RAD=L/32.0
    IF(I9.EQ.2) GO TO 200
190 WRITE(6,11) RAD,R1(I),R2(I),CF1(I),CF2(I),CF3(I),CF4(I)
 11 FORMAT(' ',F7.5,3X,D12.4,3X,D12.4,3X,D12.4,3X,D12.4,3X,D12.4,3X,
   $D12.4)
    GO TO 30
200 WRITE(6,12) RAD,R1(I),R2(I),CF1(I),CF2(I),CF3(I),CF4(I),
   $CF5(I)
 12 FORMAT(' ',F7.5,3X,D12.4,3X,D12.4,3X,D12.4,3X,D12.4,3X,D12.4,3X,

   $D12.4,3X,D12.4)
 30 CONTINUE
    RETURN
    END
```

Sample Output of INTGRTE:

Möhring Flux

```
(0,0) AND (0,1) MODES     GAMMA=  0.5000D 01   512 INTERVALS
 K1=   0.873439D 00     K2=   0.479845D 00

 LAMINAR FLOW PROFILE, MMAX=0.3

 MOHRING FLUX TERMS.

INT(1) = -0.1413D 00       0.00 PER CENT UNCERTAINTY       6 ROMBERG INTEGRATION STEPS
INT(2) =  0.7745D-01       0.00 PER CENT UNCERTAINTY       6 ROMBERG INTEGRATION STEPS
INT(3) =  0.6293D-01       0.00 PER CENT UNCERTAINTY       6 ROMBERG INTEGRATION STEPS
INT(4) =  0.9186D-03       0.03 PER CENT UNCERTAINTY       6 ROMBERG INTEGRATION STEPS
INT SUM=  0.44696D-05
```

RADIUS	EIGENVECTORS		CF1	CF2	CF3	CF4
0.00000	0.5118D 00	-0.2272D 01	-0.1104D 01	-0.2267D 01	0.0000D 00	0.0000D 00
0.03125	0.5125D 00	-0.2265D 01	-0.1101D 01	-0.2262D 01	0.4286D-03	-0.1856D-03
0.06250	0.5145D 00	-0.2244D 01	-0.1090D 01	-0.2248D 01	0.1710D-02	-0.7336D-03
0.09375	0.5179D 00	-0.2209D 01	-0.1072D 01	-0.2224D 01	0.3832D-02	-0.1618D-02
0.12500	0.5227D 00	-0.2161D 01	-0.1048D 01	-0.2191D 01	0.6772D-02	-0.2796D-02
0.15625	0.5289D 00	-0.2100D 01	-0.1016D 01	-0.2148D 01	0.1050D-01	-0.4211D-02
0.18750	0.5364D 00	-0.2026D 01	-0.9779D 00	-0.2094D 01	0.1497D-01	-0.5791D-02
0.21875	0.5453D 00	-0.1940D 01	-0.9331D 00	-0.2030D 01	0.2013D-01	-0.7456D-02
0.25000	0.5556D 00	-0.1842D 01	-0.8822D 00	-0.1955D 01	0.2591D-01	-0.9114D-02
0.28125	0.5673D 00	-0.1733D 01	-0.8255D 00	-0.1867D 01	0.3223D-01	-0.1067D-01
0.31250	0.5803D 00	-0.1614D 01	-0.7634D 00	-0.1768D 01	0.3900D-01	-0.1204D-01
0.34375	0.5947D 00	-0.1486D 01	-0.6967D 00	-0.1657D 01	0.4609D-01	-0.1312D-01
0.37500	0.6104D 00	-0.1350D 01	-0.6259D 00	-0.1533D 01	0.5339D-01	-0.1383D-01
0.40625	0.6275D 00	-0.1207D 01	-0.5519D 00	-0.1397D 01	0.6073D-01	-0.1410D-01
0.43750	0.6459D 00	-0.1057D 01	-0.4758D 00	-0.1249D 01	0.6797D-01	-0.1388D-01
0.46875	0.6653D 00	-0.9034D 00	-0.3985D 00	-0.1089D 01	0.7491D-01	-0.1314D-01
0.50000	0.6861D 00	-0.7460D 00	-0.3213D 00	-0.9174D 00	0.8136D-01	-0.1185D-01
0.53125	0.7078D 00	-0.5866D 00	-0.2456D 00	-0.7360D 00	0.8713D-01	-0.1006D-01
0.56250	0.7306D 00	-0.4267D 00	-0.1728D 00	-0.5460D 00	0.9199D-01	-0.7796D-02
0.59375	0.7541D 00	-0.2678D 00	-0.1042D 00	-0.3493D 00	0.9576D-01	-0.5149D-02
0.62500	0.7783D 00	-0.1115D 00	-0.4138D-01	-0.1480D 00	0.9821D-01	-0.2227D-02
0.65625	0.8030D 00	0.4066D-01	0.1428D-01	0.5492D-01	0.9917D-01	0.8330D-03
0.68750	[illegible]	0.1870D 00	0.6150D-01	0.2565D 00	[illegible]	0.5871D-02
0.71875	0.8526D 00	0.3259D 00	0.9918D-01	0.4530D 00	0.9598D-01	0.6712D-02
0.75000	0.8770D 00	0.4558D 00	0.1265D 00	0.6408D 00	0.9161D-01	0.9172D-02
0.78125	0.9006D 00	0.5750D 00	0.1428D 00	0.8155D 00	0.8534D-01	0.1107D-01
0.81250	0.9229D 00	0.6822D 00	0.1482D 00	0.9732D 00	0.7718D-01	0.1224D-01
0.84375	0.9436D 00	0.7758D 00	0.1428D 00	0.1109D 01	0.6725D-01	0.1256D-01
0.87500	0.9620D 00	0.8545D 00	0.1275D 00	0.1220D 01	0.5573D-01	0.1191D-01
0.90625	0.9775D 00	0.9172D 00	0.1035D 00	0.1303D 01	0.4286D-01	0.1027D-01
0.93750	0.9895D 00	0.9629D 00	0.7276D-01	0.1353D 01	0.2900D-01	0.7659D-02
0.96875	0.9972D 00	0.9906D 00	0.3740D-01	0.1371D 01	0.1455D-01	0.4177D-02
1.00000	0.1000D 01	0.1000D 01	0.0000D 00	0.1353D 01	0.0000D 00	0.0000D 00

Sample Output of INTGRTE:

Blockhintsev Flux

CROSS MODE INTEGRATION

(0,0) AND (0,1) MODES GAMMA= 0.5000D 01 512 INTERVALS
K1= 0.873439D 00 K2= 0.479845D 00

LAMINAR FLOW PROFILE, MMAX=0.3

BLOCKHINTSEV FLUX TERMS.

INT(1) =	-0.1413D 00	0.00 PER CENT UNCERTAINTY	6 ROMBERG INTEGRATION STEPS
INT(2) =	0.7745D-01	0.00 PER CENT UNCERTAINTY	6 ROMBERG INTEGRATION STEPS
INT(3) =	0.6277D-01	0.00 PER CENT UNCERTAINTY	6 ROMBERG INTEGRATION STEPS
INT(4) =	0.8237D-03	0.02 PER CENT UNCERTAINTY	6 ROMBERG INTEGRATION STEPS
INT(5) =	0.2540D-03	0.01 PER CENT UNCERTAINTY	6 ROMBERG INTEGRATION STEPS
INT SUM=	0.44735D-05		6 ROMBERG INTEGRATION STEPS

RADIUS	EIGENVECTORS		CF1	CF2	CF3	CF4	CF5
0.00000	0.5118D 00	-0.2272D 01	-0.1104D 01	-0.2267D 01	0.0000D 00	0.0000D 00	0.0000D 00
0.03125	0.5125D 00	-0.2265D 01	-0.1101D 01	-0.2262D 01	0.4202D-03	-0.1940D-03	0.1641D-07
0.06250	0.5145D 00	-0.2244D 01	-0.1090D 01	-0.2248D 01	0.1677D-02	-0.7666D-03	0.2602D-06
0.09375	0.5179D 00	-0.2209D 01	-0.1072D 01	-0.2224D 01	0.3759D-02	-0.1690D-02	0.1298D-05
0.12500	0.5227D 00	-0.2161D 01	-0.1048D 01	-0.2191D 01	0.6647D-02	-0.2920D-02	0.4016D-05
0.15625	0.5289D 00	-0.2100D 01	-0.1016D 01	-0.2148D 01	0.1031D-01	-0.4395D-02	0.9538D-05
0.18750	0.5364D 00	-0.2026D 01	-0.9779D 00	-0.2094D 01	0.1471D-01	-0.6039D-02	0.1912D-04
0.21875	0.5453D 00	-0.1940D 01	-0.9331D 00	-0.2030D 01	0.1980D-01	-0.7769D-02	0.3399D-04
0.25000	0.5556D 00	-0.1842D 01	-0.8822D 00	-0.1955D 01	0.2551D-01	-0.9488D-02	0.5527D-04
0.28125	0.5673D 00	-0.1733D 01	-0.8255D 00	-0.1867D 01	0.3177D-01	-0.1110D-01	0.8374D-04
0.31250	-0.5803D 00	-0.1614D 01	-0.7634D 00	-0.1768D 01	0.3848D-01	-0.1250D-01	0.1198D-03
0.34375	0.5947D 00	-0.1486D 01	-0.6967D 00	-0.1657D 01	0.4554D-01	-0.1361D-01	0.1631D-03
0.37500	0.6104D 00	-0.1350D 01	-0.6259D 00	-0.1533D 01	0.5281D-01	-0.1433D-01	0.2130D-03
0.40625	0.6275D 00	-0.1207D 01	-0.5519D 00	-0.1397D 01	0.6015D-01	-0.1459D-01	0.2677D-03
0.43750	0.6458D 00	-0.1057D 01	-0.4758D 00	-0.1249D 01	0.6740D-01	-0.1433D-01	0.3251D-03
0.46875	0.6653D 00	-0.9034D 00	-0.3985D 00	-0.108[illegible]D 01	0.7437D-01	-0.1354D-01	0.3822D-03
0.50000	0.6851D 00	-0.7460D 00	-0.3213D 00	-0.917[illegible]D 00	0.8088D-01	-0.1219D-01	0.4356D-03
0.53125	0.7078D 00	-0.5866D 00	-0.2456D 00	-0.736[illegible]D 00	0.8671D-01	-0.1033D-01	0.4818D-03
0.56250	0.73[illegible]D 00	[illegible]	-0.1728D 00	-0.5460D 00	0.9165D-01	-0.7987D-02	0.5169D-03
0.59375	0.7541D 00	-0.2676D 00	-0.1042D 00	-0.3493D 00	0.9549D-01	-0.5264D-02	0.5378D-03
0.62500	0.7783D 00	-0.1115D 00	-0.4138D-01	-0.1480D 00	0.9802D-01	-0.2272D-02	0.5417D-03
0.65625	0.8030D 00	0.4066D-01	0.1428D-01	0.5492D-01	0.9906D-01	0.8479D-03	0.5273D-03
0.68750	0.8278D 00	0.1870D 00	0.6150D-01	0.2565D 00	0.9842D-01	0.3932D-02	0.4942D=03
0.71875	0.8526D 00	0.3259D 00	0.9918D-01	0.4530D 00	0.9598D-01	0.6802D-02	0.4440D-03
0.75000	0.8770D 00	0.4558D 00	0.1265D 00	0.6408D 00	0.9164D-01	0.9274D-02	0.3798D-03
0.78125	0.9006D 00	0.5750D 00	0.1428D 00	0.8155D 00	0.8539D-01	0.1117D-01	0.3064D-03
0.81250	0.9[illegible]9D 00	0.6822D 00	0.1482D 00	0.9732D 00	0.7724D-01	0.1233D-01	0.2298D-03
0.84375	0.943[illegible]D 00	0.7758D 00	0.1428D 00	0.1109D 01	0.6730D-01	0.1262D-01	0.1566D-03
0.87500	0.9620D 00	0.8545D 00	0.1275D 00	0.1220D 01	0.5576D-01	0.1195D-01	0.9340D-04
0.90625	0.977[illegible]D 00	0.9172D 00	0.1035D 00	0.1303D 01	0.4288D-01	0.1029D-01	0.4540D-04
0.93750	0.9845D 00	0.9629D 00	0.7276D-01	0.1353D 01	0.2900D-01	0.7667D-02	0.1533D-04
0.96875	0.9972D 00	0.9906D 00	0.3740D-01	0.1371D 01	0.1455D-01	0.4178D-02	0.2160D-05
1.00000	0.1000D 01	0.1000D 01	0.0000D 00	0.1353D 01	0.0000D 00	0.0000D 00	0.0000D 00

Sample Output of INTGRTE:

Physical Energy Flux

```
(0,0) AND (0,1) MODES      GAMMA=  0.5000D 01     512 INTERVALS
 K1=    0.873439D 00      K2=    0.479845D 00

 LAMINAR FLOW PROFILE, MMAX=0.3

 PHYSICAL FLUX TERMS.

INT(1) = -0.7913D-01        0.00 PER CENT UNCERTAINTY        6 ROMBERG INTEGRATION STEPS
INT(2) =  0.1053D 00        0.00 PER CENT UNCERTAINTY        6 ROMBERG INTEGRATION STEPS
INT(3) =--0.3008D-01        0.00 PER CENT UNCERTAINTY        6 ROMBERG INTEGRATION STEPS
INT(4) =  0.3888D-02        0.02 PER CENT UNCERTAINTY        6 ROMBERG INTEGRATION STEPS
INT SUM=  0.39681D-05
```

RADIUS	EIGENVECTORS		CF1	CF2	CF3	CF4
0.00000	0.5118D 00	-0.2272D 01	-0.6587D 00	-0.2028D 01	0.0000D 00	0.0000D 00
0.03125	0.5125D 00	-0.2265D 01	-0.6570D 00	-0.2024D 01	-0.1240D-03	-0.3496D-03
0.06250	0.5145D 00	-0.2244D 01	-0.6516D 00	-0.2012D 01	-0.4968D-03	-0.1384D-02
0.09375	0.5179D 00	-0.2209D 01	-0.6427D 00	-0.1991D 01	-0.1120D-02	-0.3058D-02
0.12500	0.5227D 00	-0.2161D 01	-0.6303D 00	-0.1961D 01	-0.1996D-02	-0.5300D-02
0.15625	0.5289D 00	-0.2100D 01	-0.6142D 00	-0.1923D 01	-0.3128D-02	-0.8009D-02
0.18750	0.5364D 00	-0.2026D 01	-0.5945D 00	-0.1876D 01	-0.4520D-02	-0.1106D-01
0.21875	0.5453D 00	-0.1940D 01	-0.5711D 00	-0.1819D 01	-0.6172D-02	-0.1432D-01
0.25000	0.5556D 00	-0.1842D 01	-0.5442D 00	-0.1753D 01	-0.8087D-02	-0.1760D-01
0.28125	0.5673D 00	-0.1733D 01	-0.5137D 00	-0.1676D 01	-0.1026D-01	-0.2075D-01
0.31250	0.5803D 00	-0.1614D 01	-0.4798D 00	-0.1588D 01	-0.1269D-01	-0.2358D-01
0.34375	0.5947D 00	-0.1486D 01	-0.4426D 00	-0.1490D 01	-0.1535D-01	-0.2591D-01
0.37500	0.6104D 00	-0.1350D 01	-0.4023D 00	-0.1380D 01	-0.1824D-01	-0.2756D-01
0.40625	0.6275D 00	-0.1207D 01	-0.3593D 00	-0.1260D 01	-0.2132D-01	-0.2838D-01
0.43750	0.6458D 00	-0.1057D 01	-0.3140D 00	-0.1128D 01	-0.2456D-01	-0.2822D-01
0.46875	0.6653D 00	-0.9034D 00	-0.2668D 00	-0.9849D 00	-0.2790D-01	-0.2700D-01
0.50000	0.6861D 00	-0.7460D 00	-0.2185D 00	-0.8317D 00	-0.3127D-01	-0.2466D-01
0.53125	0.7078D 00	-0.5866D 00	-0.1697D 00	-0.6689D 00	-0.3461D-01	-0.2118D-01
0.56250	0.7306D 00	-0.4267D 00	-0.1214D 00	-0.4976D 00	-0.3782D-01	-0.1663D-01
0.59375	0.7541D 00	-0.2678D 00	-0.7457D-01	-0.3193D 00	-0.4078D-01	-0.1114D-01
0.62500	0.7783D 00	-0.1115D 00	-0.3017D-01	-0.1358D 00	-0.4337D-01	-0.4887D-02
0.65625	0.8030D 00	0.4066D-01	0.1062D-01	0.5059D-01	-0.4545D-01	0.1855D-02
0.68750	0.8278D 00	0.1870D 00	0.4666D-01	0.2373D 00	-0.4689D-01	0.8757D-02
0.71875	[illegible]	0.3259D 00	0.7603D-01	0.4212D 00	-0.4751D-01	0.1543D-01
0.75000	0.8770D 00	0.4558D 00	0.1001D 00	0.5990D 00	-0.4718D-01	0.2144D-01
0.78125	0.9006D 00	0.5750D 00	0.1156D 00	0.7670D 00	-0.4575D-01	0.2633D-01
0.81250	0.9229D 00	0.6822D 00	0.1227D 00	0.9213D 00	-0.4310D-01	0.2964D-01
0.84375	0.9436D 00	0.7758D 00	0.1210D 00	0.1058D 01	-0.3914D-01	0.3095D-01
0.87500	0.9620D 00	0.8545D 00	0.1107D 00	0.1173D 01	-0.3381D-01	0.2992D-01
0.90625	0.9775D 00	0.9172D 00	0.9214D-01	0.1263D 01	-0.2712D-01	0.2629D-01
0.93750	0.9895D 00	0.9629D 00	0.6641D-01	0.1325D 01	-0.1914D-01	0.2000D-01
0.96875	0.9972D 00	0.9906D 00	0.3502D-01	0.1355D 01	-0.1003D-01	0.1113D-01
1.00000	0.1000D 01	0.1000D 01	0.0000D 00	0.1353D 01	0.0000D 00	0.0000D 00

Appendix A11

TABULATED ENERGY-WEIGHTING FUNCTION RESULTS

Table A11.1

(0,0) MODE ENERGY-WEIGHTING FUNCTIONS

		Physical Energy Flux		Möhring/Blockhintsev Energy Flux		
	γ	Exact	Slug Flow Approximation	Möhring Exact	Blockhintsev Exact	Slug Flow Approximation
M_{max} = 1 one-seventh power profile	0.50	1.080	1.082	1.168	1.168	1.170
	1.50	1.075	1.082	1.162	1.162	1.170
	3.00	1.055	1.082	1.140	1.140	1.170
	6.00	0.983	1.082	1.061	1.061	1.170
	10.00	0.845	1.082	0.911	0.911	1.170
	15.00	0.669	1.082	0.720	0.720	1.170
	20.00	0.534	1.082	0.573	0.573	1.170
M_{max} = 0.3 one-seventh power profile	0.50	1.245	1.245	1.550	1.550	1.550
	1.50	1.229	1.245	1.530	1.530	1.550
	3.00	1.179	1.245	1.468	1.468	1.550
	6.00	1.013	1.245	1.256	1.256	1.550
	10.00	0.764	1.245	0.942	0.942	1.550
	15.00	0.544	1.245	0.665	0.665	1.550
	20.00	0.420	1.245	0.508	0.508	1.550
M_{max} = 0.5 one-seventh power profile	0.50	1.413	1.408	1.995	1.995	1.983
	1.50	1.390	1.408	1.962	1.962	1.983
	3.00	1.318	1.408	1.857	1.857	1.983
	6.00	1.088	1.408	1.525	1.525	1.983
	10.00	0.779	1.408	1.075	1.075	1.983
	15.00	0.540	1.408	0.735	0.735	1.983
	20.00	0.412	1.408	0.554	0.554	1.983

Table A11.1 (cont.)

		Physical Energy Flux		Möhring/Blockhintsev Energy Flux		
	γ	Exact	Slug Flow Approximation	Möhring Exact	Blockhintsev Exact	Slug Flo Approximation
M_{max} = 0.7 one-seventh power profile	0.50	1.586	1.572	2.506	2.506	2.470
	1.50	1.558	1.572	2.459	2.460	2.470
	3.00	1.468	1.572	2.315	2.315	2.470
	6.00	1.187	1.572	1.854	1.854	2.470
	10.00	0.828	1.572	1.265	1.265	2.470
	15.00	0.566	1.572	0.848	0.848	2.470
	20.00	0.429	1.572	0.633	0.633	2.470
M_{max} = 0.9 one-seventh power profile	0.50	1.765	1.735	3.086	3.087	3.010
	1.50	1.732	1.735	3.029	3.029	3.010
	3.00	1.628	1.735	2.837	2.837	3.010
	6.00	1.305	1.735	2.244	2.244	3.010
	10.00	0.896	1.735	1.501	1.502	3.010
	15.00	0.607	1.735	0.991	0.991	3.010
	20.00	0.457	1.735	0.733	0.734	3.010
M_{max} = 0.163 laminar flow profile (same flow-rate as M_{max} = 0.1 one-seventh power profile)	0.50	1.084	1.082	1.177	1.177	1.170
	1.00	1.074	1.082	1.166	1.166	1.170
	1.50	1.058	1.082	1.148	1.148	1.170
	3.00	0.979	1.082	1.059	1.059	1.170
	6.00	0.760	1.082	0.813	0.813	1.170
	10.00	0.535	1.082	0.563	0.563	1.170
	15.00	0.397	1.082	0.413	0.413	1.170
	20.00	0.324	1.082	0.335	0.335	1.170

Table A11.2

(1.0) MODE ENERGY-WEIGHTING FUNCTIONS

		Physical Energy Flux		Möhring/Blockhintsev Energy Flux		
	γ	Exact	Slug Flow Approximation	Möhring Exact	Blockhintsev Exact	Slug Flow Approximation
M_{max} = 0.1 one-seventh power profile	2.00	0.290	0.288	0.295	0.295	0.296
	3.00	0.586	0.592	0.618	0.618	0.629
	4.00	0.656	0.671	0.699	0.699	0.719
	6.00	0.687	0.723	0.736	0.736	0.779
	10.00	0.656	0.748	0.704	0.704	0.808
	15.00	0.577	0.756	0.620	0.620	0.818
	20.00	0.496	0.759	0.532	0.532	0.821
M_{max} = 0.3 one-seventh power profile	2.00	0.348	0.336	0.357	0.358	0.355
	3.00	0.650	0.663	0.748	0.748	0.776
	4.00	0.722	0.760	0.858	0.858	0.915
	6.00	0.737	0.826	0.894	0.894	1.013
	10.00	0.648	0.859	0.792	0.792	1.064
	15.00	0.515	0.869	0.626	0.626	1.080
	20.00	0.412	0.873	0.499	0.499	1.086
M_{max} = 0.5 one-seventh power profile	2.00	0.435	0.409	0.446	0.452	0.438
	3.00	0.723	0.735	0.887	0.889	0.926
	4.00	0.798	0.847	1.035	1.036	1.121
	6.00	0.802	0.928	1.080	1.080	1.271
	10.00	0.681	0.969	0.926	0.926	1.352
	15.00	0.520	0.982	0.704	0.704	1.377
	20.00	0.407	0.987	0.547	0.547	1.387

Table A11.2 (cont.)

	γ	Physical Energy Flux		Möhring/Blockhintsev Energy Flux		
		Exact	Slug Flow Approximation	Möhring Exact	Blockhintsev Exact	Slug Flow Approximation
M_{max} = 0.7 one-seventh power profile	2.00	0.538	0.497	0.551	0.567	0.536
	3.00	0.804	0.810	1.032	1.040	1.078
	4.00	0.880	0.934	1.223	1.227	1.336
	6.00	0.879	1.028	1.290	1.291	1.549
	10.00	0.731	1.079	1.094	1.094	1.670
	15.00	0.547	1.095	0.816	0.816	1.709
	20.00	0.424	1.101	0.625	0.625	1.723
M_{max} = 0.9 one-seventh power profile	2.00	0.650	0.595	0.666	0.699	0.642
	3.00	0.895	0.889	1.184	1.205	1.232
	4.00	0.971	1.021	1.422	1.432	1.555
	6.00	0.962	1.128	1.521	1.524	1.845
	10.00	0.792	1.188	1.292	1.292	2.017
	15.00	0.588	1.207	0.953	0.953	2.075
	20.00	0.452	1.214	0.724	0.724	2.095
M_{max} = 0.163 laminar flow profile (same flow-rate as M_{max} = 0.1 one-seventh power profile	2.00	0.300	0.288	0.293	0.293	0.296
	3.00	0.566	0.592	0.587	0.587	0.629
	4.00	0.613	0.671	0.643	0.643	0.719
	6.00	0.598	0.723	0.630	0.630	0.779
	10.00	0.495	0.748	0.519	0.519	0.808
	15.00	0.389	0.756	0.404	0.404	0.818
	20.00	0.322	0.759	0.332	0.332	0.821

Table A11.3

(2,0) MODE ENERGY-WEIGHTING FUNCTIONS

	γ	Physical Energy Flux		Möhring/Blockhintsev Energy Flux		
		Exact	Slug Flow Approximation	Möhring Exact	Blockhintsev Exact	Slug Flow Approximation
M_{max} = 0.1 one-seventh power profile	3.50	0.291	0.292	0.299	0.299	0.302
	4.00	0.385	0.389	0.401	0.401	0.408
	5.00	0.471	0.481	0.497	0.497	0.511
	6.00	0.509	0.526	0.540	0.540	0.562
	8.00	0.535	0.552	0.571	0.571	0.591
	10.00	0.536	0.586	0.573	0.573	0.631
	15.00	0.502	0.604	0.537	0.537	0.652
	20.00	0.451	0.610	0.483	0.483	0.659
M_{max} = 0.3 one-seventh power profile	3.50	0.329	0.329	0.348	0.349	0.356
	4.00	0.424	0.432	0.468	0.468	0.486
	5.00	0.514	0.539	0.592	0.593	0.631
	6.00	0.551	0.593	0.648	0.648	0.709
	8.00	0.567	0.646	0.678	0.678	0.786
	10.00	0.551	0.669	0.664	0.664	0.822
	15.00	0.474	0.693	0.572	0.572	0.857
	20.00	0.395	0.701	0.477	0.477	0.869
M_{max} = 0.5 one-seventh power profile	3.50	0.384	0.382	0.413	0.415	0.423
	4.00	0.474	0.483	0.544	0.546	0.569
	5.00	0.565	0.598	0.694	0.695	0.753
	6.00	0.612	0.660	0.766	0.767	0.862
	8.00	0.612	0.723	0.804	0.804	0.976
	10.00	0.586	0.752	0.781	0.781	1.031
	15.00	0.486	0.781	0.652	0.652	1.087
	20.00	0.394	0.791	0.528	0.528	1.107

Table A11.3 (cont.)

	γ	Physical Energy Flux		Möhring/Blockhintsev Energy Flux		
		Exact	Slug Flow Approximation	Möhring Exact	Blockhintsev Exact	Slug Flow Approximation
M_{max} = 0.7 one-seventh power profile	3.50	0.452	0.447	0.489	0.497	0.501
	4.00	0.533	0.541	0.626	0.633	0.656
	5.00	0.622	0.659	0.801	0.805	0.877
	6.00	0.659	0.727	0.892	0.894	1.018
	8.00	0.664	0.799	0.944	0.945	1.177
	10.00	0.632	0.834	0.917	0.918	1.257
	15.00	0.514	0.869	0.756	0.756	1.340
	20.00	0.413	0.881	0.604	0.604	1.371
M_{max} = 0.9 one-seventh power profile	3.50	0.529	0.520	0.573	0.590	0.586
	4.00	0.602	0.605	0.716	0.730	0.750
	5.00	0.685	0.722	0.913	0.923	1.003
	6.00	0.721	0.795	1.024	1.031	1.178
	8.00	0.722	0.842	1.098	1.101	1.300
	10.00	0.684	0.915	1.070	1.071	1.497
	15.00	0.552	0.956	0.880	0.881	1.616
	20.00	0.440	0.971	0.699	0.699	1.660
M_{max} = 0.163 laminar flow profile (same flow-rate as M_{max} = 0.1 one-seventh power profile)	3.50	0.288	0.292	0.289	0.289	0.302
	4.00	0.373	0.389	0.380	0.380	0.408
	5.00	0.443	0.481	0.457	0.457	0.511
	6.00	0.466	0.526	0.484	0.484	0.562
	8.00	0.464	0.552	0.484	0.484	0.591
	10.00	0.441	0.586	0.460	0.460	0.631
	15.00	0.371	0.604	0.385	0.385	0.652
	20.00	0.314	0.610	0.325	0.325	0.659

Table A11.4

(0,1) MODE ENERGY-WEIGHTING FUNCTIONS

		Physical Energy Flux		Möhring/Blockhintsev Energy Flux		
	γ	Exact	Slug Flow Approximation	Möhring Exact	Blockhintsev Exact	Slug Flow Approximation
$M_{max} = 0.1$ one-seventh power profile	4.00	0.304	0.303	0.309	0.309	0.308
	4.50	0.548	0.549	0.569	0.569	0.570
	5.00	0.675	0.677	0.709	0.709	0.710
	6.00	0.822	0.818	0.874	0.874	0.867
	8.00	0.975	0.940	1.048	1.048	1.006
	10.00	1.077	0.993	1.163	1.163	1.067
	15.00	1.337	1.043	1.451	1.451	1.125
	20.00	1.684	1.060	1.832	1.832	1.145
$M_{max} = 0.3$ one-seventh power profile	4.00	0.395	0.383	0.406	0.406	0.396
	4.50	0.614	0.616	0.669	0.669	0.671
	5.00	0.746	0.752	0.840	0.841	0.846
	6.00	0.915	0.914	1.071	1.071	1.064
	8.00	1.129	1.005	1.371	1.371	1.193
	10.00	1.319	1.130	1.630	1.630	1.375
	15.00	1.893	1.194	2.383	2.383	1.472
	20.00	2.422	1.217	3.063	3.063	1.506
$M_{max} = 0.5$ one-seventh power profile	4.00	0.530	0.504	0.545	0.546	0.524
	4.50	0.709	0.705	0.791	0.792	0.791
	5.00	0.831	0.841	0.978	0.979	0.989
	6.00	1.001	1.013	1.257	1.258	1.263
	8.00	1.243	1.184	1.666	1.666	1.560
	10.00	1.481	1.264	2.046	2.047	1.706
	15.00	2.177	1.344	3.107	3.107	1.857
	20.00	2.618	1.372	3.760	3.760	1.912

Table A11.4 (cont.)

		Physical Energy Flux		Möhring/Blockhintsev Energy Flux		
	γ	Exact	Slug Flow Approximation	Möhring Exact	Blockhintsev Exact	Slug Flow Approximation
M_{max} = 0.7 one-seventh power profile	4.00	0.684	0.644	0.704	0.706	0.670
	4.50	0.826	0.815	0.934	0.937	0.928
	5.00	0.933	0.942	1.127	1.130	1.142
	6.00	1.092	1.118	1.441	1.442	1.466
	8.00	1.337	1.305	1.936	1.937	1.852
	10.00	1.593	1.397	2.415	2.416	2.057
	15.00	2.330	1.493	3.704	3.704	2.278
	20.00	2.693	1.527	4.317	4.318	2.361
M_{max} = 0.9 one-seventh power profile	4.00	0.848	0.792	0.871	0.877	0.826
	4.50	0.960	0.939	1.092	1.097	1.079
	5.00	1.049	1.056	1.288	1.293	1.305
	6.00	1.190	1.228	1.626	1.630	1.673
	8.00	1.424	1.426	2.191	2.194	2.151
	10.00	1.679	1.530	2.749	2.751	2.423
	15.00	2.422	1.640	4.228	4.229	2.731
	20.00	2.741	1.681	4.841	4.842	2.849
M_{max} = 0.163 laminar flow profile (same flow-rate as M_{max} = 0.1 one-seventh power profile)	4.00	0.305	0.303	0.312	0.312	0.308
	4.50	0.537	0.549	0.565	0.565	0.570
	5.00	0.666	0.677	0.711	0.711	0.710
	6.00	0.838	0.818	0.910	0.910	0.867
	8.00	1.106	0.940	1.223	1.223	1.006
	10.00	1.371	0.993	1.530	1.530	1.067
	15.00	1.789	1.043	2.004	2.004	1.125
	20.00	1.555	1.060	1.727	1.727	1.145